Università degli Studi di Firenze
Scuola di Ingegneria
DIEF - Department of Industrial Engineering of Florence

PhD School: *Energetica e Tecnologie Industriali ed Ambientali Innovative*
Scientific Area: ING-IND/08 - *Macchine a Fluido*

Development of advanced numerical tools for the prediction of wall temperature and heat fluxes for aeroengine combustors

PhD Candidate: Ing. Simone Paccati

Tutor: Prof. Ing. Bruno Facchini

CoTutor: Dr. Ing. Antonio Andreini

PhD School Coordinator: Prof. Ing. Giampaolo Manfrida

XXXIII PhD School Cycle - 2017-2020

@ Università degli Studi di Firenze – Faculty of Engineering
Via di Santa Marta, 3, 50139 Firenze, Italy.

To my family,
because if I am the man I am today,
it's all thanks to you.

To my sweetheart,
because if you'll be always with me,
everything will be fine.

Thats ”mamba mentality”:
we don’t quit, we don’t cower, we don’t run.
We endure and conquer.
(Kobe Bryant)

Abstract

Current trends in the design of modern combustor concepts are addressed to improve the engine performances by exploiting increasing Operating Pressure (OP) and Turbine Inlet Temperature (TIT) with a consequent significant augmentation of heat loads on combustor liners. This aspect is made even more critical by the introduction of lean burn combustors driven by the need to respect the increasingly strict regulations imposed by ICAO-CAEP in terms of pollutant emissions. This concept causes a strong reduction of coolant available for ensuring the thermal resistance of combustor hot components since the largest amount of air is employed to control the combustion process. Consequently, the design of more and more effective cooling systems for aeroengine combustors, such as the most promising effusion cooling, has become a key factor to ensure further development of gas turbine engine and, at the same time, it demands for more accurate methodologies for the estimation of metal temperature.

The emergence of Computational Fluid Dynamics (CFD) as a detailed investigation tool has made numerical design an integral part of the gas turbine combustor development process, considering also the extremely expensive experimental campaigns carried out in pressurized reactive environments. Due to the multiphysics nature of the Conjugate Heat Transfer (CHT) problem in combustion chambers, there is an increasing need for high-fidelity CFD tools which are able to model the interactions between turbulence, combustion, radiation and heat transfer with a feasible computational cost in a scale-resolving framework. In fact, the latter is mandatory to overcome the well-known limits of standard RANS approaches in describing the high unsteadiness of reacting flows in aeroengine combustors. The computational effort is even more significant when the investigated combustor is equipped with an effusion cooling system since finer grids are required for a proper discretization of a high number of film cooling holes. Therefore, it is clear the need to develop simplified CFD approaches for coolant injection modelling which represent a valid trade-off between accuracy and computational savings.

In the present work, a multiphysics loosely-coupled tool, called U-THERM3D, is assessed as a detailed investigation tool for high-fidelity prediction of combustion and near-wall processes in a LES CHT simulation framework, allowing a deep understanding of heat transfer modes influence with an affordable computational cost. The numerical analysis is carried out on a laboratory-scale combustor representative of a Rich-Quench-Lean (RQL) concept, emphasizing the effect of radiative and wall heat losses on the highly sooting flame and the improvements in the wall temperature prediction with respect to a steady calculation.

In addition, a novel approach based on the application of 2D boundary sources to simulate the injection of coolant from effusion cooling holes is presented to overcome the issues related to the discretization of the effusion perforation, employing Reduced-Order Model (ROM) techniques from a Machine Learning framework. For this scope, an in-house external code is combined with the CFD package within the U-THERM3D framework. The numerical tool is firstly validated on simplified geometries in RANS and SBES calculations and, then, applied on a non-reactive single sector planar rig representative of a real combustor geometry to test the robustness of the proposed strategy in presence of a more complex flow field. Nevertheless, several improvable aspects are highlighted, pointing the way for further enhancements.

Contents

Nomenclature

Acronyms

ACARE	Advisory Council for Aeronautics Research in Europe
ASC	Axially Staged Combustor
BC	Boundary Condition
BR	Blowing Ratio
CAEP	Committee on Aviation Environmental Protection
CFD	Computational Fluid Dynamics
CHT	Conjugate Heat Transfer
CRVP	Counter-Rotating Vortex Pair
DAC	Double Annular Combustor
DES	Detached Eddy Simulation
DLR	Deutsches Zentrum für Luft-und Raumfahrt
DoE	Design of Experiment
DOM	Discrete Ordinate Method
DR	Density Ratio
EU	European Union
FGM	Flamelet Generated Manifold
FIRST	Fuel Injector Research for Sustainable Transport
FOM	Full Order Model

GPR	Gaussian Process Regression
HTC	Heat Transfer Coefficient
$ICAO$	International Civil Aviation Organization
IRZ	Inner Recirculation Zone
$JICF$	Jet-In-Cross-Flow
$K-M$	Kelvin-Helmholtz
LDI	Lean Direct Injection
LES	Large Eddy Simulation
LII	Laser-Induced Incandescence
LPP	Lean Premixed Prevaporized
LTO	Landing Take-Off
MoM	Method of Moments
$NEWAC$	NEW Aero engine core Concepts
$NHFR$	Net Heat Flux Reduction
$NMRSE$	Normalized Mean Root Square Error
$NSEs$	Navier Stokes Equations
ODE	Ordinary Differential Equation
OPR	Overall Pressure Ratio
ORZ	Outer Recirculation Zone
PAH	Polycyclic Aromatic Hydrocarbon
PCA	Principal Component Analysis
PDF	Probability Density Function
$PERM$	Partial Evaporation and Rapid Mixing
PID	Proportional-Integral-Derivative
PIV	Particle Image Velocimetry
PM	Particulate Matter
PSD	Power Spectral Density
PSR	Perfectly Stirred Reactor
PVC	Precessing Vortex Core
$RANS$	Reynolds Averaged Navier Stokes
ROM	Reduced-Order Model
RQL	Rich-Quench-Lean

RR	Reaction Rate
RTE	Radiative Transfer Equation
$SAFE$	Source bAsed eFfusion modEl
$SBES$	Stress-Blended Eddy Simulation
SFC	Specific Fuel Consumption
$SIMPLEC$	Semi Implicit Method for Pressure Linked Equations-Consistent
SM	Surrogate Model
SN	Swirl Number
$SOPRANO$	SOot Processes and Radiation in Aeronautical inNOvative combustors
SST	Shear Stress Transport
$SV-CARS$	Shifted Vibrational Coherent Anti-stokes Raman Scattering
SVD	Singular Value Decomposition
$TAPS$	Twin Annular Premix System
TBC	Thermal Barrier Coating
TIT	Turbine Inlet Temperature
TKE	Turbulent Kinetic Energy
$TRPIV$	Time-Resolved Particle Image Velocimetry
TS	Transported Scalar
UHC	Unburned Hydrocarbon
$URANS$	Unsteady RANS
VR	Velocity Ratio

Greeks

α	Absorptivity	$[-]$
α	Injection Angle	$[deg]$
α	Thermal diffusivity	$[m^2s^{-1}]$
β	Exctinction Coefficient	$[-]$
γ	Compound Angle	$[deg]$
δ	Thermal Flame Thickness	$[m]$

ϵ	Emissivity	$[-]$
ϵ	Turbulence eddy dissipation	$[m^2s^{-3}]$
η	Effectiveness	$[-]$
θ	Zenith Angle	$[rad]$
κ	Absorption Coefficient	$[-]$
λ	Eigenvalue	$[-]$
λ	Wavelength	$[-]$
μ	Dynamic viscosity	$[kgm^{-1}s^{-1}]$
ν	Kinematic viscosity	$[m^2s^{-1}]$
ρ	Density	$[kgm^{-3}]$
ρ	Reflectivity	$[-]$
σ	Stefan-Boltzmann constant	$[-]$
σ	Scattering coefficient	$[-]$
τ	Time Scale	$[s]$
τ	Transmissivity	$[-]$
ϕ	Azimuthal Angle	$[rad]$
ϕ	Eigenvector	$[-]$
χ_{st}	Scalar Dissipation Rate	$[s^{-1}]$
ω	Solid Angle	$[sr]$
ω	Turbulence eddy frequency	$[s^{-1}]$
Δ	Gradient	$[-]$
Φ	Equivalence Ratio	$[-]$

Letters

A	Area	$[m^2]$
Bi	Biot Number	$[-]$
C_D	Discharge coefficient	$[-]$
c	Speed of light	$[ms^{-1}]$
c	Progress Variable	$[-]$
c_p	Spec. heat capacity at const. P	$[Jkg^{-1}K^{-1}]$
D	Diameter	$[m]$
Da	Damköhler Number	$[-]$
E	Emission Power	$[Wm^{-2}]$

E_a	Activation Energy	$[J]$
Fo	Fourier Number	$[-]$
G	Irradiation	$[Wm^{-2}]$
h	Heat Transfer Coefficient	$[Wm^{-2}K^{-1}]$
I	Intensity of Radiation	$[Wsr^{-1}]$
I	Momentum Flux Ratio	$[-]$
K	Equilibrium Kinetic Constant	$[-]$
k	Thermal Conductivity	$[Wm^{-1}K^{-1}]$
k	Turbulent kinetic energy	$[m^2s^{-2}]$
Ka	Karlovitz number	$[-]$
L	Hole length	$[m]$
L	Reference length	$[m]$
M	Ratio of modelled and resolved k	$[-]$
$\dot{m}$	Mass flow rate	$[kgs^{-1}]$
Nu	Nusselt number	$[-]$
P	Prandtl number	$[-]$
P	Pressure	$[Pa]$
$\dot{q}$	Specific heat flux	$[Wm^{-2}]$
R	Specific gas constant	$[Jkg^{-1}K^{-1}]$
r	Radius	$[m]$
Re	Reynolds number	$[-]$
S	Pitch	$[m]$
S_L	Laminar Flame Speed	$[ms^{-1}]$
S_T	Turbulence Flame Speed	$[ms^{-1}]$
s	Direction of the Radiation Beam	$[-]$
T	Temperature	$[K]$
t	Solid thickness	$[m]$
t	Time	$[s]$
$U/V/v$	Velocity	$[ms^{-1}]$
y^+	Non-dimensional wall distance	$[-]$
Z	Mixture Fraction	$[-]$

Subscripts

0	Total
$adiab$	Adiabatic
air	Air
b	Backward
b	Blackbody
c	Chemical
c	Coolant
$comb$	Combustion
$cond$	Conductive
$conv$	Convective
eff	Effusion
f	Fluid
f	Forward
$fuel$	Fuel
g	Gas Phase
h	Hole
is	Isentropic
k	Kolmogorov scale
ov	Overall
rad	Radiation
ref	Reference
t	Turbulent
w	Wall
PIV	Particle Image Velocimetry
∞	Freestream
λ	Wavelength

Introduction

Because of the huge increase of air traffic, the attention to the environmental impact of civil aviation growth has become a key topic of public awareness and political concern during last years. In fact, the aviation sector is growing fast and it will continue to grow: according to the most recent estimates [1], air transport will increase by an average of 4.3% per annum over the next 20 years, as highlighted in Figure 1.

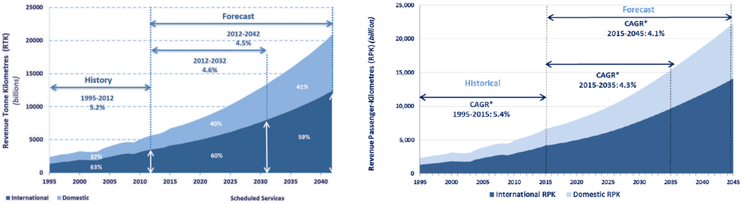

(a) *(b)*

Figure 1: Evolution of (a) the total kilometres travelled and (b) the total passenger traffic for civil aviation (adapted from [1]).

Together with the growth of air traffic, the effects of aircraft pollutant emissions on the local air quality increase. In this sense, aviation emissions generally affect both the local air quality, specifically in the vicinity of airports, and the global climate [2]. Therefore, the efforts devoted to the reduction of noise and chemical pollutants increase as well as the environmental awareness.

In order to address this growing issue, the Advisory Council for Aeronautical Research in Europe (ACARE) has set several ambitious goals with the Flightpath 2050 [3] to reduce noise and emissions, fixing a roadmap to ensure further development of civil aviation in Europe in a safe, more efficient and environmentally-friendly manner. In particular, Flightpath 2050 objectives set targets of 75% and 90% reductions per passenger kilometre for CO_2 and NO_x emissions respectively and of 65% for perceived noise, relative to year-2000 aircraft [3]. In line with these goals, the emission regulations for aircrafts are established by the International Civil Aviation Organisation (ICAO) and its Committee on Aviation Environmental Protection (CAEP), becoming more and more stringent and, thus, creating a strong driver for investigating novel aeroengine designs that produce less CO and NO_x emissions. Since NO_x has been considered as a primary issue, ICAO adopted more stringent regulations regarding its emissions during the subsequent CAEP meetings in the past, as shown in Figure 2. In recent years, the attention of CAEP has been focused on the development of global standards also for CO_2 emission and non-volatile Particulate Matter (nvPM) [2].

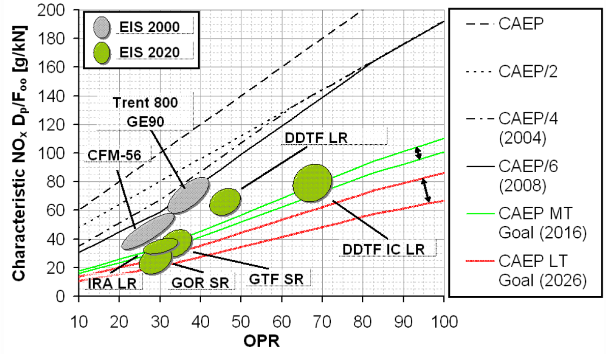

Figure 2: NO_x emissions assessment for different future aeroengine design concepts [4].

Since the generation of pollutant emissions is mainly related to the combustion process, the combustor represents the component on which the most of the research efforts must be spent for the development of new environmentally-friendly engines. However, the control of the generated chemical emissions has been more challenging due to the current augmentation of the Overall Pressure Ratio (OPR) and of the Turbine Inlet Temperature (TIT) which leads to higher aeroengine performances but, at the same time, to higher flame temperatures. Considering that NO_x emissions have an exponential dependence on temperature by means of the largest contribution of *thermal* NO_x, it is clear that the potential improvements derived from higher OPR and TIT may be counterbalanced by high NO_x formation rates. The highest temperatures within a combustion chamber occur in the regions where a local stoichiometric condition is achieved. Therefore, the reduction of nitrogen oxide emissions requires to minimize the formation of such zones as well as of the residence time (to limit nitrogen oxidation) by means of an accurate control of the local air-fuel mixture quality.

With the progress of technology, several gas turbine combustor architectures have been widely investigated to reach ultra-low emission levels and some of these technologies have been successfully applied to aviation engines. Starting from the rich burn combustor design paradigm for flame stability, the Rich-Quench-Lean (RQL) concept has been developed to reduce the residence time of the reacting flow in stoichiometric condition during the transition from the primary rich to the secondary lean regions and it has become the state-of-the-art for low emission aeronautical burners, providing a stable combustion and, hence, a safe operability of the engine during all the flight operations. Currently, this technology is still the object of various studies aimed at achieving further improvements in terms of low emissions but it presents some intrinsic limitations in respecting the future NO_x emission regulations (i.e. difficulties in a precise control of the local air-fuel mixture quality due to the necessary rapid mixing).

Consequently, the research has pushed towards the investigation of alternative combustor concepts such as the Lean combustors which are characterized by a deep modification of the internal flow split, as shown in Figure 3.

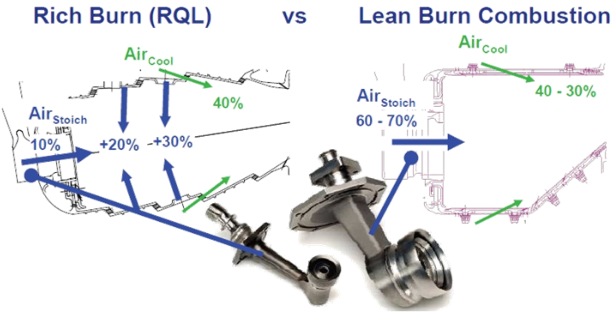

Figure 3: Rich burn (on the left) and lean burn (on the right) combustor concepts.

In fact, the largest amount of air coming from the compressor is here supplied through the injector in order to develop a combustion process in lean conditions, avoiding the generation of high temperature spots related to the presence of local stoichiometric conditions and, so, providing a decrease of NO_x emissions. On the other hand, this combustion strategy is characterized by several technological drawbacks, such as flame stabilization, flashback or blowout or the occurrence of thermoacoustics phenomena. All these potential issues require an extremely detailed investigation during the design process.

Regarding the safe operability of the combustion system, both the described low emission architectures present some critical aspects for the thermal management of hot gas path components which is fundamental to fulfil all the technological requirements demanded to a modern combustor. Whereas the RQL concept is characterized by a rich and high temperature primary zone, the lower flame temperature of Lean combustors is mitigated by the strong reduction in air availability for liner cooling, since up to 70% of the overall air mass flow is employed for fuel preparation and control of lean combustion [5]. In this context, a key aspect to ensure longer hot components durability is represented by the development of highly-effective cooling strategies as well as their optimization in order to maintain high performances during all the combustor flight conditions and to not affect the combustion process and the flame stability, causing its blowout or a not desired increase of emissions.

Consequently, several research studies have been focused on the investigation of advanced cooling techniques which are able to maintain the solid temperature below the melting point with a limit coolant air consumption. Among all strategies, the most promising one is represented by the effusion cooling by means of multi-perforated liners (see Figure 4) which ensures a more uniform protection of the liner from hot gases together with a significant heat sink effect within the holes thanks to the convective heat transfer related to the passage of coolant air [6, 7, 8].

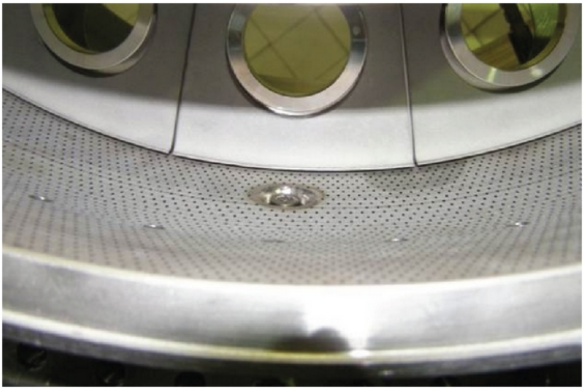

Figure 4: Combustor prototype of European Project NEWAC [9].

For these reasons, this cooling strategy has been experimentally and numerically investigated to detect the optimal hole pattern and geometry as well as the fluid dynamics parameters that influence the adiabatic effectiveness and, so, the resulting metal temperature distributions. Due to the high pressure reactive systems under investigation, experiments show strong limitation to understand the involved multiple mechanisms since the experimental investigations are generally carried out on simplified and isothermal test cases, far from the real aeroengine combustor operating conditions. Moreover, the associated high cost and time efforts make them unfeasible during a preliminary design process of a combustor.

Compared to the expensive experimental tests which generally provide only global and macroscopic information, CFD is very attractive for practical applications since it can br repeated during the design process to examine the effects of small design changes and to obtain a very deep insight of the investigated system with much lower costs. From a numerical point of view, multiphysics approaches are mandatory to achieve a reliable prediction of wall temperatures and heat fluxes since several complex and extremely coupled phenomena (i.e. turbulence, combustion, radiation, pollutant generation) must be taken into account when a CHT problem within a combustion chamber is considered. The complexity of the employed numerical strategies depends on the desired accuracy. The Reynolds Averaged Navier-Stokes (RANS) approach has been widely employed as the standard CFD tool for combustor design in industrial framework because of its affordable computational cost in computing only the mean flow quantities by means of ad hoc models for accounting the turbulence effects. However, it has been demonstrate how such approach is not able to correctly describe the unsteadiness of the fully-turbulent reacting flows in practical jet engines, strongly affecting the prediction of fluid-wall interactions and the resulting wall temperature distribution. The use of scale-resolving approaches, such as Large Eddy Simulation (LES) or hybrid RANS/LES models, allows to overcome the RANS drawbacks with an accurate estimation of turbulent mixing and flame evolution [10, 11, 12] as well as a better resolution of turbulent structures in the near-wall region. This leads to an improvement in the prediction of the interaction of the reactive flow with the wall and, so, to a more accurate estimation of heat loads and wall temperatures [13].

On the other hand, higher computational efforts are required and this is even more challenging in a multiphysics problem. In fact, the different time scales for the involved phenomena do not permit to perform efficient numerical simulations with an affordable computational cost by means of a *fully-coupled* strategy where the entire set of governing equations is solved together by one solver. Several coupling methodologies have been studied among which the so-called *loosely-coupled* method is very interesting since each physics is here computed with a dedicated solver for which the most suitable mesh and numerical setup are employed according to the characteristic scales of the addressed phenomenon. The exchange of proper quantities between the simulations allows to take into account the relative interactions. In addition, simulating a real aeroengine combustor means generally to deal with the discretization of thousand of holes of the equipped effusion cooling system with proper fine grids to correctly solve the coolant injection, leading to an abrupt increase of the computational cost of the whole simulation. Therefore, simplified CFD approaches are required to model the film cooling injection with a reduced computational effort and to improve and speed up the design process of such systems, searching for the best trade-off between accuracy and computational resources.

Aim of the work

The main purpose of the present research activity is the development and the validation of advanced numerical tools for the aero-thermal analysis and for a proper prediction of wall temperatures and heat fluxes in aeroengine combustors. In this context, a loosely-coupled multiphysics tool (U-THERM3D) developed by Bertini [14] within ANSYS Fluent has been assessed as a detailed investigation tool on a laboratory-scale combustor with high-fidelity prediction of combustion and near-wall processes in an unsteady CHT simulation framework. Having the possibility of splitting the contributions of different heat transfer mechanisms (convection, conduction and radiation) by employing different simulations for each physics, a deep understanding of heat transfer modes influence on the aero-thermal fields of the investigated system is achieved together with a reliable prediction of wall temperature pattern, focusing the attention on the impact of radiation and on the effect of solid-fluid coupling. Keeping in mind as a long-term objective an industrial application of the adopted procedure, such investigation is carried out with an affordable computational cost thanks to the loosely coupling strategy which leads to a desynchronization of time-steps between the involved unsteady simulations. In fact, another main outcome of the present work is that scale-resolving methods are mandatory for a proper computation of the internal flow fields in order to obtain a reliable prediction of reactive flow behaviour and turbulent mixing as well as of the flame-wall interaction.

Furthermore, great efforts have been spent for the development of a novel modelling strategy of effusion cooling jets in CFD calculations, since one of the major issues in the numerical design of effusion cooled combustor is the large number of cells required for an appropriate spatial discretization of thousand holes. Therefore, an innovative approach to avoid the meshing of discrete holes has been implemented by coupling the CFD solver with a MATLAB code where a Reduced-Order Model (ROM) has been developed for the prediction of coolant injection velocity and turbulence, starting from the results of a Design of Experiment (DoE) performed on a single effusion hole. In fact, these quantities strongly influence the mainstream-coolant interaction, the prediction of film coverage and, so, the adiabatic effectiveness distribution which in turn highly affects the wall temperature estimation. From an industrial point of view, this represents a good compromise between an accurate modelling of Jet-In-Cross-Flow (JICF) phenomena and a speed-up of the design process by employing lower computational resources. Both in steady and unsteady applications, the effusion model has been numerically validated on several geometries of increasing complexity against a full-mesh approach and experimental data where available.

Thesis outline

As far as the contents of the present manuscript are concerned, numerical investigations of heat transfer and cooling in aeroengine combustors have been reported in the context of unsteady applications. Therefore, large efforts have been devoted for a deep understanding of such aspects in modern combustor concepts. For a proper thermal design and analysis from a numerical point of view, there is the need of employing high-fidelity approaches such as scale-resolving techniques which can strongly affect the feasibility of CHT simulations in an industrial framework. In this sense, the assessment of a loosely-coupled multiphysics tool as a detailed thermal investigation procedure and the proposal of a novel approach for effusion modelling are pointed out as the main achievements to cut down the computational efforts related to high-fidelity CHT simulations of effusion cooled aeroengine combustors. Consequently, a detailed description of the state of the art in the numerical strategies for unsteady CHT calculations and in the effusion modelling is provided by means of a comprehensive review of approaches already available in technical literature. Regarding the strategies for coolant injection, the review highlights the lack of a formulation for the flow field prediction at hole outlets, justifying the research efforts then spent for the development of the novel approach. The dissertation will be structured as follows:

- **Chapter 1**: the description of modern aeroengine combustors is reported with particular attention to lean burn technology and their cooling problems, explaining the context into which the numerical tools have been developed;

- **Chapter 2**: this chapter is devoted to the knowledge of the involved phenomena when the heat transfer within an aeroengine combustor is considered and of their mathematical formulations in order to emphasize the significant differences in terms of time and space scales;

- **Chapter 3**: here, the attention is focused on the description of the common cooling strategies adopted for the combustor thermal management with particular attention to the effusion cooling technique and to its geometric and fluid dynamics characteristic parameters and their influences;

- **Chapter 4**: in this chapter, the numerical strategies adopted to perform the simulations reported in this manuscript are described. At first, the U-THERM3D procedure is presented together with an explanation of the need of a loosely-coupled approach to numerically deal with the different characteristic spatial and temporal scales of the heat transfer mechanisms involved in the framework of unsteady CHT calculations. In this sense, a comprehensive review of such approaches available in technical literature is also reported. Then, the development of the proposed approach for effusion modelling is discussed, describing the employed RO techniques and the coupling strategy with the CFD solver within U-THERM3D structure. Also in this case, the advantages of such approach with respect to the state of the art in effusion modelling are highlighted;

- **Chapter 5**: the multiphysics numerical tool U-THERM3D is employed for an aero-thermal analysis of a RQL laboratory-scale combustor, highlighting the importance of a scale-resolving approach for a high-fidelity prediction of combustion and near-wall processes by means of comparisons with previous RANS results and experimental data. The aim of this chapter is to demonstrate the capability of U-THERM3D as a detailed investigation tool to understand the influence of wall and radiative heat losses and to properly predict solid temperature with affordable computational costs;

- **Chapter 6**: the validation of the developed effusion model is here presented. Firstly, a numerical analysis of the DoE results is provided in order to prove the goodness of the generated ROM. Then, model results are compared with respect to full-mesh solutions and to the results obtained with the previous effusion modelling strategy implemented in U-THERM3D. The assessment has been carried out on simplified single-hole and multi-perforated geometries by considering several operating conditions for the effusion system in the context of steady and unsteady calculations;

- **Chapter 7**: the application of the innovative effusion model to a non-reactive test rig representative of a real effusion cooled combustor is the main goal of this chapter. The results are compared to those of a previous full-mesh SBES simulation and to experimental data in term effusion flow fields. In addition, a numerical analysis of coolant and adiabatic effectiveness distribution on the effusion plate is carried out.

In the last chapter, a summary of the main achievements of this research activity is given together with conclusions and recommendations for future works.

Chapter 1

Aeroengine combustor technologies

During last years, large research efforts have been devoted to the development of new aeroengine combustor concepts. Such technological tendency has been driven by the necessity of achieving low-pressure losses, high combustion efficiency, low weight and compact design [15] but, especially, to meet the increasingly stringent regulations in terms of pollutant emissions. In fact, NO_x, Unburned Hydrocarbons (UHC), CO and Particulate Matter (PM) are the main pollutant chemical species emitted by aircrafts. Clearly, they represent an extremely dangerous aspect for human health and global climate.

As shown in Figure 1.1, the aircraft emissions are regulated by standards published and updated by the ICAO-CAEP, referring to the Landing Take-Off (LTO) cycle to simulate the aircraft operations below 915 m that include idle, take-off, climb-out and approach phases [16]. In addition, ACARE collects a set of strategic guidelines for an environmentally-friendly development of civil aviation. Concerning this, ACARE imposes, first in Vision 2020 then in Flightpath 2050, a reduction of 75% and 90% per passenger kilometre respectively for CO_2 and NO_x emissions and a reduction of 65% for perceived noise [17].

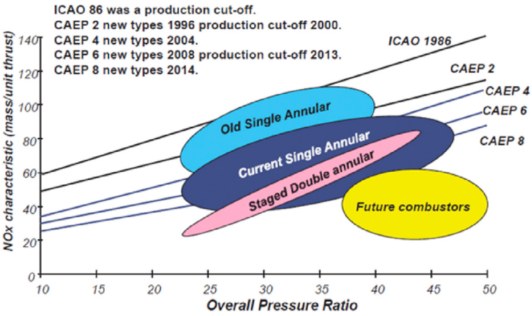

Figure 1.1: Trends for low-emission combustors together with NO_x emission levels with respect to ICAO standards [16].

Such implications related to air transportation have become more critical due to the current trends in aviation industries, resulting in an increase of OPR and TIT. In fact, these design factors promote NO_x production which is still one of the main critical aspects in the design of modern aeroengine combustors.

Among all factors influencing the NO_x emissions in gas turbine combustors, such as system geometry, fuel distribution and inlet pressure, the most relevant is the flame temperature, as highlighted by Figure 1.2.

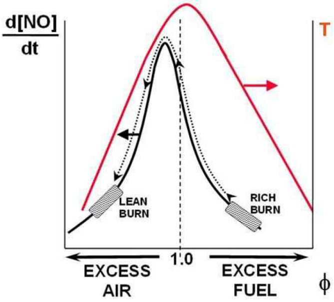

Figure 1.2: Flame temperature and NO_x formation rate as functions of equivalence ratio Φ (adapted from [18]).

This is related to the exponential temperature dependence of the formation rate of thermal NO_x, according to Zeldovich mechanism [19]. Consequently, higher levels of this pollutant chemical species occur in combustor regions which are characterized by air-fuel ratio close to stoichiometric conditions. Therefore, low rates of NO_x are obtained by minimizing the residence time of the reacting flow in stoichiometric and high temperature zones by means of a careful control of air distribution and, so, of local air-fuel ratio. Considering the amount of generated NO_x as a function of the equivalence ratio Φ (Figure 1.2), it is evident that the system should work with less air (rich burn) or excessive air (lean burn), far away from the highest flame temperature which occurs around the unitary value for Φ.

These considerations represent the principles on which the two main concepts and technologies in the context low-emission combustors are based, Rich-Quench-Lean and Lean Burn combustors.

1.1 Rich-Quench-Lean combustors

Currently, the most common strategy for low-emission aeroengine combustors is represented by the Rich burn - quick Quench - Lean burn (RQL) concept, introduced for the first time in 1980s in order to reduce NO_x emission in gas turbine engines [20]. According to Figure 1.3, RQL combustion technology is a special staged combustion method where the oxidation process occurs through three consecutive different regions: a rich primary zone ($\Phi = 1.2 - 1.6$) where the combustion process starts by reacting a fraction of the total employed air with all the fuel; a queching zone where a rapid injection of air is performed in order to abruptly reduce the equivalence ratio; a final lean region ($\Phi = 0.5 - 0.7$) where the reaction is completed.

Since the initial zone is characterized by rich burn condition, better ignition conditions are created and the stability of the combustion reaction is enhanced by means of the production of high concentration of energetic hydrogen and hydrocarbon radical species, together with reduced levels of

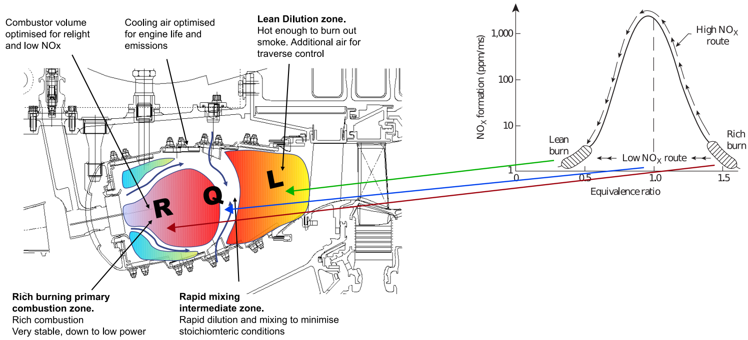

Figure 1.3: Rich-Quench-Lean combustor concept, RR Trent XWB (adapted from `http://www.newac.eu` and [21]).

NO_x due to the relative low gas temperature and to the oxygen depletion. In the quenching stage, the rapid production of thermal NO_x at stoichiometric condition is prevented by injecting through *dilution holes* a large amount of air which mixes with burnt gas from the primary zone and processes the partial products of combustion, transiting rapidly to lean condition. Finally, in the lean burn zone high temperature rise occurs for the completion of the combution process where the lean equivalence ratio promotes the decrease of pollutant emissions. Therefore, the RQL technology represents an optimal combination of combustion with high temperature rise and low emission [22].

Clearly, one of the most critical aspect of RQL concept is a careful design of the quenching section by means of a strict control of the airflow in this zone. In fact, the addition of the oxidation air can promote local critical values of $\Phi \approx 1$ where both the temperature and oxygen atom concentrations are elevated, causing higher production of oxides of nitrogen. Moreover, the design becomes even more critical since the air flow split which ensures the best mixing may not necessarily minimize NO_x [23, 24].

As stated before, another critical aspect is the control of the equivalence ratio in the lean burn region in which the completion of the combustion process must occur. As shown in Figure 1.4, the temperature must be high enough to burn partially oxidized species, such as CO, UHC and soot, generated in the primary rich region and as a consequence of local flame quench, especially in the near-wall region, resulting in a high combustion efficiency and satisfying all emissions requirements.

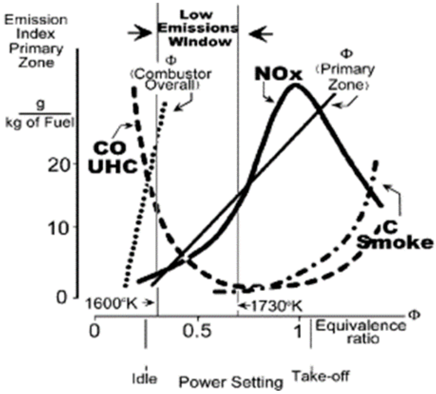

Figure 1.4: Evolution of NO_x, UHC and CO emissions with temperature and equivalence ratio [25].

A more demanding challenge is also the design of effective cooling systems to ensure liner durability. Due to the large amount of air employed for the quenching of the flame, limited quantities of the remaining air can be used for liner cooling. Moreover, the high content of carbon particles in the rich primary zone leads to an increase of radiative heat loads which may give rise to local peaks of wall temperature upstream the quenching section. On the other hand, the presence of dome film cooling can here affect the equivalence ratio distribution, resulting in local peaks of NO_x formation rate due to stoichiometric values. In this sense, high efficiency is mandatory in order to ensure the thermal resistance of hot components with lower quantity of coolant air. At the same time, low interactions with the reactive flow is required to avoid the formation of local stoichiometric conditions.

Despite the described critical features, RQL combustors are actually preferred in aeroengine applications due to the safety and overall stability throughout the whole operating cycle and research efforts are still spent for their improvements. In particular, advanced fuel spray nozzles are studied to improve the fuel-air mixing and optimization processes are carried out about the position of dilution holes also for a control of temperature profile at turbine inlet [2], as highlighted by Figure 1.5.

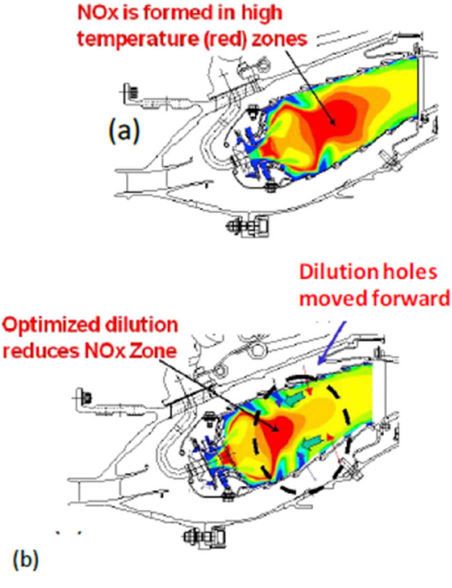

Figure 1.5: The effect of dilution holes on NO_x formation [26].

However, the mentioned combustor characteristics represent intrinsic limitations in order to respect the expected next NO_x reduction targets and, therefore, innovative alternative technologies must be developed.

1.2 Lean combustors

Lean burn technologies are today considered as the key architecture for aero-engine combustion systems to further improve fuel efficiency and, at the same time, to achieve future legislative requirements for NO_x. The main idea of this concept is the creation of a lean environment where the combustion process occurs. In this way, the combustor works in a range of $1800 - 1900$ K and with an equivalence ratio of $0.5 - 0.7$, reaching a trade-off between CO and NO_x, as shown in Figure 1.6

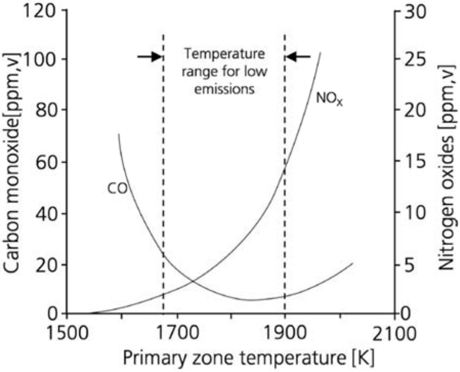

Figure 1.6: Operating priciple of lean burn technologies [27].

In order to obtain lean condition, a large amount of air should be accurately mixed with the fuel before entering the combustion zone, since the primary region of the combustor has to be characterized by high excess of air. Several strategies have been studied, differentiating on the way through which the fuel-air mixing is carried out.

1.2.1 Fuel staging

Fuel staging has represented the first attempt of implementation of lean burn concept by exploiting the lean combustion at high power operating conditions of the combustor by means of a careful control of fuel or air injection in different combustion locations [28]. Therefore, the system is divided in multiple zones which are "activated" or "deactivated" depending on the required power, trying to maintain high combustion efficiency and stability and low CO and NO_x emissions throughout all engine conditions (see Figure 1.7).

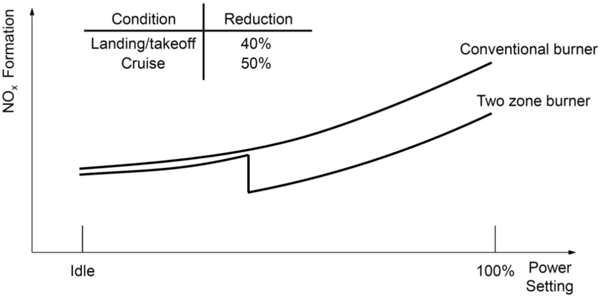

Figure 1.7: NO_x emissions vs. power for conventional and staged combustors (adapted from [28]).

A radially staging strategy is adopted by the Double Annular Combustors (DAC), identifying two different radial zones, as observed in Figure 1.8.

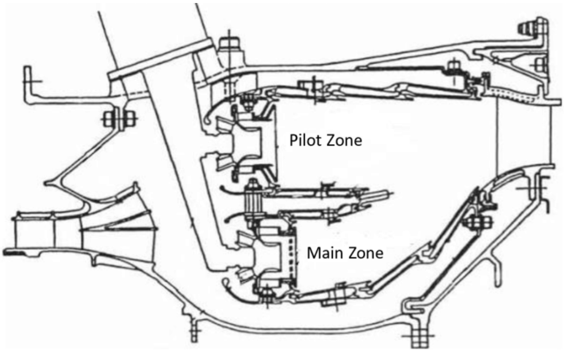

Figure 1.8: Double Annular Combustor cross-section [29].

Both the pilot and the main zones are fed with air but only part of combustion zones operates, depending on the current power setting of the system. At low power conditions, only the pilot zone is fuelled and ignited, working with a relatively high equivalence ratio ($\Phi \approx 0.8$) in order to achieve high combustion efficiency with low CO and UHC emissions and simultaneously to avoid the risk of lean instability. On the contrary, at higher power settings also the main zone is involved in the combustion process, reaching a global low operating equivalence ratio in the whole combustion chamber and, so, allowing a lean combustion for NO_x and smoke reduction. However, such configuration introduces challenges in cooling due to larger dome surface areas and in controlling the exit temperature profile due to possible low mixing between the pilot and the main flows and, consequently, due to the presence of stoichiometric high temperature spots [2].

The same working principle characterizes the Axially Staged Combustors (ASC) but, in this case, the different combustion zones are located in the axial direction by placing the pilot zone at the upstream of the combustor whereas the main one downstream, as depicted in Figure 1.9.

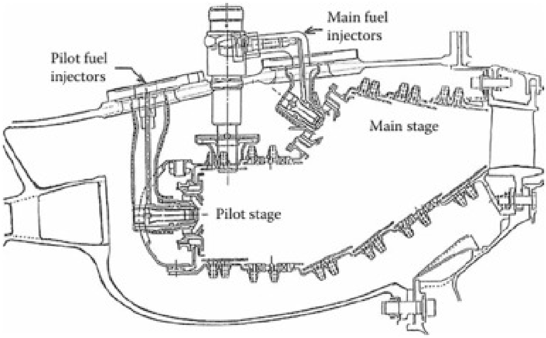

Figure 1.9: Axially Staged Combustor geometry (Pratt & Whitney V2500-A5) [2].

With respect to the previous concept, ASC provides a good combustion efficiency and stability (low CO and UHC) together with a rapid and reliable ignition for the main zone thanks to the upstream hot gases coming from the pilot region on which the main unfuelled airflow has no quench effect. On the contrary, the disposition of the nozzles can introduce structural problems for the main injectors which are surrounded by hot gases.

Combustion staging can be also achieved by employing a variable geometry control system to regulate the air flow and, consequently, to control the combustion equivalence ratio in the primary zone of the combustor. However, the main drawback of these architectures is the increase of the complexity of the systems employed to control the large volume flow of combustion air with higher weight and cost of the combustion device.

1.2.2 Lean Premixed Prevaporized

With the aim of achieving a drastic NO_x descrease related to spray combustion, the Lean Premixed Prevaporized (LPP) concept has been introduced. The working principle of this strategy is to focus the attention on the fuel preparation before entering the combustion chamber. In this sense, the liquid fuel is completely evaporated and mixed with air in a premixer device in order to supply a fuel-air mixture as homogeneous as possible, resulting in a combustion process which occurs at an equivalence ratio very close to the lean blowout limit. An example is reported in Figure 1.10, where the GE's lean premixed LM6000 aero-derivative engine can be seen.

In this way, the flame temperature is maintained low with no hot spots, leading to a strong reduction of NO_x and soot levels and favouring also the liner durability thanks to the lower convective and radiative heat loads. To promote also the complete oxidation of partially burnt species like CO and UHC, the combustor is generally designed to have a longer residence time [31]. However, the application of this concept is limited by the increasing risks of auto-ignition and flashback of the flame within the LPP injection system with high operating pressure and temperature as far as by stability issues due the higher lean blowout risks.

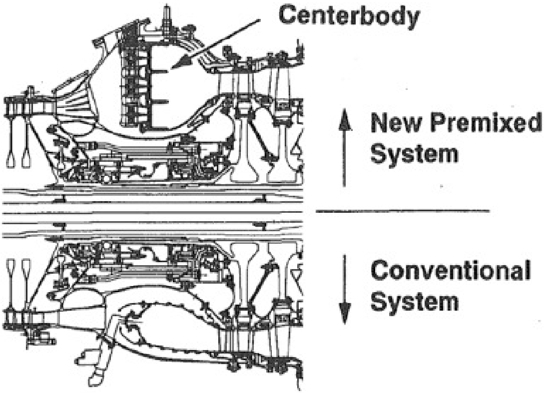

Figure 1.10: Comparison of LPP (top) and the conventional LM6000 (bottom) [30].

1.2.3 Lean Direct Injection

Considering the mentioned drawbacks related to LPP technology and that modern civil engines have increasingly high OPRs in order to reduce engine Specific Fuel Consumption (SFC), the LDI (Lean Direct Injection) concept has been proposed. Here, the liquid fuel is injected directly into the combustion chamber and quickly mixed with a large fraction of air thanks to strong recirculation motions generated by the injector. In this way, hot spots due to local stoichiometric conditions are eliminated and the peak flame temperature is reduced, allowing low NO_x emissions. Since the larger part of air is supplied through the injector, a constant equivalence ratio is maintained throughout the combustion chamber without the need of dilution holes. In this context, a strict control is mandatory to avoid the occurrence of flame instability and blowout, causing an undesired augmentation of CO and UHC.

Therefore, the main challenge is to achieve a rapid mixing between fuel and air before the reaction takes place in a short distance downstream the fuel injection region. For this purpose, a key role is assumed by the injector and it is evident that great attention must be focused on atomization and evaporation processes. To do this, a fuel staging is generally arranged by means of a pilot and main nozzles within the injector. The fuel splitting varies according to the engine operating conditions: the staging utilises pilot alone for idle, pilot and part of the main for approach, and pilot and all main for cruise and higher power conditions [2].

Developed during GE and NASA sponsored programmes and mounted on GEnx jet engine series, the Twin Annular Premixing Swirler (TAPS) technology belongs to this category, since it is composed of pilot and main stages with both concentrically mounted, as shown in Figure 1.11.

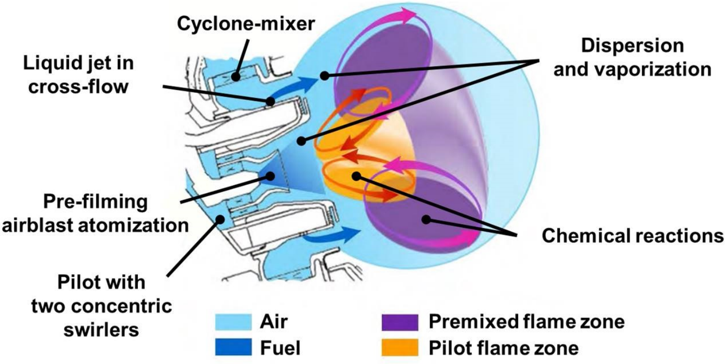

Figure 1.11: Schematic representation of TAPS technology [32].

At low power operating conditions, 100% of the fuel is injected by the pilot stage which consists in a simplex atomizer surrounded by two co-rotating or counter-rotating swirling flows. Here, the fuel spray is generated and directed towards the pre-film lip where it is atomized by the two axial air streams in an air blast mode. Consequently, a pilot flame occurs and it is strongly stabilized by recirculation zone generated by the swirling flows. This leads to a high combustion efficiency and stability. At higher power, the fuel is split between the pilot (70%) and the main mixer (30%) in order to give rise to a partially premixed combustion. In fact, the main quota of the fuel is injected through a series of transverse jets into a premixing channel where a high swirling flow generated by a

Cyclone swirler passes. This allows to establish a lean premixed main flame in the mixing layer between the pilot and the main stages. In this way, the hot gas and radicals coming from the pilot combustion feed and stabilize the lean main flame in the surrounded space.

Such technology is characterized by ultra-low NO_x emissions which highlight the goodness of premixed combustion in respecting the future regulations. Moreover, a higher control of the combustor exit temperature distribution is achieved with a strong reduction of hot spots which can highly affect the liner and turbine lifes. As the LPP concept, large efforts have to be devoted to avoid the auto-ignition and flashback of the flame which can be also subjected to combustion instability.

A similar concept of partially premixed combustion has been developed in the framework of NEWAC project with the aim of overcoming the risks of auto-ignition and flashback which may occur at medium and high OPR for LPP technologies. In this context, the so-called Partially Evaporating and Rapid Mixing (PERM) injection system is based on the adoption of prefilming airblast atomizers for liquid fuel atomization in order to ensure a first partial evaporation within the injector followed by a rapid mixing between vapour fuel and air, allowing a lean stabilized flame, as shown in Figure 1.12.

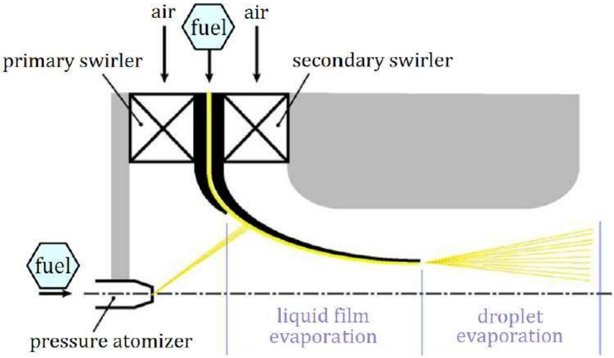

Figure 1.12: Sketch of PERM technology [33].

Main air is supplied through a double swirler configuration whereas the fuel is injected between the two co-rotating swirled flows, forming a liquid film over the inner surface of the lip which separates the swirlers. As the film reaches the edge of the lip, primary atomization occurs and the fuel spray is generated. Due to the strong interactions with the two co-rotating swirled flows, the spray consists of fine droplets which provide the partially premixed mixture by means of a rapid mixing with the surrounded air. To ensure the stability of the flame at low power operating conditions, a hollow cone pressure atomizer is employed as pilot injector, contributing to the formation of the liquid film and to the feed of the combustion process. An important role in avoiding combustion instability is played by the strong primary recirculation of hot gases related the vortex breakdown and generated by the double swirler configuration. Similar advantages and drawbacks of TAPS technology are obtained.

1.3 Concluding remarks

Considering all the mentioned lean burn concepts, it is evident that the adoption of such technologies is currently limited by complex challenges regarding firstly the operational safety of the combustor in addition to emission levels. High altitude-relight capability and avoidance of auto-ignition and flashback respectively related to possible local quenching of the lean flames and to the use of premixing systems must be ensured. Concerning these issues, strong attention has to be focused on the aerodynamics of injection devices and on the control of flow pattern within the combustion chamber.

In parallel, stable combustion is an additional critical challenge since lean burn combustors are more prone to thermo-acoustic instabilities, a phenomenon generated by the coupling between combustor acoustic modes, pressure fluctuations in the flow field and unsteady heat release due to combustion instabilities. This can lead to serious damages of the combustor solid structure. In fact, these self-sustained instabilities start from pressure oscillations associated to acoustic noise generated during the combustion process. These acoustic waves propagate within the combustion chamber, interact with the boundaries and come back to the combustion zone. The pressure fluctuations affect the flow field and they may give rise to different driving mechanisms for thermo-acoustic instabilities (i.e. perturbations of the local equivalence ratio, reactant distributions, flame front or thermodynamic properties in the flame region) [34]. As a consequence, unsteady behaviour in the heat release occurs and such disturbances may be in phase with pressure oscillations, leading to a resonance phenomenon and, so, an amplification of the acoustic energy of the system which in turn causes dangerous structural vibrations of the combustor hardware. To avoid the onset of thermo-acoustic instabilities, it is mandatory to identify the characteristic scales of these processes and to employ active or passive techniques of damping.

As far as the thermal management is concerned, lean combustors are subjected to opposite problems with respect to RQL concept. Thanks to the lean and almost homogeneous reacting mixture in the primary zone, lower flame temperatures occur with a strong reduction of soot particles generation and, consequently, with a decrease of radiative heat loads on liners. However, most of the air coming from the compressor is employed for liquid fuel preparation and atomization and for combustion process control, causing a strong reduction in air availability for liner cooling. Therefore, the development of modern effective cooling systems together with their optimization have become key aspects for the design of these new combustor concepts in order to maintain wall temperatures below the melting point throughout the combustor operating conditions. At the same time, large efforts have to be spent on the analysis of cooling air flow field to avoid interactions between the coolant and the reactive mixture, determining phenomena of local extinction of the flame and a reincrease of CO and UHC species.

To design high efficiency cooling systems, a deep understanding of heat transfer phenomena and of their mutual interactions is required, since their relative contributions depend on the combustor operating conditions and on the employed burner and cooling architectures. Therefore, in the following chapters the main aspects related to heat transfer mechanisms will be described in detail together with an overview of the common cooling techniques with a particular focus on full coverage film cooling or *effusion cooling*.

Chapter 2

Heat transfer in gas turbine combustors

Beyond the goals of low emission levels, a major requirement in the design of aeroengine combustors is the constrain on the integrity of combustor hardware in order to ensure an operational safety of the system throughout the whole working cycle. As mentioned in Chapter 1, thermoacoustic instabilities could promote high intensity vibrations which can cause damage irremediably from a structural point of view until the break of the combustor device. Considering the high temperature and the reactive environment related to the presence of the flame, the combustor hardware is also subjected to significant thermal loads and gradients which could affect the durability, the efficiency and, then, the overall operating cost of the engine. Taking into account the design criteria of the modern aero-engines in last decades, such aspect has become more critical both, directly, by the increase of TIT and, so, by higher temperature levels and, indirectly, by the increase of OPR which leads to more intense luminous radiation. Notwithstanding the progress in material technology to ensure higher thermal resistance, the flame temperature is constantly over the melting point during last years, according to Figure 2.1. The gap between these two reference temperatures is recovered by the use of highly-effective cooling systems which can act both on the cold side by increasing the cooling effect by means of higher Heat Transfer Coefficient (HTC) and on the hot side by promoting a reduction of the convective and radiative heat loads.

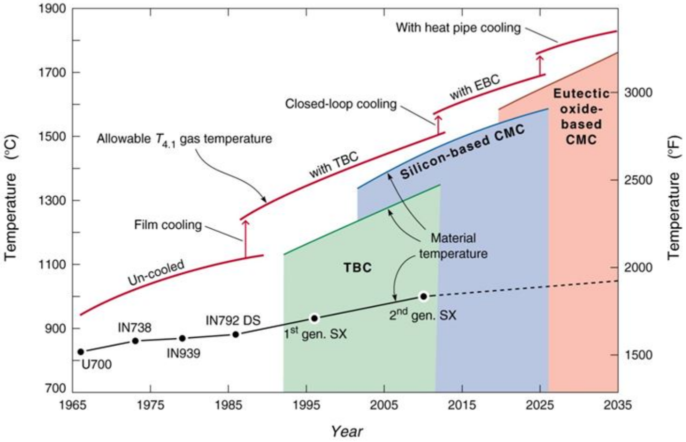

Figure 2.1: *The evolution of allowable gas temperature at the entry to the gas turbine and the contribution of superalloy development, film cooling technology, thermal barrier coatings and (in the future) Ceramic Matrix Composite (CMC) air foils [35].*

Different complex phenomena are involved when heat transfer within a combustor is concerned (i.e. combustion, turbulence, conduction, radiation, pollutant generation) and they strongly interact between each other. Therefore, a multiphysics approach is mandatory to obtain a reliable prediction of wall temperatures and heat fluxes which is required for a safety thermal design of an aeroengine combustor. Solid temperature is determined by the thermal balance of all involved convective, conductive and radiative loads which in turn depend also on the gas and solid temperatures, leading to a very challenge coupled problem.

For a proper thermal design, a deep comprehension of the main aspects of a CHT problem is required. In this context, the governing equations and the characteristic features of each involved heat transfer mechanism will be investigated from a theoretical point of view.

2.1 CHT framework

As said before, three different heat transfer mechanisms concur in determining wall temperature pattern in an aeroengine combustor: convection, conduction and radiation. In this context, an additional complex phenomenon is involved and it is represented by the oxidation process which makes also significant the contribution of radiative heat fluxes. Such multiphysics aspects of a CHT framework are described by different governing equations and they occur in different domains with characteristic time and space scales which vary from very small to large orders of magnitude, as shown in Figure 2.2.

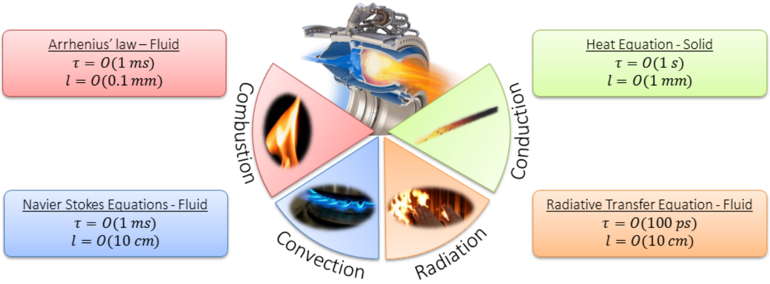

Figure 2.2: Comparison between the characteristic time and space scales of the involved phenomena in a CHT framework.

2.1.1 Combustion

Combustion is defined as a chemical reaction during which usually a hydrocarbon fuel (C_xH_y) reacts with an oxidant (typically oxygen O_2) to form products, accompanied by a high release of energy in the form of heat and light in the form of flame. A combustion process always takes place in gaseous state, since the elementary reaction occurs only when a molecular mixing is achieved. In case of liquid fuels, the oxidation process does not start until the fuel evaporation is not completed. Generally, the oxidation reaction is represented by a set of numerous processes in which the reactants combine with high rate and speed as a consequence of the energy generation, resulting in an increase of temperature and in an acceleration of the reaction itself if such energy is not dissipated around. Moreover, the high reactive nature of the system is favoured by the presence of some highly-reactive intermediate species, the so-called *chain carriers*, which are characterized by small concentration and short lifetime. These chemical species are responsible of the fundamental chemical species attack during a series of consecutive reaction steps (*chain branching reactions*).

In the current combustion systems, the global residence time of the reacting flow is extremely short and, therefore, the development of the combustion process occurs in a time frame which is generally not suitable to reach the completion of all the involved reactions. In this context, chemical kinetics plays a key role in the design of combustion devices. From a chemical point of view, a simple reaction can be expressed as:

$$aA + bB \leftrightarrow cC + dD \tag{2.1}$$

The rate at which a chemical reaction occurs can be defined as the variation in the unit of time of the concentration of each chemical species weighted with its own stoichiometric coefficient, according to:

$$RR = \frac{1}{a}\frac{dA}{dt} = \frac{1}{b}\frac{dB}{dt} = \frac{1}{c}\frac{dC}{dt} = \frac{1}{d}\frac{dD}{dt} \tag{2.2}$$

The resulting reaction rate is the difference between the forward and the reverse rates:

$$RR = RR_f - RR_b \tag{2.3}$$

According to the law of mass action, it is possible to employ the following formulations:

$$RR_f = K_f(T) C_A^{\alpha} C_B^{\beta} \tag{2.4}$$

$$RR_b = K_b(T) C_C^{\gamma} C_D^{\delta} \tag{2.5}$$

where K_f and K_b are the *kinetic constants* of the related reactions. When the chemical equilibrium is reached, the concentrations of reactants and products are constant in time and the rates of the forward and the backward reactions are equivalent:

$$RR_f = RR_b = \frac{K_f(T)}{K_b(T)} = \frac{C_C^{\gamma} C_D^{\delta}}{C_A^{\alpha} C_B^{\beta}} = K(T) \tag{2.6}$$

where K is called the *equilibrium kinetic constant* of the reaction. The reaction rate law expression relates the rate of a reaction to the concentrations of the reactants. The kinetic constants are generally temperature dependent and most reactions accelerate as temperature increases, since the molecules move faster and the collision frequency increases. The effect of temperature is generally correlated by the Arrhenius equation [36]:

$$K(T) = A_f T^{\beta} e^{-\frac{E_a}{RT}} \tag{2.7}$$

where $A_f T^{\beta} (0 < \beta < 1)$ and the exponential term are called respectively the *collision frequency* and the *Boltzmann factor* whereas E_a is the *activation energy*. According to the Arrhenius model (Figure 2.3), a minimum amount of energy is required to transform reactants into products. Such energy allows to activate a special type of collision, which is generally called *activated complex*, which sustains the reactive process. The Boltzmann factor is an index of the fraction of collisions that have energy level greater than the activation energy [37].

Gaseous flames can be classified as either premixed or diffusion flames, depending on the state of mixture of the reactants when they reach the flame zone. However, in both cases the reaction rates related to the oxidation process express how fast the reaction advances and, so, how fast the

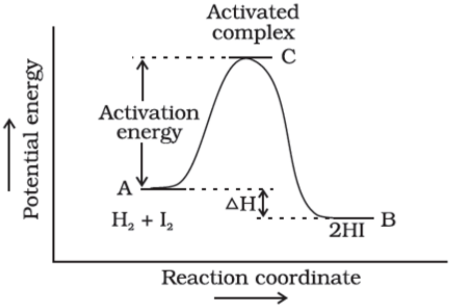

Figure 2.3: Schematic representation of Arrhenius model [37].

reactants (generally fuel and air) are converted in products (burnt gases). From a macroscopic point of view, this is directly linked to the velocity at which a flame propagates within a combustion system. According to that said before, it is evident that mixing processes of fresh reactants with hot combustion products represent a key factor for the progress of the reactive phenomena and for the flame propagation. In this context, the type of flow field in which the oxidation reaction occurs obviously determines the laminar or turbulent nature of the flame. Whereas laminar flames are characterized by small reaction rates since the mixing occurs only by means of molecular diffusion, in turbulent flames the turbulence enhances the mixing processes as a consequence of the presence of eddies and of their interaction with the flame. The reaction rate is increased as long as the chemical reactivity of the system is sufficiently fast by reacting the mixture with adequate speed to the frequency of mixing induced by turbulence.

Considering a 1D freely propagating premixed laminar flame as shown in Figure 2.4, fresh gases (fuel and oxidizer mixture) and combustion products (burnt gases) are separated by a thin reaction zone, called *thermal flame thickness* δ_l, through which a strong temperature gradient occurs. This identifies the laminar flame front. The velocity at which the flame front tends to rise towards the fresh mixture is called *laminar flame speed* S_L which is defined as the velocity at which fresh gases move through the combustion wave in the direction normal to the flame front [39]. The

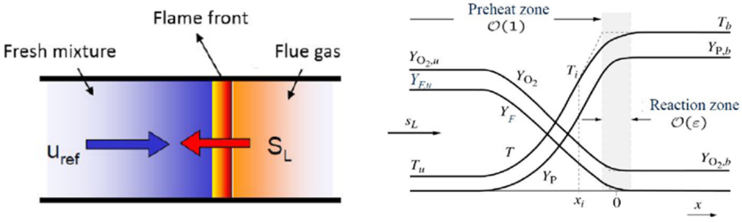

Figure 2.4: 1D premixed laminar flame (on the left) and temperature and species concentration profiles (on the right) (adapted from [38]).

value of S_L is affected by the type of fuel and by the thermodynamic properties of the reacting mixture, such as temperature and pressure. The laminar flame speed is correlated to the thermal flame thickness by means of the kinematic viscosity of the fresh gases υ:

$$Re_f = \frac{\delta_l S_L}{\upsilon} \approx 4 \tag{2.8}$$

since the flame Reynolds number Re_f is almost constant. The thermal flame thickness is defined as the flame zone in which a raise of temperature corresponding to the 98% of temperature difference between fresh reactants and burnt products is observed [40].

Generally, the laminar flame speed is too low to allow a completion of the combustion process according to the extremely small residence time of the reacting mixture within a gas turbine combustor. However, most practical combustion devices create flow conditions so that the fluid state of the fuel–oxidizer mixture is turbulent. Turbulent flow fields enhance the reactants mixing processes, accelerating the propagation of the flame within the system. Depending on the flame type, turbulence affects differently its structure. As far as a diffusion flame is concerned, the augmentation of the reaction velocity is caused by an increased mixing of fuel and oxidant, leading to a greater fuel consumption with the same flame height and to a greater heat release per unit volume. On the opposite, the instantaneous front of a premixed flame is wrinkled by the action of turbulent eddies, generating a *flame brush* defined as the spatial region over which the instantaneous turbulent flame fronts are located, spreading with a velocity S_L normally to the front [41]. Analogously at the laminar flame speed for a laminar flame front, it is possible to define a *turbulence flame speed* for the flame brush as:

$$S_T = S_L \frac{A_T}{A_L} \tag{2.9}$$

where A_L and A_T are the flame front surface in laminar and turbulent regimes, respectively.

Several length, velocity and time scales related to the description of turbulent flow field and chemical reactions are involved in turbulent combustion. In this framework, it is useful to define some dimensionless groups to distinguish the different turbulent combustion regimes. The first one is the *turbulence Reynolds number* which represents the ratio between the turbulent transport and viscous forces:

$$Re_t = \frac{u' l_t}{\upsilon} \tag{2.10}$$

where u' is the velocity RMS, l_t is the turbulence integral length scale and υ the kinematic viscosity of the flow. As previously said, turbulent eddies enhance the fuel consumption by introducing fluctuations of velocity, temperature, density, pressure and concentration. Therefore, the interaction between turbulence and chemistry must be taken into account. The comparison between the relative characteristic time scales is an index of the degree to which fluctuations affect the chemical reactions. In general, indicating with τ_c the temporal scale related to chemical reactions and with τ_t the one of fluid-mechanical fluctuations, the *Damköhler number* can be written as:

$$Da = \frac{\tau_t}{\tau_c} \tag{2.11}$$

According to this definition, if $Da >> 1$, the chemical time scale is much shorter then the turbulent one. In this case, the flame front is only distorted and macroscopically transported by the flow field, since the turbulent eddies does not affect the internal structure, only straining the flame surface [40]. On the opposite, if $Da << 1$, the system is characterized by slow chemical reactions. Consequently, reactants and products are perfectly mixed before the reaction takes place, leading to the assumption of a Perfectly Stirred Reactor (PSR) and to the possibility of employing Arrhenius law to compute the mean reaction rate, using mean mass fractions and temperature. Referring to premixed flames, the ratio of the thermal flame thickness δ_l with the laminar flame speed S_L represents the chemical time scale τ_c whereas the turbulent time $\tau_t = l_t/u'$ is a function of the turbulent integral scale and of velocity fluctuation. Substituting in the Damköhler number definition:

$$Da = \frac{\tau_\mathrm{t}}{\tau_\mathrm{c}} = \frac{l_\mathrm{t}}{\delta_l}\frac{S_\mathrm{L}}{u'} \tag{2.12}$$

In this way, the Damköhler number allows to distinguish between several turbulent combustion regimes as a function of the relative values assumed by constituent ratios, according to the Borghi diagram highlighted in Figure 2.5.

In the diagram, another important dimensionless group appears, the *Karlovitz number*, defined as:

$$Ka = \frac{\tau_c}{\tau_k} = \frac{\delta_l}{l_k}\frac{u_k}{S_L} \tag{2.13}$$

where τ_k, l_k and u_k are respectively the time scale, the length scale and the velocity related to the smallest turbulent eddies (the Kolmogorov scales). This number indicates the effect of the smallest turbulent scales on the flame structure. The unitary value of the Karlovitz number identifies the *Klimov-Williams criterion* for which the flame thickness is equal to the Kolmogorov spatial scale: for $Ka < 1$, the flamelet regime is observed whereas the turbulent motions are able to interact with the flame inner structure, transitioning to the *distributed combustion regime*, for $Ka > 1$. According to [43], turbulent eddies affect gradually larger portions of the flame brush, depending on the characteristic Karlovitz number. Considering the classification performed by Veynante and Vervisch [40],

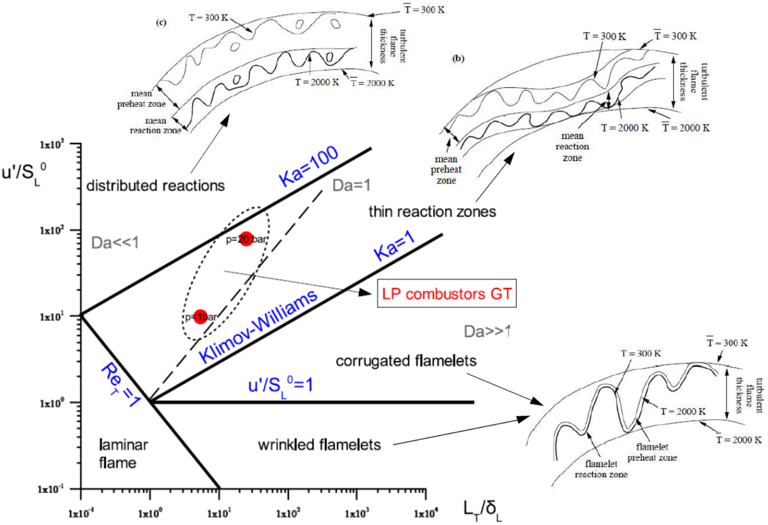

Figure 2.5: Turbulent premixed combustion diagram (adapted from [42]).

two different flamelet regimes can be identified for $Ka < 1$, depending on the velocity ratio u'/S_L:

- for $u'/S_L < 1$, the *wrinkled flamelets regime* is observed. The effect of turbulent motions on the combustion is limited, since the turbulent structures only wrinkle the flame surface;
- for $u'/S_L > 1$, the *corrugated flamelets regime* occurs. In this case, the larger turbulent structures lead to the generation of pockets.

Moving towards the *thin reaction zone* for $1 < Ka < 100$, the flame preheat zone is thickened by the actions of turbulent eddies whereas no effect is observed on the reaction zone which remains thin and laminar. Finally, the laminar flame structure is disrupted by turbulence with affection of both preheat and reaction zones in the *distributed reactions regime* for $Ka > 100$ where the combustion process is limited by the chemistry.

In the case of non-premixed flames, the definition of the characteristic scales and combustion regimes is more difficult since a fixed reference length scale related to the flame thickness cannot be easily defined due to the aerodynamics influence on it. In this context, generally two different thickness are defined (Figure 2.6): firstly, the *diffusion layer thickness* L_d identifies the region where a variation of the fuel and oxidizer relative concentrations can be appreciated; then, the *reaction zone thickness* L_r is related to the local layer where the reaction rate is different from zero.

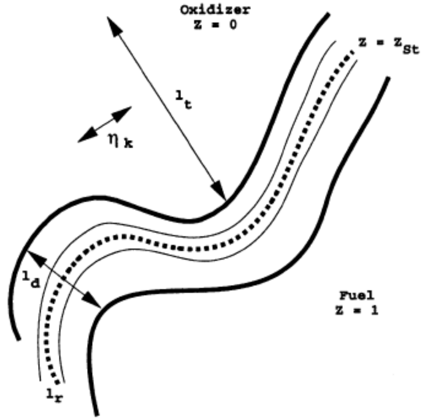

Figure 2.6: Turbulent diffusive flame structure. Z is the mixture fraction and l_t is the turbulence integral length [40].

At this point, it is possible to define respectively a *Damköhler flamelet number* and a general Damköhler number as:

$$Da^* = \frac{\tau_\mathrm{f}}{\tau_\mathrm{c}} \quad Da = \frac{\tau_\mathrm{t}}{\tau_\mathrm{c}} \tag{2.14}$$

where $\tau_f = 1/\chi_{st}$ represents the mixing time related to the local characteristics of the flow in correspondence of the flame, computed through the Scalar Dissipation Rate χ_{st} whereas τ_t is the mixing time related to the turbulent characteristics of the freestream. Consequently, the diagram shown in Figure 2.7 allows to distinguish turbulent diffusive combustion regimes as a function of several dimensionless groups.

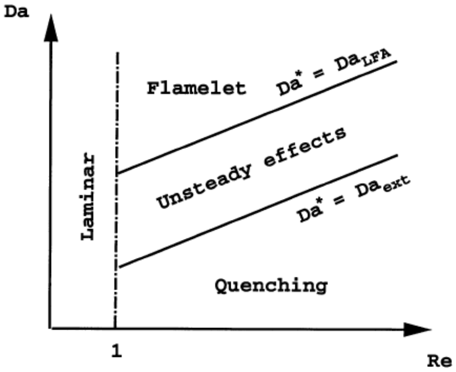

Figure 2.7: Diagram of non-premixed turbulent combustion regimes as a function of Damköhler and Reynolds numbers [40].

When $Da > Da^* = Da_{LFA}$, the flame front may be viewed as a steady laminar flame element and its inner structure is not affected by vortices. On the other hand, when $Da \leq Da^* = Da_{ext}$, the chemistry is too slow or turbulence levels are too high and, so, the flame extinction occurs. In the intermediate Damköhler number range, strong unsteadiness effects are observed.

2.1.2 Conduction

Heat transfer by conduction is a diffusion process (also called *thermal diffusion*) which takes place at the molecular level by means of the transfer of energy from the more energetic molecules to those with a lower energy level [44]. In this way, heat is transferred through complex submicroscopic mechanisms during which atoms interact between each other to propagate the energy from regions at higher to regions at lower temperature. The conduction can occur in any state of matter: in gas and in liquid phases, the transfer is due to the collisions between the atoms, whereas in solids the main vehicle is related to the vibration of atoms [45]. Although conduction also occurs in liquids and gases, the contribution of convection to the heat flux is always much higher.

The amount of transferred heat depends on the geometry and on the property of the body which is involved in the conduction, but mainly on a driving "force" that is represented by the temperature gradient ∇T:

$$\nabla T = \vec{i}\frac{\partial T}{\partial x} + \vec{j}\frac{\partial T}{\partial y} + \vec{k}\frac{\partial T}{\partial z} \tag{2.15}$$

which is the vector that represents in each point the magnitude and the direction of the maximum increase of temperature. From a mathematical point of view, the propagation rate of conductive heat transfer can be predicted by Fourier's law as:

$$\vec{q} = -k\nabla T \tag{2.16}$$

which resolves itself into three components:

$$q_x = -k\frac{\partial T}{\partial x} \quad q_y = -k\frac{\partial T}{\partial y} \quad q_z = -k\frac{\partial T}{\partial z} \tag{2.17}$$

where the coefficient k is the thermal conductivity. This encodes the mechanistic features of the process into a physical property. It generally depends on position and temperature, but it is usually possible to consider it only as a function of temperature, according to the hypothesis of homogeneity of the material.

The conduction equation represents the conservation of energy in a solid domain and it can be derived by applying the energy balance on an elemental volume of material, supposing that heat is being transferred only by conduction. Therefore, according to Figure 2.8 and taking into account only the x-coordinate, the conduction equation can be written as:

$$-kA\left.\frac{\partial T}{\partial x}\right|_{x} + \dot{q}_G A\Delta x = -kA\left.\frac{\partial T}{\partial x}\right|_{x+\Delta x} + \rho A\Delta x c\frac{\partial T(x+\Delta x/2,t)}{\partial t} \tag{2.18}$$

where the Fourier's law is employed to compute the conduction terms and $\dot{q}_G$ represents the rate of energy generation per unit volume inside the control volume. From a macroscopic perspective, the equation expresses the equivalence between [46]:

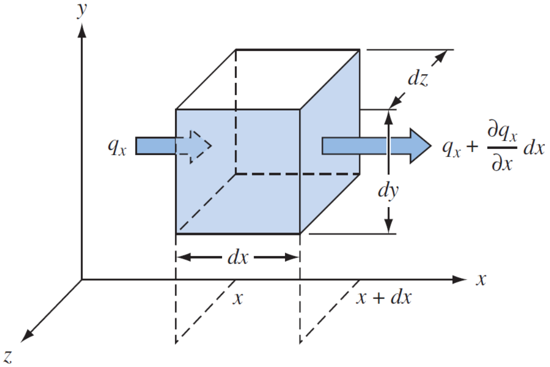

Figure 2.8: Conductive energy balance applied on an elemental volume of material [46].

- **left side**: sum of the rate of heat conduction transferred into the volume control with the rate of heat generated inside it;

- **right side**: sum of the rate of heat conduction transferred out of the volume control with the rate of heat stored within it.

Dividing Equation 2.18 by the control volume $A\Delta x$ and rearranging, it is possible to write:

$$k\frac{(\partial T/\partial x)_{x+\Delta x} - (\partial T/\partial x)_x}{\Delta x} + \dot{q}_G = \rho c \frac{\partial T(x + \Delta x/2, t)}{\partial t} \tag{2.19}$$

Considering the limit $\Delta x \to 0$, the first term on the left side can be reformulated as:

$$\left.\frac{\partial T}{\partial x}\right|_{x+dx} = \left.\frac{\partial T}{\partial x}\right|_x + \frac{\partial}{\partial x}\left(\left.\frac{\partial T}{\partial x}\right|_x\right) dx = \left.\frac{\partial T}{\partial x}\right|_x + \left.\frac{\partial^2 T}{\partial x^2}\right|_x dx \tag{2.20}$$

whereas on the right side the Taylor expansion can be applied:

$$\frac{\partial T}{\partial t}\left[\left(x + \frac{\Delta x}{2}\right), t\right] = \left.\frac{\partial T}{\partial t}\right|_x + \left.\frac{\partial^2 T}{\partial x \partial T}\right|_x \frac{\Delta x}{2} + \dots \tag{2.21}$$

Taking into account only the order Δx, the conduction equation can be finally rewritten as:

$$k\frac{\partial^2 T}{\partial x^2} + \dot{q}_G = \rho c \frac{\partial T}{\partial t} \tag{2.22}$$

This equation allows to compute the one-dimensional temperature distribution in a solid by summing the net rate of heat conduction into the control volume (first term on the left side) with the rate of energy generation inside it (second term on the left side) and comparing it to the rate of increase of internal energy of the body (term on the right side) [46]. Assuming that the temperature $T(x, y, z, t)$ can be a function of all three coordinates as well as time, the three dimensional form of the conduction equation is:

$$\frac{\partial^2 T}{\partial x^2} + \frac{\partial^2 T}{\partial y^2} + \frac{\partial^2 T}{\partial z^2} + \frac{\dot{q}_G}{k} = \frac{1}{\alpha}\frac{\partial T}{\partial t} \tag{2.23}$$

where α is the *thermal diffusivity* of the material, defined as:

$$\alpha = \frac{k}{\rho c} \tag{2.24}$$

From a physical point of view, this equation is usually more explanatory in the dimensionless form, since each dimensionless group encodes a particular aspect which governs the conduction problem [46]. By defining a dimensionless temperature, x-coordinate and time through the following expressions:

$$\theta = \frac{T}{T_r} \quad \xi = \frac{x}{L_r} \quad \tau = \frac{t}{t_r} \tag{2.25}$$

and substituting them into Equation 2.22, it is possible to obtain:

$$\frac{\partial^2 \theta}{\partial \xi^2} + \frac{\dot{q}_G L_r^2}{k T_r} = \frac{L_r^2}{\alpha t_r}\frac{\partial \theta}{\partial \tau} \tag{2.26}$$

where T_r, L_r and t_r are the correspondent reference quantities. In this form, the *Fourier number Fo* can be defined as:

$$\mathrm{Fo} = \frac{\alpha t_r}{L_r^2} = \frac{(k/L_r)}{(\rho c L_r/t_r)} \tag{2.27}$$

representing the ratio between the rate of heat transfer by conduction and the rate of energy storage in the system. Consequently, this number is able to synthetically describe the characteristic time of the investigated conduction problem, resulting in a more (high Fo) or less (low Fo) fast transient behaviour of the analyzed system.

In addition, it is possible to identify an another dimensionless group as an index of the dispersion of the heat eventually generated within the body as the ratio of the internal heat generation to heat conduction through the volume:

$$\dot{Q}_G = \frac{\dot{q}_G L_r^2}{k T_r} \tag{2.28}$$

In a common CHT problem, both convective and conductive heat transfer mechanisms are involved in the thermal interaction between a solid and a fluid domains. In this case, the resulting temperature change in the system is influenced by the relative contribution of each heat transfer mode. From a physical point a view, the dimensionless parameter *Biot number Bi* synthetically expresses a criterion which gives a direct indication of the relative importance of conduction and convection in determining the temperature history of a body being heated or cooled by convection at its surface. Computing the conduction and the convection thermal resistances respectively as $R_k = r_o/k$ and $R_c = 1/\bar{h}_c$ with $\bar{h}_c$ the mean HTC on the body surface, the Biot number can be written as:

$$\mathrm{Bi} = \frac{R_k}{R_c} = \frac{\bar{h}_c r_\alpha}{k} \tag{2.29}$$

where the physical limit of the ratio are:

$$\begin{array}{llll} \mathrm{Bi} \to 0 & \text{when} \quad R_k = \left(\frac{r_o}{k}\right) \to 0 & \text{or} & R_c = \frac{1}{\bar{h}_c} \to \infty \\ \mathrm{Bi} \to \infty & \text{when} \quad R_c = \frac{1}{\bar{h}_c} \to 0 & \text{or} & R_k = \frac{r_o}{k} \to \infty \end{array}$$

As schematically highlighted by Figure 2.9, the temperature gradient is mainly concentrated in the fluid at the interface when the Biot number tends to zero as well as the conductivity of the solid or the convection resistance tend to high values. As a result, the solid can be modelled as an isothermal body. On the opposite, the Biot number approaches infinity when the thermal resistance in the solid is much higher compared to convection resistance and, so, mostly the solid is subjected to the temperature change [46].

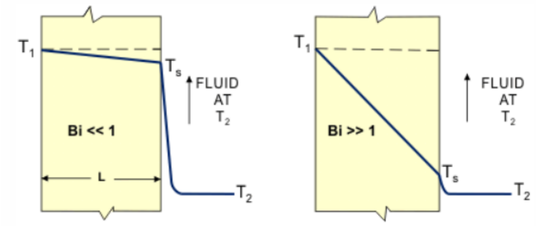

Figure 2.9: Comparison between thermal systems characterized by opposite values of Bi [46].

Consequently to these considerations, it is interesting to underline that different approaches or hypotheses can be employed to model the analyzed CHT problem, depending on the Biot number value.

2.1.3 Convection

Convective heat transfer describes the exchange of heat between a bounding surface and a fluid in motion. It is related to the energy transfer by means of macroscopic motions of fluid parcels induced by an external force. In the *natural convection*, this force is due to a density gradient whereas *forced convection* occurs when the fluid parcels motion is caused by a pressure difference generated by a pump or a fan [44].

Whereas in a solid the heat transfer takes place always by means of conduction since solid molecules are not in motion, a fluid is characterized by both the convection and the conduction, depending respectively on the presence or not of moving particles within it. Consequently, the convective heat transfer is more complex due to the superposition of the fluid motion with the conduction. In fact, the moving particles increase the heat transfer, bringing into contact hot and cold fluid parts. This results in an augmentation of conductive heat fluxes in fluid portions gradually wider. Hence, the amount of heat transferred by convection is higher compared to that one transferred by means of conduction and it is proportional to the velocity fluid.

Considering a plate at surface temperature T_w licked by a fluid at temperature T_∞ which moves parallel to the plate, Figure 2.10 highlights the velocity and temperature profiles associated to the convection heat transfer.

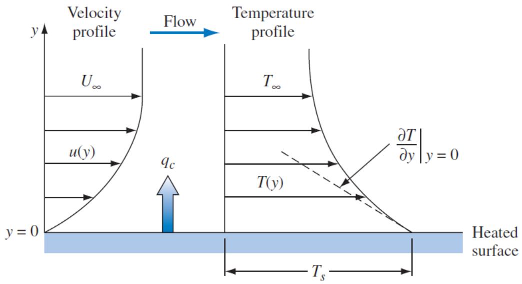

Figure 2.10: Velocity and temperature profiles associated to convection heat transfer between a bounding surface and a fluid over the plate [46].

The considered process can be described by introducing the *Newton's law of cooling*:

$$q'' = h(T_w - T_f) \tag{2.30}$$

where T_w is the surface temperature, h is the local HTC and T_f is a characteristic fluid temperature which is generally defined as the temperature of the undisturbed fluid far away from the surface (T_∞). Instead, the heat transfer coefficient h is influenced by the geometry of the surface or of the considered system, by the velocity as well as by the physical properties of the fluid (i.e. dynamic viscosity μ, thermal conductivity λ, density ρ and specific heat c_p) and by temperature difference. As a consequence, its value is not generally constant, varying from point to point. In this context, it is useful to distinguish between a local h and an average $\bar{h}$ convection heat transfer coefficient, according to the following formulations:

$$dq = hdA(T_w - T_\infty) \tag{2.31}$$

$$\bar{h}_c = \frac{1}{A}\int_A h_c dA \tag{2.32}$$

where A is the area of the investigated plate. Since $q'' = q/A$, it is possible to define the *thermal resistance* in convection heat transfer as the resistance at solid-fluid interface:

$$R_c = \frac{1}{\bar{h}A} \tag{2.33}$$

Regarding the motion of a fluid over a plate, the fluid velocity profile from zero at the wall to freestream velocity away from the surface is related to the action of viscous forces. As a result, the heat is transferred by conduction at the interface. Knowing the temperature gradient and the thermal conductivity at this interface, the Fourier's law can be applied to compute the rate of conductive heat transfer at the surface:

$$q'' = -k_{\mathrm{f}} A \left|\frac{\partial T}{\partial y}\right|_{\text{at } y=0} \tag{2.34}$$

where the temperature gradient is affected in turn by the energy transfer within the fluid, induced by macroscopic and microscopic motions. At this point, the Newton's and the Fourier's laws can be combined in order to obtain:

$$h = \frac{q''}{T_w - T_f} = -\frac{k(\partial T/\partial y)|_{y=0}}{T_w - T_f} \tag{2.35}$$

It is worth to note that, for the heat transfer coefficient, the temperature gradient at the wall has to be calculated.

When the fluid is represented by high-velocity gas flows, the rate of convective heat transfer can be written as a function of the commonly called *adiabatic wall temperature* or *recovery temperature* T_{aw}:

$$q'' = h(T_w - T_{aw}) \tag{2.36}$$

which is the equilibrium temperature reached by the surface in absence of any heat transfer to or from the surface [44]. Generally, this temperature depends on the properties of the bounding wall and of the fluid. As already seen for other problems, it is useful to combine the involved variables in dimensionless groups in order to reduce the number of parameters which should be taken into account. By dimensionalizing the heat transfer coefficient h, the *Nusselt number* can be computed as:

$$Nu = \frac{h\delta}{k} \tag{2.37}$$

where k is the fluid thermal conductivity and δ is the characteristic length of the investigated system. The Nusselt number represents the ratio between the convective heat transfer and the heat transferred by conduction through a fluid in presence of a temperature gradient. In fact, considering a fluid layer of thickness δ subjected to a temperature difference ∇T, the rates of convective (fluid in motion) and conductive heat transfer (fluid in a quiet state) can be respectively computed as:

$$\begin{aligned} q_{conv} &= h\Delta T \\ q_{cond} &= k\tfrac{\Delta T}{\delta} \end{aligned} \tag{2.38}$$

and computing the ratio:

$$\frac{q_{conv}}{q_{cond}} = \frac{h\Delta T}{k\frac{\Delta T}{\delta}} = \frac{h\delta}{k} = \mathrm{Nu} \tag{2.39}$$

For increasing values of Nu, the convection becomes more and more predominant.

As mentioned before, the convective heat transfer coefficient depends on several geometrical and fluid dynamics properties of the involved system and it is generally computed by different case-dependant formulations and correlations. In this framework, the Nusselt number is generally expressed as a function of two important dimensionless groups which encode the physics of the analyzed problem, the *Reynolds* and the *Prandtl numbers*:

$$\mathrm{Re} = \frac{\text{inertia forces}}{\text{viscous forces}} = \frac{\rho U_\infty \delta}{\mu} \tag{2.40}$$

$$\mathrm{Pr} = \frac{\text{molecular momentum diffusivity}}{\text{thermal diffusivity}} = \frac{\mu c_p}{k} \tag{2.41}$$

$$Nu = CRe^m Pr^n \tag{2.42}$$

where m and n are case-dependant. Whereas the Reynolds number indicates the state of the fluid (laminar or turbulent), the Prandtl number is the ratio between the momentum diffusivity and the thermal diffusivity, representing an index of the relative importance of the convective heat transfer with respect to the conduction. Due to the velocity fluctuations and to the increased mixing, turbulent flows are characterized by higher values of the heat transfer coefficient.

2.1.4 Radiation

Thermal radiation indicates a process through which heat is transferred from a body by virtue of its temperature without the aid of any intervening medium. Hence, radiation can occur also in absence of a material medium, differing from the previous described heat transfer mechanisms. Moreover, the driving "force" does not depend on temperature but on the absolute temperature raised to the fourth power. The thermal radiation is continuously emitted due to vibratory and rotational motions of molecules, atoms and electrons of every body which has a temperature above the absolute zero. Since the temperature is an index of the intensity of such microscopic motions, the emission of thermal radiation is governed by the temperature of the emitting body.

As far as radiative heat transfer is described, a theoretical concept is employed as reference, defining a *blackbody* (or ideal radiator) as a body which emits and absorbs at any temperature the maximum possible amount of radiation at any given wavelength [46]. From a macroscopic perspective, the thermal radiation emitted by an ideal radiator depends on the wavelength λ of the spectral emission and on the temperature T of the emitting body, according to the *Planck's law*:

$$E_{b\lambda}(T) = \frac{C_1}{\lambda^5 \left(e^{C_2/\lambda T} - 1\right)} \tag{2.43}$$

where $E_{b\lambda}(T)$ is the monochromatic emissive power of a blackbody at absolute temperature T whereas C_1 and C_2 are the first and the second radiation constants respectively. The graphic representation of such formulation is reported in Figure 2.11.

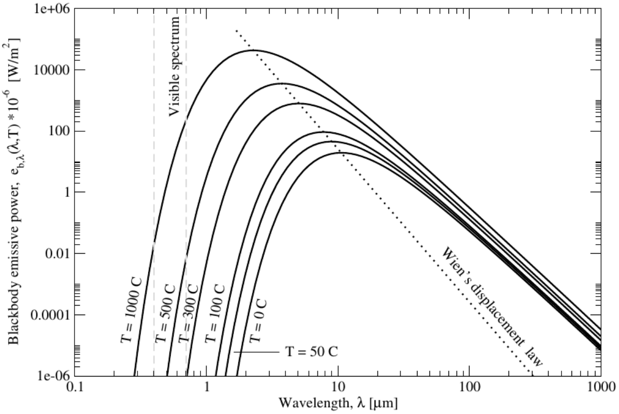

Figure 2.11: Spectral blackbody emissive power and the Wein's displacement law (dash line) [47].

It is worth to note that, for each blackbody temperature, there is a wavelength at which the monochromatic emissive radiation is maximum. This relationship between the temperature and the wavelength values is known as *Wien's displacement law*:

$$\lambda_{\max} T = 2.898 \cdot 10^{-3} \; m \; K \tag{2.44}$$

and it can be derived from the Planck's law by satisfying the condition for a maximum:

$$\frac{dE_{b\lambda}}{d\lambda} = \frac{d}{d\lambda} \left[\frac{C_1}{\lambda^5 \left(e^{C_2/\lambda T} - 1 \right)} \right]_{T=\text{const}} = 0 \tag{2.45}$$

Since a blackbody is able to emit the maximum radiation at any temperature and for any wavelength, it is possible to compute the total emission by means of *Stefan-Boltzmann law*:

$$E_b(T) = \frac{q_r}{A} = \sigma T^4 \tag{2.46}$$

where A is area of the blackbody emitting the radiation and σ is the Stefan-Boltzmann constant. It is important to underline that such formulation relates the emitted radiation to the fourth power of temperature, highlighting a strong non-linear dependency, and it represents the area under each curve of Figure 2.11, since the total emissive power represents the total thermal radiation emitted over the entire wavelength spectrum:

$$\int_0^\infty E_{b\lambda} d\lambda = \sigma T^4 = E_b(T) \tag{2.47}$$

As mentioned before, the blackbody is only a theoretical concept. In this context, radiative properties are employed to express the radiation characteristics of a real body with respect to the ideal radiator. The *emissivity* of a real surface is an index of the ability of that surface to emit radiation in comparison with the ideal emission of a blackbody, according to the following formulation:

$$\varepsilon = \frac{E(T)}{E_b(T)} = \frac{E(T)}{\sigma T^4} \tag{2.48}$$

where its value is always between zero and the unity, since a blackbody emits the maximum possible radiation at a given temperature. Other dimensionless quantities allow to characterize the behaviour of the considered surface when a radiation is incident on it. The *absorptivity*, *reflectivity* and *transmissivity* describe how the total incident radiation is split as described by Figure 2.12 by means of the following relationship from a mathematical point of view:

$$\alpha + \rho + \tau = 1 \tag{2.49}$$

where the absorptivity α, reflectivity ρ and transmissivity τ are respectively the fractions absorbed, reflected and transmitted of the incident radiation. According to their definitions, all the radiative properties vary between zero and the unity.

The radiative properties can generally depend on the wavelength and on the direction of the incident radiation. For *grey* bodies, the properties

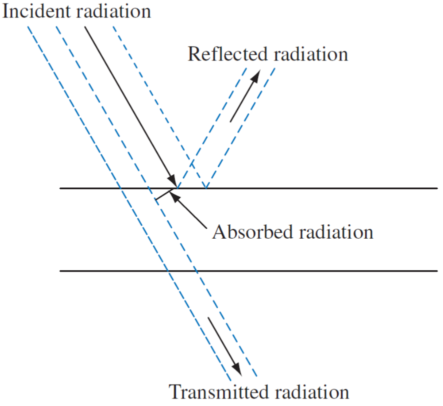

Figure 2.12: Sketch of how the incident radiation on a surface is distributed [46].

are constant throughout the whole spectrum whereas they are independent from the direction for *diffuse* surfaces. Moreover, a body is defined *opaque* when its trasmissivity is equal to zero ($\tau = 0$), whereas it is defined as *totally transparent* if all the incident radiation is transmitted through the surface ($\tau = 1$).

According to the previous considerations, when two bodies exchange heat by radiation in vacuum, the net heat exchange is then proportional to the difference in T^4. Figure 2.13 illustrates the radiative heat transfer between two arbitrary surfaces. The net heat exchange Q_{net} from the hotter to the cooler surface is influenced by several factors, such as the radiative properties of the involved materials but also the areas, the shapes, the orientation and the spacing of the considered surfaces. Synthetically, it can be written that:

$$Q_{\text{net}} = A_1 \mathcal{F}_{1-2} \sigma \left(T_1^4 - T_2^4 \right) \tag{2.50}$$

where $\mathcal{F}_{1-2}$ is the *transfer factor* which allows to take into account both the geometric view factor and the properties of the surfaces.

Therefore, the total radiant energy exchanged between elements varies,

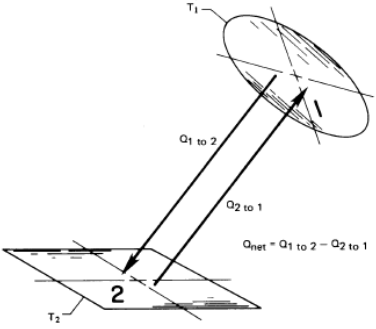

Figure 2.13: Radiative heat transfer between two arbitrary surfaces [48].

depending on the location of each element and on its orientation with respect to the others. Moreover, in many engineering applications, the radiative heat transfer generally occurs in a material medium, such as the reacting flow within a combustion chamber. This medium may be not inert but rather radiatively participating and, so, its interaction with thermal radiation must be taken into account. In this case, it is better to describe the radiative problem in terms of a fundamental and mathematically convenient quantity, the *intensity of radiation* I which is defined as the amount of radiation passing in a given direction. Along its trajectory, the radiation beam could interact with the participating media, surfaces and solid particles which modify its intensity or direction.

The rate of radiative heat flux per unit surface area which comes from a body and which travels in a given direction can be measured by computing the radiation through an element of the surface of a hemisphere centered on the radiating surface, as shown in Figure 2.14. From a mathematical perspective, it is useful to define the *differential solid angle* $d\omega$ as:

$$d\omega = \frac{dA_n}{r^2} \tag{2.51}$$

where $dA_n = rd\theta r$ is the unit area through which the radiation beam is passing whereas r is the radius of the considered hemisphere. Taking

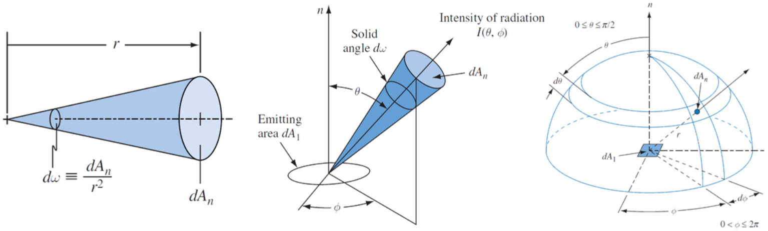

Figure 2.14: Schematic representation of the intensity of radiation in a spherical coordinate system (adapted from [46]).

into account this geometrical system, the intensity of radiation $I(\theta, \phi)$ is the rate of radiation (or total energy) emitted per unit area of emitting surface projected in the direction (θ, ϕ) per unit time into a solid angle $d\omega$, centered on a direction that can be defined in terms of the zenith angle θ and the azimuthal angle ϕ where the differential area dA_n is perpendicular to the radiation beam direction [44]. Accounting for the whole spectrum:

$$I(\theta, \phi) = \int_0^\infty I_\lambda(\theta, \phi) d\lambda \tag{2.52}$$

At this point, the intensity of radiation can be related to the rate q_r at which the radiation coming from the emitting black body surface dA_1 passes through dA_n in the radiation beam direction:

$$I_b(\theta, \phi) = \frac{dq_r}{dA_1 \cos\theta d\omega} \tag{2.53}$$

Computing the total amount of radiation passing through the hemispherical surface located above the emitting surface, a relationship between the intensity of radiation and the emissive power is defined, since the hemispherical surface intercepts all the radiation beams coming from the source. In the case of a blackbody and perfectly diffuse surface for which I_b does not depends on the direction:

$$\left(\frac{q}{A}\right) r = \int_0^{2\pi} \int_0^{\pi/2} I_b(\theta, \phi) \cos\theta \sin\theta d\theta d\phi = \phi I_b = E_b \tag{2.54}$$

As seen before, a net exchange of radiative heat flux occurs when the radiation between two bodies is considered as a result of the heat balance on each body. Consequently, it is mandatory to compute not only the radiation leaving but also the radiation incident on the body. In an analogous manner, a similar spherical coordinate system (Figure 2.15) can be employed for the mathematical description of the incident radiation in order to express it as a function of the *incident spectral intensity* $I_{\lambda,i}$. The latter is defined as the rate at which radiant energy at wavelength λ impinges from direction (θ, ϕ) per unit area of the intercepting surface normal to this direction, per unit solid angle about the direction (θ, ϕ), per unit wavelength interval $d\lambda$ at λ [46].

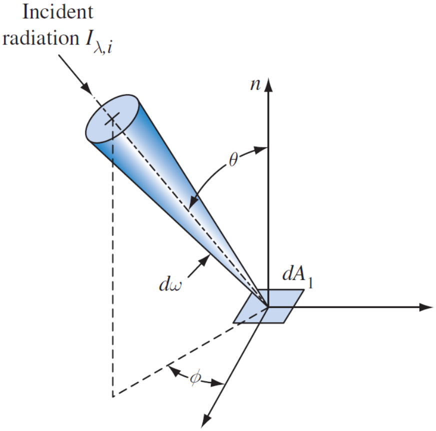

Figure 2.15: Schematic representation of the incident spectral intensity in a spherical coordinate system [46].

The radiation coming from all direction and impinging on a surface is indicated with the term *irradiation*. According to this term, the *spectral irradiation* G_λ can be defined as the rate at which monochromatic radiation at wavelength λ is incident on a surface per unit area of that surface. From a mathematical point of view:

$$G_\lambda = \int_0^{2\pi} \int_0^{\pi/2} I_{\lambda,i}(\lambda, \theta, \phi) \cos\theta \sin\theta d\theta d\phi \tag{2.55}$$

where $sind\theta d\phi$ is the unit solid angle. Integrating the spectral irradiation on the whole spectrum, the total irradiation can be computed as:

$$\begin{aligned} G &= \int_0^\infty G_\lambda(\lambda) d\lambda \\ &= \int_0^\infty \int_0^{2\pi} \int_0^{\pi/2} I_{\lambda,i}(\lambda, \theta, \phi) \cos\theta \sin\theta d\theta d\phi d\lambda \end{aligned} \tag{2.56}$$

As mentioned before, when the medium through which radiative energy passes is *participating*, each incident beam is attenuated by absorption and scattering due to the presence of the medium and solid particles but, at the same time, it also gains energy by emission from the medium, as well as by scattering from other directions into the direction of travel. Indicating the travel direction of the radiation beam as $\hat{s} = (\theta, \phi)$, the absolute amount of intensity attenuated is proportional to magnitude of the incident energy as well as to the distance that the beam travels through the medium:

$$(dI_\lambda)_{att}(\hat{s}) = -\beta_\lambda I_\lambda(\hat{s}) ds \tag{2.57}$$

where β_λ is the *extinction coefficient*, representing the energy lost per unit length by the beam whereas the negative sign is related to the decrease of intensity. The extinction coefficient allows to take into account both the absorbed and the scattered energy regulated by:

$$\beta_\lambda = \kappa_\lambda + \sigma_\lambda \tag{2.58}$$

where the two constants are respectively the linear *absorption* and *scattering coefficients*. Whereas the absorbed energy is converted into internal energy, the scattered one is simply deviated and appears as augmentation along another direction. In the latter case, to compute the augmentation in one direction $\hat{s}$, the contributions from all other directions must be taken into account by integrating over all solid angles, since the scattering causes a redistribution of the radiant energy related to the radiative beam. Therefore, the energy flux scattered into the direction $\hat{s}$ from all incoming directions $\hat{s_i}$ is:

$$(dI_\lambda)_{\text{sca}}(\hat{s}) = ds\frac{\sigma_{s\lambda}}{4\pi}\int_{4\pi} I_\lambda(\hat{s}_i)\,\phi_\lambda(\hat{s}_i,\hat{s})\,d\Omega_i \tag{2.59}$$

where ϕ_λ is the *scattering phase function* and it encodes the probability that a beam from one direction $\hat{s}_i$ will be scattered into a certain other direction $\hat{s}$ [49]. In the end, the augmentation related to medium emission is proportional to the length of the path and to the associated local energy content of the medium. Thus:

$$(dI_\lambda)_{em}(\hat{s}) = j_\lambda ds \tag{2.60}$$

where j_λ is the *emission coefficient.* At this point, the conservation equation for a spectral intensity of radiation $I_\lambda(\vec{r},\hat{s},t)$ in a position identified by $\vec{r}$ along a given direction $\hat{s}$ can be written as:

$$\frac{1}{c}\frac{\partial I_\lambda}{\partial t} + \frac{\partial I_\lambda}{\partial s} = j_\lambda - \kappa_\lambda I_\lambda - \sigma_{s\lambda} I_\lambda + \frac{\sigma_{s\lambda}}{4\pi}\int_{4\pi} I_\lambda(\hat{s}_i)\,\phi_\lambda(\hat{s}_i,\hat{s})\,d\Omega_i \tag{2.61}$$

This equation is called Radiative Transfer Equation (RTE). It is important to observe that all the previous computed source/sink terms compare in it, contributing to the change of the radiation intensity (emission, absorption, scattering away from the direction $\hat{s}$ and scattering into the direction of $\hat{s}$). For the most of engineering applications, the speed of light c is so large compared to the characteristic temporal and spatial scales of the investigated system. Consequently, the temporal evolution term of RTE may be generally neglected. As all conservation equations, proper boundary conditions must be provided to have a numerical solution.

Obviously, the radiant energy represents an additional volumetric source or sink for the total energy of a system (i.e. combustion chamber) which influences its temperature distribution. In fact, the RTE is coupled with energy equation through the temperature and the relative source term can be computed by integrating over all directions and in the whole spectrum:

$$\dot{\omega}_{rad} = \int_0^\infty \kappa_\lambda \left[4\pi I_{b\lambda}(T) - G_\lambda\right] d\lambda \tag{2.62}$$

2.2 A multi-time scales problem

As previously said, the various mechanisms by which thermal energy is generated and transported involve several types of materials which could be in a different state of matter (gas, liquid and solid) and, consequently, they could present different thermo-transport properties which in turn determine the thermal response of the whole system. From a transient point of view, this leads to a multi-time scales problem that has to be fully understood, especially when a numerical analysis is carried out as will be discussed in the following.

In a real aeroengine combustor, convection is enhanced by turbulence by means of eddies developed on a wide range of spatial, temporal and velocity scales, carrying mass and heat in a range which varies from an integral macroscopic scale, at which the energy is supplied, to a Kolmogorov microscale where energy is dissipated by viscosity. This is also reflected at the wall where the energy transfer involves the whole turbulence spectrum with different contributions to the metal temperature, depending on the considered scale. In this sense, the smallest eddies related to the Kolmogorov scale influence the turbulent diffusion of heat in the fluid within the *energy cascade process*, whereas a moderate effect is provided on the solid temperature distribution. On the contrary, the largest temperature fluctuations in the fluid are caused by the integral scale eddies, affecting the transient evolution of wall temperature. Starting from these considerations, the characteristic convective time scale can be expressed as:

$$\tau_{conv} = \frac{L}{U} \tag{2.63}$$

where L and U are respectively a reference length and velocity related to the geometry and the inlet conditions of the analyzed system, such as the combustor length and the hot gas bulk velocity. In a design framework, typical order of magnitude for these quantities are $L = o(0.1\ m)$ and $U = o(100\ m/s)$ with a consequent τ_{conv} of the order of 1 ms.

Regarding the conductive heat transfer, the heat is propagated through the solid with a characteristic velocity α/L which depends on the thermal diffusivity α of the material. As a consequence, characteristic conductive time scale is:

$$\tau_{cond} = \frac{t^2}{\alpha} \tag{2.64}$$

with the solid thickness t as reference length. The order of magnitude for τ_{cond} is 1 s since, in this case, the reference values for a combustor are $t = o(0.001\ m)$ and $\alpha = o(10^{-6}\ m^2/s)$.

As far as the radiative heat transfer is concerned, the heat propagation can occur also without a material medium, as discussed before. Therefore, the speed of the beams is globally not affected by the material properties, coinciding with the speed of light c independently by the wavelength. Also in this case, the reference length is the combustor size L since the flametube walls are opaque, limiting the beam propagation into the gas phase. According to these assumptions, the characteristic radiative time scale can be expressed as:

$$\tau_{rad} = \frac{L}{c} \tag{2.65}$$

resulting in a τ_{rad} of the order of 1 ps with the speed of light about $3 \cdot 10^8\ m/s$.

Comparing the computed heat transfer time scales, it is worth to notice that the convective time scale τ_{conv} is at least two order of magnitude lower than the solid conductive one τ_{cond} whereas the radiation is characterized by an extremely small time scale, occurring instantaneously. Therefore, the latter can be treated as a steady-state process with respect to the other heat transfer mechanisms.

In addition, a reacting flow is involved in a CHT problem within an aeroengine combustor. The chemical time scales governing the combustion differ by many orders of magnitude since the oxidation process includes both fast ($o(10^{-9}\ s)$) and slow ($o(1\ s)$) reactions which determine the advancement speed of the combustion. In the context of combustion phenomenon, the laminar flame speed S_L can be considered as a reference velocity and the laminar flame thickness δ_L as a characteristic length. Therefore, a characteristic time scale for combustion can be computed as:

$$\tau_{comb} = \frac{\delta_L}{S_L} \tag{2.66}$$

where $S_L = o(10^{-1}) - o(1)$ m/s for aviation fuels whereas the laminar flame thickness can be approximated by means of the ratio D/S_L between the mass diffusivity D and the laminar flame speed. Considering an order of $o(10^{-5}) - o(10^{-4})$ m for δ_L, this results in a range of combustion time scales of $o(10^{-4}) - o(10^{-3})$ s which could be smaller than both conduction and convective scales.

Chapter 3

Cooling in gas turbine combustors

As said in Chapter 1, the current trends in the design of modern aero-engines are addressed to improve the thermal efficiency of a gas turbine by increasing the compressor pressure ratio and the TIT. The effect on the combustor hardware of these design criteria is the heating of the walls beyond the melting point of the combustor material. As a result, the mechanical resistance is reduced where local heating is high, may leading to the onset of buckling failures as well as cracks in the hardware. Therefore, service failure of the flametube occurs without an adequate protection of the combustor walls. Moreover, the introduction of lean flames has caused a strongly increased demand for primary air to control the local composition and, so, the oxidation process. Consequently, the combustor has to generally operate with a strong reduction in air availability for liner cooling. In this framework, the need for effective cooling becomes more and more evident.

In the following, the attention will be focused on the cooling methodologies generally employed on aeroengine combustors with an exhaustive description of the effusion system, retained as the most efficient cooling technique, especially for lean combustors where the air available for liner cooling is extremely reduced.

3.1 Liner cooling techniques

The basic method to cool a combustor liner is the forced convection of air at the back of flametube by passing the fluid within the annuli, as shown in Figure 3.1.

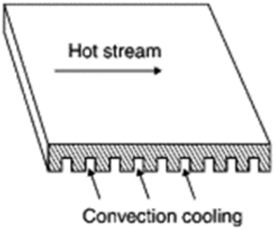

Figure 3.1: Forced convection cooling strategy (adapted from [50]).

Despite its simplicity, large amount of cooling air is required and it is generally inadequate for high temperatures within the combustor flametube. As a consequence, different configurations were studied with the aim of increasing the heat transfer surfaces and coefficients on the coolant side. In this sense, the use of *ribs* or turbulators in general allows to enhance the turbulence levels, leading to an increase of heat transfer coefficients of 2-3 times with respect to smooth surfaces. However, when the OPR is increased, the radiative heat flux on the liner wall will raise, causing a further augmentation of required coolant air. Moreover, the increase in pressure will also lead to higher combustor inlet temperature that will affect the annulus air capacity to cool the wall by convection [21].

Referring to heat-transfer enhancement strategies, the most significant technique to increase the local HTC is represented by *jet impingement*. In this cooling method, high-velocity air exhausts as jets from perforated holes, impinging on the surface to be cooled, as shown in Figure 3.2.

The turbulence intensity at the jet core generated by the impact with the target surface can be significantly high. Thanks to the high velocity

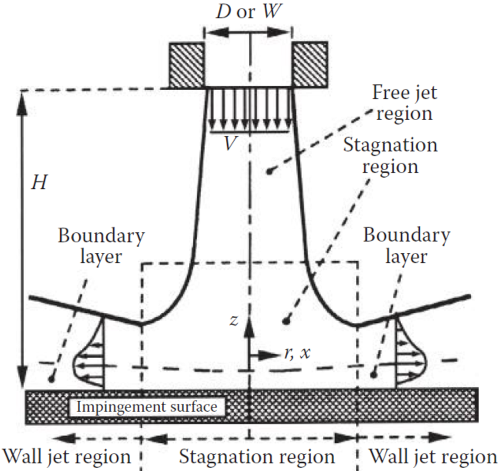

Figure 3.2: Schematic representation of the impingement cooling strategy (adapted from [51]).

together with significant fluctuations, turbulent mixing is increase as well as the heat-transfer enhancement capability of the jet. Employing this approach, the surface heat transfer coefficients are increased by one order of magnitude with respect to the basic convection method [51]. However, the impingement cooling has not been widely applied for combustor cooling, since the structural integrity of the combustor is weakened by the presence of this configuration of multi-perforated walls.

During last years, research efforts have been spent also in the investigation of the effects of employing the *Thermal Barrier Coating* (TBC) for the protection of liner hot side. The combustor flame side is coated with a thin layer of ceramic material characterized by low thermal conductivity. The surface formed is then smoothed in order to avoid residuals which will affect the flow aerodynamics. TBC represents an insulating layer, leading to a direct reduction of the below metal temperature. At the same time, the increase of TBC temperature allows to decrease hot side contribution of the radiative heat transfer. In spite of these advantages, the effect on the combustor metal walls in the event of loss or damage of the coating is to sharply increase the local surface temperature, resulting in high thermal stresses which lead to cracks in coating-loss locations.

Film cooling is anyway the most employed strategy to ensure the thermal resistance of the combustion chamber and of the liners in particular. According to [52], film cooling consists in the injection of coolant air at one or more discrete locations along the hot side of the surface that has to be cooled. In this way, a thick coolant coverage is created to protect that surface not only in the immediate region of injection but also in the downstream zone. Shielding the wall from the direct action of hot gases, the protective film allows to decrease the adiabatic wall temperature which regulates the convective heat transfer (Equation 2.36). If the coolant injection temperature is extremely low, an additional cooling effect occurs directly. On the opposite, the coolant injection can promote an augmentation of local turbulence levels and turbulent mixing, leading to higher values of the local HTC and, consequently, to higher convective thermal loads. Therefore, the main aim of film cooling is to provide a full coverage of the coolant on the surface, preserving its integrity as it moves downstream.

There are various geometrical configurations which can be exploited to generate film cooling. In terms of cooling effectiveness, the best performances are obtained by means of two-dimensional coolant film layer (i.e. uniform along the span of the surface) injected through a slot on the wall. The slots may be obtained from sheet stock or machined from forged or rolled stock, as shown in Figure 3.3. Slots fabricated from sheet metal are similar, but contain a joint and tend to have less flexibility in the design of specific features. Slots are generally fed with cooling air coming from one or more lines of individual drilled or punched holes around the combustor circumference.

Considering the performances of such strategy in presence of a flat plate, the cooling effectiveness depends on the geometrical and fluid dynamics features of the system but its characteristic trend along the plate is generally consistent with the one depicted in Figure 3.4. The decay of the cooling effectiveness occurs with downstream distance starting from

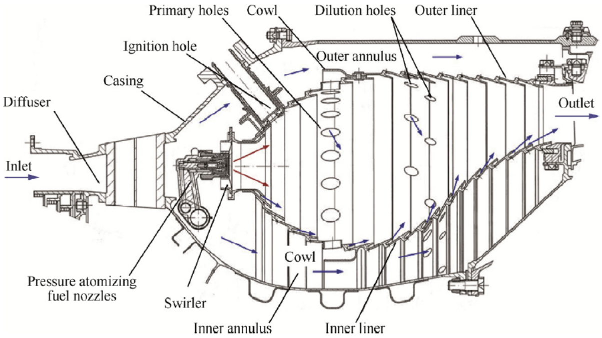

Figure 3.3: Sketch of an annular combustion chamber equipped with slot cooling system [53].

a complete coverage of the surface ($\eta = 1$). The decay is due to the entrainement of hot mainstream gases into the cooler film enhanced by the turbulent mixing. Consequently, the normal solution is to repeat a succession of slots along the liner length. However, this practice may seriously affect the structural integrity of the combustor hardware since the slots could represent high stressed zones as well as a preferred path

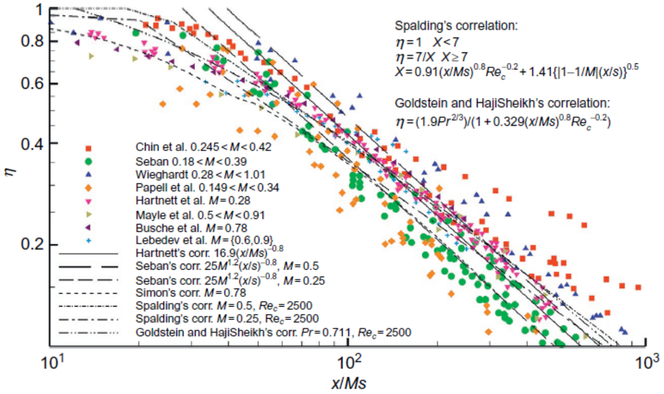

Figure 3.4: Slot cooling effectiveness [54].

for the onset of creeps.

A way to improve the film cooling performances is to take advantage of the passage of cooling air through the surface that has to be cooled, exploiting the consequent heat removal by convection. The main advantage of such strategy over the others is the possibility of maintaining the surface temperature at the desired level by controlling the coolant flow rate. In this sense, *transpiration cooling* represents the best way to do this by constructing the liner wall from a porous material. Thanks to the material pores, a very large area is available for the heat transfer, ending then in the creation of a film layer along the hot side. Sintered metal porous material [55], porous ceramic [56], Ceramic Matrix Composite [57], platelet structure [58], sintered woven wire structure [59] and multilaminate sheets (Transply [60] or Lamilloy [61]) are typically employed as porous materials for transpiration cooling. However, their application in gas turbine combustor has been limited by two serious disadvantages: the low mechanical properties of porous materials together with the possible occlusion of the internal micro-tunnels during the system operation, causing overheating and failures [62].

In recent years, the improvement of drilling capability has allowed to perform a large amount of extremely small holes, creating a multi-perforated system which provides a simil-transpiration behaviour with a slight decrease in performances but without the same structural disadvantages. Such cooling technique is referred as *effusion cooling* and it allows higher cooling effectiveness with a reduced amount of coolant air consumption compared to the other cooling strategy [63]. For these reasons, the following section will be devoted to a deep comprehension of this very promising cooling method, exploring its characteristic operational parameters and its main advantages which have led it to be the state-of-the-art of liner cooling technology for modern combustors.

3.2 Effusion cooling

Effusion cooling system consists of multi-perforated liners with thousands of drilled submillimetric angled holes. In this way, it allows to maintain hot components temperature below the melting level by injecting coolant from a huge number of small holes. The dense array of holes gives rise to a more uniform film protection of the wall which increases moving downstream thanks to the *superposition effect*. At the same time, a significant heat sink effect occurs as a consequence of the forced convection within the holes, exploiting a high length-to-diameter ratio (L/D) related to the typical small injection angles [6, 7, 8]. Moreover, the cold side mass bleeding determines here a general increase of the HTC [64].

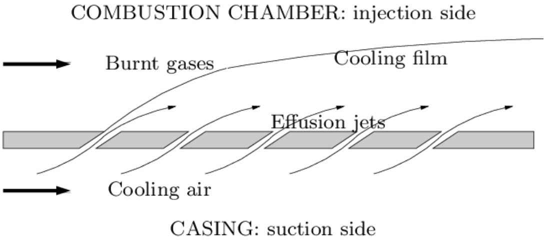

Figure 3.5: Schematic view of an effusion system with a multi-perforated plate which separates the combustion chamber (hot gases) from the casing (cold air) [65].

According to the experimental results shown in Figure 3.6 and to the outcomes of works belonging to several research groups [66, 67, 68, 69], the film layer coverage and cooling effectiveness in the first part of an effusion-cooled plate are lower with respect to a two-dimensional slot cooling system (Figure 3.4), since several effusion rows are required to achieve an asymptotic fully developed adiabatic cooling effectiveness level due to the superposition effect.

However, pure effusion cooling system permits to avoid the over-cooling which occurs with a typical 2D slot cooling in the region next to the injection due to the large amount of employed air to ensure a sufficient

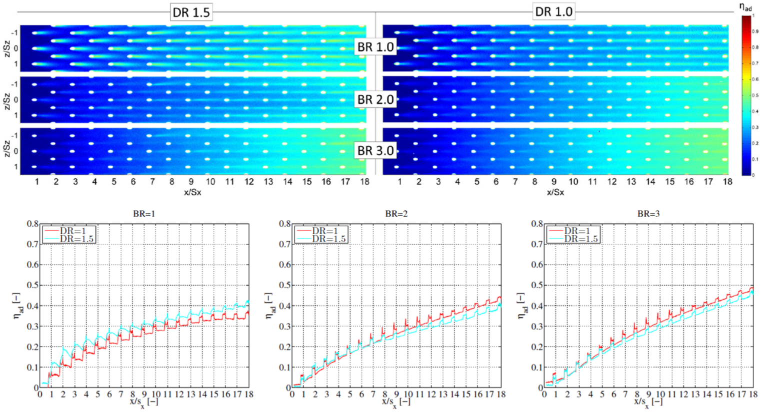

Figure 3.6: Experimental adiabatic effectiveness distributions on a effusion plate (adapted from [70]).

survival of the film layer. Exploiting the multiple injections and the heat sink effect within each hole, the effusion scheme provides a more uniform temperature distribution throughout the multi-perforated plate together with a reduced coolant consumption. Considering their individual features, different strategies have been investigated in order to exploit the advantages of both technologies by combining slot cooling with an effusion cooled scheme [71, 72, 73, 74, 75].

Due to the complex nature of fluid flow interaction between the coolant jets and the mainstream referred as *Jet-In-Cross-Flow* (JICF) phenomenon, several factors affect the film cooling distribution and its effectiveness [76]. Table 3.1 summarizes the main factors, splitting them into three main groups. For this reason, it is useful to provide a brief description of the typical features of the JICF and of the associated flow structures in order to better comprehend the influence of these factors on the performances of an effusion cooling system.

Table 3.1: Factors affecting film cooling performance [76].

Injection Flow Parameters	**Injection Geometry**	**Mainstream Flow**
Mass flux ratio	Primary injection angle	Freestream turbulence
Momentum flux ratio	Secondary injection angle	Incoming wakes
Velocity ratio	Hole shape	Surface curvature
Density ratio	Hole spacing	Pressure gradient
Pulsation		Mach number
		Approach boundary layer

3.2.1 Jet-In-Cross-Flow structure

Discrete film cooling can be more broadly considered as a JICF which presents characteristic flow features developed from the mainstream-coolant interactions. Figure 3.7 depicts the typical vortical structures associated with the investigated phenomenon.

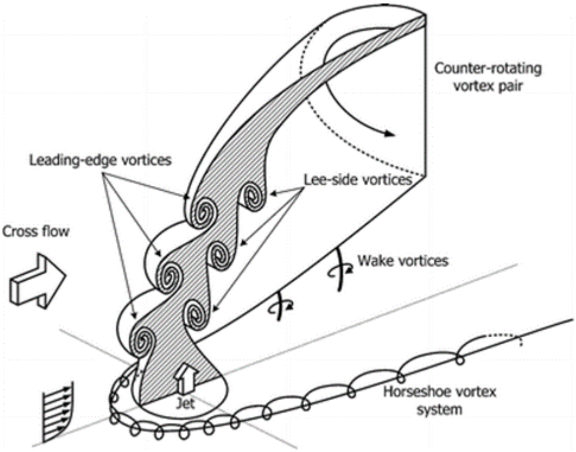

Figure 3.7: Jet-In-Cross-Flow vortical structures [77].

According to the reported schematization, several coherent structures can be identified:

- **Counter-Rotating Vortex Pair (CRVP) (or the Kidney-**

Pair Vortex): this vortical structure is a signature feature of the film cooling jet flow which is generated within the hole and it persists far downstream where it is strengthened by the interaction with the cross-flow, bending the jet and causing strong shear stresses on its sides. CRVP is responsible for the lifting of the jet and for the entrainement of the main flow into it, spreading the coolant over an increased area as well as promoting the mixing with the cross-flow. Depending on the fluid dynamics conditions of the two interacting flows, the film coverage can be enhanced or inhibited by the combination of these effects. Different mechanisms leading to the CRVP have been suggested, taking into account the evolution of vorticity in the jet's shear layer [78, 79, 80, 81] as well as pressure differences between the upstream and downstream regions of the jet [82, 83].

- **Leading edge vortices**: these vortices are generated as a consequence of the onset of Kelvin–Helmholtz (K-H) instabilities within the shear layer between the jet and the cross-flow. These structures are also referred as *ring vortices* since they are formed in the windward side of the jet, taking a ring shape around the jet circumference. The vortices are formed in the near field of the jet and, then, they break up further downstream into fully three-dimensional structures in the far field [54].

- **Horseshoe vortices**: these vortices are formed upstream of the hole leading edge where the upstream boundary layer approaches the jet. The jet obstruction creates adverse pressure gradients which cause the separation of the incoming boundary layer and its deflection on either side of the jet. The related vorticity reorganizes at the base of the jet forming the horseshoe span-wise vortices which move around the jet along the wall [84].

- **Wake vortices**: these vortical structures develop downstream the injection location in presence of high velocity ratio and Reynolds number as upright vortices, extending from the wall to the leeward side of the jet. They are caused by the entertainement and the reorientation of the boundary layer into the wake region immediately next to the jet [85]. Consequently, their formation is associated with the main lifting behaviour of the jet.

The size, the intensity and the evolution of the described vortical strictures depend on the geometry of the effusion system and on the fluid dynamics properties of the main and coolant flows. The reader interested into more details about the JICF is addressed to a review article by [86] which gives a good overview on the whole problem.

3.2.2 Geometrical parameters

Several parameters take part in the geometrical description of an effusion cooling system, as shown in Figure 3.8. Hole diameter (D) and length (L), stream-wise and span-wise pitches (S_x and S_y), inclination and compound angles (α and γ) affect simultaneously the formation of the protective film coverage along the wall.

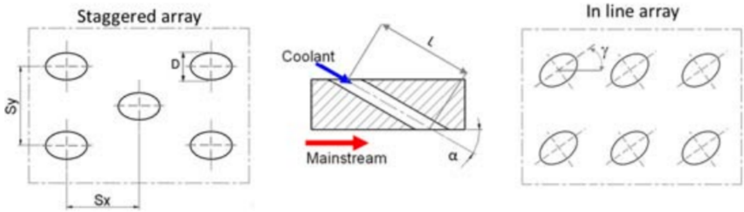

Figure 3.8: Main geometrical features for an effusion cooling system.

As reported in the following, large research efforts have been devoted to specify the best values for each of these parameters in terms of cooling performances, but it is mandatory to find a compromise with the manufacturing costs of the hypothesized effusion configuration. According to state of the art, $\alpha = 20° - 45°$, no compound angle, $L/D = 3 - 6$ are typically adopted in gas turbine combustor design. Concerning the hole spacing, it is quite variable from engine to engine.

Another important geometrical factor for the efficiency of the effusion cooling system is the shape of the hole through which the coolant is injected. Figure 3.9 reports various types of *shaped holes* investigated as alternatives to the classical cylindrical hole.

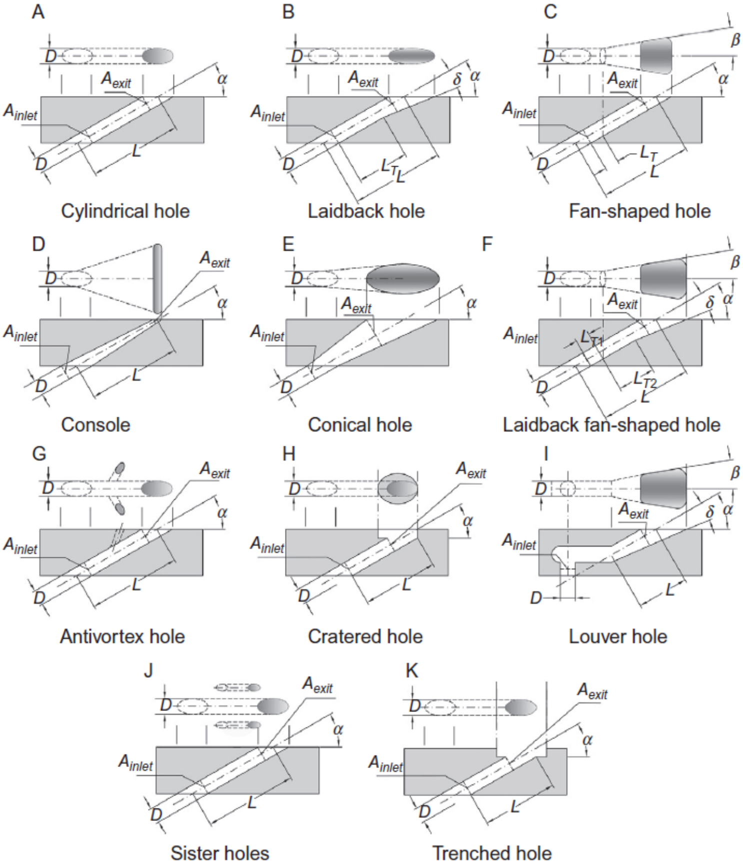

Figure 3.9: Shaped hole geometries investigated for film cooling [54].

The main aim of such configurations is generally to maintain the film layer closer to the wall and to promote its lateral spreading as in the case of the Laidback fan-shaped hole. However, the flow field generated by these geometries is quite complex as well as the description of the effect of the geometrical and fluid dynamics parameters on the resulting film effectiveness. Despite their evident advantages, shaped holes are generally not employed for the effusion cooling system on real aeroengine combustors, since their implementation would entail a not affordable manufacturing cost.

3.2.3 Injection flow parameters

In Section 3.2.1, the typical vortical structures associated with the JICF phenomenon have been reported. The size and the intensity of these flow features are strong influenced by the entity of the main-coolant interactions which in turn depend on the fluid dynamics properties of the coolant air with respect to those of cross-flow. In fact, the coolant jet typically has different density and velocity than the mainstream. In this sense, the JICF behaviour is characterized by several dimensionless parameters and specific flow pattern can be observed depending on their values:

- **Velocity ratio (VR)**: it is defined as the ratio of the average coolant velocity to the mainstream velocity.

$$VR = \frac{V_c}{V_\infty} \tag{3.1}$$

- **Density ratio (DR)**: it is defined as the ratio between the coolant and the mainstream densities.

$$DR = \frac{\rho_c}{\rho_\infty} \tag{3.2}$$

- **Blowing ratio (BR)**: it is defined as the mass flux ratio of the coolant to the main flow.

$$BR = \frac{\rho_c V_c}{\rho_\infty V_\infty} \tag{3.3}$$

- **Momentum flux ratio (I)**: it is defined as the momentum flux ratio of the coolant to the main flow.

$$I = \frac{\rho_c V_c^2}{\rho_\infty V_\infty^2} \tag{3.4}$$

- **Reynolds number ($\mathbf{Re_c}$)**: it is referred to the coolant jet and it is computed considering typically the jet hole diameter normal to the hole axis D. It controls the heat transfer and the pressure losses within the hole.

$$Re_c = \frac{\rho_c V_c D}{\mu_c} \tag{3.5}$$

In particular, the velocity ratio allows to distinguish between three different flow regimes: for $VR < 0.25$, *mass addiction regime* occurs where the film effectiveness increases with the blowing ratio due to higher quantity and, so, thermal capacity of the coolant air; for $0.25 < VR < 0.8$, *mixing regime* is observed for which the film coverage depends on the BR and on the DR since the augmentation of coolant thermal capacity is counterbalanced by higher jet penetration; for $VR > 0.8$, *penetration regime* is identified with the jet lift-off from the surface and with higher turbulent mixing with the main flow.

In presence of a uniform flow over a flat plate, the values of such parameters can be uniquely determined whereas their computation is more complex when the effusion system of a modern aeroengine combustor is considered. Here, the working conditions are highly variable due to the different flow split and operating pressure and temperature experienced by the combustion chamber during its mission cycle, but also due to the local velocity and temperature gradients induced by the highly unsteady flow field and by the presence of the flame. The potential range can vary for blowing ratio to $BR \approx 1 - 9$ whereas for density ratio to $DR \approx 1 - 2.5$.

3.2.4 Performance metrics

Several parameters were proposed in literature to measure how well the surface is cooled, considering an injection of the coolant at temperature

T_c and a cross-flow being at temperature T_∞. As previously said in this Chapter, one of the main effect of the introduction of coolant air as a thick film layer over the wall is the reduction of the freestream side temperature with which the wall convectively exchanges heat, indicated as adiabatic wall temperature according to Equation 2.36. Such temperature can be employed as a measure of film coverage quality and, at the same time, of the main-coolant mixing in a non-dimensional form as a *adiabatic effectiveness*:

$$\eta_{adiab} = \frac{T_\infty - T_{aw}}{T_\infty - T_c} \tag{3.6}$$

According to this definition, η_{adiab} can vary between 0 and 1. For high values of adiabatic effectiveness (i.e. adiabatic wall temperature equal to coolant temperature) film cooling effectiveness is unity. When the adiabatic effectiveness is equal to zero, the adiabatic wall temperature is equal to the mainstream temperature and no film cooling protection occurs.

The adiabatic effectiveness does not allow to take into account the other important benefit provided by the passage of coolant air through the multi-perforated plate which is the heat removal by means of convection. In order to give information about the overall performance of an effusion system, the combined contributions of film protection and heat sink effect must be considered, leading to the definition of *overall effectiveness*:

$$\eta_{ov} = \frac{T_\infty - T_w}{T_\infty - T_c} \tag{3.7}$$

where the actual wall temperature in presence of both film cooling and heat flux on the surface T_w appears.

However, the interaction between the cross-flow and coolant air may lead to an increase of turbulence levels in the near-wall region, affecting the hot side HTC. Since the final aim of a cooling system is the reduction of the heat transfer to the surface, there is the need to define a parameter in order to take into account the opposite contributions of HTC augmentation and film coverage and to measure the resulting effect. In this sense, Sen et al. [87] suggest to use the Net Heat Flux Reduction (NHFR) parameter to quantify the global heat transfer achieved on a cooled surface. It is computed as the ratio between the heat flux reduction due to film cooling and the heat flux occurring without cooling:

$$NHFR = \frac{q - q_0}{q_0} = 1 - \frac{HTC_{main}}{HTC_0}\left(1 - \eta_{aw}\theta\right) \tag{3.8}$$

where q is the heat flux with the coolant, q_0 is the heat flux in absence of film cooling, HTC_{main} and HTC_0 are the reference heat transfer coefficients with the presence or not of the film cooling respectively whereas θ is the non-dimensional temperature, defined as:

$$\theta = \frac{T_{main} - T_{cool}}{T_{main} - T_w} \tag{3.9}$$

This parameter represents effectively the advantage provided by the cooling system: higher values of NHFR are achieved by a reduction in HTC_{main}/HTC_0 and an enhancement in η_{aw}. This means that a possible augmentation of the local HTC due to the flow field generated by the main-coolant interaction must be counterbalanced by a better film coverage, otherwise the heat transfer reduction is not achieved.

3.2.5 Review on the influence of effusion parameters

Several studies have been carried out to analyze the impact of the geometry on the efficiency of an effusion cooling system. One of the most important features is the injection angle, since it strongly determines how the coolant is distributed over the wall. In fact, a shallow injection angle minimizes the tendency to the lifting of the coolant jet downstream the injection point, approaching the ideal slot cooling configuration and, so, improving the film cooling effectiveness. From this point of view, Foster and Lampard [88] investigated the effects of the injection angle considering a set of geometries with $\alpha = 35^\circ,\ 55^\circ,\ 90^\circ$. The study revealed a strong influence of this parameter in conjunction with the main-coolant blowing ratio, showing the highest cooling effectiveness with small injection angles at low blowing ratios whereas large injection angles are advantageous at high blowing ratios. Similar stream-wise angle levels ($\alpha = 30^\circ,\ 60^\circ,\ 90^\circ$)

were studied by Balduf et al. [89] and by Yuen and Martinez-Botas [90], exploring optimum flow conditions for efficient cooling for a wide range of configurations. An effectiveness improvement was observed by Behrendt et al. [91] for lower cooling hole angles (20°) in the framework of advanced combustor cooling concepts with realistic operating conditions.

The performances of different injection angles are also influenced by several fluid dynamics factors such as free-stream turbulence levels and coolant to mainstream density ratio, as investigated more recently by Andreini et al. [67] with two different hole inclinations ($\alpha = 30°, 90°$). An interesting investigation on the efficiency of an effusion cooling system in presence of a high swirling flow was carried out by the same authors [92] to take into account actual combustor flow field features. Considering different injection angles ($\alpha = 20°,\ 30°,\ 90°$), the results showed that the 20° geometry ensures the best film protection, thanks to the higher resistance to the destructive action of the impinging swirling jet and to the limited penetration of the cooling jets, as shown in Figure 3.10.

Film cooling holes can also be oriented with respect to the mainstream with a secondary compound angle. Compound angle configurations typically allow better film coverage of the surface, as investigated by Ligrani et al. [93, 94] and Ekkad et al. [95], highlighting higher effectiveness in the near field of the jet and a more pronounced lateral spreading of the coolant. As for the primary injection angle, the effect of different secondary angle depends on the operating conditions of the system. From this point of view, Ekkad et al. [95] indicated that increasing inclinations have to be employed moving towards higher blowing ratios, since the coolant is maintained closer to the surface, especially with lower density ratio cases which are more susceptible to separation. Similar conclusions derived from the works carried out by Schmidt et al. [96] and Al-Hamadi et al. [97] whereas Nasir et al. pointed out that the positive effect of the compound angle occurs only with lower and higher blowing ratios far way from the unity value.

As far as the diameter and the spacing of effusion holes are concerned, Andrews et al. [7] experimentally studied the influence of hole size on

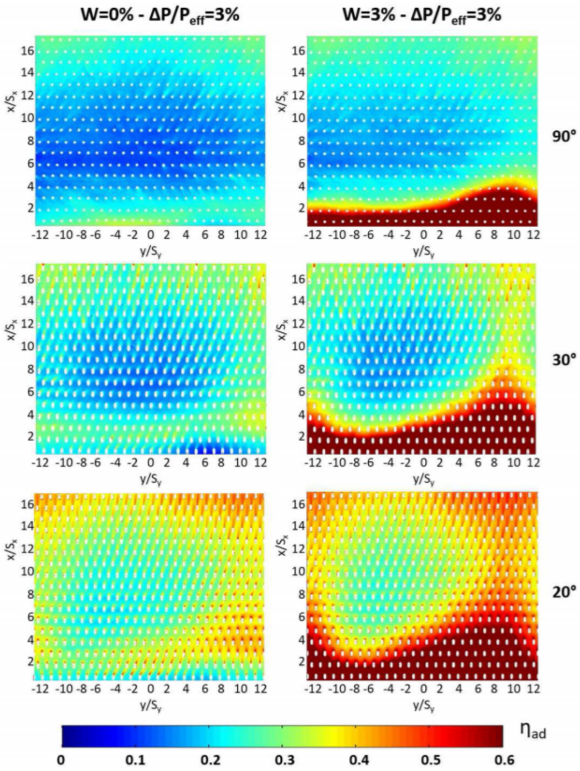

Figure 3.10: Adiabatic film cooling effectiveness distributions on an effusion plate equipped by a real aeroengine combustor geometry [92].

discrete hole film cooling. Better cooling performances in terms of overall effectiveness were observed increasing the hole diameter. At the same time, an augmentation in the number of holes for coolant injection together with smaller diameters leads to a substantial increase in η, since a lower main-coolant mixing is induced. Similar considerations also derived from the experimental investigations of Gustafsson et al. [8]. As experimentally investigated by Liu et al. [98], a simil-transpiration behaviour was obtained with a densely arranged cooling holes whereas a significant drop in the effectiveness was experienced increasing hole spacing, as highlighted by Goodro et al. [99].

Regarding the hole length to diameter ratio, Burd et al. [100, 101] carried out hydrodynamic measurements for simple angle cylindrical hole with L/D being 2.3 and 7.0. In this experimental study, the short-L/D holes exhibited worse performances due to enhancement of turbulent mixing caused by the coolant jet topology. An exhaustive experimental campaign was conducted by Lutum et al. [102] on a simple angle cylindrical holes with L/D from 1.75 to 18, as reported in Figure 3.11. The results indicated that decreased film effectiveness was obtained for short hole and film effectiveness remained almost unchanged for $L/D > 5$.

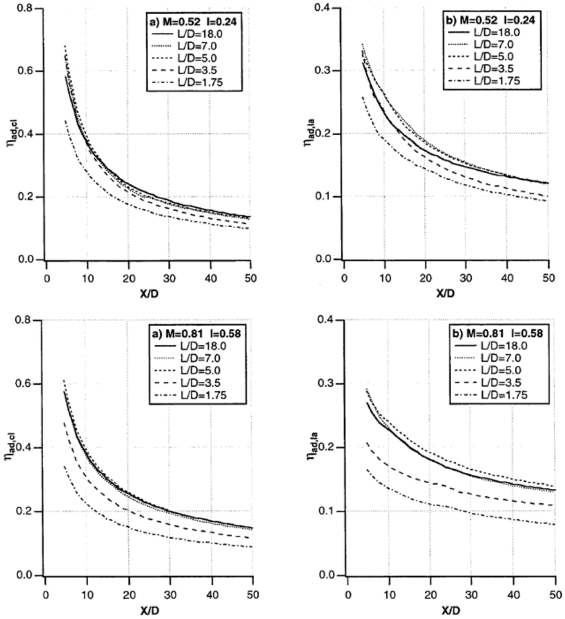

Figure 3.11: Centerline (on the top) and laterally averaged (on the bottom) adiabatic film cooling effectiveness distributions at various length-to-diameter ratios (adapted from [102]).

As already seen, the film cooling effectiveness of an effusion system is strongly affected by the separation and the reattachment of the coolant jet downstream the injection point as well as by its lateral spreading. These film cooling behaviours depend on the injection flow parameters which determine the intensity of the vortical structures generated by the interaction with the main flow. Many different studies (i.e. Sinha et al. [103], Pedersen et al. [104] , Johnson et al. [105]) have highlighted that the coolant remains attached to the surface for low BR due to the strong deflection suffered by the high-momentum main flow. In this case, no significant effect is observed by varying the DR [54]. On the contrary, the density ratio becomes important to characterize the coolant injection when the BR increases and the effusion jets tend to lift-off. For a constant BR, higher density ratio dampens the coolant tendency to detach from the surface, resulting in higher effectiveness. On the opposite, decreasing the density ratio at a constant blowing ratio makes the coolant more likely to separate, causing lower effectiveness, as reported in Figure 3.12. According to these studies, the BR value at which the change in DR does not influence the cooling performances may depend on the upstream boundary layer or on the Reynolds number.

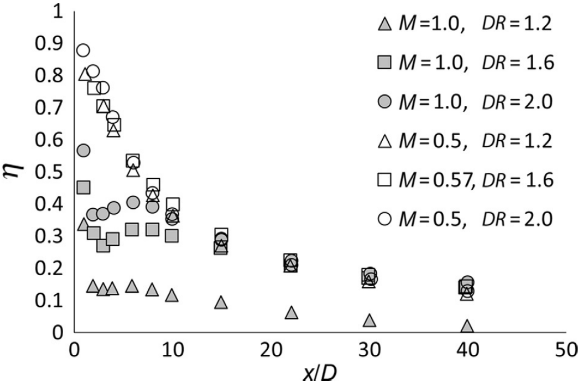

Figure 3.12: Centerline film cooling effectiveness for a 35-degree injection varying BR and DR [103].

According to its definition (Equation 3.4), the momentum ratio encodes the combined effect of BR and DR. For this reason, it is considered the key parameter in determining the jet penetration as highlighted by the outcomes of the experimental campaigns carried out by Goldstein et al. [106], Baldauf et al. [107] and Bernsdorf et al. [108] on a flat plate at various blowing and density ratios and with different injection angles. The strength and the distance from the wall of the counter-rotating vortex depend on the I value as well as on the intensity of the main flow entrainement effect, determining the jet trajectory and the thickness of the coolant layer over the wall. Generally, when the coolant jet detaches from the surface immediately downstream the injection due to high blowing and density ratios, intense eddies are generated by the passage of the mainstream beneath the jet and an undesired increase of the HTC along the wall occurs. Therefore, it can be concluded that decreasing the momentum ratio with an augmentation of the density ratio typically leads to an increase of the film cooling effectiveness, since the thermal capacity of the coolant is increased. At the same time, the jet is kept close to the surface, preventing also a counter-productive HTC augmentation.

Chapter 4

Numerical modelling for unsteady CHT simulations

Considering the outcomes of the previous chapters, particular attention must be devoted in dealing with the multiphysics problem of heat transfer within a combustion chamber in order to ensure hot components durability and, therefore, the operational safety of the system throughout its working cycle. However, the complexity of the involved phenomena makes the CHT problem very challenging. In this context, CFD calculations permit a reduction of times and costs of new designs and a practically unlimited level of detail of results with respect to expensive reactive high-pressure experimental campaigns. Therefore, CFD has become a key and complementary tool to understand the involved phenomena. The rapid development of computational facilities and the evolution of computational fluid dynamics allow to find new highly-effective numerical strategies for conjugate heat transfer analyses in order to achieve a reliable prediction of wall temperatures and heat fluxes.

Steady CHT RANS simulations represent the standard in industrial applications and they are widely exploited during the preliminary design process thanks to their ever lower computational time as a consequence of the significant increase of CPU power and speed. Despite its computational advantages, RANS approaches are anyway not able to correctly describe the fully-turbulent reacting flows which typically characterize the aeroengine combustors together with their strong unsteadiness related to the complex flow field generated by the swirling motion, resolving only the mean flow. This results in an incorrect computation of the turbulent mixing, of the flame structure and of the flame-wall interactions which generally cause a wrong estimation of heat loads acting on combustor walls. Due to the well-known limitations of RANS approaches, LES models, or hybrid RANS-LES for wall bounded configurations in order to overcome the issues related to the spatial resolution requirements in the near-wall region with fully-LES calculations, are becoming currently more feasible with the development of computational facilities.

In the framework of scale-resolving CHT simulations, the different requirements for the involved phenomena, mainly concerning time and space resolutions and, in particular, the related large time scale disparities (as discussed in Chapter 2), demand for alternative strategies with respect to a direct coupling of the different heat transfer mechanisms solutions. In this case, the small time-step necessary to correctly solve the governing equations of the fluid domain is also employed for the temporal discretization of the longer transient behaviour of the solid part, leading to a significant waste of computational resources. Moreover, the gain in computational cost derived from the use of more effective coupling strategy could permit a deeper insight of the impact of the heat transfer modes on the thermal behaviour of the analyzed system.

The computational effort is even higher when a CHT simulation of an entire aeroengine combustor equipped with an effusion cooling system is addressed. In Chapter 3, this cooling technique has been presented as the most promising to deal with the increasing flame temperature and with the reduced availability of coolant air which characterize the modern combustor concepts. However, the proper discretization of all holes required for a simil-LES calculation is not compatible with the stringent time requirements typical of industry. With the aim of improving the feasibility of this kind of investigation, an innovative approach for effusion modelling is proposed in the context of this research work.

For these purposes, the coupling strategy employed for the unsteady CHT simulations reported in this manuscript and the proposed novel approach for effusion modelling will be here described after brief reviews of the state of the art available in technical literature on these topics. The specific numerical models employed to perform each calculation will be instead presented in the related chapters.

4.1 Classification of CHT approaches

In the framework of 3D CHT simulations, several strategies are available and they differ in terms of required computational cost and time, accuracy and numerical stability of the calculation, solution method of the involved governing equations in addition to the complexity of their implementation. From a multiphysics perspective, the adopted numerical methodology must ensure the continuity of the energy-related quantities between the domains which are involved in the heat transfer analysis. Such continuity has to be respected at the so-called *coupling interfaces* which identify the regions where two distinct physics show their coupling. Referring to the fluid/solid coupling, the interfaces are represented by the combustor walls at which the heat fluxes and temperatures must equal on the two sides. Instead, the fluid domain constitutes the fluid/radiation coupling interface and, in this case, the continuity is imposed in terms of aero-thermal fields (i.e. pressure, temperature and chemical species) as well as radiation energy contribution (i.e. source/sink effect). On the other hand, the radiation/solid coupling occurs again at the solid walls (or also within the solid if its material is semi-transparent) where the radiative heat fluxes and temperatures computed in the two domains must be equal.

The continuity of the energy-related quantities can be more or less easily ensured depending on the employed coupling strategy, distinguishing between *strongly* and *loosely* coupled approaches, as depicted in Figure 4.1. In the former methods, all the different fields are solved simultaneously in a large system of equations by a single solver which automatically ensures the continuity as a convergence criterion before the next iteration. The second one consists in solving each set of governing equations separately in a segregated manner with dedicated solvers. The solutions obtained in the sub-domains are need to be coupled further at the interfaces by transferring certain parameters between the simulations during specific *coupling iterations* [109].

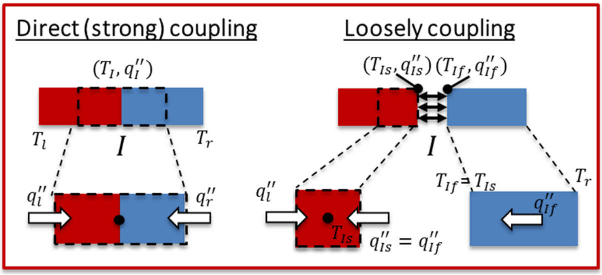

Figure 4.1: Sketches of Strong and Loosely coupling strategies.

Depending on the objective of the numerical analysis, *steady* coupling differs from *unsteady* coupling. The first approach is employed when steady analysis is carried out aiming at the mean metal temperature while the latter allows to compute the transient evolution of wall temperature or its fluctuations over time in a scale-resolving framework.

Within the loosely coupled class, two possible iteration/time-step advancement technique are available, as shown in Figure 4.2: *sequential* and *parallel* coupling. In a sequentially coupled approach, the solvers run one at a time: each solver gets information from the previous one and provides data to the next one. Using a parallel coupling, instead, the solvers run simultaneously and exchange quantities at the same time at a given frequency. In literature, steady coupled methods are usually solved in a sequential manner while unsteady coupling is efficiently employed with a parallel algorithm.

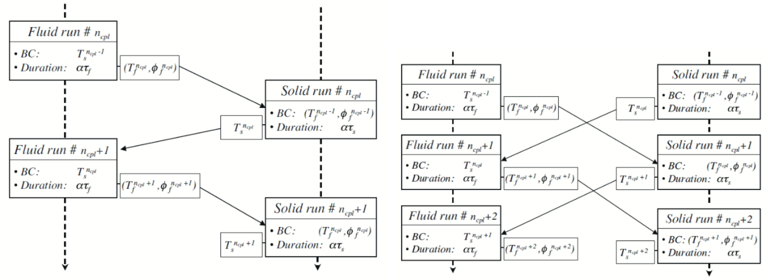

(a) (b)

Figure 4.2: (a) Sequential and (b) parallel coupling strategies (adapted from [109]).

Due to the different time scales of heat transfer modes, only the loosely coupled approaches are suitable for CHT analyses in the context of scale-resolving simulations which are in turn required to have a deeper insight of the complex reacting flow fields and to improve the accuracy of results. For this reason, this type of coupling strategy is considered in the following.

4.2 State of the art on unsteady CHT modelling

Right from the emergence of computational based CHT analyses, various researchers have dedicated their time and efforts to investigate several coupling techniques for CHT solvers. In the context of this work, unsteady CHT simulations have been performed by employing an in-house loosely coupled approach. For this purpose, a brief review of the unsteady loosely coupled strategies available in technical literature is here reported.

This numerical technique has been adopted and investigated by many researchers [110, 111, 112, 113, 114, 115]. Since the loosely coupling method involves separate solvers to model the different physics and heat transfer mechanisms in fluid and solid domains, it allows to update the fluid flow, the conductive and the radiative calculations as a complete CHT code without much modification in the existing base codes [116]. In this sense, the main advantage is the possibility of solving each simulation with the most proper time-step size, chosen according to the characteristic time scale of the involved phenomenon. This overcomes the principal drawback of a direct coupling approach in which the same time-step size has to be employed for all the heat transfer phenomena, leading to a strong increase of the computational cost and time since also the transient thermal behaviour of the solid ($\tau_{cond} = o(1\ s)$) will be temporal discretized with the smallest characteristic time scale ($\tau_{comb} = o(10^{-4}) - o(10^{-3})\ s$) with a significant waste of computational resources.

On the other hand, the implementation of an efficient algorithm to pass information at interfaces between fluid, solid and radiative domains becomes fundamental from a numerical point of view. At the same time, there is the necessity of proper matching of energy-related quantities at the domains interfaces. The performances of the employed loosely coupling methodology depend on the stability and the accuracy of the coupling strategy followed at the interfaces. Alonso et al. [117] underlined that the accuracy and the stability of the simulations are significantly influenced by the boundary conditions applied to the various domains as well as by the variables exchanged between the solvers. Moreover, employing different time-steps for the fluid and solid solvers introduces constraints in frequency of information exchange among different domains, so as to ensure the temporal consistency of the numerical solutions.

A loosely coupling methodology to deal with LES-CHT simulations on massively parallel architectures was proposed by Duchaine et al. [109] (Figure 4.2b) . In this case, a coupling relaxation parameter h is used to provide a Dirichlet/Neumann mixed boundary condition on heat flux and temperature at the solid-fluid interfaces, ensuring a stable coupling at a constant frequency. For this reason, the procedure is suitable for the prediction of steady-state metal temperature but not for the reconstruction of the thermal fluctuations at the wall. In this work, the coupling between the codes (AVBP and AVTP [118] respectively as fluid and solid solvers) is managed by means of the OpenPALM software [119] which also optimizes the computational resources, distributing the CPU between the solvers in order to limit the queue time. In addition, a deep one-dimensional stability analysis was carried out, leading to the identification of mainly two parameters that determine the stability and the cost of the coupled simulations: the mesh Biot number of the solid domain and the coupling synchronization time parameter α which defined the time between two coupling events. The developed coupling strategy has been successfully applied to a cooling turbine blade problem at first and then extended to a CHT analysis of a reverse flow RQL combustor by adding the radiative solver. In the context of these works, a sensitivity analysis on both the coupling relaxation parameter and the coupling synchronization time parameter was carried out, since they could affect the stability and the accuracy of the whole simulation. The reader interested into more details about these numerical works is addressed to the mentioned references.

Regarding the temporal coupling, an adaptive coupling time-step size approach was proposed by Zhang et al. [120, 121] in the framework of conjugate heat transfer problems in hypersonic flows over a long period of time. This technique introduced significant improvements in terms of computational efficiency with respect to a fixed time-step size approach by adapting the coupling time-step size on the real physical evolution of the solutions by means of a Proportional-Integral-Derivative (PID) controller.

Unlike the coupling strategy developed by Duchaine et al. [109], a method for the analysis of both steady-state and transient thermal behaviour of solid domain was introduced by He et al. [122]. In this case, the near-wall fluid temperature is subjected to a time-scale decomposition where the mean value is employed by the steady solver of the solid conduction whereas a Fourier transform is used to decompose the fluctuating component in its harmonics. After that, a semi-analytical interface model is adopted to compute the wall temperature in the spectral domain, starting from the pairs amplitude-frequency derived from the Fourier decomposition. As depicted in Figure 4.3, this model couples the heat fluxes from the flow field solution on the fluid side with an analytical 1D solution of conduction in a semi-infinite domain on the solid side, according to the energy conservation.

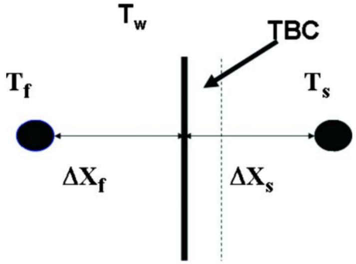

Figure 4.3: Semi-analytical interface model at fluid/solid interface in He et al. model [122].

The wall temperature thus obtained in the spectral domain is transformed in the time domain to sum it with the mean value provided by the steady solid solver. In this way, the complete information about wall temperature is recovered and imposed as time-dependent interface boundary condition for the fluid solver. An additional unsteady conduction solver is considered to reconstruct the thermal fluctuations at the wall where the boundary conditions consist in the same wall temperature spectrum used for the fluid solver. This methodology was validated in presence of URANS as well as fully-LES turbulence models for which the reader may refer to [122, 123, 124] and references therein.

An alternative to the previous described strategies is represented by the approach developed by Koren et al. [125, 126]. As for the Duchaine et al. methodology, the software OpenPALM is employed to perform the coupling and the data exchange between the involved simulations, according to the scheme reported in Figure 4.4. In this framework, the energy conservation is respected thanks to a Hybrid-Cell interface model where the energy balance equation is solved on a hybrid cell around the interface which includes the first cell layer of fluid and solid meshes. From this dedicated ODE solver, the common interface temperature is computed and prescibed as Dirichlet boundary condition on both the domains. As in [120], a PID controller dynamically adjusts the coupling time-step size to ensure the numerical stability of the ODE solver. However, this does not permit the application of the desynchronization technique and, so, the solid solver is split into a steady (for mean value) and unsteady (for fluctuating component) solid solvers in order to predict the transient evolution of wall temperature with an affordable computational time. Depending on the considered solid solver, different quantities are prescribed at the interface boundaries: mean wall heat flux coming from the fluid solver is imposed for the steady solid solver while the fluctuating part is employed for the unsteady one. Computing respectively the mean and the fluctuating components of the wall temperature, the double solver accelerates the passage from a transient behaviour to a permanent regime for the solid temperature. In fact, at first the mean wall heat flux is highly affected by the fluctuating components, since the data are averaged over a small time during the first coupling steps. Hence, the contribution of the highest frequencies is not filtered by the meaning process and, so, it strongly influences the steady solid solver. For a complete comprehension of the described strategy, the reader is addressed to the mentioned references.

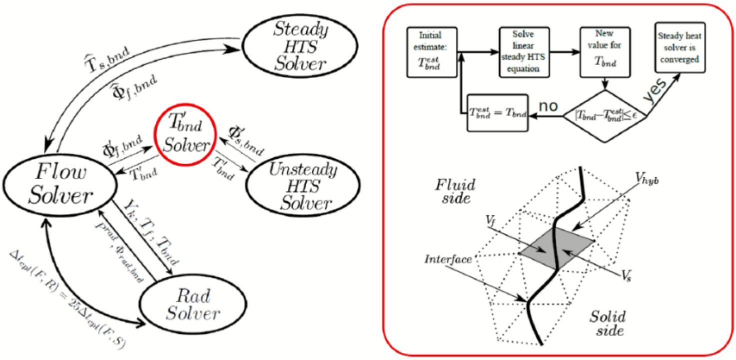

Figure 4.4: Schematic representation of Koren et al. coupling strategy. In red box, the interface fluctuating temperature model is reported (adapted from [125]).

4.3 U-THERM3D tool

Here, a brief description of the in-house unsteady CHT strategy employed for the multiphysics simulations discussed in this work is reported. For further details about the theoretical fundamentals, the reader may refer to [14] and references therein. U-THERM3D is a 3D loosely coupled approach developed by Bertini within ANSYS Fluent to solve conjugate heat transfer problems in the context of unsteady multiphysics calculations. The described procedure has represented an extension to scale-resolving simulations of the coupled strategy implemented in ANSYS CFX by Mazzei [127] for the steady thermal design of combustor liners.

The numerical concept on which the U-THERM3D procedure is based is a *desynchronization* of the time-steps in the solution of the involved heat transfer mechanisms, convection together with the combustion process, conduction in the solid and radiation. For this purpose, three different simulations are performed with a parallel coupling strategy as depicted in Figure 4.5, optimizing and adjusting the numerical setup of each calculation on the fluid dynamics characteristics of the solved domain and heat transfer method.

As shown in the schematic representation, the CFD and conduction calculations are performed in an unsteady manner advancing in time with their own time-steps ∇t_i whereas a steady solver is exploited for the radiative heat transfer. In this way, each involved phenomenon is solved respecting its characteristic time scale (the radiation can be considered as a steady process because of the extremely small time scale compared to the others). The mutual interactions among the simulations are carried out by means of the use of specific boundary conditions at the solid/fluid, solid/radiation and fluid/radiation interfaces which are updated at each *coupling time-step*. In fact, the solvers are kept synchronized every $n_f \nabla t_f$ and $n_s \nabla t_s$ time-steps respectively for the CFD and conduction unsteady simulations and every n_r iterations for the steady radiative calculation.

According to [109], instantaneous values are exchanged at the coupling time-step and consist of surface quantities (wall temperatures and

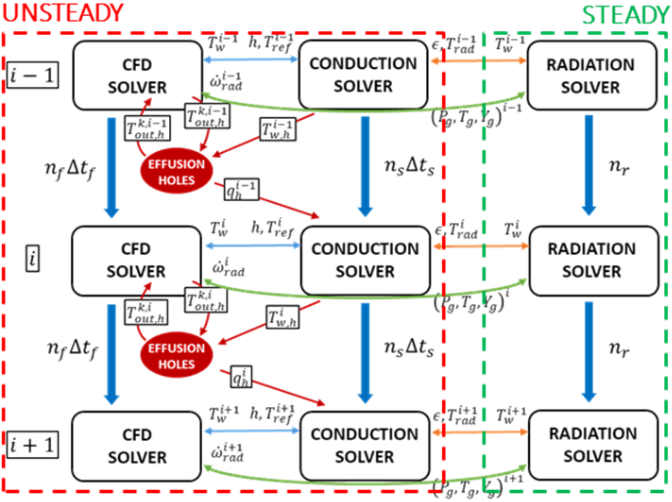

Figure 4.5: U-THERM3D parallel coupling strategy (adapted from [14]).

heat fluxes) for the solid/fluid and solid/radiation interactions whereas volume quantities (aero-thermal fields) for the fluid/radiation coupling. With the aim of ensuring the numerical stability of the CHT simulation, convective wall heat flux is sent to the conduction solver in the form of a coupling relaxation parameter h and a reference convective temperature T_{ref} which allow the respect of the wall heat flux computed by the CFD solver, according to the following formulation:

$$q''_{\text{conv}} = h\left(T_{ref} - T_w\right) \tag{4.1}$$

An analogous approach is employed for the radiative heat flux computed by the radiation solver by means of a black-body model:

$$q''_{\text{rad}} = \epsilon\sigma_0\left(T_{rad}^4 - T_w^4\right) \tag{4.2}$$

defining an emission relaxation parameter ϵ and a reference radiative gas temperature T_{rad}. Therefore, a Robin BC is imposed at the solid boundaries whereas a Dirichlet BC is exploited for the CFD and radiation solvers by prescribing the wall temperature coming from the conduction solution. Even though the employed mixed Dirichlet-Robin BC does not ensure a conservative behaviour at the interfaces, it provides a stable coupling. The inaccuracies, however, are definitely below the global error of the methodology if a high coupling frequency is set. Concerning the volumetric quantities, the aero-thermal fields (i.e. gas pressure, temperature and composition) computed by the CFD solver are interpolated in the radiative domain on which the RTE is solved. The resulting energy source/sink due to absorption and emission phenomena is returned to the flow field calculation and added to the energy transported equation. The solver communication occurs by the use of User Defined Functions (UDFs) employed to handle the synchronization together with Scheme scripts to provide the exchange of interface data.

In addition to being able to adopt different time-step sizes for the convective and conductive solvers with a strong reduction of the computational time of the CHT simulation, U-THERM3D procedure allows to optimize each simulation in terms of numerical domain, setup and computational grid. In particular, it is possible to compute the numerically-expensive radiative calculation in a steady manner on a coarser mesh compared to the fluid solver one. Moreover, it generally includes only the combustor flametube where the impact of radiation is more significant. Finally, computing separately each heat transfer mode, the in-house loosely coupled strategy permits a deep investigation of the effects of wall and radiative heat losses on the aero-thermal fields of the considered combustor device with affordable computational costs, as it will show in the following.

4.3.1 Effusion holes solver

As mentioned at the beginning of this chapter, simplified CFD techniques are required when an effusion cooling system is included in the investigated numerical domain in order to minimize the computational efforts related to a full-discretized approach for the effusion holes. Here, a brief description of the native effusion holes solver integrated in U-

THERM3D is provided. It is worth to underline that this methodology represents the starting point for the novel effusion model developed in the framework of this research work and presented in the following sections.

The pre-existing effusion model is based on the imprinted technique [128] and it is coupled with the fluid flow and solid solvers from a thermal point of view, as depicted in Figure 4.5. According to this technique, the effusion holes are not discretized and replaced by an inlet and an outlet boundary conditions respectively on the hot and cold sides, as shown in Figure 4.6.

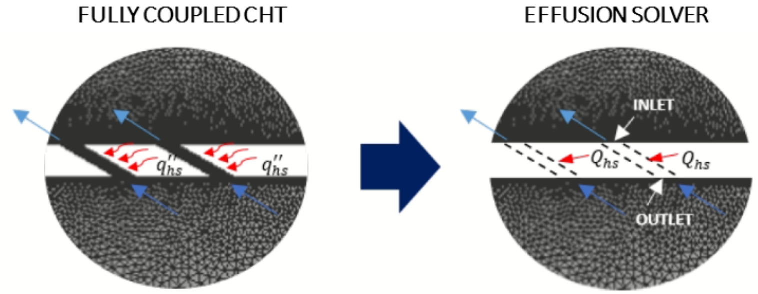

Figure 4.6: Imprinted effusion model integrated within U-THERM3D (adapted from [14]).

A Fluent UDF is employed to compute the gas temperature at the inlet boundary of the fluid domain by taking into account the heat sink effect computed by means of the following expression:

$$Q_{EFF} = HTC \cdot A_h \cdot \left(\bar{T}_{w,h} - \bar{T}_f\right) \tag{4.3}$$

where A_h is the internal hole area, $\bar{T}_{w,h}$ is the mean temperature on such area, HTC is the local HTC while $\bar{T}_f$ is the film temperature within the effusion hole, expressed as the mean between the outlet and the inlet coolant temperatures. A proper correlation provides the HTC value and, in this sense, the Gnieliski correlation [129] is generally used for aeroengine combustor applications. In this case, the related Nusselt number Nu_D is expressed as:

$$Nu_D = \frac{(f/2)\,(Re_D - 1000)\,Pr}{1 + 12.7(f/2)^{1/2}\,(Pr^{2/3} - 1)} \left[1 + \left(\frac{D}{l}\right)^{2/3}\right] \tag{4.4}$$

where Re_D is the Reynolds number based on hole diameter D, l is the hole length and f is the Fanning friction factor [130] that depends on Re_D:

$$f = [1.58 \ln (Re_D) - 3.28]^{-2} \tag{4.5}$$

The resulting inlet gas temperature is thus imposed on the relative boundary condition in the fluid flow simulation. The mass flow rate through each hole derives from a flow split assumption or from a previous resolved simulation whereas uniform components are prescribed for the injection velocity components, according to the effusion holes geometry.

4.4 State of the art on effusion modelling

Several approaches have been developed in which the effusion holes are not generally included in the computational domain and replaced with properly computed sources. One of the first coolant injection models was proposed by Crawford et al. [131] in which a 2D boundary layer code is employed for introducing coolant at each row of holes together with a turbulence augmentation model for simulating the shear layer interaction within the boundary layer. However, many authors have proposed to take into account the presence of effusion holes through the use of point or volumetric sources. Distributed volumetric sources of mass, momentum, energy and turbulence quantities in a layer with a thickness of the order of the hole diameter above the wall were employed by Heidmann and Hunter [132] as an improvement for coarse mesh grids of the model proposed by Hunter [133] in which the source terms were applied in the first grid cell. A different location for the application of such source terms was detected by Burdet et al. [134] through the use of a plane of injection located downstream the hole exit (see Figure 4.7) in order to consider the blockage effect related to the coolant jet, obtaining a good agreement with experimental data.

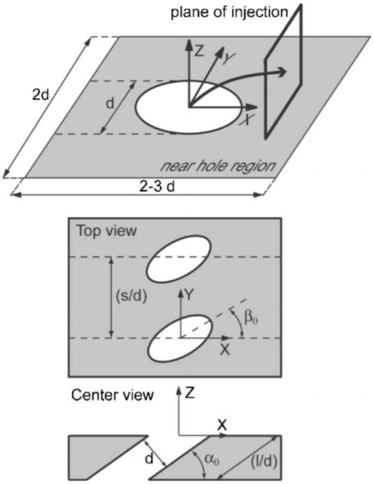

Figure 4.7: Plane of injection in Burdet et al. model [134].

In this case, the effusion model is embedded in a CFD code using the implicit immersed boundary method and a set of submodels provides the trajectory, the mixing and the secondary flows of the jet starting from several flow parameters, such as injection angle and momentum flux ratio. Volume sources are also employed in the model developed by auf dem Kampe and Völker's [135] within the commercial code ANSYS CFX, getting good results in comparison with detailed CFD calculations and experimental measurements. Here, the sources are located in a confined volume at hole outlets, as shown in Figure 4.8, computing their fluid dynamics characteristics through correlations based on several film cooling parameters.

Also the model proposed by Voigt et al. [136] and further developed by Andreini et al. [137] was implemented in ANSYS CFX, accounting for the effusion cooling through point sources for coolant aspiration and injection, as reported in Figure 4.9. In this case, efforts were devoted to model the heat sink effect within the holes, an effect which is mandatory

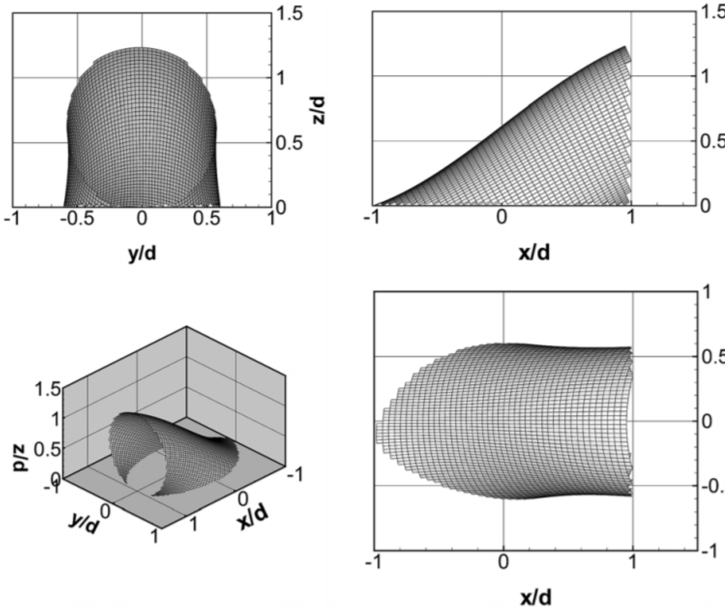

Figure 4.8: Example of a source volume envelope in auf dem Kampe and Völker's model [135].

to take into account in a CHT simulation. In the DLR approach, a preliminary detailed simulation of a single hole allows to specify source values, in terms of mass flow rate, velocity components, total temperature and turbulence quantities, in addition to the heat sink. On the contrary, the UNIFI model, named SAFE (Source bAsed eFfusion modEl), employs a local pressure drop dependent formulation for the automatic calculation of the mass flow rate through each hole and a correlation for the Nusselt number to compute the in-hole heat pick-up, introducing therefore a strongly saving of computational resources.

Both models show a good accuracy and agreement with experimental data in the context of both effusion cooled flat plates [136, 138] and complex configurations, such as an actual combustor test rig [137]. An

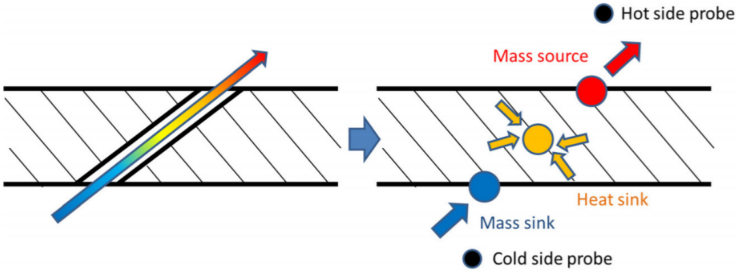

Figure 4.9: Conceptual representation of Andreini et al. effusion hole modelling [137].

evolution of the UNIFI approach and, at the same time, a simplification with respect to auf dem Kampe and Völker's model was proposed by Andrei et al. [139]. In this case, a volume affected by the jet near the hole outlet is identified and constant source terms (calculated from in-house developed correlations) are computed in the transport equations of mass, momentum and energy and located within the injection volume. Model results were compared to experimental data and numerical results (obtained with complete cooling holes meshing) on several test cases reproducing flat plate cooling configurations for different coolant conditions, proving the feasibility of the procedure.

Differently from the previous models, the application of homogeneous boundary conditions on both hot and cold sides of multi-perforated liners is the main idea on which the approach proposed by Mendez and Nicoud [140] is based, reproducing the average effect of an effusion cooling system and allowing to employ coarse grids. In this model, the effusion plate is considered as a porous plate where the coolant is injected through its whole surface with an uniform velocity, computed in order to respect the mass and momentum fluxes across the boundary. The numerical approach is able to reproduce the global structures in a RANS framework, considering also complex geometries representative of real gas turbine combustors.

However, the use of specific boundary surface sources located in correspondence of hole imprints on the liner is particularly interesting, since it allows to take into account the real shape of effusion holes, they take advantage from grid resolution improving the mixing representation and, ultimately, these approaches are easier to implement in a CFD code and computationally more robust. In this context, the imprinted effusion model was developed by Rida et al. [128]. The main idea is to imprint the effusion holes on the liners, ensuring the geometric fidelity as highlighted by Figure 4.10, and to apply a mass flow outlet condition on the cold side and a mass flow inlet condition on the hot side, according to Bernoulli's equation and to a proper discharge coefficient. Good level of accuracy have been obtained in both steady and unsteady simulations.

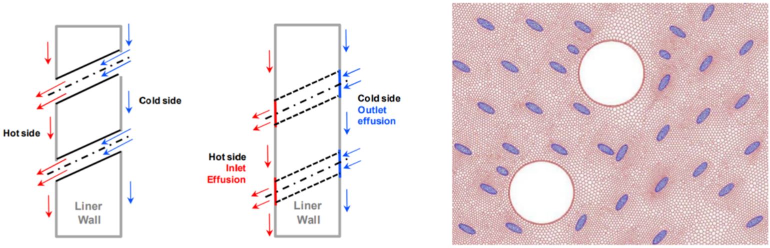

Figure 4.10: Illustration of the imprinted effusion concept of Rida et al. [128].

Instead, Lahbib [141] and Bizzarri et al. [142] overcame the drawbacks of Mendez and Nicoud's approach [140] with the heterogeneous model in which an automatic thickening of the hole dimension is provided where the mesh is too coarse. An example of this methodology is illustrated in Figure 4.11. Similar formulations were employed to ensure proper mass and momentum fluxes. In [143], the homogeneous and the heterogeneous models are applied and compared in a LES framework on a combustor simulator, resulting in a more realistic representation of the film cooling for the Lahbib and Bizzarri approaches with a reasonable level of additional cost.

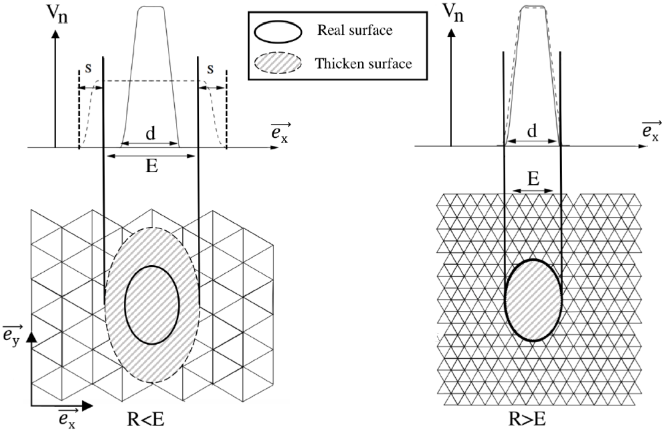

Figure 4.11: Thickened-hole model developed by Bizzarri et al. [142].

Nevertheless, in all the presented boundary sources approaches, uniform profiles for velocity and turbulence quantities are employed at hole outlets to model the coolant injection. As discussed in Chapter 3, the JICF presents characteristic vortical structures whose evolution strongly depends on the flow field at hole exit. Therefore, its proper computation is mandatory for an accurate computation of the jet interaction and mixing with the cross-flow.

For this purpose, a new effusion model which is able to predict 2D velocity and turbulence profiles depending on the operating conditions of the investigated effusion cooling system is presented in the framework of this research work. This novel approach is based on the combination of Reduced-Order (RO) and Regression methodologies applied to the results of a Design of Experiment (DoE) carried out on a single effusion hole. This leads to the development of a Surrogate Model (SM) which can properly predict the flow fields at the hole outlet, starting from a limited number of CFD simulations. In the context of this work, Principal Component Analysis (PCA) is combined with Kriging within a MATLAB code which is then coupled with the CFD solver in the U-THERM3D structure.

PCA is a statistical technique employed to represent a data-set of several inter-correlated dependent variables with an ensamble of orthogonal low-dimensional basis functions by extracting the invariant physics-related information of the considered system (Principal Components-PCs) and identifying the system's coefficients which, instead, are related to the operating conditions (PCA scores) [144]. Then, Kriging is employed to generate a meta-model for the scores. The combination of the PCs and of the meta-models for the PCA scores allows to predict the desired variables (velocity and turbulent quantities in this case) at unexplored conditions. This kind of modelling has been already applied for combustion problems [145] and for the development of digital twins of realistic engineering systems for visualization, real-time control, optimization and troubleshooting [146, 147] with good results in terms of accuracy and computational efficiency. To authors' knowledge, no works can be found in technical literature on the application of such approach to model coolant injection in effusion cooling systems. Therefore, the objective of the present work is to extend its application to the effusion modelling in order to overcome the lacks of the state-of-the-art effusion models and to develop a robust numerical tool to be coupled with a CFD solver to improve and speed up the design process of aeroengine combustors.

4.5 Description of the novel effusion model

In the following, the proposed effusion model is described together with the coupling strategy with the CFD solver in the U-THERM3D architecture. In addition, a brief description is reported about the theoretical and mathematical fundamentals on which the employed RO and Regression methodologies are based.

4.5.1 Principal Component Analysis

PCA is a dimensionality reduction technique with the main aim of representing a certain data-set of observations of several inter-correlated dependent variables with its projection on a reduced number of new orthogonal low-dimensional basis functions, called Principal Components (PCs) or PCA modes [144], as shown in Figure 4.12.

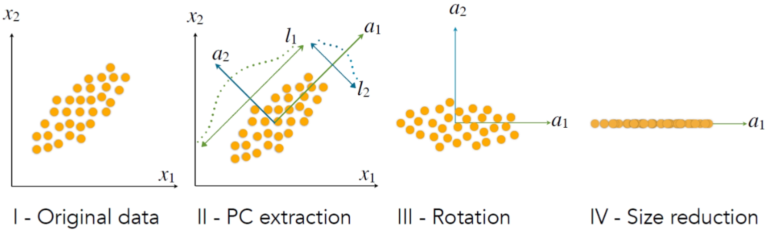

Figure 4.12: An example of PCA application on a 2D data-set, where the yellow circles are the observations whereas a_1 and a_2 are two PCA modes.

In this sense, PCA is an adaptive data analysis technique since the new variables (PCs) are related to the considered data-set and not defined *a priori*. The orthogonal basis functions allow retaining as much as possible of the original data variance, improving the interpretability of the data table by extracting only the most important features but, at the same time, minimizing information loss. In fact, starting from the first one, each principal component is computed under the constraint of representing the largest possible variance (or inertia) of the data-set and of being orthogonal to the previously calculated components [148]. Projecting the observations onto the basis functions, PCA scores are derived. In order to compute these features, an eigenvalue/eigenvector problem is solved, applying the Singular Value Decomposition (SVD) to a covariance matrix associated with the data-set [144]. Consequently, the PCA provides a transformation of the original data space to a linear combination of PCA modes and scores, permitting the detection of particular structures between the variables of the original multidimensional data-set.

Supposing to have a Full Order Model (FOM), a data table $\mathbf{Y}(n \text{ x } m)$ of m observations of n physical variables can be written as:

$$\mathbf{Y}(\mathbf{X}) = F(\mathbf{X}) \tag{4.6}$$

where F is the considered detailed model (i.e. CFD solver) whereas $\mathbf{X}$ represents the input parameters in the model space (i.e. the employed boundary conditions in a CFD simulation). Generally, a centering and a scaling operations are applied to the data table which can strongly affect the computed low-dimensional basis functions and, as a consequence, the quality of features retrieved [149, 150]:

$$\mathbf{Y}_0 = \mathbf{D}^{-1}\left(\mathbf{Y} - \overline{\mathbf{Y}}\right) \tag{4.7}$$

where $\mathbf{D}$ represents a diagonal matrix of scaling factors whereas $\overline{\mathbf{Y}}$ is a matrix in which the means of each of the n variables over the m observations are collected. At this point, the SVD is applied to the covariance matrix $\mathbf{C}$ which can be written as:

$$\mathbf{C} = \frac{1}{m-1}\mathbf{Y}_0\mathbf{Y}_0^T \tag{4.8}$$

Since the covariance matrix $\mathbf{C}$ is symmetric and $rank(\mathbf{C}) = rank(\mathbf{Y}) = min(n, m)$, the eigenvectors are composed of real values and they are pairwise orthogonal when their eigenvalues are different [148]. A maximum number $p = rank(\mathbf{C})$ of PCA modes $\boldsymbol{\phi_i}$ (eigenvectors) can be retrieved by solving the following set of eigenproblems:

$$\mathbf{C}\boldsymbol{\phi_i} = \lambda_i\boldsymbol{\phi_i} \qquad \forall i = 1, 2, ..., p \tag{4.9}$$

together with the related eigenvalue λ_i which is an index of the original data variance associated to each mode [148]. As a consequence, a n x p matrix $\mathbf{\Phi}$ can be defined as:

$$\mathbf{\Phi} = \{\boldsymbol{\phi_1}, \boldsymbol{\phi_2}, ..., \boldsymbol{\phi_p}\} \tag{4.10}$$

in which PCs are arranged in order of importance. The importance is related to the variance (or inertia) of the original data taken into account by each mode and encoded by the associated eigenvalue λ_i. In this sense, only the first PCA modes can be considered for a satisfactory representation of the original data, since the contributions of the others to the reconstruction are gradually negligible. At this point, the matrix $\mathbf{Y}_0$ can be projected onto the PCs to obtain the m x p matrix $\mathbf{S}$ of PCA scores such that:

$$\mathbf{S} = \mathbf{Y}_0 \mathbf{\Phi} \tag{4.11}$$

Therefore, by applying the PCA reduction, it is possible to obtain the closest rank-p approximation of the original matrix $\tilde{\mathbf{Y}}$ as:

$$\mathbf{Y} = \overline{\mathbf{Y}} + \mathbf{D}\mathbf{Y}_0 \approx \overline{\mathbf{Y}} + \mathbf{D}\mathbf{\Phi}\mathbf{S} = \tilde{\mathbf{Y}} \tag{4.12}$$

considering that $\mathbf{Y} = \{\mathbf{y}_1, \mathbf{y}_2, ..., \mathbf{y}_m\}$ is the data-set, $\mathbf{S} = \{\mathbf{s}_1, \mathbf{s}_2, ..., \mathbf{s}_p\}$ is the matrix where the computed PCA scores are collected and where each coefficient is a function of the input parameter space $\mathbf{X} = \{\mathbf{x}_1, \mathbf{x}_2, ..., \mathbf{x}_m\}$ of the FOM.

4.5.2 Kriging

Since PCs are invariant whereas PCA scores depend on the input parameter space $\mathbf{X}$, an efficient regression technique must be employed for an estimation of the values of the second ones at unexplored conditions $\mathbf{x}^*$ and, therefore, for a proper prediction of the new data-set of original variables as a linear combination of invariant PCA modes and predicted PCA scores.

In this context, Kriging or Gaussian Process Regression (GPR) is a method of interpolation for which the interpolated values can be described by a Gaussian distribution [151, 152], where the estimated value of the considered function at a given point is computed as a weighted average of the known values of the function in the neighborhood of that point, as highlighted by the example reported in Figure 4.13. In fact, considering the vector of m observations $\mathbf{Y} = \{\mathbf{y}_1, \mathbf{y}_2, ..., \mathbf{y}_m\}$ and the input parameter space $\mathbf{X} = \{\mathbf{x}_1, \mathbf{x}_2, ..., \mathbf{x}_m\}$ of v input variables on which the data-set $\mathbf{Y}$ depends, the main idea is that each observed data follows a Gaussian process. In this framework, it can be expressed as a combination of a *trend function* $\mu(\mathbf{x})$ and a *residual* or *random function* $r(\mathbf{x})$ with zero

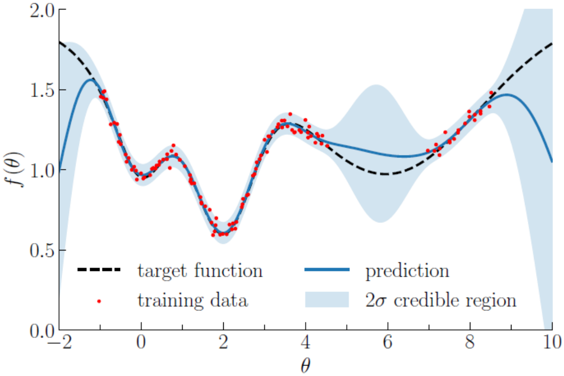

Figure 4.13: Representation of a Kriging regression for a one-dimension function [153]. The blue line is the mean prediction of the computed regression whereas the shaded region highlights the related uncertainty.

mean and standard deviation $\sigma(\mathbf{x})$ [154]:

$$\mathbf{Y}(\mathbf{X}) = \mu(\mathbf{X}) + r(\mathbf{X}) \tag{4.13}$$

$$E[r(\mathbf{X})] = 0 \tag{4.14}$$

$$\sigma(\mathbf{X}) = \sqrt{\mathrm{Var}(r(\mathbf{X}))} \tag{4.15}$$

The trend function is usually computed as a linear combination of $p+1$ polynomial functions $\mathbf{f}(\mathbf{X}) = \{\mathbf{f}_0(\mathbf{X}), \mathbf{f}_1(\mathbf{X}), ..., \mathbf{f}_p(\mathbf{X})\}^T$ with coefficients $\mathbf{a} = \{\mathbf{a}_0, \mathbf{a}_1, ..., \mathbf{a}_p\}^T$ obtained through a Generalized Least Squares (GLS) technique:

$$\mu(\mathbf{X}) = \sum_{l=1}^{k} \mathbf{a}_l \mathbf{f}_l(\mathbf{X}) \tag{4.16}$$

Since the shape of the target function in certain unexplored locations is influenced by its known values in the space around those locations, the coefficient $\mathbf{a}_l$ depends on the mutual covariances between data points:

$$C_{i,j} = \mathrm{Cov}\left(Z\left(\mathbf{x}_i\right), Z\left(\mathbf{x}_j\right)\right) \tag{4.17}$$

and on the covariances between data points and the target unexplored points $\mathbf{x*}$:

$$c_i = \mathrm{Cov}\left(Z\left(\mathbf{x}_i\right), Z(\mathbf{x}^*)\right) \tag{4.18}$$

Generally, a *covariogram model* or *kernel* or *correlation function* is employed to approximate these unknown covariances, modelling them and, so, the residual function $r(\mathbf{x})$ as a Gaussian process through a set of hyper-parameters $\mathbf{\Psi}$ computed by a Maximum Likelihood Estimation (MLE) [154].

In the context of this work, the target function is the matrix $\mathbf{S} = \{\mathbf{s}_1(\mathbf{x}), \mathbf{s}_2(\mathbf{x}), ..., \mathbf{s}_p(\mathbf{x})\}$ of PCA scores in the input parameter space spanned by $\mathbf{X}$. Consequently, the new value of the $i-th$ PCA score $\mathbf{s}(\mathbf{x}^*)$ at unexplored conditions $\mathbf{x}^*$ is expressed as a combination of a trend function and a residual [155]:

$$\mathbf{z}(\mathbf{x}^*) = \mu(\mathbf{x}^*) + r(\mathbf{x}^*) = \sum_{i=0}^{p} a_i f_i(\mathbf{x}^*) + r(\mathbf{x}^*) = \mathbf{f}^T(\mathbf{x}^*)\mathbf{a} + r(\mathbf{x}^*) \tag{4.19}$$

where $\mu(\mathbf{x}^*)$ is generally a low-order polynomial regression which globally approximates the objective function in the input parameter space whereas $r(\mathbf{x}^*)$ gives rise to local deviation, relying on the distance of the observations in the training set to the target point $\mathbf{x}^*$ and interpolating them [145, 156].

In comparison with other meta-modeling techniques such as polynomial, regression splines, radial basis functions and artificial neural network, Kriging is a very efficient interpolation technique since:

- the type and the number of input variables do not affect the construction of the surrogate model [157];
- a wide range of functions can be efficiently approximated;
- an index of the uncertainty in the form of a standard deviation is provided together with the predicted value;
- according to the data-set type, the user can choose the polynomials $\mathbf{f}(\mathbf{x})$ and covariogram model, adding prior knowledge into the

problem [145].

4.5.3 Effusion model

As said before, the results of a DoE carried out on a single effusion hole geometry have been used for the development of the presented effusion model. Referring to Section 4.5.1, the CFD solver employed for the sampled simulations represents the FOM whereas the vector $\mathbf{X} = \{\mathbf{x}_1, \mathbf{x}_2, ..., \mathbf{x}_m\}$ encodes the set of input parameters values (geometrical and fluid dynamics quantities) on which the DoE is based. In the context of this manuscript, four input parameters have been considered to generate the computed simulations, as explained in the following: the inclination angle α, the ratio between the length and the diameter of the hole L/D, the BR and the DR. For each $\mathbf{x}_i$, a vector $\mathbf{y}_i$ of observations of certain physical variables of interest is computed by the FOM. In the present work, these variables are the three velocity components V_x, V_y, V_z and the turbulent quantities k, ω profiles extracted in proximity of the hole outlet, as highlighted by Figure 4.14. In order to take into account the different shape of the hole imprint as the geometrical characteristics of the effusion hole change, the extracted profiles are interpolated on a dynamic rectangular mesh grid including the hole imprint during a pre-processing phase.

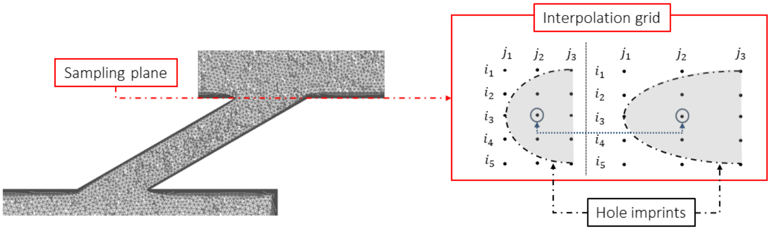

Figure 4.14: Interpolation on a dynamic rectangular grid of a 2D profile extracted from a CFD simulation.

This allows a consistent comparison between the distributions obtained from different sampled simulations since the grid points with equal indices are characterized by analogous flow conditions in the interpolated maps. Therefore, the vector $\mathbf{y}_i$ can be written for each physical variable of interest as:

$$\mathbf{y}_i = \left[V_x \left(g_1, \mathbf{x}_i \right), \ldots, V_x \left(g_L, \mathbf{x}_i \right) \right]^T \tag{4.20}$$

where L is the total number of interpolation grid points, g_j is the j-th spatial location and $\mathbf{x}_i$ is the i-th array of input parameters values. Considering m simulations (or observations) computed by the FOM, $\mathbf{Y} = \{\mathbf{y}_1, \mathbf{y}_2, ..., \mathbf{y}_m\}$ represents the data-set on which the PCA will be applied. In this way, the original variables are projected on a set of basis functions $\mathbf{\Phi} = \{\boldsymbol{\phi_1}, \boldsymbol{\phi_2}, ..., \boldsymbol{\phi_p}\}$ with $p < m$, the PCA modes, which do not depend on the DoE input parameters $\mathbf{X}$. At the same time, PCA scores $\mathbf{S}(\mathbf{X}) = \{\mathbf{s}_1(\mathbf{X}), \mathbf{s}_2(\mathbf{X}), ..., \mathbf{s}_p(\mathbf{X})\}$ are the result of this projection and, differently from PCs, they represent the system-dependent information, varying with $\mathbf{X}$. Therefore, PCA modes are computed for each physical variable of interest, defining also the related PCA scores. At this point, a response surface for each PCA score is computed by applying Kriging interpolation and p meta-models are generated for each variable of interest, according to Equation 4.19. Then, the meta-models can be employed to predict the new PCA scores at unexplored input parameters values $\mathbf{x}^*$. The described approach provides a limit number of meta-models (p equal to PCA modes/scores number) with a consequent lower complexity of the compressed data and a lower computational cost. Moreover, using PCA scores as bases for the generation of meta-models allows to preserve the correlation between the original variables which could be lost if different interpolations are performed separately for each physical variable of interest [145].

The set of PCA modes and meta-models for the prediction of PCA scores at unexplored conditions constitutes the effusion model created within MATLAB during a pre-processing phase. Afterwards, the MATLAB code is coupled with the CFD solver within U-THERM3D architecture and the input parameters values are extracted run-time from the CFD simulation. In Figure 4.15, a schematic representation of the employed procedure is depicted.

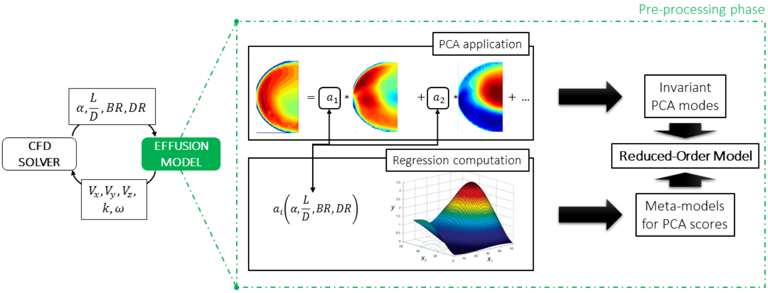

Figure 4.15: Reduced-Order Model generation and coupling strategy.

Such values are passed to the effusion model which predicts the desired velocity and turbulence profiles at hole outlets as a linear combination of invariant PCA modes and predicted PCA scores according to the effusion system operating conditions. The computed profiles are imposed as boundary conditions within the CFD solver at hole imprints on the hot side, since the holes are not discretized as depicted in Figure 4.10. In the framework of this coupling, the cycle continues until the numerical simulation is converged. In order to be conservative, the imposed profiles are scaled on the mass flow rate through each hole which is calculated in agreement with discharge coefficient definition:

$$\dot{m} = C_D \dot{m}_{is} \tag{4.21}$$

with:

$$\dot{m}_{is} = P_0 \left(\frac{P}{P_0}\right)^{\frac{\gamma+1}{2\gamma}} \sqrt{\frac{2\gamma}{(\gamma-1)RT_0}\left[\left(\frac{P_0}{P}\right)^{\frac{\gamma-1}{\gamma}} - 1\right]} \frac{\pi}{4} D_h^2 \tag{4.22}$$

where the coolant and main flow conditions are computed run-time in correspondence of the inlet and the outlet of the effusion hole through proper probe locations which are also employed for the computation of local BR and DR. These parameters together with the α and L/D values are required as input parameters of the ROM for the prediction of velocity and turbulence profiles at injection locations.

4.6 Final remarks

This chapter described the numerical tools employed for the CHT analyses reported in this manuscript and for the development of an innovative model for effusion cooling holes. The latter allows the run-time calculation of the mass flow rate through effusion holes, depending on local fluid dynamics conditions together with the prediction of the aerodynamics profiles (velocity and turbulent quantities) at hole outlets on which the accurate estimation of JICF phenomenon depends.

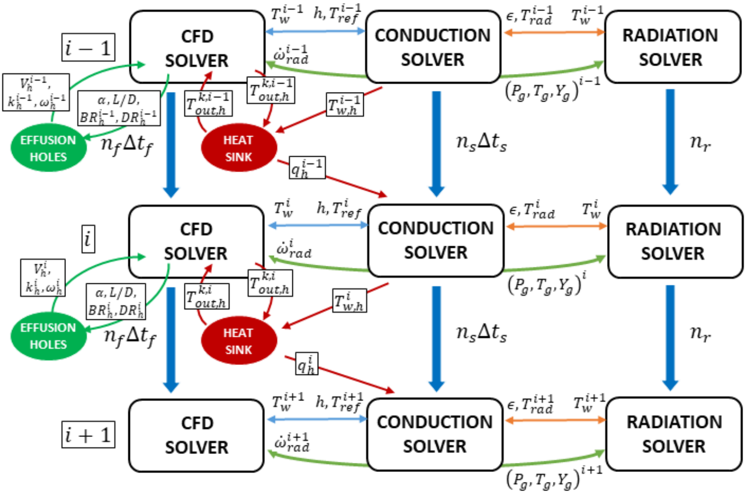

Figure 4.16: Revised U-THERM3D parallel coupling strategy (adapted from [14]).

Figure 4.16 shows the revised U-THERM3D parallel coupling strategy after the introduction of the novel effusion model developed within MATLAB. It is worth to notice that the heat sink model employed for the computation of the coolant temperature at hole outlets is now complemented by the MATLAB code for the calculation of the aerodynamics fields. It is worth mentioning that this kind of approach can be extended by taking into account different operating parameters of the effusion cooling system but also different effusion hole geometry (i.e. shaped holes), simply adapting the DoE to the desired objectives.

Chapter 5

DLR confined pressurized burner

In this chapter, the loosely coupled multiphysics tool U-THERM3D developed by Bertini [14] and based on the modelling strategies described in Chapter 4 is employed for a detailed numerical investigation of wall and radiative heat losses effect on a model aeroengine combustor, developed and experimentally investigated in the framework of the EU-funded project FIRST by Geigle et al. [158, 159] at the Deutsches Zentrum für Luft-und Raumfahrt (DLR). This experimental test rig is characterized by a wide range of experimental measurements under isothermal and reactive conditions in terms of velocity and temperature distributions as well as soot mass concentration within the combustion chamber.

According to [158, 159], the typical features of a RQL technology can be identified, representing a real aeroengine technology. In this sense, the combustor is characterized by high level of soot production in the primary rich zone. The formation of such carcinogenic particles is a consequence of complex chemical processes which are highly sensitive to the temperature distribution that, in turn, depends on mixing, radiative heat transfer and on soot volume fraction itself, leading to a very challenging coupled problem. Therefore, a reliable computation of the reactive flow field and a proper prediction of the contributes of all heat transfer mechanisms are mandatory for an accurate estimation of heat loads on combustor walls. The specific goal of this numerical investigation is to prove that the in-house procedure U-THERM3D permits a reliable prediction of wall temperature and that it can be used, as a long-term objective, as an advanced numerical tool to gain fundamental knowledge on turbulent flames with high-fidelity prediction of combustion and near-wall processes in an unsteady CHT simulation framework with an acceptable computational cost for an industrial context. Moreover, this approach allows to split the contribution of different heat transfer mechanisms on the aero-thermal fields, providing a deep understanding of their complex interactions.

First of all, the experimental test case is presented together with the description of the employed mathematical models and computational setup. Due to the very interesting experimental data, several numerical studies have been carried out by many authors and, so, a brief literature review about them is also provided. Then, numerical results are shown and compared against experimental data. For a thorough investigation, cold flow results are firstly reported in order to underline the importance of an accurate prediction of general flow features, such as the swirling and the recirculating flows in the primary zone, as well as the fraction of the secondary oxidation air that is transported upstream and downstream. Then, several details of the computed aero-thermal fields in the reactive simulations are provided, focusing the attention on velocity, temperature and soot fields of gas phase and considering the critical flow features which influence the reacting mixture behaviour. In this context, a comparison between experimental measurements and the results of four different reactive simulations is reported:

- a coupled reactive RANS, performed with the steady-state THERM3D approach developed by Mazzei [127] (RANS T3D, from now on);
- an adiabatic reactive LES (LES adiab);
- a coupled reactive LES without radiation modelling, (LES noRad);
- a fully-coupled reactive LES with radiation modelling, (LES UT3D).

Afterwards, the attention is focused on the U-THERM3D validation through the comparison of the predicted wall temperature obtained in LES UT3D simulation with the experimental data. It is worth specifying that all reactive unsteady simulations were performed employing the U-THERM3D procedure, deactivating the coupling with the solid domain for the adiabatic calculation and, instead, not considering the radiative solver for the LES noRad simulation. In order to avoid any misunderstanding and for a better readability of the results, a summary of the reported computational cases is highlighted in Table 5.1.

Table 5.1: Simulations Summary.

Case	Simulation Type	Turbulence Model	Combustion Model	Conduction Solver	Radiation Solver
1	Cold RANS	Realiz. k-ϵ	Disabled	Disabled	Disabled
2	Cold LES	Dyn. Smagorinsky	Disabled	Disabled	Disabled
3	THERM3D RANS	Realiz. k-ϵ	Enabled	Enabled	Enabled
4	Adiabatic LES	Dyn. Smagorinsky	Enabled	Disabled	Enabled
5	No Radiation LES	Dyn. Smagorinsky	Enabled	Enabled	Disabled
6	U-THERM3D LES	Dyn. Smagorinsky	Enabled	Enabled	Enabled

5.1 Presentation of the test case

In the following, a brief recap of the principal characteristics of the considered test case is reported. For a detailed description of the experimental setup and of the investigated operating conditions, the reader may refer to [158] and references therein. In Table 5.2, the conditions of the operating point studied in the present numerical investigation are summarized and they will be employed for both the non-reactive and the reactive cases.

A sketch of the main geometrical features is reported in Figure 5.1. The combustion chamber has a square section of 68x68 mm^2 and its height is 120 mm. The combustion chamber is surrounded by a stainless-steel pressure housing. Combustor and housing walls consist of quartz windows mounted between four water-cooled metal posts in order to ensure optical access within the combustion chamber to collect the experimental data. A cylindrical exhaust tube is located at the top of the test rig, connected to the combustion chamber through a curvature. Consequently, this region

Table 5.2: Investigated operating conditions.

Operating pressure	3	[bar]
Equivalence ratio Φ	1.2	[-]
$Q_{air,primary}$	140.8	[slm]
$T_{air,primary}$	300	[K]
$Q_{air,secondary}$	187.4	[slm]
$T_{air,secondary}$	300	[K]
Q_{fuel}	39.3	[slm]
T_{fuel}	300	[K]
Fuel composition	C_2H_4	[-]

is characterized by high velocity which prevents any backflow.

Three concentric nozzles form the burner. Primary air is supplied through a dual radial swirler. The inner swirler has a Swirl Number $SN = 0.82$ and consists of 8 vanes, whereas the outer one is composed of 12 vanes ($SN = 0.78$). This configuration generates a recirculation zone and a highly turbulent region next to the injector outlet. An additional system of ducts for the injection of dilution air, used to quench the reaction zone, is located at each of the four corners of the combustion chamber 80 mm downstream the swirler exit plane. Ethylene is injected by means of a concentric ring of 60 equally spaced straight channels between the

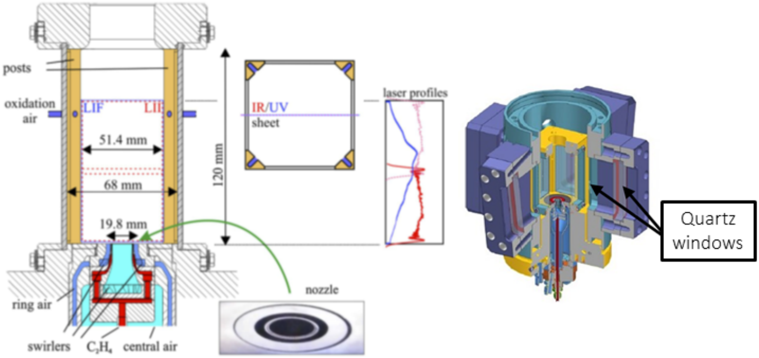

Figure 5.1: DLR-FIRST burner (adapted from [158] and [159]).

internal and the external air channels.

As far as the experimental campaign is concerned, available data consist of measurements in terms of velocity components with Stereo-PIV (Particle Image Velocimetry), temperatures with SV-CARS (Shifted Vibrational Coherent Anti-stokes Raman Scattering) [159] and in terms of soot volume fraction adopting LII (Laser-Induced Incandescence) [158].

5.2 Review of previous numerical works

Several works in technical literature have dealt with numerical investigations of aero-thermal fields of the considered combustor in a LES framework with significant differences regarding soot modelling. A two-equation soot model was employed by Franzelli et al. [160] and by Eberle et al. [161]. In the first work, a reasonable agreement is achieved in terms of gas temperature whereas soot levels are under-predicted due to the very simple soot model which has been employed. In the second one, an additional sectional approach was also used for the computation of PAH concentration, obtaining a significant qualitative and quantitative improvements in the computation of soot distribution within the combustion chamber. Another main outcome of this work is the strong anti-correlation of OH and soot species together with the necessity of an accurate description of turbulent structures of the flame as computed by LES approach in order to properly predict the distributions of these species.

Grader et al. [162] extended the sectional approach also to the computation of the soot distribution, considering each soot section as monodisperse. Different levels of agreement have been achieved depending on the investigated operating conditions, highlighting a too fast soot oxidation in the secondary region of the combustor.

More detailed soot models have been adopted by Koo et al. [163], Chong et al. [164] and Pitsch et al. [165], where a detailed investigation on the complex phenomena related to soot formation and on their impact on gas phase fields was performed through a Method of Moments (MoM) approach. Koo focused the attention on the spatial and temporal intermittency of soot formation due to the trajectories followed by the soot particles and that soot particle growth occurs only in a small portion of the combustor with suitable conditions. According to this, Chong investigated the dilution effects on soot formation, revealing that such intermittency promotes the soot growth especially for particles entrained in the Inner Recirculation Zone (IRZ). The reader interested into more details about these numerical works is addressed to the mentioned references.

However, with the exception of the work of Rodriguez [166], no information have been provided about heat fluxes on combustor walls and how these affect the radiative heat transfer and the soot generation. All the previous works have been indeed carried out with adiabatic walls boundary condition [160, 164, 165] or by imposing fixed wall temperatures on solid boundaries according to experimental measurements [161, 162, 167]. This motivates the present investigation that is aimed at presenting and assessing the in-house loosely coupled multiphysics approach to obtain a reliable prediction of wall temperatures for the DLR burner, employing a scale-resolving methodology, together with an analysis of the effect of radiative and wall heat losses. In this sense, preliminary assessments of the steady version of the in-house numerical tool (THERM3D) has been performed by the author of the present manuscript and reported in [168, 169], comparing the loosely coupled simulations with experimental data and with the numerical results of a simulation carried out with the standard direct coupling approach. Moreover, a sensitivity to radiation and soot modelling is also reported in [169] as a preliminary investigation for the unsteady results shown in the following. These results have highlighted the necessity to take into account the radiative heat transfer which is strongly coupled with soot production, affecting both temperature and soot volume fraction fields. In terms of wall temperature prediction, lower values have been observed with respect to experimental measurements due to the employed steady approach which fails in the computation of the flow radial spreading and of the flame-wall interaction, underlining that a scale-resolving approach is mandatory.

5.3 Numerical details

All the simulations here reported were carried out with the commercial code ANSYS Fluent 2019R1® [170]. The main aspects of the modelling approach are reported below.

5.3.1 Turbulence modelling

The compressible Navier Stokes Equations (NSEs) have been solved employing a LES turbulence modelling by using the Dynamic Smagorinsky model [171] for the closure of the sub-grid stress tensor. In this approach, the eddy viscosity μ_t is related to the resolved strain rate $\overline{S}$ as:

$$\mu_t = \rho L_s^2 |\overline{S}| \tag{5.1}$$

Here, L_s and $\overline{S}$ are, respectively, the characteristic SGS mixing length and the traceless symmetric part of the square of the velocity gradient tensor defined as:

$$L_s = min\left(\kappa d, C_s V^{1/3}\right) \tag{5.2}$$

$$|\overline{S}| = 2\sqrt{\overline{S}_{ij}\overline{S}_{ij}} \tag{5.3}$$

where κ is the von Karman constant, d is the local distance to the closest wall, C_s is the Smagorinsky constant and V is the cell volume. C_s is dynamically computed based on the information provided by the resolved scales of motion.

5.3.2 Combustion modelling

As far as combustion modelling is concerned, the Flamelet Generated Manifold (FGM) model was adopted to describe the reactive flow behaviour and the flame characteristics, parametrizing the chemical state and reaction progress space only as function of two control variables, i.e. the mixture fraction Z and the normalized progress variable c [172] which has been defined as the sum of CO and CO_2 mass fractions divided by the local equilibrium value. A two-dimensional manifold $\phi(Z, c)$ of 64x64 points was built by solving non-premixed adiabatic 1D flamelets (opposed jets), varying the scalar dissipation rate from equilibrium up to extinction. The native built-in tool of ANSYS Fluent has been used to create the look-up table which reports the thermo-chemical state and the reaction progress as functions of the two control variables Z and c.

The turbulence-chemistry interaction is included through a presumed β Probability Density Function (β-PDF) approach for both mixture fraction and progress variable [173]. Assuming a statistically independence of Z and c in the flame, a generic turbulent quantity $\tilde{\psi}$ is computed as:

$$\tilde{\psi} = \int\int \psi(c, Z) P(\tilde{c}, \widetilde{c^{"2}}) P(\tilde{Z}, \widetilde{Z^{"2}})\, \mathrm{d}c\mathrm{d}Z \tag{5.4}$$

where $\psi(c, Z)$ is the corresponding laminar quantity. As shown in Equation 5.4, both mean values $(\tilde{\cdot})$ and variances $(\widetilde{\cdot''^2})$ relying on a Favre-averaging of mixture fraction and progress variable are employed to account for turbulence. As a result, a 4D tabulation is required for all the manifold quantities but a fifth dimension was added to include the non-adiabatic effects through an enthalpy defect strategy [174]. Once the values of these quantities have been computed, the manifold data are retrieved and an interpolation on tabulated values is performed.

Two additional transport equations have been solved for mean values of mixture fraction and un-normalized progress variable:

$$\frac{\partial \overline{\rho}\tilde{Z}}{\partial t} + \frac{\partial \overline{\rho}\tilde{u}_j\tilde{Z}}{\partial x_j} = \frac{\partial}{\partial x_j}\left(\overline{\rho}D_{eff}\frac{\partial \tilde{Z}}{\partial x_j}\right) \tag{5.5}$$

$$\frac{\partial \overline{\rho}\widetilde{Y}_c}{\partial t} + \frac{\partial \overline{\rho}\tilde{u}_j\widetilde{Y}_c}{\partial x_j} = \frac{\partial}{\partial x_j}\left(\overline{\rho}D_{eff}\frac{\partial \widetilde{Y}_c}{\partial x_j}\right) + \overline{\dot{\omega}}_c \tag{5.6}$$

where $\overline{\dot{\omega}}_c$ is the mean source term of progress variable provided by the PDF table. Unknown variances are computed by means of an algebraic gradient-based closure [174]:

$$\widetilde{Y_c^{"2}} = C_{var}\frac{L_s^2}{Sc_t}(\nabla\widetilde{Y}_c)^2 \tag{5.7}$$

$$\widetilde{Z"^2} = C_{var} L_s^2 (\nabla \widetilde{Z})^2 \tag{5.8}$$

where $C_{var,Z} = 0.5$ and $C_{var,c} = 0.1$ are model constants whereas Sc_t is the sub-grid turbulent Schmidt number equal to 0.7 for this work. Such approximation is widely exploited in literature for LES-FGM computations [175, 176, 177], being able to provide a good accuracy with a lower computational effort.

5.3.3 Soot modelling

In the reactive calculations, the presence of soot has been included through the Moss-Brookes model [178], where two transport equations for radical nuclei concentration and soot mass fraction are solved in order to model soot formation:

$$\frac{\delta\left(\rho b^*_{nuc}\right)}{\delta t} + \bigtriangledown \cdot \left(\rho \overrightarrow{v} b^*_{nuc}\right) = \bigtriangledown \cdot \left(\frac{\mu_t}{\sigma_{nuc}} \bigtriangledown b^*_{nuc}\right) + \frac{1}{N_{norm}} \frac{dN}{dt} \tag{5.9}$$

$$\frac{\delta\left(\rho Y_{soot}\right)}{\delta t} + \bigtriangledown \cdot \left(\rho \overrightarrow{v} Y_{soot}\right) = \bigtriangledown \cdot \left(\frac{\mu_t}{\sigma_{nuc}} \bigtriangledown Y_{soot}\right) + \frac{dM}{dt} \tag{5.10}$$

where M is the soot mass concentration and N is the soot particle number density. In Equation 5.9, the instantaneous production rate of soot particles is the result of two opposite contributions, nucleation from the gas phase (source) and coagulation in the free molecular regime (sink):

$$\begin{aligned} \frac{dN}{dt} = & \underbrace{C_\alpha N_A \left(\frac{X_{prec} P}{RT}\right)^l exp\left\{-\frac{T_\alpha}{T}\right\}}_{\text{Nucleation}} \\ & \underbrace{- C_\beta \left(\frac{24RT}{\rho_{soot} N_A}\right)^{1/2} d_p^{1/2} N^2}_{\text{Coagulation}} \end{aligned} \tag{5.11}$$

where C_α, C_β and l are model constants. The source term for soot mass concentration is affected by different mechanisms of nucleation (source), surface growth (source) and oxidation (sink):

$$\frac{dM}{dt} = \underbrace{M_P C_\alpha \left(\frac{X_{prec}P}{RT}\right)^l exp\left\{-\frac{T_\alpha}{T}\right\}}_{\text{Nucleation}}$$
$$+ \underbrace{C_\gamma \left(\frac{X_{sgs}P}{RT}\right)^m exp\left\{-\frac{T_\gamma}{T}\right\}\left[(\pi N)^{1/3}\left(\frac{6M}{\rho_{soot}}\right)^{2/3}\right]^n}_{\text{Surface Growth}} \tag{5.12}$$
$$- \underbrace{C_{oxid}C_\omega \eta_{coll}\left(\frac{X_{OH}P}{RT}\right)\sqrt{T}(\pi N)^{1/3}\left(\frac{6M}{\rho_{soot}}\right)^{2/3}}_{\text{Coagulation}}$$

where C_γ, C_{oxid}, C_ω, m and n are additional model constants. The employed values for the mentioned constants are reported in Table 5.3.

Table 5.3: Soot model constants.

C_α	C_β	l	C_γ	C_{oxid}	C_ω	m	n
54	1	1	11700	105.81	8903.51	1	1

It is worth to specify that the components of the source terms of each equation present a strong non-linear temperature dependence that highly affects soot distribution within the combustor. At the same time, it is important to note the source term dependence on the mole fraction of soot precursors. Therefore, a proper chemical description is crucial for a reliable prediction of soot distribution. The reaction mechanism for ethylene of Wang and Laskin [179] has been adopted in the present study, counting 75 species and 529 reactions.

5.3.4 Radiation modelling

In order to take into account the radiative heat transfer between solid and gas phases as discussed in Chapter 2, included the gas-gas and the solid-solid radiative interactions, the computation of the RTE should be carried out, employing a proper model for its resolution.

In this work, the Discrete Ordinate (DO) model has been adopted. It solves the RTE for a number of discrete solid angles, each related to a vector direction $\vec{s}$ projected in the spatial coordinates (x, y, z). Concerning this model [180], a transport equation for radiation intensity is solved for each discretized direction, as shown in Figure 5.2.

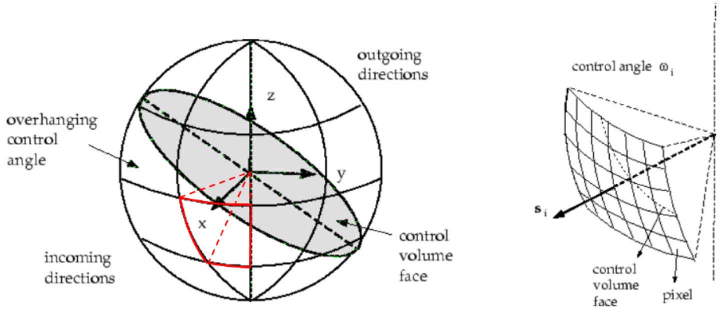

Figure 5.2: Discretization of the angular space and pixelation on a control angle overhang (adapted from [170]).

For the present study, a 4x4 angular discretization and a 3x3 pixelation for each direction have been employed. Finer discretizations were investigated in RANS context, highlighting negligible improvements in the results [181]. In addition, spectral radiation model has been included through a weighted sum of grey gases, employing Modest expression [49] to account for the presence of soot.

5.3.5 Setup

As shown in Figure 5.3, the numerical domain includes the injector and the flametube. The secondary air ducts and the fuel line have not been considered in the attempt of reducing the computational cost. Their effect was shown to be negligible thanks to a RANS sensitivity carried out for the definition of the numerical domain. These features were replaced by inlet patches with a velocity profile computed by RANS calculation and a constant temperature as well as a synthetic turbulence to prevent

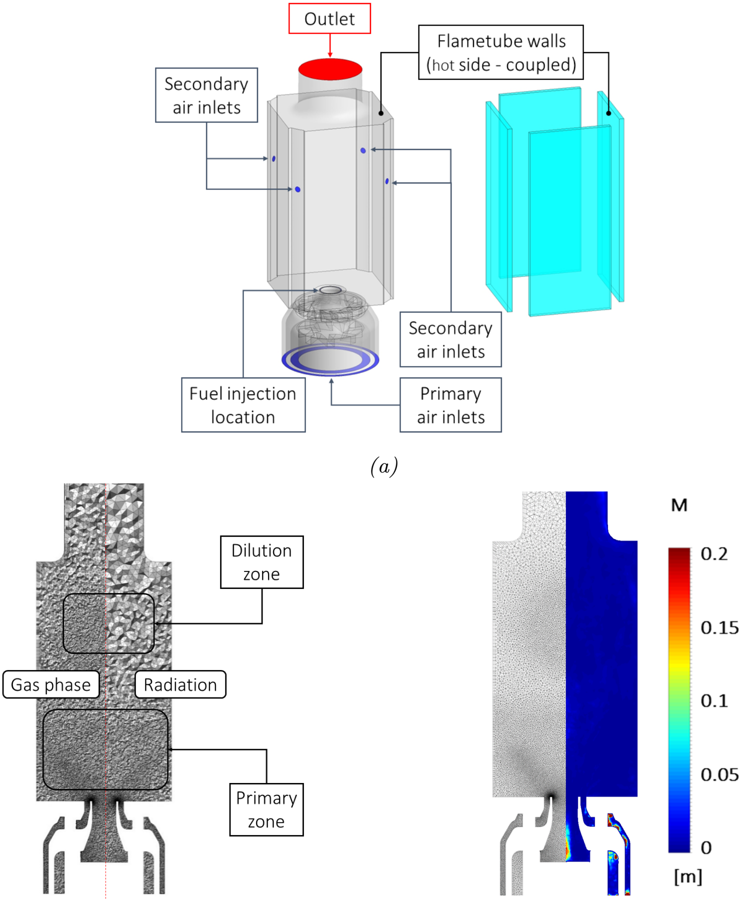

(a)

(b)

(c)

Figure 5.3: (a) Computational domain and boundary conditions, (b) gas phase and radiation mesh grids and (c) Pope criterion.

laminarization of the jets. Regarding primary inlet, the mass flow rate has been prescribed while a pressure-outlet condition has been imposed at the outlet. It is worth mentioning that the final portion of the domain was extruded for 2.5 of the outlet diameter to avoid non-physical disturbances in the flametube.

All the walls have been treated as smooth no slip surfaces, but different treatments have been set concerning their temperature depending on the performed calculation. A zero heat flux boundary condition has been imposed for the cold flow simulation and for the adiabatic reactive calculation. On the contrary, the fluid hot side of quartz windows have been coupled with the solid computation and its temperature is provided by the conduction solver in the multiphysics simulations, according to the previous described U-THERM3D approach. In this case, temperature on the remaining walls has been prescribed in the convective calculation as provided in [167]. To reduce the computational effort of the coupled simulation, on the cold side of quartz windows, a convective boundary condition has been set, following the method explained in [182] to compute a reference temperature ($T_{ref} = 313\ K$) and heat transfer coefficient ($HTC_{ref} = 121\ W/m^2K$). In terms of radiative properties, the windows have been treated as fully transparent to radiation whereas the other walls have been considered grey surfaces with emissivity equals to 0.8. The previous assumption about the windows avoids the solution of the RTE in the solid and it is justified by the mostly transparent behaviour of quartz at high temperatures, as confirmed by [182].

As required by U-THERM3D procedure, three different computational grids were generated with ANSYS Fluent Meshing for the gas phase, the solid and the radiation solvers. The mesh employed for the CFD solver has been chosen by observing the results of the cold flow calculation. In this sense, the governing equations have been discretized and solved on two different tetrahedral grids of 18 M and 32 M elements with 3 prismatic layers for the discretization of the near-wall region. Different local refinements were carried out in the primary and dilution zones (respectively with a minimum size of 0.4 mm and 0.3 mm for the coarser mesh and of 0.35 mm and 0.15 mm for the finer one) which are characterized by a strong unsteadiness. As reported in the following, the higher computational cost provided by the finer mesh was not justified by the accuracy in the flow field prediction and, therefore, the coarser mesh was employed for the reactive simulations. After the calculation, the resolution of the turbulence field in the reactive cases was checked *a posteriori* by means of the M criterion proposed by Pope [183] as shown by the Figure 5.3c. The parameter M represents the ratio between modelled and total turbulence kinetic energy, showing that over 90% of the turbulent kinetic energy is solved in the most part of the domain (M values below 0.1).

Considering the solid domain, an hexahedral mesh of 2.5 M elements has been employed to solve conduction in the quartz windows with 10 elements within its thickness whereas the computational effort for the radiative problem in the gas field has been minimized using a coarser mesh counting 8 M tetrahedral elements, as shown in 5.3b. Time-steps have been chosen relying on the requirements of the different solvers and applying the desynchronisation technique explained in [109]. As a result, fluid time-step has been set to $2 \cdot 10^{-6} s$ with 12 iterations performed every time-step, so as to achieve adequate residuals ($1 \cdot 10^{-5}$ for the continuity and $1 \cdot 10^{-6}$ for the momentum and energy equations), whereas the solid solver has been advanced with a larger time-step of $1 \cdot 10^{-3} s$. The coupling between simulations was performed every 10 fluid time-steps, 50 solid time-steps and 10 radiative iterations.

The complete multiphysics simulation (LES UT3D) was run on 160 CPU (Xeon E5-2630v4), requiring 2 and 3 flow through times respectively for flushing and averaging with a total effort of 85000 CPU hours against a hypothetical cost of 42 M CPU hours in the case of direct coupling. The flow through time was computed considering the chamber length (0.19 m) and an average bulk velocity ($\approx 10\ m/s$). The use of the total chamber length and of an average bulk velocity represents a precautionary criterion for the calculation of the flow through time. Therefore, the adopted value for the time-averaging have been considered sufficient for an adequate statistical convergence of the solution. For this scope, the instantaneous and the time-averaged temperature trends during the sampling period for 4 different axial positions along the centerline of the combustor are reported in Figure 5.4 in order to demonstrate the mentioned convergence of the time-averaging. The same computational cost was spent for each reactive simulation since the fluid calculation represents the bottleneck for the advancement of the coupled simulation during the coupling time-step due to the limited available computational resources.

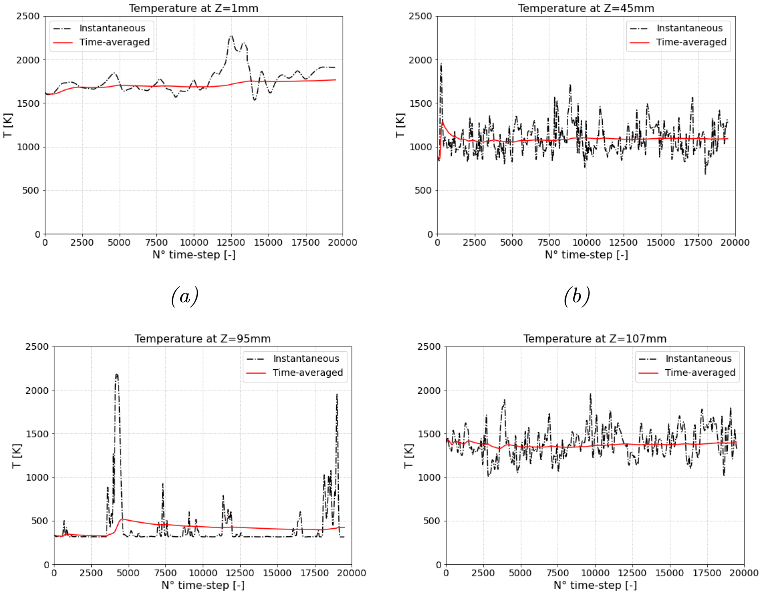

(a) *(b)*

(c) *(d)*

Figure 5.4: Comparison between instantaneous and time-averaged temperature values during the sampling period of the Case 6 for 4 different axial locations along the centerline of the combustor: (a) $Z = 1$ *mm, (b)* $Z = 45$ *mm, (c)* $Z = 95$ *mm and (c)* $Z = 107$ *mm.*

As far as numerical schemes are concerned, a bounded central difference scheme for spatial discretization and a second order implicit formulation for time discretization were employed. Pressure-velocity coupling was solved by the pressure-based SIMPLEC (Semi-Implicit Method for Pressure Linked Equations-Consistent) algorithm.

Concerning the RANS results reported in [168, 169], it is important to underline that a similar numerical setup has been employed except for the turbulence modelling (Realizable k-ϵ model [184]) and that the thee different simulations related to the three different solvers have been performed on coarser computational grids: a tetrahedral mesh of 14 M elements with 3 prismatic layers close to the wall was employed for the gas phase simulation, a hexahedral mesh of 600 k elements for the heat conduction calculation within the solid framework and a coarser tetrahedral mesh of 2.6 M elements for the radiative solver of the THERM3D simulation.

5.4 Results

5.4.1 Cold flow fields

A cold flow calculation has been performed in order to preliminary validate the combination of LES model, turbulence closure and numerical grid. In Figure 5.5 and in Figure 5.6, unsteady and steady numerical results in terms of velocity magnitude and axial velocity respectively are shown on the mid-plane of the combustor. In the latter figure, black isolines represent the zero axial velocity so as to highlight the recirculation zones.

The flow structure is typical of swirling flows with a corner vortex located all around the burner (Outer Recirculation Zone) and a central recirculation zone (Inner Recirculation Zone) which extends to the height of injection of secondary air. Comparing time-averaged LES and RANS axial velocity, significant differences can be observed next to the burner outlet and in the region of dilution jets interaction. In LES calculation, the swirling flow shows a stronger jets spreading with a lower opening angle. The IRZ is present inside the swirler, unlike the steady simulation where positive velocity is computed within the injector. Moreover, a stronger penetration of the dilution jets is predicted by LES, promoting the dilution air to be splitted in upstream and downstream fluxes closer to the burner axis with higher velocities, as highlighted in Figure 5.7 where the time-averaged velocity magnitude and axial velocity on a mid-plane

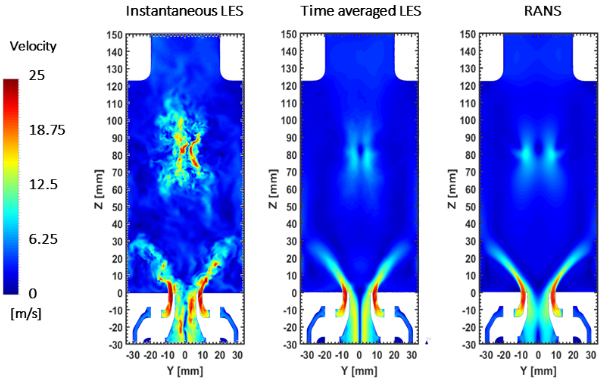

Figure 5.5: Velocity magnitude in a mid-plane of the combustor for the Case 1 (on the right) and for the Case 2 (in the mid and on the left). The reported LES fields are related to the solution on the finer computational grid.

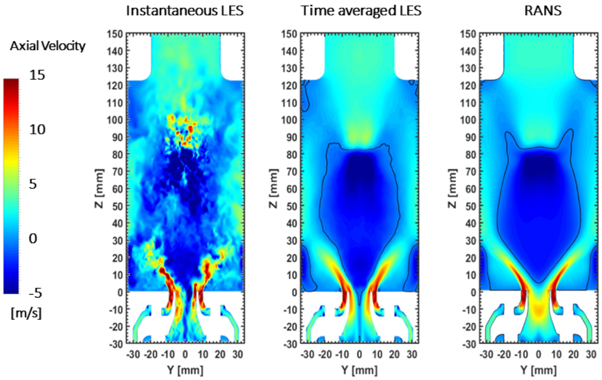

Figure 5.6: Axial velocity in a mid-plane of the combustor for the Case 1 (on the right) and for the Case 2 (in the mid and on the left). The reported LES fields are related to the solution on the finer computational grid.

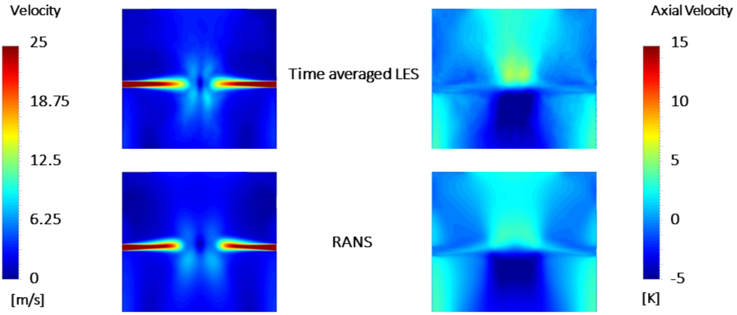

Figure 5.7: Time-averaged velocity magnitude (on the left) and axial velocity (on the right) in a portion at the secondary jets height of the mid-plane of the combustor passing through the dilution holes for the Case 1 (on the bottom) and for the Case 2 (on the top). The reported LES fields are related to the solution on the finer computational grid.

of the combustor passing through the dilution jets are reported.

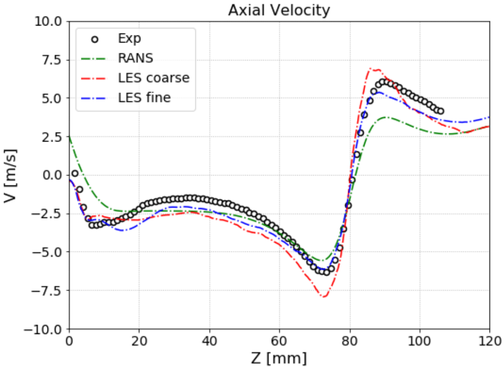

Figure 5.8: Comparison in terms of time-averaged axial velocity profile along the centerline of the combustor for the Case 1 and for the Case 2.

The previous considerations are confirmed by taking into account

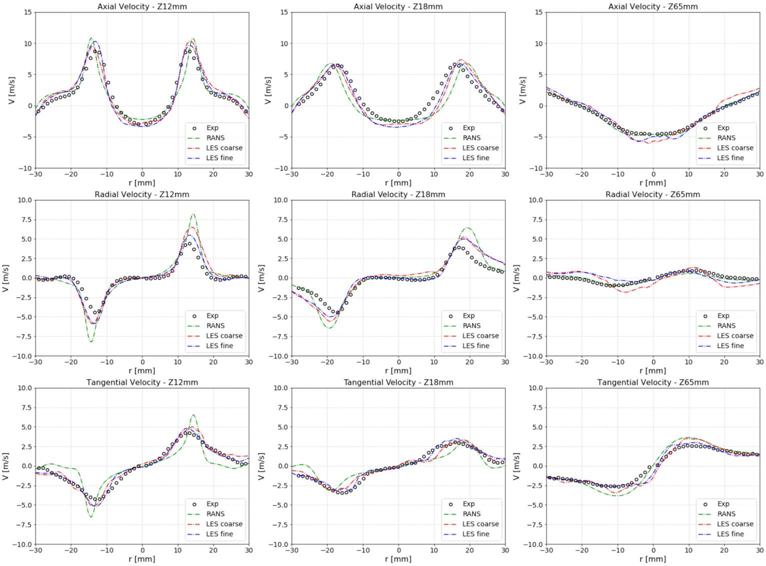

(a) (b) (c)

Figure 5.9: Radial distributions of time-averaged axial, radial and tangential velocity components (a) at $Z = 12$ mm, (b) at $Z = 18$ mm and (c) at $Z = 65$ mm for the Case 1 and 2.

a quantitative comparison of axial velocity along the centerline of the combustor (see Figure 5.8) and the radial distributions of axial, radial and tangential components of velocity for three different axis locations (see Figure 5.9). As far as the centerline axial velocity profile is concerned, an overall improvement in the prediction of the relevant flow features can be observed for scale-resolving approach, especially if a fine enough mesh is employed in LES. In this way, it is possible to compute correctly both the IRZ penetration, despite a slight over-prediction of negative velocities, and the splitted fractions of secondary air. Interestingly, this flow of fresh air moves upstream in the primary zone and downstream towards the outlet of the combustor, as highlighted by the positive and negative peak values of velocity. Instead, the proper prediction of the flow radial spreading is highlighted by the radial distributions of the velocity components and particularly by the correct location of the peak values, underlining a fairly good agreement with experimental data. It is possible to note that LES profiles are smoother with respect to the RANS ones near peak value locations, suggesting a proper prediction of turbulent mixing levels within the combustor. However, the differences in the prediction of velocity profiles between LES results are not enough compared to the higher computational cost of the finer mesh and such differences are mainly localized along the centerline whereas the radial distributions are much more consistent between each other. Therefore, the coarser one has been employed for the following reactive calculations.

To further demonstrate the equivalence of the two LES grids in the computation of the flow unsteadiness, the radial distributions of RMS

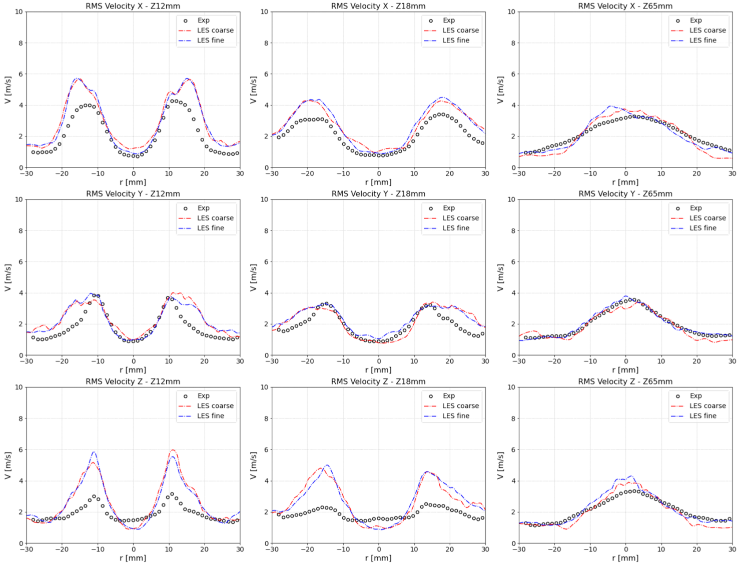

(a) (b) (c)

Figure 5.10: Radial distributions of RMS velocity components (a) at $Z = 12$ mm, (b) at $Z = 18$ mm and (c) at $Z = 65$ mm for the Case 2.

velocity components at the same axial locations are shown in Figure 5.10 together with experimental data. Once again, a fairly good agreement can be observed for the non-axial velocity components (Velocity X and Velocity Y), resulting in a well numerical prediction of both values and radial extension of the peak regions, mainly located at $-20 < r < -10$ and at $10 < r < 20$ for the first two axial locations while at $-10 < r < 10$ for the last one. In the first case, the high values are related to the fluctuation of the swirling jets coming from the burner whereas in the third axial location the peak is ascribable to the strong recirculation as a consequence of the dilution jets interaction. Instead, higher discrepancies can be noted in terms of axial velocity component (Velocity Z) for which the numerical simulations tend to over-predict the intensity of the flow unsteadiness compared to the measurements for the positions closer to the nozzle outlet. However, the behaviour of the two unsteady simulations is similar also in this case, confirming the previous considerations.

5.4.2 Reactive fields

In Figure 5.11 and in Figure 5.12, the computed instantaneous and time-averaged velocity and temperature distributions in a plane passing through the centerline of the combustor are respectively reported for LES simulations together with steady-state results. The velocity field highlights again the Inner and Outer Recirculation Zones generated by the double swirler system. Regarding the temperature field, peak values are located in the first part of the combustion chamber where the flame is stabilized and a typical M-shaped flame can be observed. This occurs since the secondary air injected by the dilution holes recirculates backwards up to the swirler, shifting the flame towards the stoichiometric conditions. Moving downstream, high temperatures can be found in the near-wall region where a significant amount of secondary air is present. Such air determines a significant quenching of the flame, strongly reducing the gas temperature towards the chamber exit.

Observing Figure 5.12, it is important to note that in LES calculations the tip of the flame moves towards the injector and its stabilization occurs

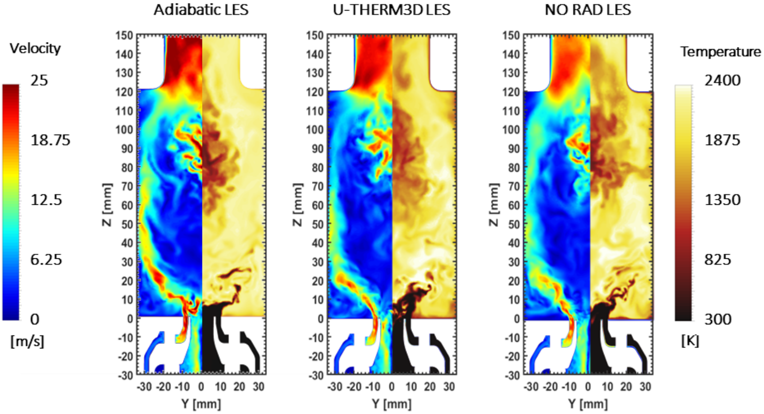

Figure 5.11: Instantaneous velocity (left) and temperature (right) distributions in a mid-plane of the combustor for the Case 4 (on the left), Case 5 (on the right) and for the Case 6 (in the mid).

at lower height compared to RANS results as a consequence of a stronger turbulent mixing with the recirculated hot gases predicted by unsteady calculations next to the burner outlet. However, the mean flame position and opening are similar throughout all the LES simulations whereas some differences can be appreciated by observing the temperatures and the velocities both in the IRZ and ORZ of the swirling flow and next to the combustor walls. Considering the presence of the glass window, a decrease of temperature with respect to adiabatic case occurs when wall heat losses are considered (NO RAD LES), leading to lower velocity downstream the swirler outlet and causing also a different flow field in the near-wall and dilution regions. This effect is amplified when radiation is computed (U-THERM3D LES) due to the heat dispersion related to radiative emissions and it obviously affects the heat loads on the walls.

This flame behaviour can be also pointed out as far as the temperature and velocity profiles along the centerline of the combustion chamber are concerned. Figure 5.13a shows a quantitative comparison with respect to experimental data and RANS results in terms of temperature, where

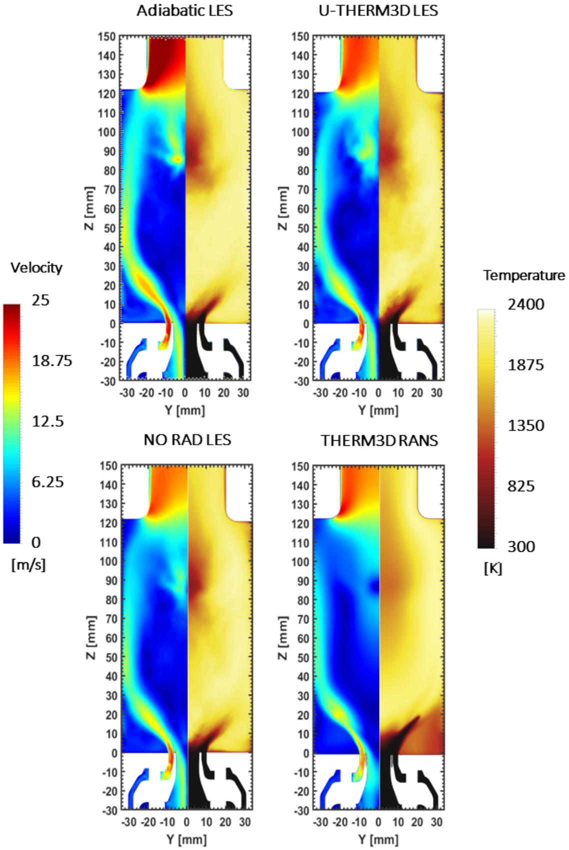

Figure 5.12: Time-averaged and steady velocity (left) and temperature (right) distributions in a mid-plane of the combustor for the Case 3 (lower-right), for the Case 4 (upper-left), for the case 5 (lower-left) and for the Case 6 (upper-right).

the black bars indicate the maximum and the minimum measured values. As expected due to the zero heat flux boundary condition, the adiabatic calculation over-predicts the gas phase temperature in the rich region whereas for the U-THERM3D case, an overall good agreement with

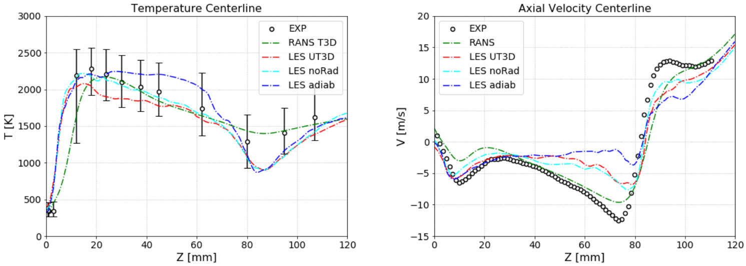

(a) (b)

Figure 5.13: Comparison in terms of time-averaged (a) temperature and (b) axial velocity profiles along the centerline of the combustor for the Case 3, 4, 5 and 6.

experiments of the temperature evolution can be observed and a better prediction of the peak location is obtained with respect to RANS. However, an under-estimation of the peak value and a general under-prediction of gas phase temperature can be noted in the U-THERM3D case. In LES simulations, gas phase temperature abruptly decreases in the dilution region compared to experimental measurements and RANS prediction. The reason of the above mentioned mismatching could be an incorrect computation of turbulent mixing levels around the injection region of the dilution jets, causing an higher penetration of the air and a lower convection towards the flame, as shown in Figure 5.14. This may be related to the absence of the secondary air ducts in the computational domain, replaced by a synthetic turbulence generator which may compute a lower turbulence intensity at ducts outlet. In NO RAD LES case, this effect is partially counterbalanced by the absence of radiative heat losses in the primary region where their contribution is greater related to the higher temperature levels. This causes a fairly good agreement with the experimental curve but it is important to underline that also these results are affected by the incorrect computation of the dilution air splitting, since the same flow behaviour is observed in the dilution region.

This can be confirmed taking into account the axial velocity profile

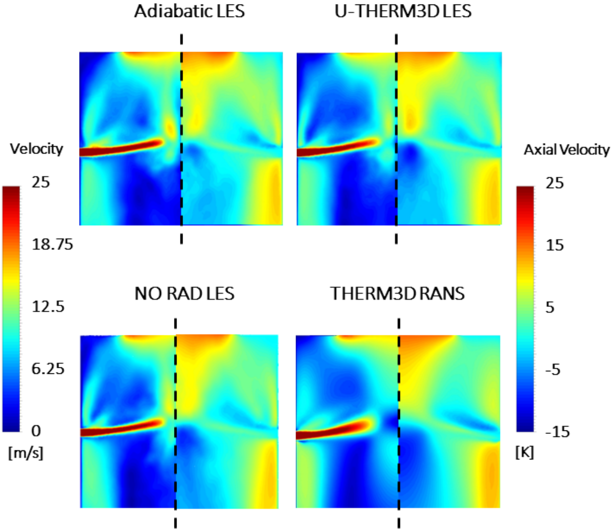

Figure 5.14: Time-averaged velocity magnitude (left) and axial velocity (right) in a mid-plane of the combustor passing through the dilution jets for the Case 3 (lower-right), for the Case 4 (upper-left), for the case 5 (lower-left) and for the Case 6 (upper-right).

along the centerline of the combustor, as shown in Figure 5.13b. In this case, a better prediction compared to RANS results and a very good matching with experimental data are achieved in the first part of the combustor with a more intense predicted IRZ next to the burner outlet. However, the level of agreement is lower compared to the cold flow for LES results moving towards the end of the rig. In fact, lower negative velocity is computed upstream of the secondary air injection probably due to the already mentioned bad prediction of the interaction between dilution jets, especially for the adiabatic case whereas the other two LES curves are substantially overlapped. This is suggested by the differences around $Z = 80\ mm$ (secondary air ducts location), leading to a lower amount of dilution air moving upstream towards the primary region as well as towards the combustor exit.

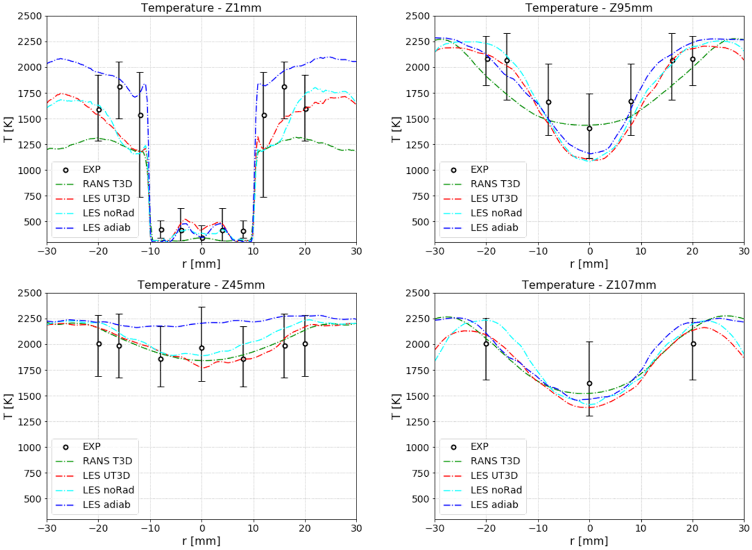

Figure 5.15: Radial distributions of time-averaged temperature at four axial locations for the Case 3, 4, 5 and 6.

In order to better understand temperature levels within the combustion chamber and to evaluate heat losses related to wall heat fluxes and radiative heat transfer towards the external environments, radial time-averaged temperature distributions at four axial locations are reported in Figure 5.15 together with experimental data and with the measured range highlighted by black bars. At all axial locations, for the U-THERM3D simulation the main differences with measurements can be observed in the central region due to the not proper computation of dilution jets interaction and secondary air recirculation, as previously said. On the contrary, a better agreement in terms of temperature trend and values compared to RANS case is achieved at higher radii, especially in the second part of the combustor as a consequence of an appropriate computation of the effect of flame-wall interaction. However, some discrepancies are still present at $Z = 1\ mm$, where temperature levels are under-predicted. This can be related to the uncertainties in the thermal boundary condition imposed at the bottom wall (considered here at 650 K, but with an uncertainty of $\pm 100K$ as estimated by DLR) and to a not proper prediction of turbulent mixing in the swirling flow coming from the burner. On the contrary, the temperatures computed by adiabatic LES over-predict the experimental data moving towards the combustor walls due to the adiabatic temperature here computed. At the same time, NO RAD LES simulation provides higher temperatures throughout the radial extension of the combustor with relevant discrepancies for $r < -20\ mm$ and $r > 20\ mm$, highlighting the importance of taking into account both wall and radiative heat losses for a proper computation of near-wall phenomena.

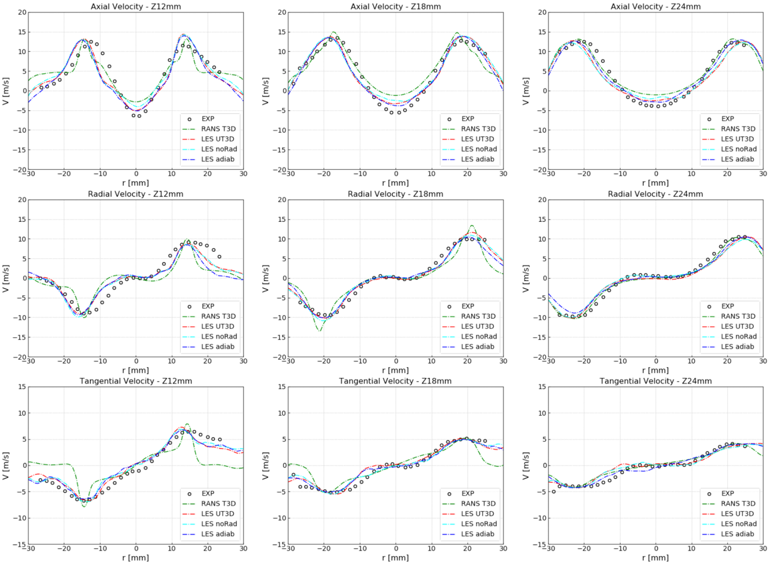

(a) (b) (c)

Figure 5.16: Radial distributions of time-averaged axial, radial and tangential velocity components (a) at $Z = 12\ mm$, (b) at $Z = 18\ mm$ and (c) at $Z = 24\ mm$ for the Case 3, 4, 5 and 6.

Figure 5.16 shows the radial distributions of axial, radial and tangential velocity components for three different axial positions located in the rich region: a significant improvement with respect to RANS calculation is achieved and an overall good agreement is obtained. It is worth to observe as the scale-resolving approach allows to accurately compute the radial spreading of the swirling flow jets coming from the burner thanks to the resolution of a wider spectrum of turbulent structures. However, some discrepancies with experimental data can be pointed out that may explain the previously mentioned temperature disagreement. Slight differences between LES calculations can be appreciated for $r < -20\ mm$ and $r > 20\ mm$ where the heat loss effects and the resulting temperature gradients begin to become significant, as previously discussed.

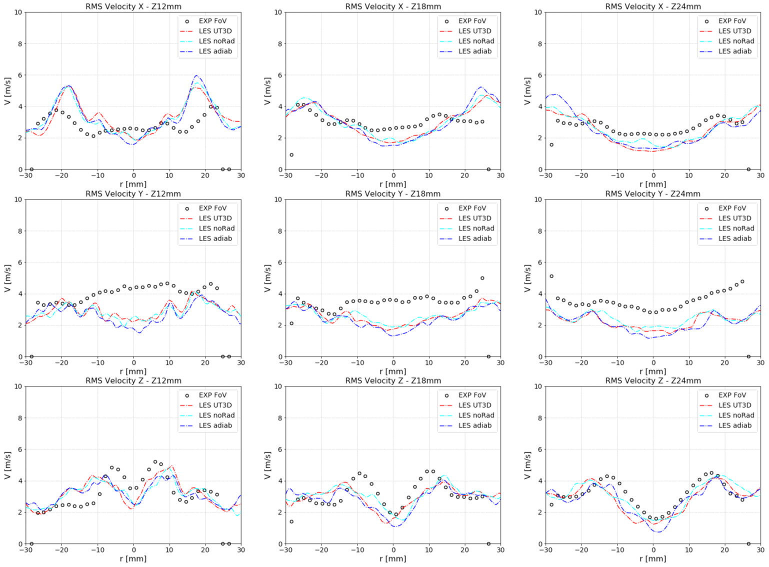

(a) (b) (c)

Figure 5.17: Radial distributions of RMS velocity components (a) at $Z = 12\ mm$, (b) at $Z = 18\ mm$ and (c) at $Z = 24\ mm$ for the Case 3, 4, 5 and 6.

In order to investigate the capability of scale-resolving simulations of capturing the turbulence fluctuations, the radial distributions of RMS velocity components at the same axial locations are shown in Figure 5.17 together with experimental data. LES simulations give rise to similar results since the same computational grids and turbulence model have been employed. In general, a reasonable agreement with measurements is achieved as far as the shape of the radial distributions is considered, especially for the axial velocity (Velocity Z). From a quantitative point of view, the major differences occur in the first location next to the burner outlet and, for the other locations, in the region around the axis of the combustor, where an under-estimation of velocity fluctuations with respect to experimental data can be observed. Also in this case, the under-prediction can be ascribed to the less amount of dilution air which recirculates and interacts with the swirling flow, probably perturbing the flow field in this region.

For a deeper understanding of the effects of turbulent fluctuations on the temperature field within the combustion chamber, a comparison between experimental and U-THERM3D results in terms of Probability Density Functions (PDFs) of instantaneous temperature is shown in Figure 5.18 (right), where r is the radial coordinate with respect to the axis of the combustor. PDFs resulting from the other LES calculations are not reported since only a shift towards higher temperatures is expected according to the previously described temperature and RMS velocity radial profiles. Also in this analysis, it is possible to note a duality between the centerline and the near-wall region in the temperature prediction. At axial locations ($r = 0\ mm$ on the left), a good agreement is obtained in terms of range and probability values, whereas a shift towards lower temperatures of the modal value occurs at each location. This is related to the under-estimation of temperature levels along the centerline of the combustor, as previously discussed. A better prediction is achieved next to the walls (on the right) where it is possible to note a fairly good agreement with experimental data in terms of both range and mode values, suggesting again a proper computation of heat losses effect. Some discrepancies can

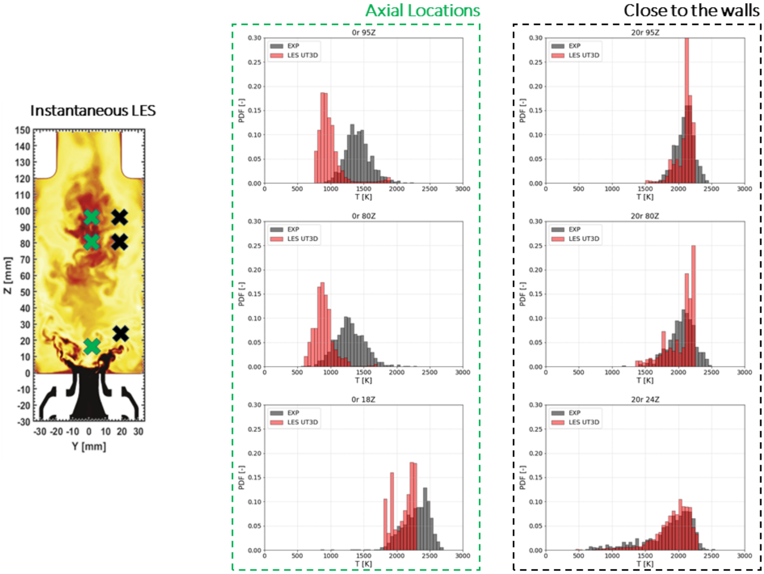

Figure 5.18: PDFs of temperature at six locations in the combustor for the Case 6.

be observed at $Z = 80\ mm$ where it seems that lower fluctuations are computed, probably due to the under-predicted spreading and turbulent mixing of dilution air.

Regarding soot formation within the combustor, Figure 5.19 shows a comparison between experimental and numerical results in terms of time-averaged distribution of soot volume fraction. From the experimental map, it can be pointed out that soot is primarily generated in the high temperature region next to the injector exit and in the outer part of the recirculation zone. High soot levels can be also observed close to the walls when the pollutant particles are transported downstream until dilution air causes soot oxidation.

From a numerical point of view, it can be observed that a similar qualitative distribution is obtained throughout the simulations and the same cone shape enclosing the peak value regions can be identified. In LES calculations, time-averaged soot levels are generally under-predicted by one order of magnitude from a quantitative point of view, whereas RANS levels are consistent with experimental data as reported in Table 5.4. Several works carried out by others research groups have also highlighted the same behaviour in the framework of unsteady simulations with an under-estimation of soot levels and an over-prediction of soot oxidation, even if more complex and, theoretically, more accurate soot models have been employed [160, 161, 162, 165].

Table 5.4: Maximum values of soot volume fraction on the mid-plane computed by reactive simulations.

	EXP	RANS T3D	LES adiab	NO RAD LES	LES UT3D
Instantaneous [ppb]	1231.35	-	13.66	35.42	6.67
Time-averaged [ppb]	36.82	26.56	4.76	10.03	3.41

This can be ascribed to the simplified soot model which is not able to properly predict the complex phenomena related to soot formation and oxidation and to accurately compute the sub-grid contributions, since the same soot model setup has been employed for both RANS and LES simulations. However, even if RANS soot peak value is more consistent to the experimental data, the rates of soot formation and oxidation seem to be not properly computed since a re-increase of soot levels occurs in the dilution region leading to the presence of the pollutant also at the combustor outlet. Such phenomena are not identifiable in the experimental map and, in this sense, LES distributions show a better agreement. Comparing the adiabatic case to the U-THERM3D calculation, the peak value is lower in the latter since the source terms of the soot equations, as aforementioned, are highly sensitive to temperature. However, the employed soot model seems to be strongly coupled with the radiation modelling as highlighted by the maximum values of soot volume fraction computed by NO RAD LES case. Such evidence was also pointed out in [168] for a steady framework and it is probably related to a different

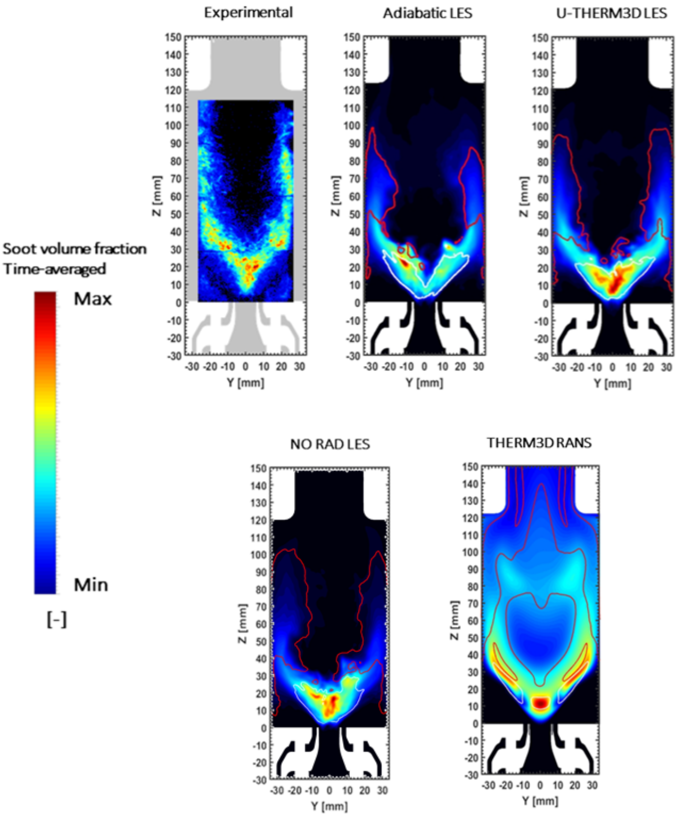

Figure 5.19: Experimental and numerical soot volume fraction distributions in a mid-plane of the combustor for the Case 3 (lower-right), for the Case 4 (upper-mid), for the case 5 (lower-left) and for the Case 6 (upper-right). White and red lines highlight source and oxidation regions, respectively.

computation of soot oxidation source term when radiative heat transfer is activated.

In the numerical maps, the white isoline bounds the region with a positive mean soot mass source value (related to soot formation) while the red isoline highlights the negative values zone (related to soot oxidation), allowing to understand where soot particles are generated and oxidized. As above described, soot formation regions are mainly located at the burner outlet where the reaction process starts. Secondary injection supplies fresh air also to the recirculation zone where oxidation can be observed, especially in LES distributions where the oxidation zone is mainly located next to the combustor walls.

5.4.3 Quartz temperature

The previous section has highlighted the capability of U-THERM3D procedure to reproduce the main features of a sooting flame in a LES framework, showing an overall accuracy of the developed approach from an aero-thermal point of view. Moreover, the loosely coupled tool has permitted to split and underline the wall and radiative heat losses effects on the flow field and flame. The gas temperature, however, is not only affected by an energy redistribution due to radiation. Convective and radiative wall heat fluxes related, respectively, to the fluid-solid and radiation-solid interactions can generate relevant heat losses that modify the aero-thermal fields. These interactions are taken into account using multiphysics tools, as U-THERM3D, whose main output is indeed the solid temperature. Therefore, in the following, an analysis of the prediction of wall temperature distribution and of the contributions of convective and radiative heat transfers to the total wall heat flux is reported, comparing the U-THERM3D results against experimental measurements and a steady-state calculation (THERM3D). The latter represents the state-of-the-art in a industrial framework when a CHT calculation is carried out. Nevertheless, in the present work, for the hypothesis of totally-transparent window, radiative wall heat flux corresponds to the incident radiation, eliminating the need of radiation-solid coupling. It is possible to assume consistent the mentioned hypothesis, considering that the quartz is mostly absorbing at low temperature levels whereas it is transparent at high temperatures [182].

Figure 5.20 shows the temperature distribution on the hot and cold

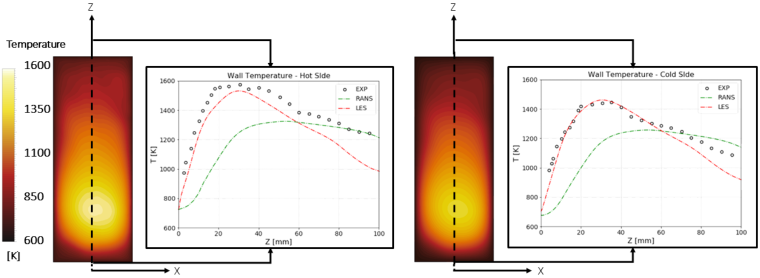

Figure 5.20: Quartz windows temperatures comparison with experiments [185] for the Case 3 and 6.

sides of the quartz window. The wall region that faces to the burner primary zone has the highest thermal load. Convective heat transfer in this zone is driven by flame-wall interactions that expose the surface to high temperatures as well as to high turbulence which increases the heat transfer coefficient. The peak temperature reaches almost 1600 K. According to the lower gas temperature at downstream positions along the axial direction, the window temperature decreases as well. Closer to the boundaries, solid temperature drops abruptly to the constant value of 900 K set on the adjoining surfaces that are not included in the conjugate heat transfer problem at this point of the work. Because of the low thermal conductivity of quartz, however, boundaries limit their influence to few millimeters and the region around the centerline is unaffected.

A comparison with experimental data on the window centerline emphasizes also the predictive capabilities of U-THERM3D as far as the wall temperature is concerned. Indeed, scale-resolving results are in good agreement with experiments along the whole surface. Compared to THERM3D results obtained with RANS in [181], the window is 200 K warmer in the peak region. This different behaviour is mainly related to the flow field and flame structure and to the resolution of turbulence scales in LES. The turbulent structures influence all the processes involved in swirling flames, from combustion to aerodynamics, playing a key role also in the convective motions. A resolution of the larger scales of the turbulent wall heat flux improves the prediction of the heat load that, in this case, is higher than the one computed by a RANS model. As a result of the major heat losses, wall temperature decreases gradually and similarly to the experimental trend moving downstream. In [185], the wall heat flux is correlated to the downstream oxidation at higher radii caused by the additional air. Indeed, the mixing with the partially-burned rich mixture releases further energy that contributes to keep the gases warm. In the present LES simulation, secondary air recirculates less than in experiments and the aforementioned phenomenon is reduced, leading to a slight under-estimation of the wall temperature for $Z > 40\ mm$. Despite that, as the U-THERM3D curves match the measurements on both the window sides with good accuracy, the overall heat flux exchanged between gas phase and solid seems well-predicted by the present methodology.

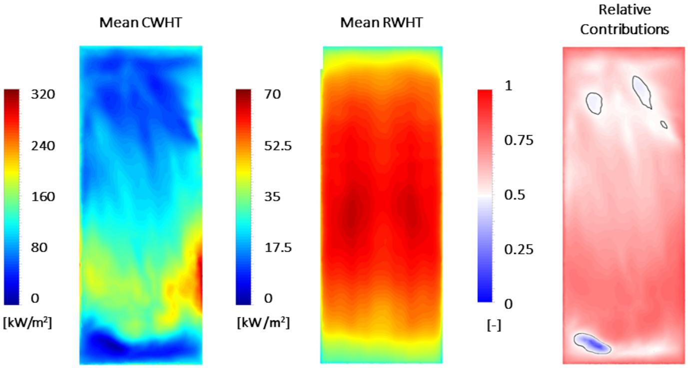

Figure 5.21: LES heat fluxes at the inner face of a quartz window: Mean Convective Heat Flux (left), Mean Radiative Heat Flux (center) and their relative contributions (right) for the Case 6.

As a consequence, a deeper analysis of combustor heat losses is useful in order to understand the relative importance of convective and radiative heat transfers. For this reason, LES heat fluxes at the inner face of a quartz window are reported in Figure 5.21 together with the relative

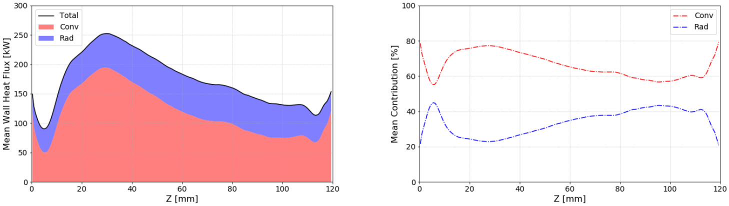

(a) *(b)*

Figure 5.22: (a) Span-wise averaged convective and radiative heat fluxes and (b) their percentage with respect to the total along the axial direction for the Case 6.

contribution of convection (on the right). Therefore, 0 and 1 indicate that local heat loss is only due to radiation (blue) or convection (red) respectively, whereas the black isoline (0.5 value) highlights where the influence of the two different heat transfer modes is equivalent. It is worth to note that convective contribution is prevalent on the whole surface and it is one order of magnitude higher than radiative one, especially in the first part of the combustion chamber where the impact of hot gases contributes to the highest wall temperatures, as said before. This is also highlighted in Figure 5.22 where span-wise averaged heat fluxes along the axial direction are reported, underlining the relative contributions in terms of percentage with respect to the total. The change in the slope of the curves at the beginning and at the end of the plots is probably due to the imposed fixed temperatures at the bottom and at the top of the combustion chamber. Comparing Figure 5.20 with Figure 5.22, the main differences between LES results and experimental measurements occur where convective and radiative contributions tend to be equivalent, pointing out the effect of the hypothesis of transparency in the radiative treatment of the glass. Probably, the use of a more complete model which can take into account particular absorption bands or the absorbing behaviour of the quartz at low temperature may improve the data matching in this sense. It can be also observed a decrease of convective thermal loads for $Z > 30\ mm$ as opposed to radiation which tends to be more constant along the combustor.

5.5 Concluding remarks

Large Eddy Simulations of a non-premixed ethylene/air sooting flame have been performed in the framework of the U-THERM3D multiphysics procedure implemented in ANSYS Fluent, employing three loosely coupled simulations for fluid, solid and radiation. This allowed to account appropriately for the mutual interactions of convective, conductive and radiative heat transfers, combustion and soot production. Three different reactive multiphysics simulations have been performed by varying the treatment of radiation and of solid coupling in order to highlight the effects of wall and radiative heat losses on the reactive flow fields. The computed results have been compared with a previous RANS calculation and with the available experimental measurements in terms of aero-thermal fields, emissions and solid temperatures.

As far as cold flow simulation is concerned, the LES calculation is able to better predict the flow structures compared to the RANS approach, leading to a fairly good agreement with experimental data. In particular, LES model allows a proper computation of the radial spreading of the flow coming from the burner together with the correct evaluation of the IRZ and of the splitting of secondary air injection.

Regarding the gas phase temperature in the reactive simulations, U-THERM3D results provide a general agreement with experiments in terms of temperature evolution along the centerline of the combustor, highlighting the importance of computing radiative and wall heat losses with respect to an adiabatic and no-radiation modelling cases. However, a slight under-prediction of the peak value in the rich region and some discrepancies downstream of the secondary air inlets can be observed with respect to experimental data. The reason of these differences has been ascribed to an under-estimated secondary air recirculation, causing a not computed enhancement of the reaction process in the rich region. These considerations have been confirmed by the analysis of PDF temperature distributions at different characteristic locations within the combustor, where a better prediction can be noted closer to the walls rather than on the combustor axis. Together with the simplified adopted model, these discrepancies have led to an under-estimation by one order of magnitude of soot volume fraction in the scale-resolving framework. However, the cone shape and the location of the peak values in the rich region are numerically predicted from a qualitative point of view and soot particles remain next to the combustor walls until they reach the oxidation region.

Concerning wall temperature distributions, U-THERM3D procedure is able to properly predict the heat loads acting on combustor walls and the conduction within the solid, showing a great improvement with respect to steady-state calculation. In fact, an accurate computation of local wall heat flux fluctuations is fundamental for a reliable wall temperature calculation which can only be provided with a scale-resolving approach, such as LES model. From a quantitative analysis of the relative contributions of convective and radiative heat transfers on the inner face of glass windows, convective heat flux is one order of magnitude higher than the radiative one especially in the first part of the combustion chamber, according to the window temperature pattern.

This numerical investigation provides an additional validation of the coupling strategy in its theoretical basis and implementation in a commercial code. Moreover, the present results promote U-THERM3D as a very useful numerical tool for a detailed investigation of the interaction of the heat transfer phenomena and of their influences on aero-thermal fields in complex geometries such as real aeroengine combustors in an unsteady framework with feasible computational costs. The proven effectiveness of the coupling strategy paves the way to further applications on different test cases as well as the implementation and test of more advanced approaches for combustion, radiation and soot modelling in an environment capable of accounting for the multiphysics effects.

Chapter 6

Development and validation of a novel effusion model

The methodologies and the coupling strategy described in Chapter 4 are here applied for the development and the validation of an innovative approach based on the application of 2D boundary sources to simulate the injection of coolant from effusion cooling holes. This new effusion model represents an attempt to overcome the possible errors in the computation of the JICF phenomenon introduced by employing flat profiles for velocity and turbulent quantities at hole outlets. Such feature is common in boundary sources approaches available in technical literature and it can strongly affect the prediction of the characteristic vortical structures related to the main flow-jet interaction which in turn influences the mixing of the coolant with the cross-flow. In the framework of CHT simulations, this may result in a lower accuracy in the computation of film coverage as well as of the adiabatic effectiveness and wall temperature distributions. For this purpose, a new effusion model which is able to predict 2D velocity and turbulence profiles depending on the operating conditions of the investigated effusion cooling system is introduced.

The chapter is structured as follows: at the beginning, a numerical analysis of the DoE results is reported in order to show its robustness and the goodness of the simulations on which the developed approach is based. In addition, PCA and Kriging methodologies are applied on the profiles extracted by DoE simulations and the previously discussed meta-models for the prediction of velocity and turbulent quantities profiles at unexplored conditions are generated and validated. Afterwards, the effusion model is coupled with the CFD solver and validated on a single-hole and a multi-hole geometries in the framework of RANS calculations at unexplored operating conditions, comparing the modelled results against full-meshing hole and flat profile simulations. The multi-hole configuration demonstrates the applicability of the model for numerical investigations of more complex configurations in which the superposition effect associated to the multiple coolant injections becomes important. Finally, a numerical application is carried out again on the single-hole geometry in a SBES framework where the advantages of the absence of the discretized holes in terms of computational resources is higher due to the necessity of having finer grids for a good resolution of turbulent spectrum associated to effusion jets.

All the reported simulations have been carried out in adiabatic conditions, not considering the fluid/solid coupling and analyzing the results in terms of aerodynamics fields and adiabatic effectiveness. In this sense, further investigations are certainly required also in terms of wall temperature distribution. However, a proper computation of velocity and turbulence distributions next to the injection points is fundamental for a correct prediction of the main-coolant interaction and mixing which influence how the coolant air is distributed in an aeroengine combustor along the walls and, so, the adiabatic effectiveness on them that in turn affects the wall temperature pattern. Hence, the proposed approach represents an attempt to overcome the lacks of the standard effusion models available in technical literature from this perspective, introducing also a computational saving derived from a not discretization of effusion holes.

6.1 Numerical details

All the simulations here reported were carried out with the commercial code ANSYS Fluent 2019R1® and the main aspects of the modelling approach are reported below.

6.1.1 Numerical setup

Figure 6.1 shows the computational domains of the single-hole and of the multi-hole configurations employed for the numerical simulations reported in the following together with the prescribed boundary conditions. The single-hole geometry has been used firstly for DoE exploration and, then, for the validation of the coupling strategy.

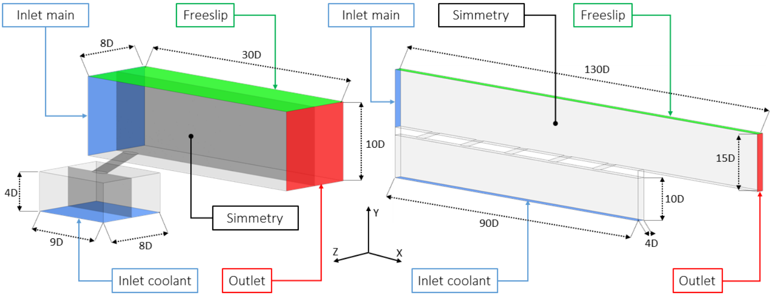

Figure 6.1: Single-hole and multi-hole computational domains and prescribed boundary conditions.

For the single-hole geometry, the hole diameter is $D = 4.75\ mm$ whereas the sizes of the cross-flow channel are $30D$, $10D$ and $8D$ respectively in the stream-wise, wall-normal and span-wise directions while the ones for the bottom plenum are $9D$, $4D$ and $8D$. Instead, the hole diameter is $D = 6.08\ mm$ for the multi-hole configuration with $130D$x$15D$x$4D$ and $90D$x$10D$x$4D$ sizes respectively for the cross-flow channel and the bottom plenum. For both the geometries, a mass flow rate and a total temperature have been specified at the main and coolant inlets according to the investigated BR and DR, whereas a pressure-outlet condition has been imposed at the outlet. In particular, the $1/7^{th}$ power law has been employed for the computation of a wall-bounded stream-wise velocity profile at the main inlet with a freestream main velocity of 10 m/s.

All other boundaries have been considered as no-slip adiabatic walls, except for the lateral surfaces where a symmetry condition has been employed. For steady simulations, the computational domains have been simplified by exploiting a symmetry condition also along the mid-plane, as depicted by Figure 6.1. In addition, a mass flow inlet condition on the hot side and a pressure-outlet with target mass flow rate on the cold side have been prescribed at hole imprints when the holes are not discretized, as highlighted in Figure 6.2. A Transported Scalar (TS) equation has been added to investigate the film coverage in terms of adiabatic effectiveness, imposing a unitary value at effusion inlets.

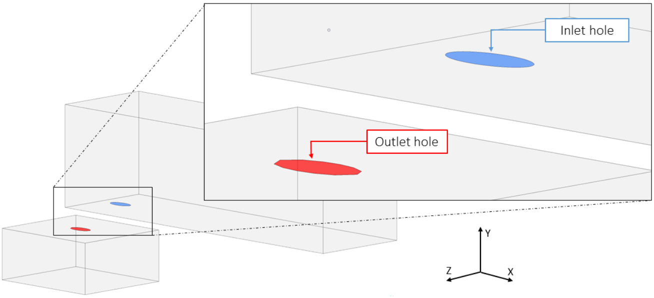

Figure 6.2: Detail of hole modelling.

Different tetrahedral computational grids were generated in ANSYS Fluent Meshing, according to the investigated geometry and to the employed turbulence model, as shown in Figure 6.3. Regarding the single-hole geometry, unstructured meshes of about 2 M elements have been used for the RANS calculations (DoE exploration and validation set) whereas SBES simulations have been computed on a finer grid of about 17 M elements. On the other hand, the multi-hole geometry has been discretized with 4 M of tetrahedral elements. Local refinements have been carried out in the region around to hole exits which is characterized by strong velocity gradients and unsteadiness in case of scale-resolving approach. A layer of 10 prisms has been added in proximity of the wall in order to ensure a $y^+ \approx 1$ for a proper resolution of the near-wall region.

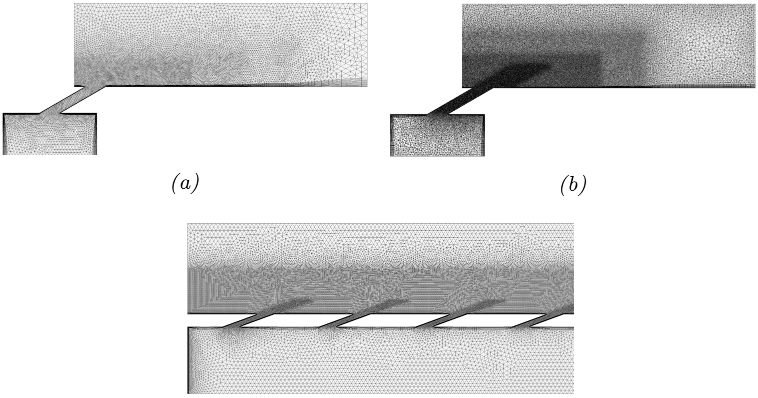
(a) (b) (c)

Figure 6.3: (a) RANS single-hole, (b) SBES single-hole and (c) RANS multi-holes computational grids.

As far as the numerical schemes are concerned, second order upwind schemes for spatial discretization and a least square cell based method for gradients calculations were adopted in RANS simulations, whereas a bounded central difference scheme for spatial discretization and a second order implicit formulation for time discretization were employed for unsteady calculations together with the pressure-based SIMPLEC algorithm for the pressure-velocity coupling.

Considering the CFD solver-effusion model interchange, the coupling was performed every 10 iterations or time-steps respectively for steady and unsteady calculations. Regarding the latter, the time-step has been set to $1 \cdot 10^{-6}$ with 15 iterations every time-step, so as to achieve adequate residuals (about $1 \cdot 10^{-5}$ for the continuity and $1 \cdot 10^{-6}$ for the momentum and energy equations), requiring 2 and 2 flow through times for flushing and averaging respectively. The flow through time was computed considering the stream-wise length of the domain (0.134 m) and the main flow velocity (10 m/s).

Finally the employed computational resources for each kind of full-discretized holes simulation are reported in Table 6.1, considering that the absence of effusion holes leads to a decrease of $10-20\%$ of the numerical costs (depending on the resolution of the original mesh).

Table 6.1: Computational resources summary.

Case	Turbulence model	Full-discretized cost [CPUh]	Modelled cost [CPUh]
DoE Single-hole	RANS	41760	-
Single-hole	RANS	288	259
Multi-hole	RANS	1440	1184
Single-hole	SBES	90500	72400

6.1.2 Turbulence modelling

Two different approaches have been tested in order to demonstrate the feasibility of the developed model in both steady and unsteady simulations. For RANS simulations, the k-ω SST model [186] for the eddy-viscosity closure was employed, including also for the DoE exploration. On the other hand, the unsteady simulations were carried out with the innovative hybrid RANS-LES approach named Stress-Blended Eddy Simulation (SBES). Such approach has been proposed by Frank and Menter [187] and it represents a further development of the Detached Eddy Simulation (DES) model. As other hybrid models, the eddy viscosity ν_t is defined as:

$$\nu_t^{SBES} = f_{SBES} \cdot \nu_t^{RANS} + (1 - f_{SBES}) \cdot \nu_t^{LES} \tag{6.1}$$

exploiting a shielding function f_{SBES} to dynamically blend between RANS and LES closures. In this context, one of the main advantages of SBES is the rapid transition from the steady RANS mode into the scale-resolving three-dimensional LES one due to the low stress levels enforced by the LES model. The shielding function f_{SBES} allows to prevent the use of LES sub-grid model for solving boundary layers, switching instead to a RANS approach. Therefore, the computational cost of the simulation is strongly reduced since a coarser numerical grid can be used for the discretization of the near-wall region. As far as the RANS modelling is concerned, a k-ω SST model has been adopted while a Dynamic Smagorisky model has been employed for the closure of the sub-grid stress tensor whose description has been reported in Chapter 5.

6.2 Results

In the following sections, the generation of the effusion model and the results of the computed numerical simulations for the validation of the coupling strategy are reported. Firstly, the data-set obtained from the DoE exploration and employed for the creation of the ROM is presented. Then, the development of the ROM is highlighted, focusing the attention on the goodness of PCA in terms of accuracy in the reconstruction of the original variables of interest and on the validation of meta-models for PCA scores prediction derived from the application of Kriging methodology. Finally, the effusion model is coupled with the CFD solver and the validation of the procedure is carried out in the context of three different type of simulations:

- RANS calculations on the single-hole geometry (RANS SH);
- a RANS sensitivity to the BR in the framework of the multi-hole configuration (RANS MH);
- a SBES simulation of the single-hole geometry (SBES SH).

Three different approaches will be compared for each investigated case: a full-discretized holes simulation (CFD), a simulation without effusion holes and with velocity and turbulence flat profiles at hole outlets (FLAT) and a simulation with effusion model coupling (EM). In this context, the FLAT calculation is representative of the state-of-the-art approaches available in technical literature.

6.2.1 DoE exploration and ROM validation

As already mentioned, the creation of the ROM is based on the application of PCA and Kriging methodologies to the velocity and turbulence profiles extracted at hole outlet from the DoE simulations of the single-hole geometry. In this sense, four input parameters have been considered to generate the computed simulations: the inclination angle α, the ratio between the length and the diameter of the hole L/D, the BR and the DR. According to the numerical experiments and the analysis of variance for film effectiveness carried out by auf dem Kampe and Völker [188], these are the parameters that mainly influence the film effectiveness distribution and the film-jet's trajectory and vortex structures. The first couple of parameters describes the geometry of the system whereas the second one encodes its fluid dynamics. As shown in Table 6.2, such parameters have been varied within ranges which are representative of the common values employed in aeroengine combustors, as reported in Chapter 1. The BR and the DR have been computed respectively as the ratio between the mass flow rates and the densities imposed at coolant inlet with respect to the ones prescribed at main inlet.

Table 6.2: Input parameter space.

Parameter	**Range**
α	$15° - 45°$
L/D	$1 - 10$
BR	$0.25 - 10$
DR	$1 - 2.5$

A total of 89 CFD simulations has been used for the construction of the data-set, employing an Optimal Space-Filling Design technique in combination with an automatic refinement for an additional sampling based on the shape of the DoE response surface to achieve a proper exploration of the input parameter space. These simulations represent also the training set of observations to build the ROM while the validation set will be reported in the next section. In order to have a better comprehension of the illustrated strategy, it is important to understand that the term *reconstruction* is related to the reconstruction of the training data from the PCs and PCA scores obtained with PCA; on the contrary, the term *prediction* is employed when the predictive capabilities of the created ROM are analyzed.

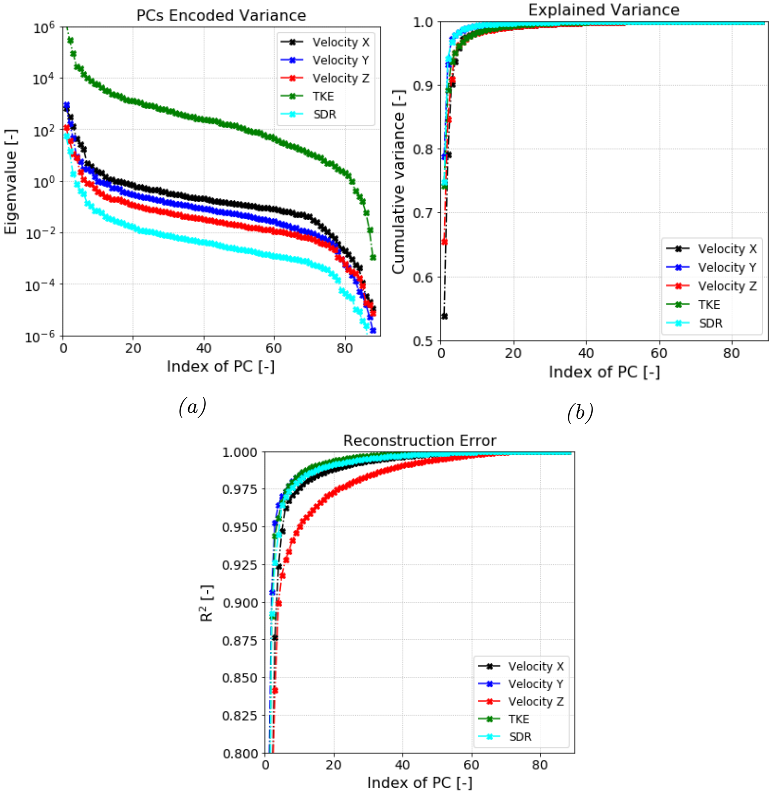

(a) *(b)*

(c)

Figure 6.4: (a) Spectrum of eigenvalues, (b) cumulative original data variance and (c) reconstruction error as functions of PC order.

As mentioned in Chapter 4, the application of PCA allows to distinguish between PCs, which are invariant representing the physics-related information of the system, and the PCA scores which, instead, are the system-dependent information associated to the changes of the input parameters. As far as the results of PCA are concerned, PCs are ordered according to the encoded part of original data variance which is expressed by the correspondent eigenvalue. Therefore, the first PCs are generally the ones carrying most of the system information. This is evident by observing Figure 6.4 where the spectrum of the eigenvalues associated to each PC is reported (Figure 6.4a) together with the cumulative explained variance (Figure 6.4b) and the R^2 values for the reconstruction of the training set (Figure 6.4c) as a function of the number of considered PCs (also known as *approximation order*). The curves are obtained for each original fluid dynamics variable of interest (velocity components and turbulent quantities) and the reconstruction error is computed as the mean error all over the 2D profiles.

Both the explained variance and the R^2 reconstruction error increase with the approximation order (the number of PCs taken into account) but it is worth to note that a limited number of PCs can be considered in order to take into account most of the original data variance, providing negligible error. As a consequence, a reduced number of PCA scores has to be interpolated by Kriging and fewer meta-models have to be generated, decreasing the complexity and the computational cost of the ROM. The analysis of these quantities allows to understand how much of the system information is recovered after the PCA decomposition and, at the same time, it represents a criterion for the choice of the number of required PCs. For this purpose, the number of retained PCs for the description of each original variable of interest has been selected in order to take into account about the 99.5% of the original data variance and it is reported in Table 6.3, representing also the number of meta-models that have to be generated.

This analysis allows also to demonstrate that the number of sampled training observations (89) is sufficient for the ROM development since this number limits the maximum number of PCs which can be extracted (equal

Table 6.3: Approximation order for each original variable of interest.

Original variable	**Retained PCs**	**Explained variance**
Velocity X	28	99.47%
Velocity Y	15	99.49%
Velocity Z	29	99.49%
TKE	24	99.5%
SDR	13	99.48%

to $m-1$) but a much lower number of retained components is enough to represent the 99.5% of the original variable variance, as previously explained.

Once the number of significant PCs and, so, the number of meta-models that have to be constructed are chosen, Krigin interpolation is applied on the correspondent PCA scores associated to the training set. To evaluate the robustness and the accuracy of the generated meta-models, a leave-one-out cross validation has been performed. In this approach, an observation from the overall available training data-set is left out and the error related to the reconstruction of such observation is computed employing meta-models based on the remaining observations. For the sake of brevity, only the results in terms of velocity components will be reported but the following considerations can be extended also to the turbulent quantities.

Figure 6.5 shows the average Normalized Root Mean Squared Errors (NRMSE) across all the PCA scores for the reconstruction of velocity components of each left-out simulation within the input parameter space. It can be observed that the leave-one-out reconstruction error is below the 7% for the most of the sampled points and it becomes higher only for operating conditions which are located near the limits of the input parameter space. This can be ascribed to the PCA methodology which tries to compress a non-linear hyper-surface (represented by the observations blue curve) to only one hyper-plane (red plane) in the data space, introducing higher discrepancies in the boundary regions, as highlighted in Figure 6.6.

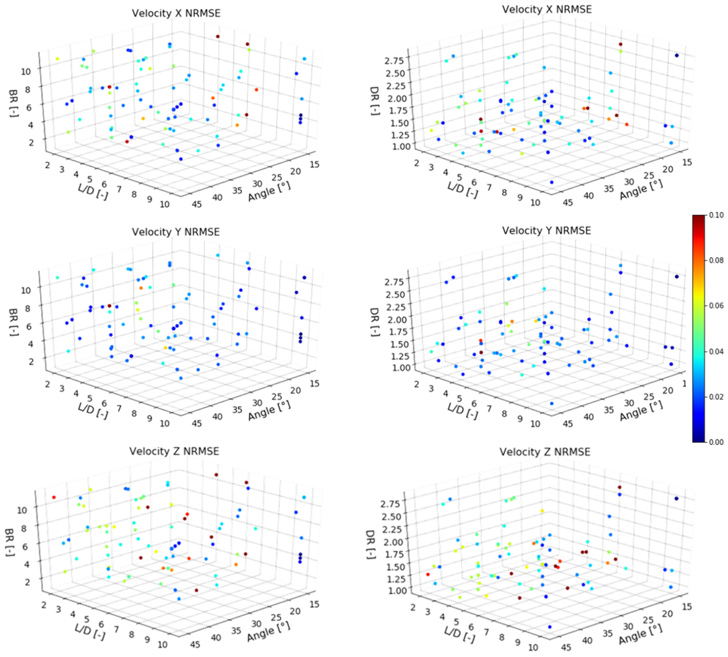

Figure 6.5: NRMSE cross-validation errors for the training set in the input parameter space (velocity components).

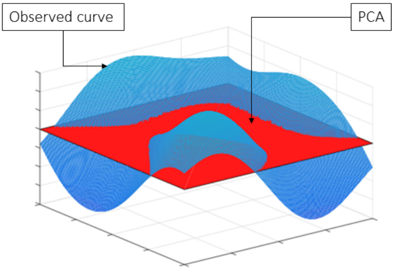

Figure 6.6: PCA representation in the data space: a non-linear hyper-surface is projected to a hyper-plane (modified from [145]).

Moreover, it would be interesting to understand the behaviour of meta-models specifically for each PC, remembering that the most of system information is encoded by the first PCA modes. For this purpose, Figure 6.7 shows the computed NRMSE across all the training set for each PC on the left and the parity plots on the right in which the observed PCA scores values are plotted against their values predicted by meta-models.

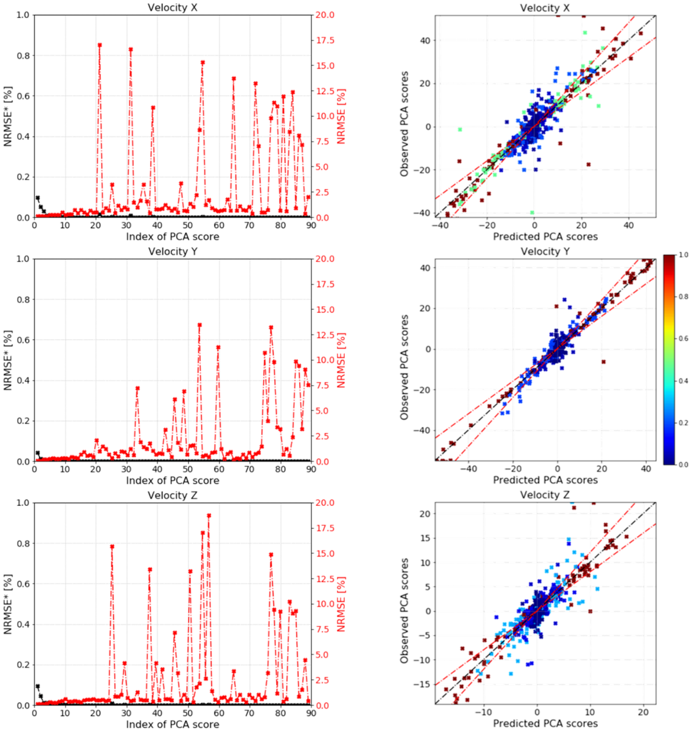

(a) (b)

Figure 6.7: (a) NRMSE and NRMSE trends and (b) parity plots for the PCA scores prediction. Red dotted lines represent the 10% of relative error.*

Also in this case, only the results of the velocity components are reported. In Figure 6.7a, the red line represents the standard NRMSE whereas the black line corresponds to the product of the NRMSE with the related PCA score eigenvalue in order to take into account their relative importance (NRMSE*). Considering the shape of the curves and that the NRMSE increases for high-order PCs, it is possible to identify a low-error range in which the number of the retained PCs has to be located. At the same time, in Figure 6.7b, the reported values are colored as a function of the associated PCA score eigenvalues, highlighting a satisfactory level of accuracy for low-order PCA scores (high encoded data variance) whose values are located within the 10% of relative error (red dotted lines). On the contrary, the error arises moving towards higher-order PCs but their contributions can be neglected during the reconstruction or the prediction due to both their lower values and the lower amount of original data variance which they represent, as explained before. Therefore, the previous considerations demonstrate the goodness of the sampled training points of the DoE and the accuracy of the generated meta-models for the prediction of PCA scores values.

For further validation, the generated effusion model has been employed to predict the velocity and turbulence profiles at unexplored operating conditions, not included in the training set (see Table 6.4). These new sampled points form the validation set which allows to prove the robustness of the model, as generally carried out in the context of predictive ROMs [189].

It is worth to note that these design points have been chosen starting from the median values of each input parameter (DP1) and then moving to the boundaries of the input parameter space, varying one parameter at time. In this way, it is possible to investigate separately their effect on the ROM. The accuracy of the developed model for the prediction of the original variables of interest can be analyzed from Figure 6.8. In this figure, the parity plots for the predicted velocity components fields all over 2D profile are reported. Also in this case, the discrepancy between the observed and the predicted values is below 10% (represented by the

Table 6.4: Input parameters values for the validation set.

Design Point	α	L/D	BR	DR
1	30°	5	5	1.25
2	40°	5	5	1.25
3	20°	5	5	1.25
4	30°	2	5	1.25
5	30°	8	5	1.25
6	30°	5	5	1
7	30°	5	5	2.5
8	30°	5	9	1.25
9	30°	5	1	1.25

dotted red lines) for most of the validation design points. Only for DP4, the prediction error increases probably due to the lower L/D ratio for which the flow field at hole outlet is strongly different from that of the other investigated operating conditions. However, the effusion cooling systems of aeroengine combustors are generally characterized by higher L/D values to much more exploit the convective heat transfer within the holes and the related heat sink effect. Therefore, these results prove the feasibility of the proposed approach for the effusion cooling modelling of such systems.

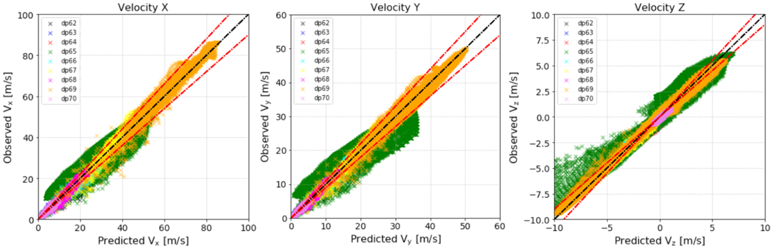

Figure 6.8: Parity plots for the prediction of velocity components at hole outlet for the validation set. Red dotted lines represent the 10% of relative error.

6.2.2 RANS SH validation

As described in Chapter 4, the developed MATLAB code is then coupled with ANSYS Fluent in order to provide run-time the velocity and turbulence profiles which are then employed as boundary conditions by the CFD solver at hole discharge. The coupled simulations have been carried out for all the design points of the validation set, employing a RANS approach. Comparing the EM calculation with the CFD and the FLAT cases, it is possible to highlight the impact of the effusion model on the prediction of the jet evolution. For the sake of brevity, only DP1 results will be shown in the following whereas quantitative analyses about the other design points are reported in Appendix A.

Figure 6.9 shows the velocity magnitude distribution on the mid-plane for each performed simulation in DP1 case. Observing the topology of the fluid flow within the hole as computed by the CFD calculation, an acceleration and an high-speed regions can be identified on the windward wall whereas a separation and a low-velocity regions occur next to the hole entrance on the leeward side as a consequence of the feed direction of the coolant. A second leeward acceleration zone is then located near the

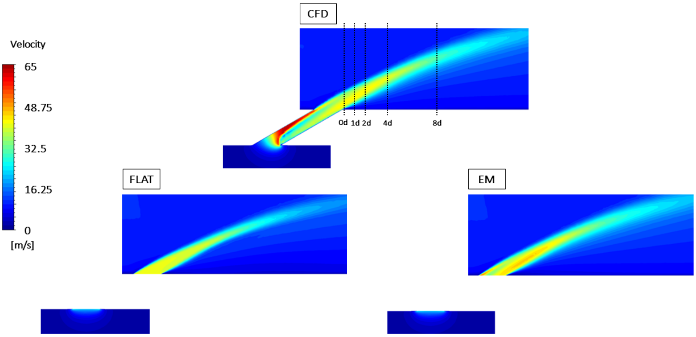

Figure 6.9: Velocity magnitude distribution on the mid-plane of the single-hole geometry for the performed simulations (DP1). Black dotted lines represent the five stream-wise locations for the quantitative comparison.

hole outlet due to the detachment of the separation bubble. Therefore, two different velocity peaks around a low-momentum region can be noted at the injection plane, leading to a lift-off and to a high penetration of the coolant jet justified by the high operating BR. Moving to EM and FLAT simulations, a very good qualitative agreement is achieved by the first one which is able to reproduce the same flow features. On the contrary, the latter is characterized by lower velocity gradients, leading to a wrong computation of jet diffusion and penetration. In fact, the developed model allows to properly predict the velocity and turbulence fields at hole discharge, as highlighted by Figure 6.10. Despite some differences in terms of absolute values, the CRVP and the related high Turbulent Kinetic Energy (TKE) region coming from the hole are well computed by EM simulation, resulting in the same CFD behaviour for the main-coolant interaction. The accuracy of the ROM is similar for all validation set.

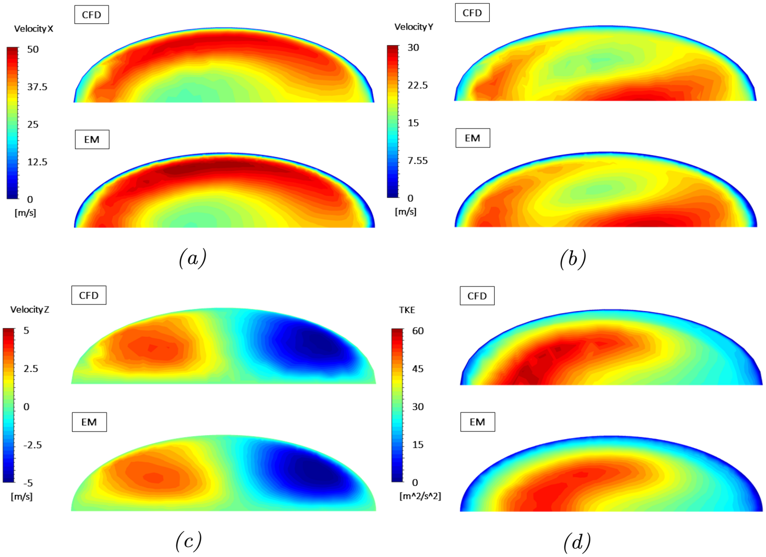

Figure 6.10: Comparison between CFD and EM profiles at hole outlet: (a) velocity X, (b) velocity Y, (c) velocity Z and (d) TKE.

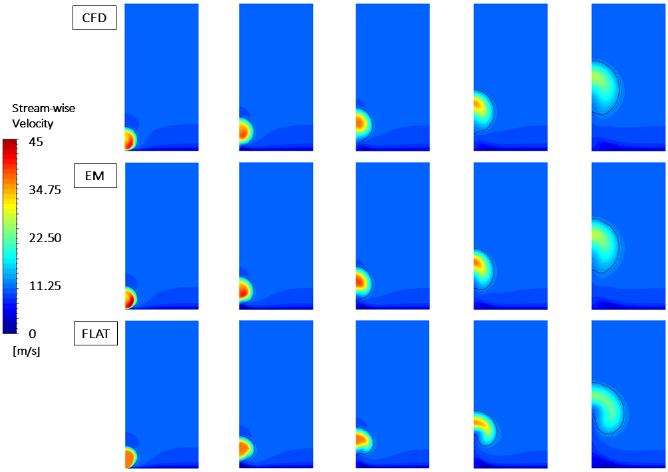

Figure 6.11: Stream-wise velocity distributions for $X/D = 0, 1, 2, 4, 8$ planes normal to jet direction (from left to right).

For a deeper understanding, the velocity distributions computed at different planes downstream the hole exit ($X/D = 0, 1, 2, 4, 8$) are reported in Figure 6.11 and 6.12, separating the stream-wise and the span-wise velocity components in order to highlight the secondary flows formed within the cooling jet. The span-wise velocity is defined as $V_{yz} = \sqrt{\bar{V_y}^2 + \bar{V_z}^2}$, representing the tangential velocity with respect to the considered plane. Tangential velocity vectors are overlapped in Figure 6.12. As the coolant comes out from the hole ($X/D = 0$), the CRVP can be observed in the CFD and EM simulations whereas it is much less intense for the FLAT case. Moving downstream, the central core of the jet lift-off from the surface and, at the same time, the main flow is entrained into the jet, spreading the coolant over an increased area. For all the investigated planes, these effects are correctly estimated by the EM calculation, providing a significant improvement in terms of prediction of counter-rotating vortices intensity and location as well as of the jet evolution within the mainstream air. In particular, the effect of entrainement is higher in

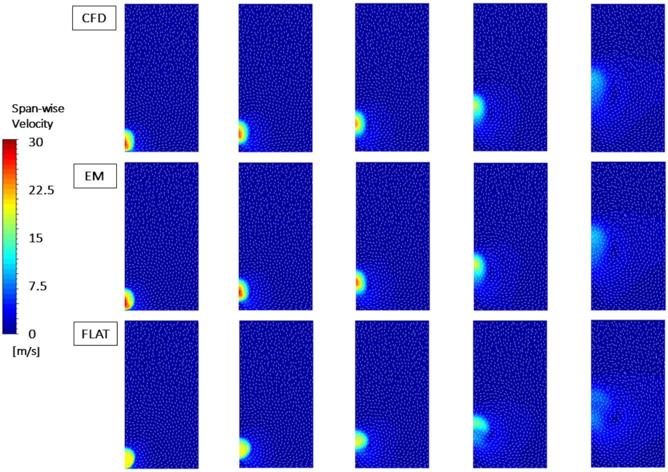

Figure 6.12: Span-wise velocity distributions for $X/D = 0, 1, 2, 4, 8$ planes normal to jet direction (from left to right).

FLAT calculation, causing a more pronounced lateral spreading of the jet. Moreover, the span-wise velocity peaks in the jet core are not predicted, leading to an incorrect computation of the position of the counter-rotating vortices centres.

In order to quantitatively highlight the improved accuracy provided by the proposed effusion model, a comparison of stream-wise and span-wise velocity profiles on the mid-plane along the normal to the wall are reported in Figure 6.13 for the same locations. A fairly good agreement between CFD and EM results is achieved: slight differences appear in the near-wall region and in the computation of the velocity peak values whereas their location and the penetration of the jet are well predicted at all stream-wise positions. On the contrary, the FLAT results are characterized by a global under-estimation all over the span of the computational domain as a consequence of the uniform injection velocity, proving the deep influence of the flow pattern at the injection plane on the main-coolant interaction.

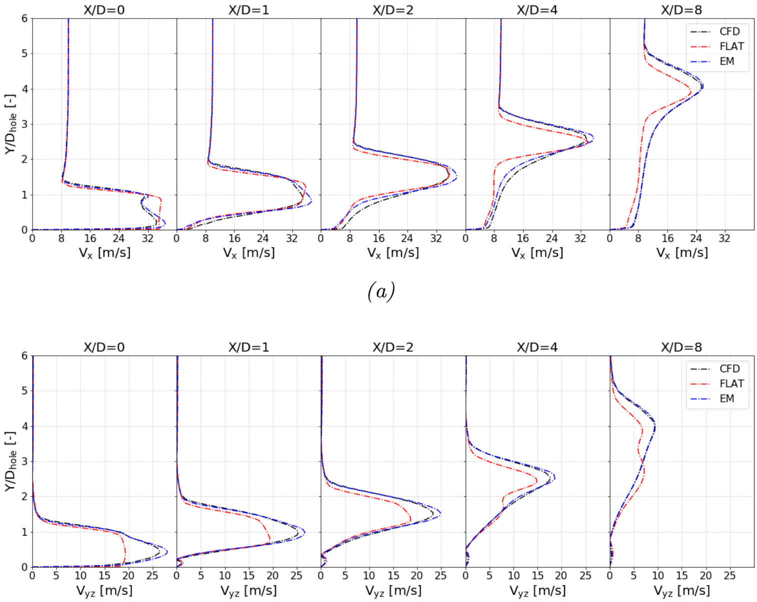

(a)

(b)

Figure 6.13: (a) Stream-wise and (b) span-wise velocity profiles along the normal to the wall on the mid-plane for $X/D = 0, 1, 2, 4, 8$.

Finally, a numerical analysis of the impact of the effusion modelling on the film coverage in terms of adiabatic effectiveness can be carried out by observing the TS concentration distributions on the wall, since the adiabatic effectiveness has a direct influence also on the wall temperature prediction in CHT framework. Figure 6.14 couples the qualitative comparison of the adiabatic effectiveness contours with the quantitative laterally averaged distributions. It can be note that the effectiveness values are low all over the wall due to the high operating BR which causes the immediate lift-off of the jet and the entrainement of the mainstream air related to the intense CRVP. Higher values are located in the near-hole region ($2.5 < X/D < 5$) where a low-velocity region occurs and the coolant

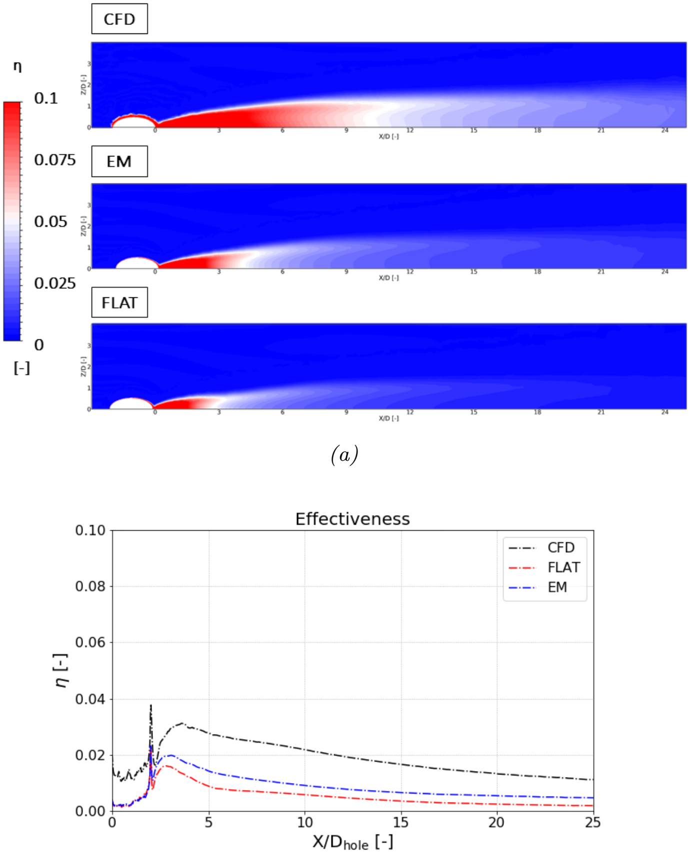

(a)

(b)

Figure 6.14: (a) Adiabatic effectiveness distributions and (b) laterally average comparisons.

tends to recirculate. In this case, the level of agreement is lower for both EM and FLAT cases which tend to under-predict the film coverage also moving downstream along the wall. This can be probably ascribed to the slightly different mesh grids around the injection region with respect to CFD case due to the present/absence of the pipe and to the different employed boundary condition for the calculations in which the hole is not discretized (unitary value for the TS). This is highlighted in Figure 6.15 where the difference between CFD and EM/FLAT results at the leading edge of the hole imprint in terms of TSC can be observed: in the first case, a low-value region due to the effect of the main flow (TSC equal to zero) is present whereas this behaviour does not appear in the other two simulations. In this sense, the grids influence the numerical results since a uniform unitary value has to be employed as boundary condition for EM and FLAT simulations as opposed to CFD case where the passive scalar transport equation is solved also within the effusion hole. Analogous considerations can be also extended to the RANS MH validation and to the SBES SH validation which will be reported in the following.

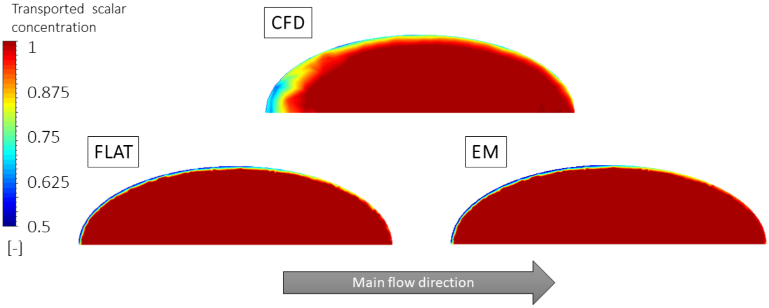

Figure 6.15: Comparison between CFD, EM and FLAT profiles at hole outlet in terms of TSC.

6.2.3 RANS MH validation

To investigate the effect of a more proper prediction of the flow field at hole outlet in presence of the typical superposition effect, the effusion model has been applied and validated also on the multi-hole configuration described in Section 6.1.1. Also in this case, RANS calculations have been performed, considering for the effusion system the unexplored operating conditions reported in Table 6.5.

Table 6.5: Input parameters values for the multi-hole geometry.

α	**L/D**	**BR**	**DR**
20°	6	1/3/5	1.5

Figure 6.16 shows the velocity magnitude contours on the mid-plane of the computational domain for all the investigated BRs for the first three rows. As generally observed in presence of uniform main flow, the consecutive jets are closer to the wall moving downstream due to the superposition effect [190], allowing the increase of film coverage together with a gradual mass addition into the film layer. This trend is more evident as the operating BR decreases, since the cooling jets tend to remain in the near-wall region and lower interaction between the coolant and the main flow occurs. From a qualitative point of view, a more consistent computation of the flow pattern in the region next to the coolant injections is introduced by the effusion model, comparing the relative solution to the full-mesh CFD result. On the contrary, the FLAT distributions are characterized by a uniform velocity zone as a consequence of the flat velocity and turbulence profiles imposed at the inlet boundaries.

As reported for the single-hole geometry, a quantitative comparison has been carried out by considering analogous stream-wise and span-wise velocity profiles at several locations ($X/D = 0, 1, 2, 5$) next to hole outlets. For the sake of brevity, only the profiles extracted downstream the second effusion hole will be reported, being able to appreciate clearly the superposition effect of the previous coolant injection. Figure 6.17 and 6.18 show respectively the mentioned comparisons. As far as the stream-wise profiles are concerned, two different velocity peaks can be identified at each stream-wise position, especially for high operating BRs: the bottom peak is related to the immediately upstream injection whereas the top one is due to the coolant coming from the previous effusion hole. For all the investigated operating conditions, a very good agreement between CFD and EM cases is achieved for both the stream-wise and span-wise

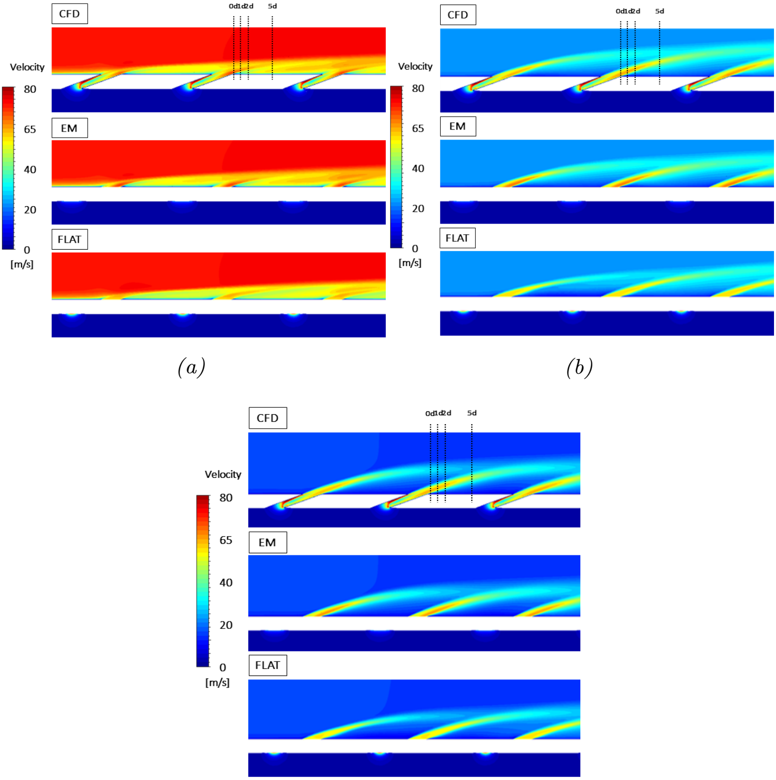

(a) (b)

(c)

Figure 6.16: Velocity magnitude distributions on the mid-plane of the multi-hole geometry for the performed simulations: (a) $BR = 1$, (b) $BR = 3$ and (c) $BR = 5$. Black dotted lines represent the five stream-wise locations for the quantitative comparison.

profiles. Instead, the flat profile leads to an under-estimation of the jets penetration as for the single-hole case and to a not correct computation of the span-wise spreading of the jets. Slight discrepancies between the CFD and EM profiles can be detected moving towards the lower operating BR of the plate. This is due to the fact that, for $BR = 1$, the parameter is

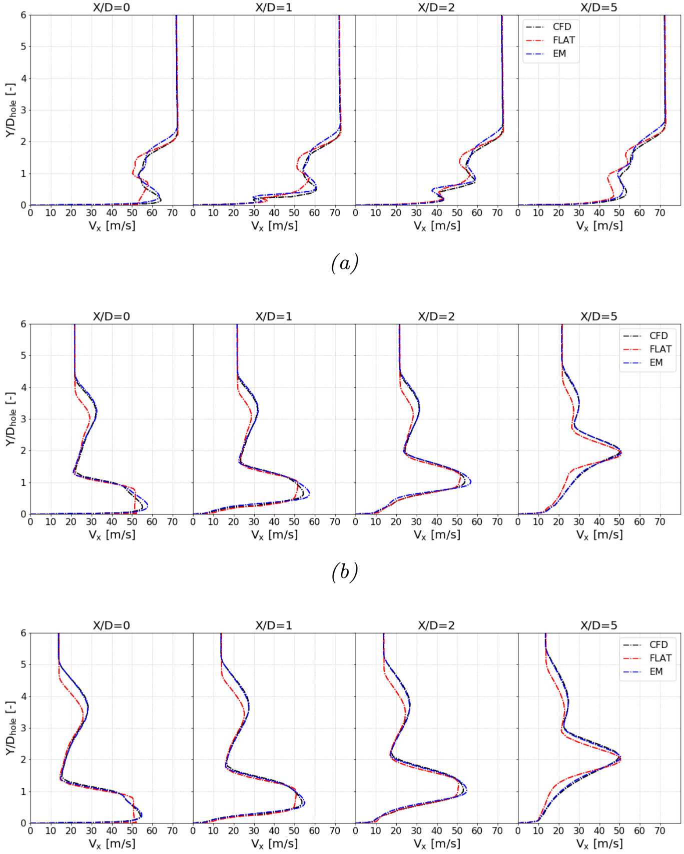

(a)

(b)

(c)

Figure 6.17: Stream-wise velocity profiles along the normal to the wall on the mid-plane for $X/D = 0, 1, 2, 5$ *downstream the trailing edge of the second hole imprint: (a)* $BR = 1$*, (b)* $BR = 3$ *and (c)* $BR = 5$*.*

assuming a value which is located at the boundaries of the input parameter space where the ROM prediction is worse, as previously specified (Figure 6.6). In fact, higher differences can be observed between the CFD and the predicted velocity and turbulence patterns at hole outlet, as shown in

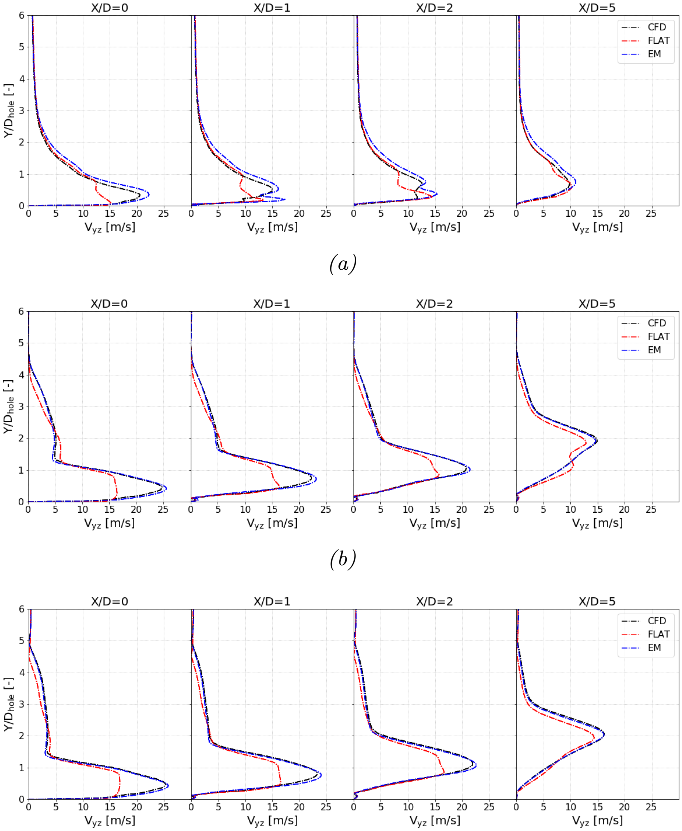

(a)

(b)

(c)

Figure 6.18: Span-wise velocity profiles along the normal to the wall on the mid-plane for $X/D = 0, 1, 2, 5$ downstream the trailing edge of the second hole imprint: (a) $BR = 1$, (b) $BR = 3$ and (c) $BR = 5$.

Figure 6.19. The low-velocity region computed by the effusion model is shifted towards the leading edge of the hole and a slight under-prediction of TKE occurs.

Such differences affect the prediction of the film coverage along the wall, as highlighted in Figure 6.20 in terms of laterally averaged adi-

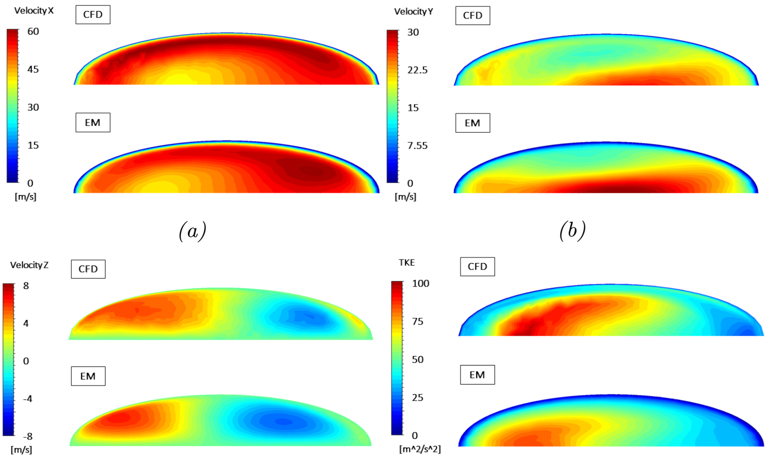

(a) *(b)*

(c) *(d)*

Figure 6.19: Comparison between CFD and EM profiles at second hole outlet for $BR = 1$*: (a) velocity X, (b) velocity Y, (c) velocity Z and (d) TKE.*

abatic effectiveness. Due to the added mass in the film layer and to the superposition effect, the effectiveness increases moving downstream along the plate for all the operating conditions, showing relative peak values in correspondence of each effusion row. The level of agreement of the effusion model depends on the investigated operating condition: a satisfactory accuracy is achieved for higher BRs whereas a general under-estimation is computed for the remain case for which the flat profile seems to behave better. According to the previously mentioned reasons, these differences are probably related to the different regime in which the system works. Considering the operating DRs, the Mixing Regime (MIX) occurs for $BR = 1$ case whereas the others are characterized by the Penetration Regime (PEN), affecting the coolant distribution on the wall. On the opposite with respect to the first one, the latter are completely dominated by a complex interaction of excessive coolant penetration and augmented turbulent diffusivity due to the high velocity ratio for which it is mandatory a more proper velocity computation in the near-wall region. Moreover, the effect of the main flow at the hole outlets in terms of TSC (Figure 6.15) decreases moving towards higher BRs as a consequence of the higher momentum of the effusion jets, approximating more and more the unitary value condition. Therefore, for these cases the effusion model succeeds in predicting more consistent velocity and turbulence profiles with respect to the ones computed by FLAT simulations.

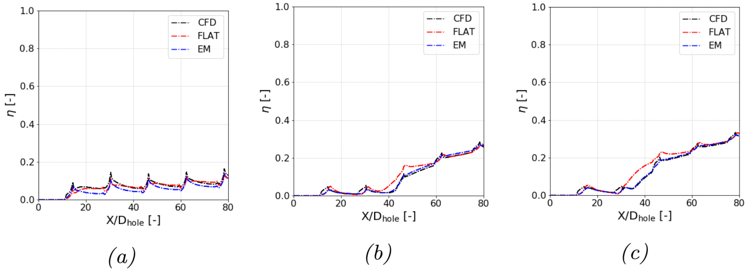

Figure 6.20: Comparison of laterally averaged adiabatic effectiveness along the multi-perforated plate: (a) $BR = 1$, (b) $BR = 3$ and (c) $BR = 5$.

6.2.4 SBES validation

Since scale-resolving approaches are generally mandatory to properly predict the reactive flow field within an aeroengine combustor, a SBES calculation of the single effusion hole has been performed for the same operating condition investigated in Section 6.2.2 and reported in Table 6.4. Such investigation provides an important assessment of the feasibility of the developed effusion model also in an unsteady framework.

In Figure 6.21, time-averaged velocity distribution is shown in the mid-plane of the computational domain for each computed simulation.

Similarly to RANS analysis, the jet tends to lift-off due to its high momentum compared to the main flow one which is not capable to main-

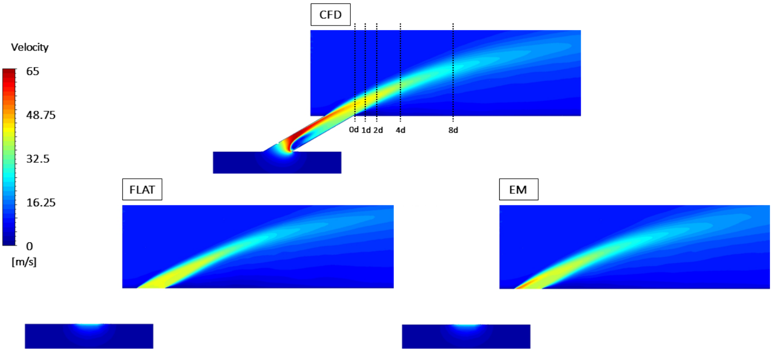

Figure 6.21: Time-averaged velocity magnitude distributions on the mid-plane of the single-hole geometry for the performed SBES simulations for DP1. Black dotted lines represent the five stream-wise locations for the quantitative comparison.

tain the coolant in proximity of the wall. Observing the CFD simulation, characteristic features regarding the topology of the flow within the hole can be again detected: the high-velocity jetting region on the windward wall and the low-momentum region on the leeward side with a shear layer separating them [191, 192]. However, comparing time-averaged velocity contour with respect to RANS results shown in Section 6.2.2, the separation region predicted by SBES is characterized by higher intensity and it extends on the leeward side for all the length of the hole. On the contrary, in RANS calculation the low-velocity region is located in the central part of the orifice causing a re-acceleration of the fluid next to leeward wall which is instead absence in the unsteady solution. This leads to a higher deflection of the jet exiting the perforation and to a lower penetration in the mainstream in SBES calculation. In addition, the nature of the scale-resolving approach, which is able to better solve the turbulent mixing, contributes to this effect and, therefore, a greater diffusion of the coolant occurs compared to RANS calculation.

In this sense, Figure 6.22 shows the shielding function distributions on the mid-plane for the SBES single-hole geometry simulations, highlighting

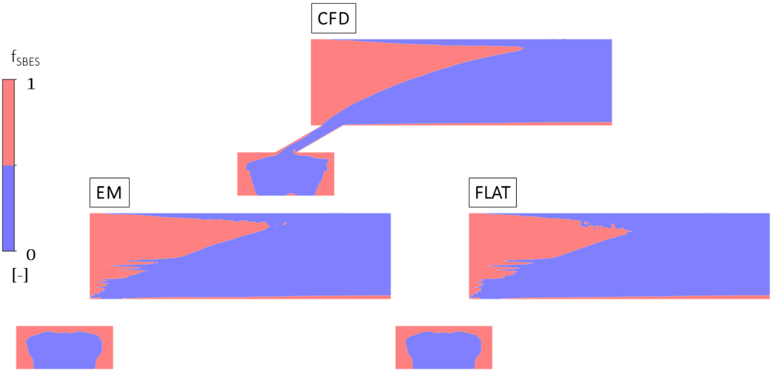

Figure 6.22: Shielding function distributions on the mid-plane of the single-hole geometry for the performed SBES simulations for DP1.

the RANS-like ($f_{SBES} = 1$) and the LES-like ($f_{SBES} = 0$) solved regions. It is worth to note how the three distributions appear similar and how most of the computational domain exhibits a LES behaviour, except for the near-wall regions (according to the SBES formulation) and the zone next to the main flow inlet due to the low turbulence level prescribed here as boundary condition. It is important to observe that also the effusion hole is solved in a LES manner in the CFD simulation, leading to a proper computation of the turbulent and vortical structures which obviously impact on the jet evolution and on the main-coolant interaction.

The different structures of the flow field within the hole computed by RANS and SBES justify the discrepancies between CFD and EM simulations, considering that the latter provides anyway a more consistent jet structure and velocity distribution with respect to FLAT case. In fact, no velocity peaks next to hole exit are present here. Figure 6.23 shows the time-averaged velocity and TKE fields at the end of the orifice for CFD and EM cases. It can be noted that the CRVP is computed in both simulations (no present in FLAT calculation due to the uniform imposed profile) but the EM pattern is more similar to the RANS results. Here, the low-velocity region is located in the centre of the hole imprint whereas

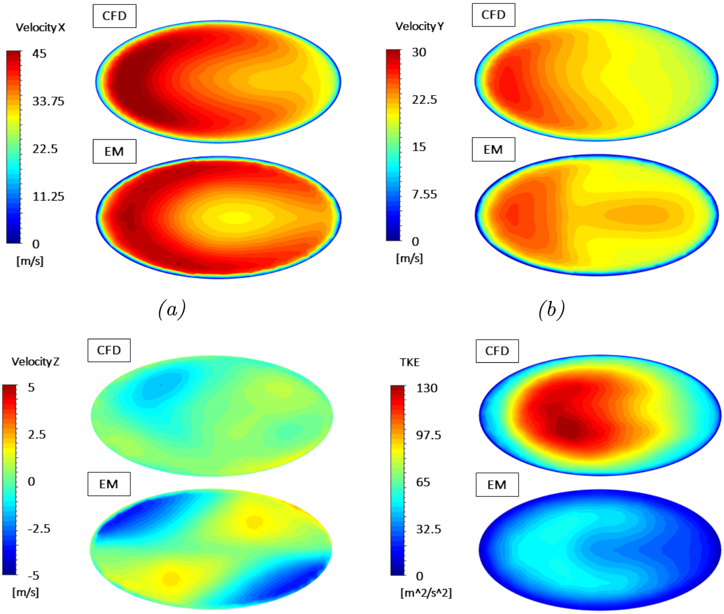

(a) *(b)*

(c) *(d)*

Figure 6.23: Comparison between CFD and EM time-averaged profiles at hole outlet: (a) velocity X, (b) velocity Y, (c) velocity Z and (d) TKE.

it is attached to the hole trailing edge in CFD simulation. Moreover, a significant under-estimation of the generated TKE occurs at hole exit. These differences can be ascribed to the RANS-based formulation of the developed effusion model, as described in Section 6.2.1.

Analogous considerations can be derived as far as instantaneous and RMS velocity distributions on the mid-plane are concerned (see Figure 6.24). In this case, it can be observed how the scale-resolving approach is able to solve the generated turbulent structures coming from the hole and related to the interaction between the coolant jet and the main flow. Comparing the results of the three methodologies, CFD and EM calculations show similar levels of velocity fluctuations which are much higher

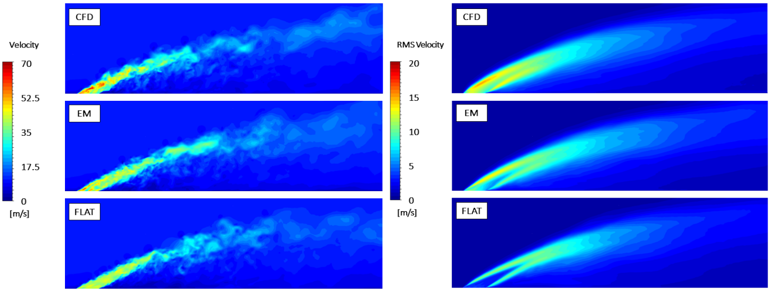

(a) *(b)*

Figure 6.24: (a) Instantaneous and (b) RMS velocity magnitude distributions on the mid-plane of the single-hole geometry for the performed SBES simulations for DP1.

compared to the ones computed in FLAT simulation, especially in the core region of the jet next to the hole outlet and on its windward side. As previously mentioned, the effusion model is able to also predict a turbulence profile which allows a better computation of the velocity fluctuations around the injection region in combination with a more proper 2D velocity distribution. However, some differences still remain along the core and the leeward regions of the jet due to the under-estimation of TKE and RANS topology predicted by the effusion model at the boundary.

In this context, it would be interesting to examine the characteristic vortices occurring within the shear layer of the cooling jet, as highlighted in Figure 6.25, where Q-criterion plots are presented together with skin coefficient visualization on the wall. Like the CFD simulation, the EM solution is characterized by the present of vortical structures in the core region (A) of the jet related to the development of K-H instabilities generated within the holes which are, instead, absent in the FLAT case. Moreover, leading edge and leeward-side vortices (B) can be distinguished as result of the interaction between the shear layer of the jet and the surrounding flow together with the horseshoe and wake vortices (C) located respectively at the base and on the leeward side of the coolant jet. It is

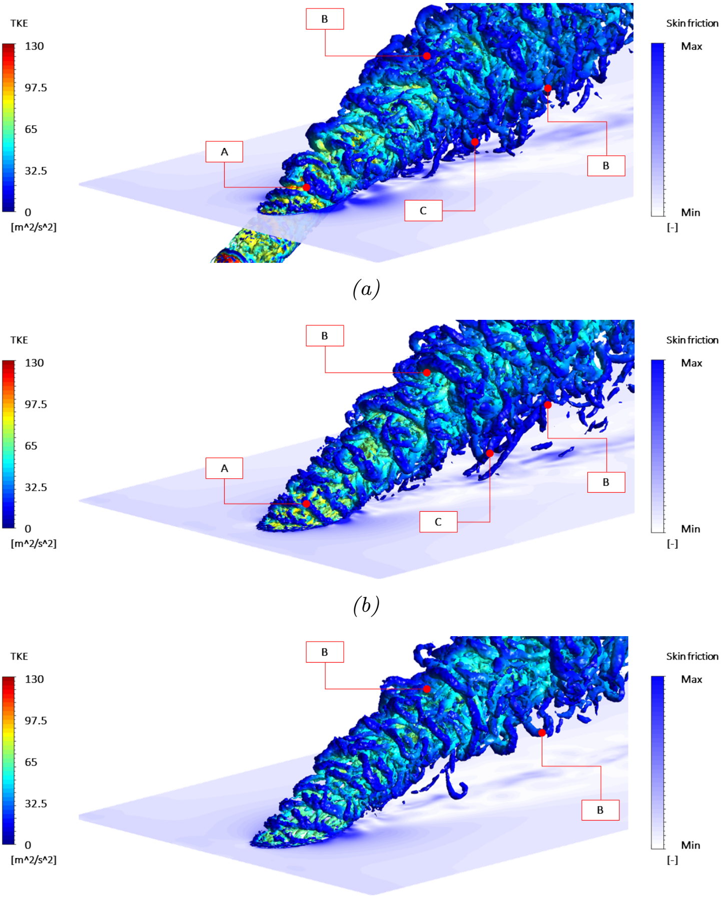

(a)

(b)

(c)

Figure 6.25: Q-criterion plots together with skin friction coefficient visualization on the wall: (a) CFD, (b) EM and (c) FLAT.

worth to note that such structures are less visible (B) or absent (C) in FLAT solution.

For a quantitative assessment of the accuracy of the developed effusion model, stream-wise and span-wise time-averaged velocity profiles on the

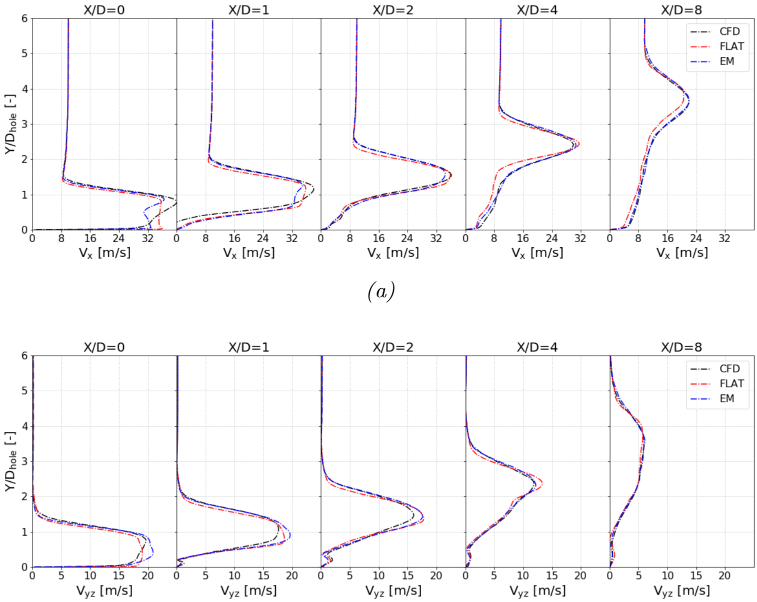

(a)

(b)

Figure 6.26: (a) Stream-wise and (b) span-wise time-averaged velocity profiles along the normal to the wall on the mid-plane for $X/D = 0, 1, 2, 4, 8$.

mid-plane along the normal to the wall for different downstream locations ($X/D = 0, 1, 2, 4, 8$) are reported in Figure 6.26. In this case, the correspondence between CFD and EM results is lower compared to the RANS validation, especially in the first locations ($X/D = 0$ and $X/D = 1$) and in the near-wall region where the influence of the mentioned differences in the flow pattern at hole discharge is stronger. The simulations where the hole is not discretized tend to under-predict and over-estimate respectively the stream-wise and the span-wise peak velocities located around $Y/D = 1$. Such differences can be ascribed to RANS-based velocity and turbulence profiles predicted by the effusion model. However, a significant improvement compared to the FLAT case can be observed in terms of jet penetration, shape of the profiles and location of the peak values. Moving downstream, a very good agreement between CFD and EM simulations is achieved both in the freestream and near-wall zones since, here, the better prediction performed by the effusion model of the CRVP structures coming from the hole and of the characteristic vortical structures becomes important for a proper resolution of the main-coolant interaction.

For a deeper understanding of the impact of velocity fluctuations on the main-coolant interaction and consequently on the development of the characteristic vortices, RMS velocity magnitude profiles on the mid-plane along the normal to the wall are also reported in Figure 6.27 for the same locations. Also in this case, a significant improvement compared to FLAT case is highlighted and a fairly good agreement with CFD simulation is achieved. As qualitatively observed, the coupling of the effusion model with the CFD solver is able to accurately compute the location and the peak value of the velocity fluctuations related to the development of leading edge vortices (top peak) from the hole outlet and moving downstream. At the same time, an under-prediction can be noted in the core region and on the leeward side of the jet probably related to the under-estimation of TKE near the trailing edge of the hole imprint, due again to the RANS-based formulation of the MATLAB model.

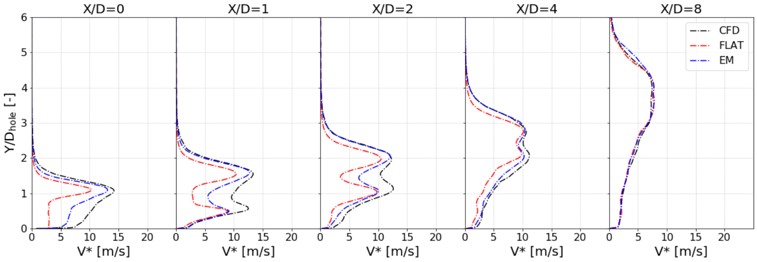

Figure 6.27: RMS velocity magnitude profiles along the normal to the wall on the mid-plane for $X/D = 0, 1, 2, 4, 8$.

In order to better analyze how the turbulent structures and the related velocity fluctuations are solved within the numerical domain according to the employed SBES approach, Figure 6.28 shows the turbulent spectrum by means of the Power Spectral Density (PSD) estimated by applying the Welch method [193] to the velocity magnitude signal. The PSD has been computed in two different positions next to the hole outlet: the first one (Figure 6.28a) is located in the RANS-solved near-wall region whereas the second one (Figure 6.28b) is included in the LES-solved freestream region ($Y/D_{hole} = 1$). This analysis has been performed only for the CFD and the EM cases since the two simulations show a similar behaviour from a turbulent point of view. For each position, the spectra appear consistent between each other and no frequency peak is measured due to the loss of the jet coherence in both positions. In the near-wall region, lower values of PSD are computed probably due to the presence of the wall which partially confines here the vortical structures.

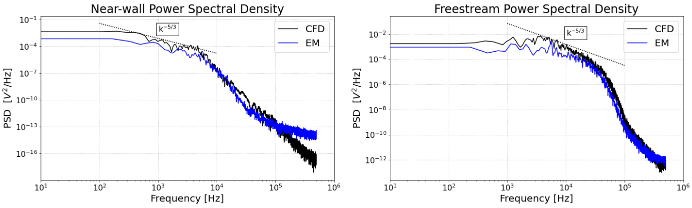

(a) *(b)*

Figure 6.28: PSD Welch estimate of the velocity magnitude signal in two different positions next to the hole outlet: (a) Near-wall and (b) Freestream.

Finally, a comparison in terms of adiabatic effectiveness is considered, since a correct prediction of the film coverage is mandatory for a reliable estimation of wall temperature when effusion cooling systems are analyzed in reactive condition. Figure 6.29 shows the TS distributions together with the laterally average along the wall. Observing the reported values, the adiabatic effectiveness is extremely low due to the detachment of the jet immediately after the injection as a consequence of the high operating BR. From both a qualitative and quantitative point of view, higher errors are located for $X/D < 5$ where a strong over-prediction occurs in FLAT

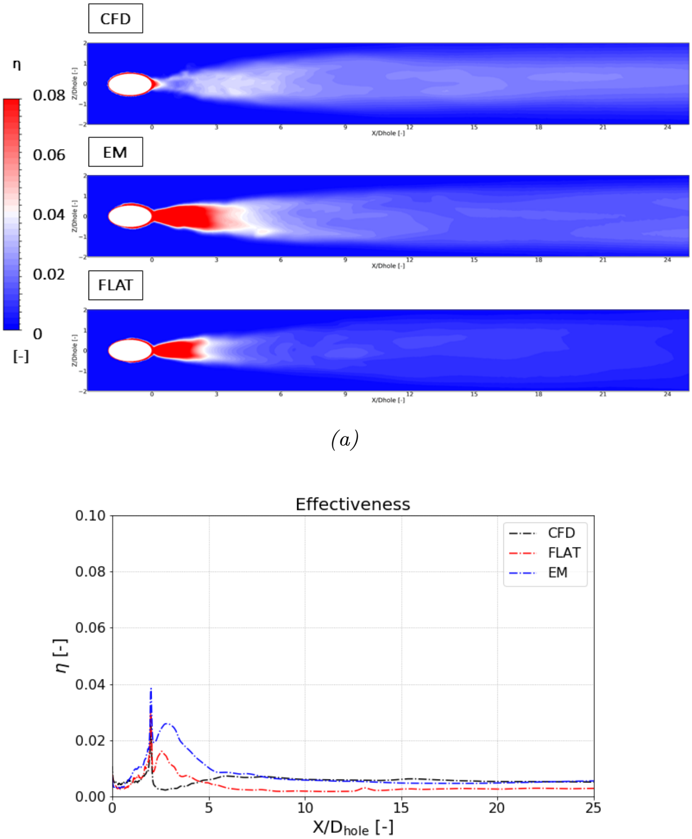

(a)

(b)

Figure 6.29: Time-averaged (a) adiabatic effectiveness distributions and (b) laterally average for SBES simulations.

and EM simulations. This can be again ascribed to the differences in the computational grids in this region and to the different employed boundary condition for the transported scalar (unitary value) together with the TKE under-estimation in FLAT and EM cases. However, in this case the adiabatic effectiveness discrepancies are limited to the region next to the hole outlet due to the higher levels of turbulent mixing predicted by the unsteady approach. Therefore, the level of agreement for the EM case increases moving downstream and the same laterally averaged value of adiabatic effectiveness are computed compared to the numerical reference (CFD). On the contrary, the FLAT calculation constantly under-predicts the film coverage. The presence of the transported scalar on the wall is caused by the jet diffusion for which a proper computation of the turbulent mixing is mandatory. In this sense, it is important to note that the application of the effusion model allows to decrease the jet penetration and to enhance its diffusion, approaching the CFD simulation, as highlighted in Figure 6.30, where the time-averaged TS distributions on the mid-plane are shown.

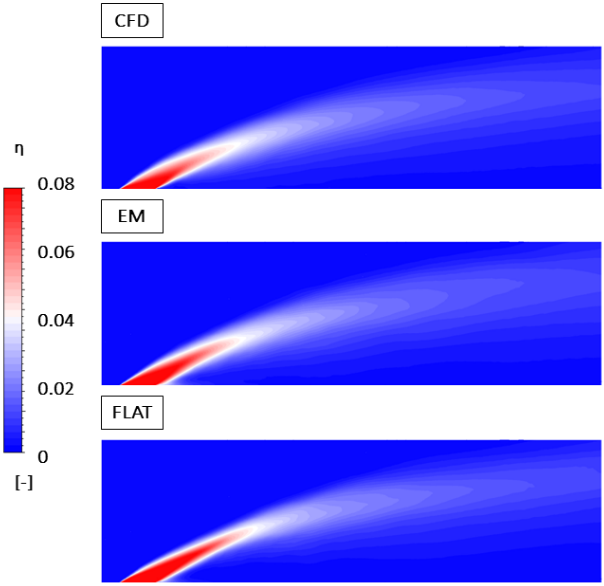

Figure 6.30: Time-averaged TS distributions on the mid-plane.

6.3 Concluding remarks

In the present chapter, the innovative approach for effusion modelling in CFD calculations is generated. The effusion model, developed as a MATLAB code during a pre-processing phase, is then coupled with the CFD solver to provide run-time the velocity and turbulence profiles at the injection points. The coupling strategy has been validated in the context of steady and unsteady calculations for single-hole and multi-hole geometries. This methodology allows to obtain consistent results compared to a full-mesh CFD simulation in terms of flow pattern at the injection region and, therefore, in terms of jet penetration and film coverage. Not computing the flow within the effusion holes, a reduction of the computational costs is permitted, especially when scale-resolving approaches are required. The numerical results obtained with the novel approach have been compared to a full-mesh and to a flat profile calculations where the latter represents the standard method employed in technical literature.

Regarding the steady calculations, the effusion model is able to provide similar flow topology at hole outlets with respect to full-mesh simulations, well predicting the characteristic flow features related to the passage within the effusion holes. Consequently, a significant improvement in the agreement with full-mesh results is obtained compared to the use of flat profiles when stream-wise and span-wise velocity profiles downstream the hole imprint are considered. Different levels of accuracy are noted depending on the investigated operating conditions. In particular, the effusion model shows lower predictive capabilities when the input parameters employed for DoE explorations assume values located at the boundaries of the input parameter space. This can be ascribed to PCA definition. A not proper prediction can be also noted in terms of film coverage on which a strong influence is exhibited by the unitary value boundary condition at hole outlets employed for the transported scalar in the no-holes cases. However, general improvements are achieved with respect to flat profiles approach which usually tends to under-estimate the film coverage.

As far as scale-resolving validation is concerned, the comparison between the full-mesh and the modelled velocity and turbulence profiles at hole outlet highlights higher discrepancies due to the RANS-based formulation of the effusion model. In spite of this, a better prediction of velocity fluctuations is carried out against to flat profiles case, resulting in a fairly good agreement in terms of jet diffusion and film coverage downstream the injection region. By computing consistent velocity gradients, the effusion model gives rise to a correct estimation of the intensity of the typical vortical structures which characterize the JICF phenomenon. Moreover, in this case the computational saving is even higher considering the fine grids which are required for a proper discretization and resolution of the flow within the effusion holes in unsteady simulation context.

Chapter 7

Non-reactive combustor simulator

In Chapter 6, the novel effusion model has been applied and validated on simple configurations with the presence of an uniform main flow over a flat effusion plate. However, the typical flow field within an aeroengine combustor is much more complex and strong interactions between a swirling main flow coming from the burner and the film cooling generated by the effusion system generally occur. In fact, the impact of the high velocity swirling jets on the multi-perforated liners may completely disrupt the film coverage, causing an increase of local heat loads which can become critically for the thermal resistance of the liners. Moreover, the high levels of unsteadiness can enhance the turbulent mixing between the main flow and the film layer which is one of the main causes of the adiabatic effectiveness reduction.

For this purpose, a numerical analysis of a non-reactive single sector planar rig representative of a real combustor geometry has been performed. The test case is equipped with an effusion cooling system in order to investigate the effect of the swirling main flow on the coolant jets coming from the multi-perforated liner. The experimental campaign has been carried out in collaboration with AVIO AERO in the context of the European Community funded project SOPRANO (SOot Processes and Radiation in Aeronautical inNOvative combustors).

From a numerical point of view, a scale-resolving approach is mandatory to achieve a reliable prediction of the flow field and to take into account the role of the complex turbulent structures on the coolant distribution [194, 195]. As in Chapter 6, an hybrid RANS-LES model has been employed since it represents an optimal trade-off between the accuracy of a fully-LES calculation and the necessity of a low computational cost which is one of the principal guidelines in an industrial framework. Moreover, considering the complexity of the investigated case, this represents a valid assessment of such methodology for future design applications. In this context, the use of the developed approach for effusion modelling is much more relevant since it allows to avoid the fine discretization of the effusion holes, cutting down the employed computational resources but, at the same time, providing a physic-related flow pattern at hole outlets. This result is a significant improvement in the computation of the JICF phenomena, especially in presence of a complex main flow like the swirling one, which influence the correct estimation of coolant distribution and film coverage that in turn will affect the wall temperature pattern in a reactive framework.

The present chapter is structured as follows: firstly, details about the experimental facility are reported. Then, a brief summary of the main outcomes of previous experimental and numerical works is provided in order to describe the characteristic flow features of the investigated test rig and to demonstrate the correctness of the employed computational setup and turbulence model. Finally, the numerical results obtained by adopting the effusion model are analyzed, comparing them with the available experimental data and with the full-mesh reference solution. This allows to highlight the accuracy of the developed effusion model together with the computational savings and to evidence the impact on the flow solution of a RANS-based formulation for coolant injection.

7.1 Presentation of the test case

A 3D representation of the test rig together with the main geometrical characteristics of the effusion plate is shown in Figure 7.1.

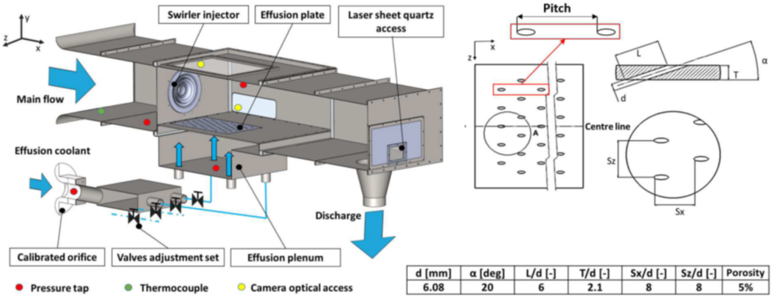

d [mm]	α [deg]	L/d [-]	T/d [-]	Sx/d [-]	Sz/d [-]	Porosity
6.08	20	6	2.1	8	8	5%

Figure 7.1: 3D scheme of the test rig (adapted from [196]).

The experimental facility is sited in an open loop wind tunnel and it is representative of a single sector of a real aeroengine combustor in a planar configuration working in ambient conditions. In fact, main air is supplied through an injector which consists in a radial swirler designed by AVIO AERO. Moving downstream, the bottom wall of test section is equipped with a multi-perforated plate, representing the effusion cooling system. A plenum chamber is located below the cooled liner and it is employed to fed the coolant air. In order to increase the spatial resolution and to facilitate a detailed investigation of unsteady structures with the instrumentation, the rig is scaled up compared to the typical engine dimensions. Regarding the effusion system, the multi-perforated plate is equipped with 55 holes in staggered configuration with a common inclination angle of 20°. In Figure 7.1, the geometrical features of the effusion holes are reported.

As far as the operating conditions are concerned, a constant pressure drop of 3.5% across the injector was set, varying instead the effusion pressure drop from 1% to 3.5% by means of a valve system. In the context of the present work, only the higher pressure drop across the effusion system has been numerically investigated.

Considering the experimental measurements, available data consist of measurements in terms of velocity with Time-Resolved Particle Image Velocimetry (TRPIV). Such experimental technique allows to characterize both the mean and the instantaneous behaviours of the system, providing information about vorticity and turbulent mixing. In addition, information about the row-to-row superposition effect and the presence of a highly unsteady main flow can be obtained [196, 197]. For this purpose, the rig is provided with three optical accesses: a quartz window is employed for the laser sheet insertion for PIV measurements whereas two ones, highlighted in yellow in Figure 7.1, have been used for the camera acquisitions.

For a detailed description of the experimental setup, the instrumentation and measurement techniques and of the investigated operating conditions, the reader may refer to [196, 197] and references therein.

7.2 Previous experimental and numerical works

To author's knowledge, the specific configuration here studied has been previously object of experimental and numerical studies carried out by Lenzi et al. [196, 197]. In the first cited work, CFD has been adopted to achieve a deeper understanding of the flow behaviour highlighted by the experiments and to demonstrate that CFD represents a valid numerical tool to predict and analyze the flow physics, showing a fairly good agreement with experimental data. In this sense, the main outcome is that the cooling jets coming from the effusion holes and their interaction with the mainstream are subjected to a strong unsteadiness which is essential to consider for a complete characterization of how the system works. In fact, the time evolution of the film cooling can highly affect the combustor operability and life-time. Instead, in [197] two different effusion plate configurations with cylindrical and with laid-back fan-shaped 7-7-7 holes in staggered arrangement were experimentally tested and compared. In this comparison, the shaped geometry exhibited a slight increase in the lateral spreading of coolant air prompted by the rotating structures of the swirler. Moreover, it seems less affected by oscillatory phenomena and swirling jet crushing. At the same time, a more defined and confined coolant sublayer is achieved for the shaped holes with respect to the cylindrical ones, providing reduced thickness of the film layer thanks to the effect of the laid-back angle. However, only the cylindrical holes configuration will be numerically investigated in the context of this work.

Regarding the results reported in [196], time-averaged and time-resolved analyses were carried out for both the swirling flow and the effusion flow fields in order to separate the macroscopic flow features (see Figure 7.2) and the contributes of unsteady vortical structures to jets evolution and main-coolant interactions (see Figure 7.3).

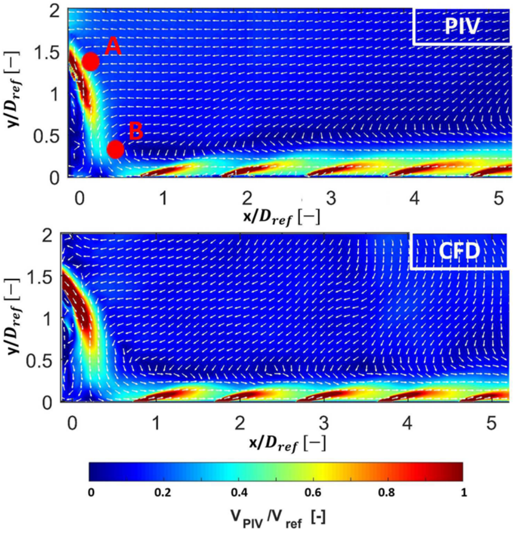

Figure 7.2: Experimental and numerical time-averaged flow fields on the mid-plane (adapted from [196]).

From time-averaged investigation, the typical features of a swirling flow can be identified with a large central recirculation region surrounded by high velocity jets. The swirling flow exhibits a high angle of aperture which gives rise to a significant vortex breakdown, leading to the described

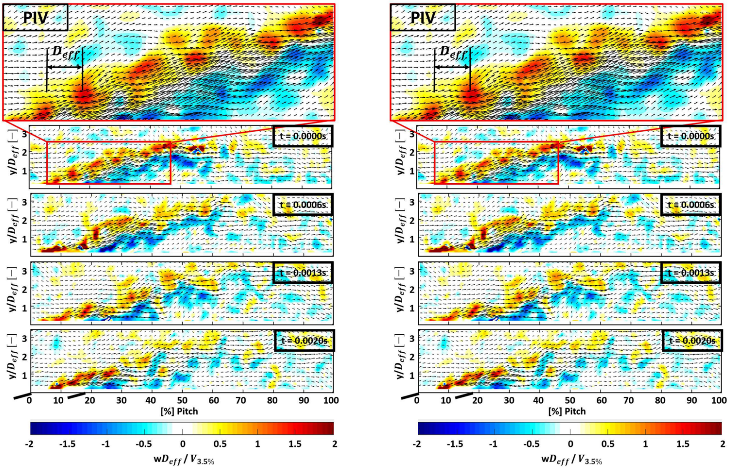

(a) (b)

Figure 7.3: (a) Experimental and (b) numerical time evolution of vorticity in the effusion flow field (adapted from [196]).

flow pattern. At the same time, the high velocity swirling jets remain in proximity of the dome, impinging on the effusion plate just before the first effusion row. Moving downstream, the swirling flow interacts with the effusion jets, pushing the coolant air towards the liner wall. Thanks to the shallow inclination angle of the effusion holes, a film layer is generated by the gradual mass addition associated to the superposition effect. From a quantitative point of view, a very good agreement was observed between numerical and experimental data in terms of velocity profiles next to the injector exit (Figure 7.4a) and in the near-wall region downstream effusion hole outlets (Figure 7.4b).

On the other hand, the analysis of time evolution of swirling flow fluctuations provides the identification of a pulsating Precessing Vortex Core (PVC) which, however, does not interact with the coolant air, dissipating before reaching the effusion plate. Instead, the presence of Kelvin-Helmholtz (K-H) instabilities, generated within the holes and by

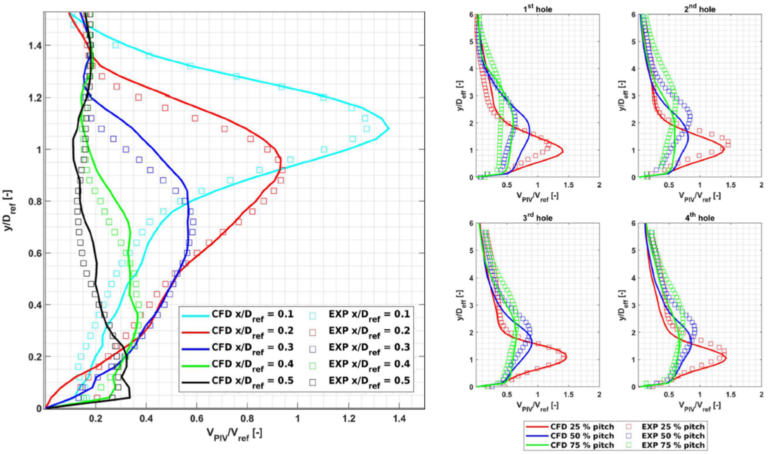

(a) *(b)*

Figure 7.4: CFD and experimental velocity profiles (a) near the dome and (b) next to effusion hole outlets (adapted from [196]).

the main-coolant interaction, characterizes the effusion jets evolution and mixing. In this sense, the numerical simulation tends to over-predict the vorticity intensity and the fluctuations with respect to the experimental results whereas a good agreement is achieved from a qualitative point of view, as highlighted in Figure 7.5.

In the context of the investigated test rig, the time-resolved analysis allowed also to detect an important behaviour which can highly affect the operational safety of the combustor and which is relatively common in presence of high velocity swirling jets: the film layer generated by the first row is partially washed away from the liner due to the interaction with the swirling flow, causing a dangerous decrease of film coverage in that zone. Therefore, these aspects should be carefully considered in order to properly evaluate the coolant distribution and its impact on the wall temperature and, so, on combustor lifetime.

The reader interested in additional details about these works and their results is addressed to [196, 197].

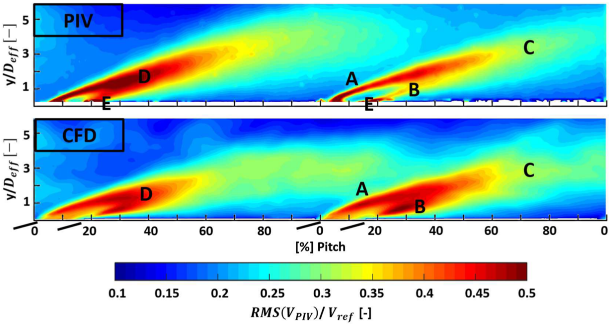

Figure 7.5: Comparison of experimental and numerical RMS velocity contours in the injection region (adapted from [196]).

7.3 Numerical details

To perform the numerical simulations whose results are described in the following, ANSYS Fluent 2019R1® has been employed [170]. Since the main objective of the present investigation is to demonstrate the feasibility and the accuracy of the developed effusion model with respect to a full-mesh simulation as carried out in [196], a similar computational setup has been adopted except for the boundary conditions at hole imprints on the liner, according to the model description in Chapter 4. This allows to provide a consistent comparison, highlighting only the effects introduced by the effusion model. A brief recap of the numerical setup is here reported whereas the reader may refer to [196] for further details.

7.3.1 Setup

Figure 7.6 shows the computational domain together with the mesh grid. Plane XY and plane ZY are the two specific planes of investigation. For well-defined boundary conditions, a total pressure condition has been adopted for both main and coolant inlets whereas a static pressure value has been imposed at outlet, according to experimental measurements (i.e. pressure drop equal to 3.5% on both sides). As described in Section 6.1.1, a

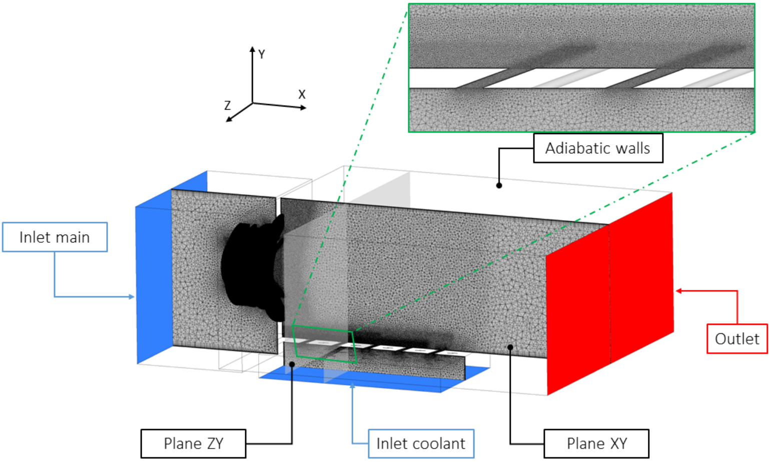

Figure 7.6: Computational domain and mesh grid.

pressure-outlet with target mass flow rate and a mass flow inlet conditions have been prescribed respectively for the cold side and the hot side hole imprints. The mass flow rate through each effusion row is computed run-time by means of the pressure-based formulation (Equation 4.21) and a discharge coefficient derived from full-mesh simulation results. The remain boundaries have been treated as adiabatic walls with a no-slip condition. An incompressible approach has been adopted for modelling the supplied air, considering a constant density at ambient conditions. Regarding the turbulence modelling, a SBES formulation has been employed (already described in Chapter 6).

As far as the computational grid is concerned, an unstructured mesh of about 50 M of tetrahedral elements has been generated in ANSYS Fluent Meshing, adding a prismatic layer of 15 elements for a correct resolution of the near-wall region. Since the effusion pipes are not included in the domain, the total number of elements is reduced to 42 M for the effusion modelled simulation. It is worth to note that the computational saving is here limited by the reduced number of holes (55) composing the multi-perforated plate, but this advantage is much higher when a real combustor geometry with thousand of effusion holes is considered.

In terms of numerical schemes, the pressure-velocity coupling has been carried out with the SIMPLEC formulation wheares a bounded central difference scheme for spatial discretization and a second order implicit formulation for time discretization have been adopted together with a least square cell-based method for gradients calculation. With the aim of maintaining the Courant number below the unity, a time-step of $5 \cdot 10^{-6}$ has been chosen, coupling the CFD solver with the MATLAB code for the effusion modelling every 10 time-steps. To reach adequate residuals (about $1 \cdot 10^{-5}$ for the continuity and $1 \cdot 10^{-6}$ for the momentum and turbulence equations), 12 sub-iterations have been imposed within each time-step. A total computational effort of about 129000 CPU hours has been devoted to perform the full-mesh simulation while the numerical cost has been reduced to about 107000 CPU hours for the modelled calculation with 20% of computational saving. The statistics were collected over 0.07 s in order to ensure an adequate number of flow-through times over the multi-perforated plate and many passages through the effusion holes. The adiabatic effectiveness distribution has been numerically computed by means of a transported passive scalar, imposing a unitary value at the coolant inlets.

7.4 Results

In the following section, the numerical results of the non-reactive combustor simulator obtained with the application of the novel effusion model are reported, comparing them with experimental data where available and showing a further validation of the proposed coupling strategy in presence of a more complex flow pattern. Following the same guideline adopted in Chapter 6, the simulation with effusion model coupling is indicated as EM and it is compared against the reference full-discretized holes simulation named as CFD and carried out by Lenzi et al. [196].

At first, flow field results are reported, highlighting how the computation of flow unsteadiness allows a proper description of the coolant jets trajectory and diffusion with the comparison against experimental measurements. Afterwards, the numerical results in terms of adiabatic effectiveness are shown to prove the effusion model capability of predicting the film coverage along the effusion plate since the coolant distribution highly affects the wall temperature and heat flux patterns when a reactive CHT simulation is performed.

It is important to underline that only the effusion flow field will be analyzed and characterized to show the impact of the novel effusion modelling strategy in the near-wall region. In fact, no effects result on the swirling flow structure since the numerical approach (i.e. setup, mesh and turbulence model) in the related zone is the same for the two calculations.

7.4.1 Effusion flow field

Figure 7.7 shows time-averaged velocity contours on the plane XY for both PIV measurements and CFD estimates, regarding the first four central effusion holes. From now on, V_{PIV} will be used to indicate the magnitude of the 2D velocity on the considered plane, neglecting the normal component which was not detected by the experimental hardware. A reference value V_{ref} is used to normalized the V_{PIV} velocity whereas the spatial coordinates are normalized with respect to effusion hole diameter D_{eff}. For the description of the results, a coordinate system whose origin is located at the leading edge of the first central effusion hole is employed.

Observing the reported flow field, the coolant jets tend to lift-off from the surface, showing a remarkable velocity and a significant penetration into the mainstream. At the same time, it is visible how an effective film coverage is however generated by the gradual coolant addition into a thick layer located near the wall thanks to the low inclination of the injection angle. In fact, the multiple jet injection prompts the typical film superposition with a clearly visible high velocity coolant substrate just below the recirculating region (see Figure 7.2). This effect is responsible of the gradual augmentation of the jet trajectories deflection towards

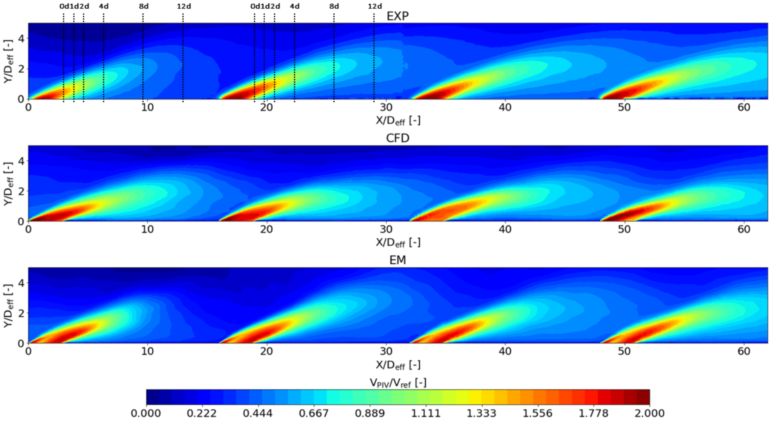

Figure 7.7: Experimental and numerical normalized time-averaged 2D velocity distributions on the plane XY of the sector rig for the first four central effusion holes. Black lines represent the considered locations for quantitative comparison.

the liner as well as of the jet velocity moving downstream along the wall. This behaviour occurs typically when an effusion plate is lapped by an uniform flow [190] but, in this case, the high velocity swirling jet coming from the injector moves along the dome, impinging the liner just upstream the first effusion row (see Figure 7.2) and losing here a large part of its momentum. Hence, the swirling flow is redirected parallel to the wall with a mostly uniform velocity profile for $Y/D_{eff} < 2$, as shown in Figure 7.8 where the numerical axial velocity distribution on a ZY plane located at $X/D_{eff} = -2$ is reported. Consequently, the effusion jets are substantially not affected by the impact of the swirling flow, except for the first hole where it can be noted a lower velocity and lower penetration of the coolant air due to the interaction with the incoming flow.

The highlighted flow features can be also observed in the numerical distributions which exhibit a general qualitative agreement with experimental measurements. The main discrepancies can be detected in the first hole region and by observing the effusion jets velocity profiles just after

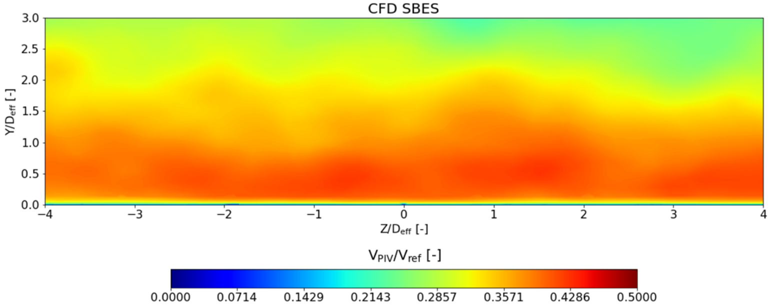

Figure 7.8: Normalized time-averaged axial velocity numerical distribution on a plane ZY located at $X/D_{ref} = -2$.

the hole outlets. Similar coolant behaviour and penetration throughout the four displayed effusion holes are computed by CFD solution where the first jet seems to be less affected by the incoming swirling flow. From this point of view, EM result is, instead, more consistent with experimental contour, predicting a faster disrupting of the injected air. Moreover, a reduced coolant thickness is exhibited by CFD jets which suffer a stronger deflection, moving closer to the wall. Despite this, the high velocity zone located next to the hole outlets is slightly wider compared to the experimental map and this flow feature also appears at the other injection points in the numerical distributions. This can be probably ascribed to the different velocity profiles with which the coolant entries the combustion chamber at the injection plane. Concerning this, the experimental jet shows a unique velocity peak in the jet core region whereas, on the opposite, this peak is shifted towards the windward side in the CFD case while a second one can be identified on the leeward side in EM calculation due to the RANS-based formulation of the developed effusion model, as already discussed in Chapter 6. Hence, it is possible to suppose that such differences are related to a different computation of flow topology within the effusion holes where an important role is played by the separation and the related low velocity regions, occurring next to the hole entrance on the leeward side as a consequence of the feed direction of the coolant.

Their size determines the reattachment location of the associated high momentum zone along the hole and, so, the velocity profile at the outlet. As seen for the single-hole geometry in Chapter 6, the CFD and EM cases exhibit an opposite flow topology in this sense whereas an intermediate behaviour probably occurs in the experimental rig.

In order to better visualize the effect of the rotational motion of the swirling flow on the staggered effusion jets and the interaction between them, Figure 7.9 shows the experimental normalized velocity values on the ZY plane at the trailing edge of the second row of holes together with the relative numerical maps.

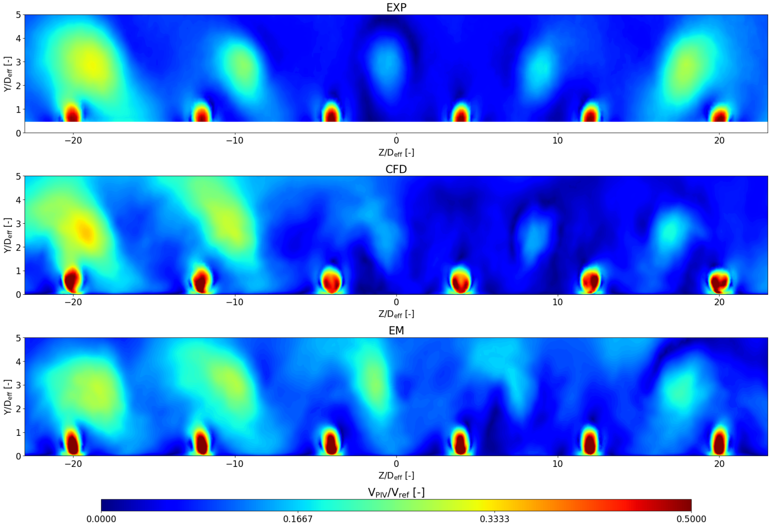

Figure 7.9: Experimental and numerical normalized time-averaged 2D velocity distributions on the plane ZY of the sector rig at the trailing edge of the second effusion row.

Focusing the attention on the experimental distribution, also in this case it is possible to observe the high velocity regions immediately exiting from the holes which generate a flow field with well-defined circular spots related to the jets core. In addition, the traces of the previous row jets are still detectable at the trailing edge of the second row. In this sense, it is interesting to notice how the three central circular spots are characterized by lower velocity due to the significant interaction and turbulent mixing with the incoming swirling flow which causes a faster disruption of the jets core, as previously highlighted. At the same time, an effect of the swirling flow on the trajectories of the jets of the previous row can be detected by observing a lateral shift of jets core according to the asymmetric main flow field. This flow feature is more evident moving towards the lateral portions of the map ($Z/D_{eff} < -15$ and $Z/D_{eff} > 15$) where the cores of the jets present a more stretched and elongated shape. This could negatively affects the film coverage during the operation of an aeroengine combustor since the shift promotes a stronger interaction between consecutive jets, reducing the beneficial effect that the staggered configuration should ensure in terms of lateral homogeneous distribution of coolant air.

Regarding the numerical distributions, an overall qualitative agreement can be appreciated with some discrepancies in the prediction of the traces of jets core and with the main flow which is generally characterized by higher velocity compared to the experimental map. Concerning the circular spots related to the injection immediately upstream of the investigated plane, in both the simulations the typical flow features associated to the presence of CRVP and of horseshoe vortices can be identified around the high velocity jets core. Consistently with experimental measurements, EM results present more coherent structures compared to CFD case where slightly lower velocities are computed. Instead, different levels of agreement can be noted by observing the traces related to the previous row effusion injection. A good prediction is achieved in terms of lateral position of the jets trajectories whereas differences can be detected in the stretching and elongating of the jets core shapes as well as in their velocity magnitude. Such differences are probably related also to the slight discrepancies in the prediction of the swirling flow reported in [196] since the interactions between the main flow and the coolant jets are here significant.

A deeper analysis is carried out by taking into account the quan-

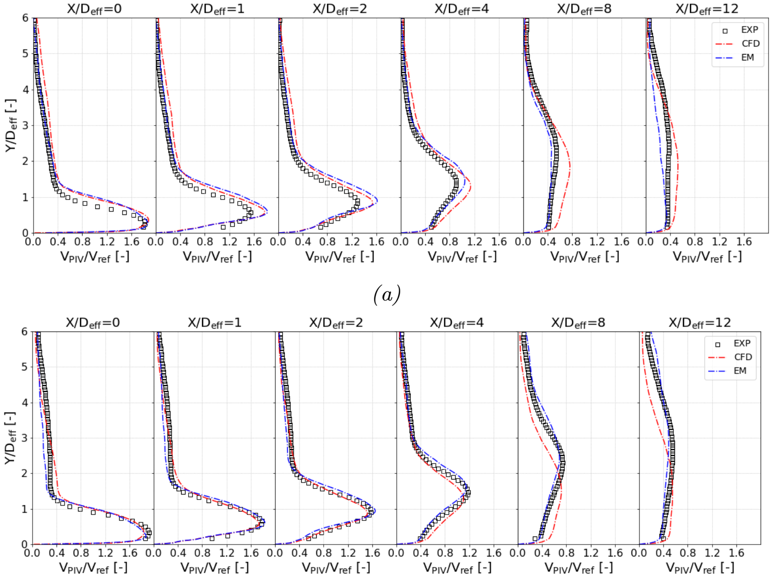

(a)

(b)

Figure 7.10: Normalized time-averaged 2D velocity profiles along the normal to the wall on the plane XY for $X/D_{eff} = 0, 1, 2, 4, 8, 12$ *downstream the holes starting from the trailing edge of the hole imprint: (a) first hole and (b) second hole.*

titative comparisons reported in Figure 7.10 in terms of normalized 2D velocity profiles along the normal to the effusion plate for the first two holes on the reference plane. The considered downstream positions ($X/D_{eff} = 0, 1, 2, 4, 8, 12$) are referred to the trailing edge of each hole imprint. In general, the results obtained from the numerical simulations exhibit a very good agreement with the experimental data. Taking into account the first hole (Figure 7.10a), the experimental velocity peak at $X/D_{eff} = 0$ is well-predicted by the numerical results which show a slight larger jet width. Moving downstream (for $X/D_{eff} = 1, 2, 4$), it can be noted that the numerical jets are subjected to a less intense turbulent mixing with the main flow, leading to an over-estimation of the velocity peak values, whereas the jet width becomes more and more consistent with the measurements. Similar outcomes derived from the analysis of the second hole (Figure 7.10b) for which the agreement between experimental and numerical profiles are even better, especially next to the injection point (for $X/D_{eff} = 0, 1, 2$). In this case, both the velocity peak values and the jet penetration and width are well-computed. From a numerical perspective, it is important to highlight the fairly good agreement of the EM results to the CFD ones, especially for the first positions where the influence of the injection velocity is more significant. This represents a further validation of the implemented effusion model also with the presence of a more complex flow field. In fact, the coupling between the CFD solver and the effusion model permits to obtain results equivalent to a full-mesh calculation with a reduced computational cost. Moreover, it is interesting to note how the modelled simulation seems to provide improvements in the prediction of the experimental flow field far away from the injection locations where the main-coolant interactions become significant (for $X/D_{eff} = 4, 8, 12$). The reason for this behaviour is probably to be found in an insufficiently fine computational grid for the full-discretized calculation within the effusion holes which does not allow a proper prediction of the internal flow field and, so, of the outlet velocity profiles that consequently affect the mixing with the main flow. In this case, a well-computed RANS profile seems to work better, still demonstrating the advantages introduced by the application of the effusion model in terms of mesh size and related computational costs when a complete effusion system with a huge number of holes has to be numerically analyzed.

With the aim of further investigating the impact of velocity fluctuations on the main-coolant interaction and, consequently, on the development of the characteristic vortices, Figure 7.11 shows the contours of RMS velocity values for the first two effusion jets on the reference plane normalized with respect to V_{ref}.

Observing the experimental map, high values of RMS occur in the shear layer of the jets starting from both the leading and the trailing edges of the holes where the K-H instabilities are generated and convected

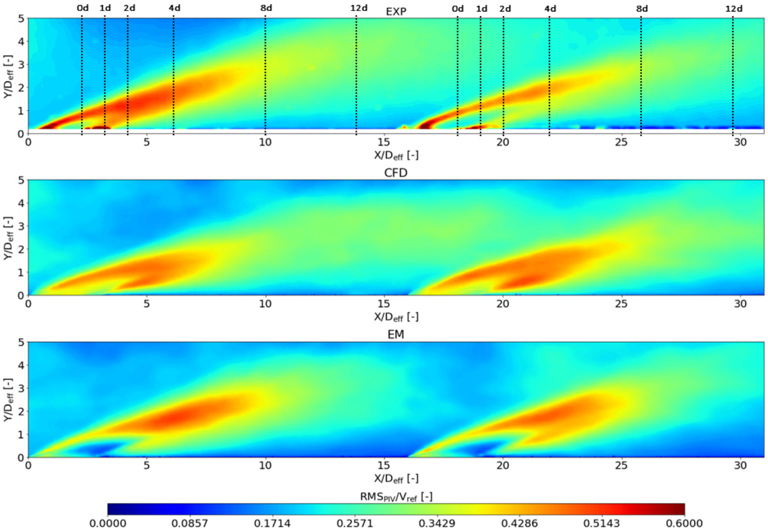

Figure 7.11: Experimental and numerical normalized 2D RMS velocity distributions on the plane XY of the sector rig for the first two effusion holes. Black lines represent the considered locations for quantitative comparison.

downstream along the windward and the leeward sides of the jets. Moving away from the holes, the velocity fluctuations decrease due to the turbulence decay and the distribution appears more homogeneous. Strong flow unsteadiness can be also detected near the trailing edge of each hole and, to a lesser degree, in the region between the jet core and the surface, identifying the wake region. Comparing the two jets, it is possible to note how the first hole is characterized by higher fluctuations. This is ascribable to the intermittent interaction with the swirling flow which convects large energy-carrying vortices, producing the jets oscillation and crushing [197].

Looking at the regions next to the injection points in the numerical maps, this different flow behaviour between the two jets is not properly computed since the RMS values around the second hole are slightly lower compared to the upstream zone. Moreover, the predicted unsteadiness on the leeward side is here stronger with respect to experimental measurements. Discrepancies between the numerical results can be observed next to the hole outlets, in the wake regions and in the mainstream zone located between the coolant jets. In the first two cases, EM simulation tends to under-estimate velocity fluctuations whereas, in the latter one, a faster turbulence decay is predicted by modelled calculation. Taking into account the RANS-based formulation of the model, it is clear that less intense turbulent structures coming from holes are computed against a full-discretized SBES simulation (CFD).

As for the velocity field, it is interesting to take into account the RMS velocity distribution also on the ZY plane at the trailing edge of the second row of holes, as reported in Figure 7.12.

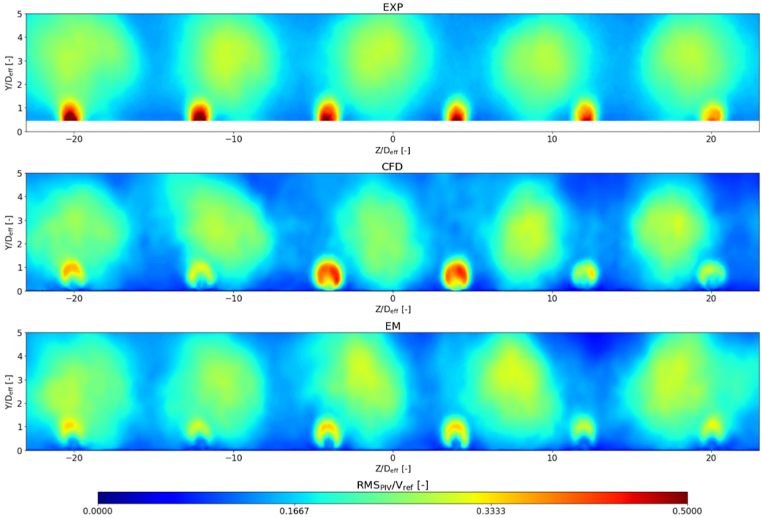

Figure 7.12: Experimental and numerical normalized 2D RMS velocity distributions on the plane ZY of the sector rig at the trailing edge of the second effusion row.

Looking at the experimental map, it is possible to distinguish two main contributes. The first one, represented by the larger homogeneous spots located in the space within the injection points, is related to the decay of turbulence generated by the previous row effusion jets and associated to the presence of CRVP. The second one is identified by the peak values zones in correspondence of hole outlets due to the intense turbulent fluctuations included within the shear layers of the jets. Such contributions can be noted also in the numerical distributions. As observed in the XY plane, the velocity fluctuations caused by the shear layer instabilities are generally under-estimated, especially in the EM case as a consequence of the RANS profiles predicted by the effusion model at the injection plane. A better agreement is reached for the CRVP contributions for which the modelled simulation seems to be more consistent with experimental data, computing similar values and spreading of the relative circular traces.

All these considerations are summarized and quantified by Figure 7.13 where the normalized 2D RMS velocity profiles along the normal to the wall downstream the holes are reported for the same locations.

For both the holes, two peaks appear at $X/D_{eff} = 0, 1, 2$ as a consequence of the K-H instabilities which are transported downstream in the shear layer of the jets and of the presence of vortical structures in the near-wall wake regions. For $X/D_{eff} > 2$, K-H contributions merge in a single peak value which gradually decreases as an effect of the turbulence decay. As far as numerical profiles are concerned, a fairly good agreement is achieved and peak values heights are properly predicted by both the CFD and EM calculations as well as the turbulence levels in the freestream, except for the EM case which exhibits lower RMS values next to the second effusion hole, as previously mentioned. Going into more details, velocity fluctuations computed by the modelled simulation are generally lower compared to CFD results, especially in the core region and on the leeward side of the jet at $X/D_{eff} = 0, 1, 2$ as a consequence of the RANS nature of the profiles predicted by the effusion model. Then, the two simulations give rise to similar profiles for $X/D_{eff} > 2$ where the flow field is more affected by the main-coolant interactions. Referring to the comparison with experimental data in the near-wall region next

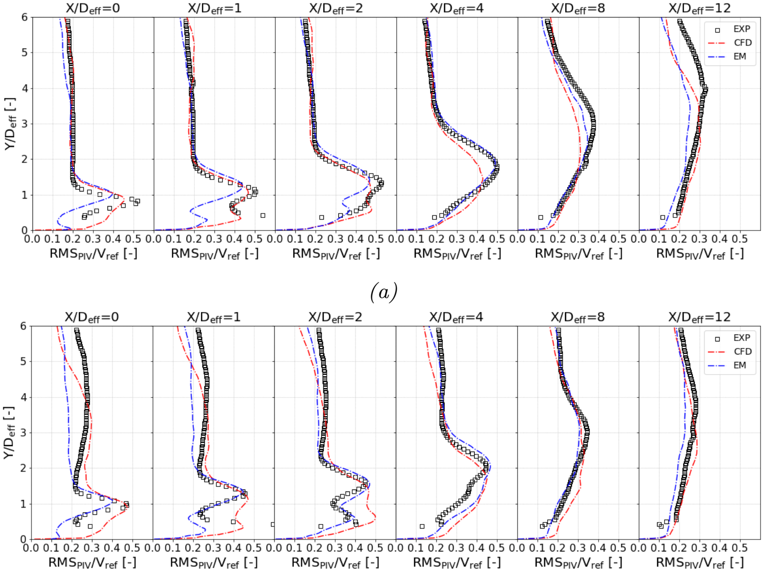

(a)

(b)

Figure 7.13: Normalized 2D RMS velocity profiles along the normal to the wall on the plane XY for $X/D_{eff} = 0, 1, 2, 4, 8, 12$ downstream the holes starting from the trailing edge of the hole imprint: (a) first hole and (b) second hole.

to the hole outlets ($X/D_{eff} = 0, 1, 2$), it is interesting to notice a dual behaviour: the full-discretized simulation is able to better match the measurements related to the first jet and the related higher values due to the intermittent interaction with the swirling flow whereas it moves away from the experimental trend for the second injection unlike the EM results. On the prediction side, it is important to point out the capability of the proposed effusion modelling approach of reproducing the characteristic features of the flow field generated by an effusion cooling system in a similar way to what can be achieved with a full-discretized calculation but with a significant computational saving.

In order to understand how the numerical simulations are able to describe the physics of the JICF phenomena, an analysis of the characteristic vortices occurring within the shear layer of the cooling jets is carried out by means of Q-criterion plots together with RMS values visualization of the Transported Scalar Concentration (TSC) on the wall, as reported in Figure 7.14.

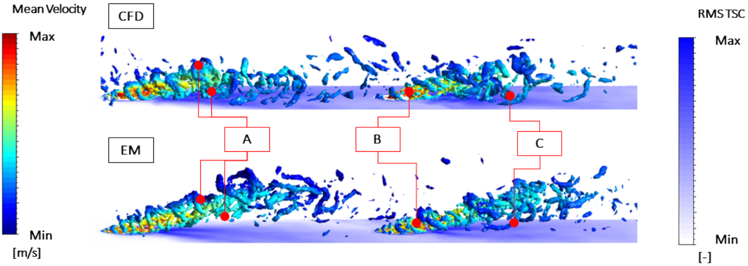

Figure 7.14: Q-criterion plots together with RMS values visualization of TSC on the wall for the first two central effusion holes.

In both calculations, the typical JICF vortical structures can be identified: shear layer vortices (A) with the presence of K-H rings on the upstream and leeward sides due to the instability propagation along the jets, vortical structures in the core region (B) associated to the turbulence generated within the effusion holes and upright wake vortices (C) located in the region included between the jets and the wall. The size of these structures depends on the intensity of main-coolant interaction, underlining the previous mentioned differences in the flow field computation between the two simulations and, in particular, in the prediction of turbulence levels just after the hole outlets. Also in this case, it is worth to underline how the trajectory of CFD jets remains closer to the wall, resulting in a thinner film layer and also leading to different TSC distribution on the wall, as discussed in the following.

For a more detailed investigation of the effects of the different behaviour of the two numerical setups in terms of turbulence prediction on the coolant spread, PDFs of the TSC at $Y = 0.5\ D_{eff}$ and at 50% of the axial hole pitch ($X/D_{eff} = 8$) are reported in Figure 7.15. Since

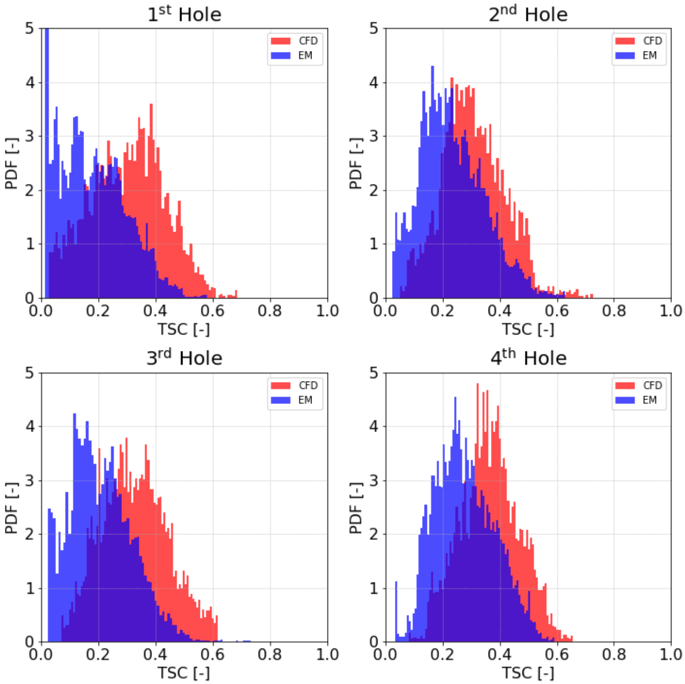

Figure 7.15: PDFs of TSC values in the near-wall region.

the element sizing is the same for the two computational grids, CFD and EM PDFs are substantially consistent in terms of shape and range, according to the correspondent RMS profiles at $X/D_{eff} = 8$ shown in Figure 7.13, where the same level of velocity fluctuations is computed by both the calculations. However, all EM plots are shifted towards lower TSC values, being therefore an index of a smaller quantity of coolant which passes through the considered position. Since the investigated point is located near to the wall, it can be inferred that, in CFD case, the coolant is accumulate in a substrate located closer to the wall due to the higher jets deflection, forming a thinner film layer over the wall. From a physics perspective, the non-symmetric distributions of the first hole, which is instead shifted towards low TSC values, suggest a different behaviour between the first and the other holes located downstream where a Gaussian-like shape PDF with mean TSC always higher than zero is appreciable. As previously discussed, the effect of the upstream swirling flow is limited to the first hole, causing here a significant disruption of the coolant momentum and tending to carry the film layer away from the liner. In a real combustor, this may lead locally to dangerous high heat loads and temperature gradients, representing a serious risk for the operational safety of the system.

7.4.2 Film cooling effectiveness

In order to understand the impact of effusion modelling in the prediction of the film coverage, an analysis of the adiabatic effectiveness distribution on the plate is carried out. Such analysis is performed only from a numerical point of view, since experimental data are not available. For this purpose, Figure 7.16 shows the time-averaged distributions of the TSC on the plate together with RMS values. With the aim of focusing the attention on the interaction between the swirling flow and the coolant jets, only a central portion located in the first part of the plate is analyzed.

Concerning the time-averaged values (Figure 7.16a), the result of the superposition effect is clear for both the numerical simulations, looking at the increasing values of adiabatic effectiveness moving downstream along the plate. The injected coolant is gradually added into the film layer enhancing the protective action and a significant film coverage is achieved for $X/D_{eff} > 30$. However, the adiabatic effectiveness is on average low in the first portion of the effusion plate due to the tendency of the jets to the lift-off from the surface. The residual rotational fluid motion associated to the swirling flow can be noted by observing the deflection of the wakes next to the hole outlets for the first two effusion rows since this effect is then dampened by the interaction with the subsequent coolant jets. This flow feature can be also detected looking at the direction of the high values streaks in the RMS distributions which are deflected according

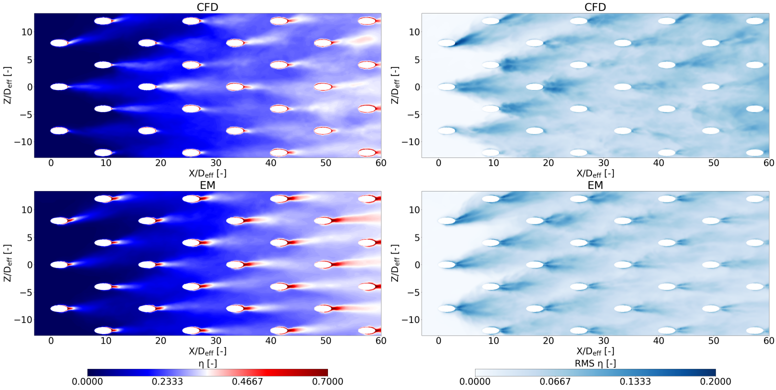

(a) *(b)*

Figure 7.16: Adiabatic effectiveness distributions on a central portion of the effusion plate: (a) time-averaged and (b) RMS values.

to the local rotational motion of the main flow.

As previously observed in Chapter 6, the main discrepancies between the CFD and the EM calculations are located at the trailing edge of each hole imprint where the effusion model gives rise to higher transported scalar concentrations. Such difference is even more pronounced moving downstream due to the superposition effect which causes an augmentation of jets deflection towards the wall. In the modelled case, the coolant jet seems to be subjected to a lower turbulent mixing, resulting also in a less pronounced lateral spreading of the coolant. This behaviour is probably caused by the lower turbulence levels computed by the effusion model compared to the full-discretized simulation but it can be also ascribable to a numerical effect: in this location, in fact, the computational grids are slightly different due to the presence or not of the pipes and, moreover, a different boundary condition is prescribed for the TS at the effusion inlets (unitary value). Consequently, the under-prediction of the turbulent mixing next to the injection locations may limit the entrainement of the main flow within the jets, resulting in a lower lateral spreading of the coolant air in EM calculation. The mentioned differences can be also pointed out as far as the laterally averaged adiabatic effectiveness distribution along the effusion plate in considered. In this sense, Figure 7.17 shows a numerical quantitative comparison where the grey bars indicate the effusion holes locations. The lateral averaging is performed for $-2 < Z/D_{eff} < 2$ in order to better distinguish the contributions of the single effusion jets of the central portion of the plate.

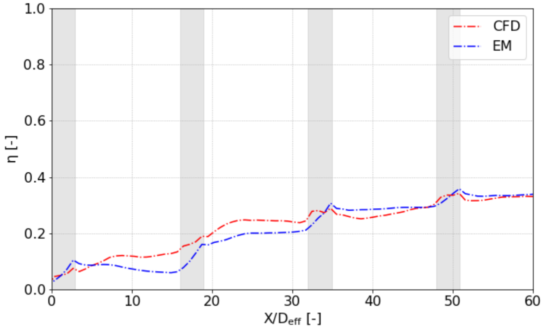

Figure 7.17: Laterally averaged adiabatic effectiveness for $-2 < Z/D_{eff} < 2$.

At the beginning, EM effectiveness is higher than the CFD one due to the high value streak located next to the first hole outlet. However, the CFD jets exhibit a lower penetration, remaining closer to the wall, and they are subjected to a stronger lateral spreading as a consequence of the higher turbulence levels predicted by the CFD case. This results in an opposite tendency for $5 < X/D_{eff} < 35$ where the full-discretized calculation provides a better film coverage despite the thinner coolant layer. For $X/D_{eff} > 35$, the two profiles are consistent with each other notwithstanding the different patterns observed in the numerical maps (see Figure 7.16a). Moving downstream, in fact, the wider lateral spreading of CFD distribution starts to be counterbalanced by the more centered but, at the same time, higher jet imprint of the EM map. Therefore, the effusion plate is globally subjected to the same film protection.

Regarding the RMS results, it is interesting to notice how EM distribution is characterized by the typical V-shape related to the counter rotating vortex coming from the effusion holes next to each outlet. Such structure is less evident in the full-mesh map. As for the time-averaged contours, the CFD streaks appear more diffused than the EM ones, highlighting again the different computed intensity of velocity fluctuations and, so, turbulence levels coming from the holes and acting in this zone. In addition, the longer length of the V-shape structures for the first rows confirms that, after the injection, the coolant remains closer to the wall in the CFD case, as deduced before by observing the time-averaged velocity maps on the mid-plane. At this moment, no comparison with experimental data is available and further investigations are required in this sense.

7.5 Concluding remarks

Numerical analyses on a non-reactive combustor simulator rig equipped with an effusion cooled plate were carried out in SBES framework. The objective of the investigation was the assessment of the novel effusion model proposed in the context of this research work in presence of a more complex flow field, where a swirling main flow interacts with the effusion jets coming from the cooled plate. In fact, the results obtained with the previously described coupling strategy between the CFD solver and the ROM code have been compared to a reference full-mesh solution and with available experimental data reported in [196, 197]. This allows to highlight the effects of the developed effusion modelling strategy in the prediction of the near-wall flow field and of the film coverage on the multi-perforated liner.

As far as velocity prediction is concerned, a fairly good agreement has been achieved with the reference numerical results. Similar flow behaviour is computed by both the simulations next to the injection points whereas some differences arise moving downstream along the plate when the mixing with the main flow becomes more significant. In this case, the modelled calculation seems to work better in the estimation of jets penetration probably due to an insufficiently fine computational grid for the CFD case within the effusion holes which does not allow a proper prediction of the internal flow field. The capability of EM case to also accurately reproduce the experimental data proves the feasibility of the proposed approach when a complete effusion system with a huge number of holes has to be numerically analyzed.

Regarding the computation of velocity fluctuations, the effusion model tends to under-estimate the turbulence levels at the injection plane due to the RANS-based formulation of the ROM employed for the prediction of velocity and turbulent quantities profiles at hole outlet. This partially affects the correct estimation of the interactions with the main flow, resulting in a slight different computation of JICF vortical structures and of the main flow entrainement effect.

In fact, higher differences are detected in terms of adiabatic effectiveness for which the modelled simulation provides higher values next to the trailing edge of the hole imprints and a lower lateral spreading of the coolant jets whereas similar laterally averaged trends are instead predicted by CFD and EM cases. In this sense, further investigations are required to also permit a correct prediction of wall temperatures in the context of reactive CHT analyses.

Conclusions

The research activity discussed in this dissertation has been carried out with the aim of deepening the knowledge about the heat transfer in aeroengine combustors through the development and the assessment of advanced numerical tools for a proper estimation of wall heat fluxes and temperatures. The interest in such investigation is justified by the current trends in the design of modern combustor concepts aimed at increasing the overall pressure ratio and the turbine inlet temperature, involving potential technological issues about the thermal management of combustor walls. In addition, the introduction of low $\mathrm{NO_x}$ combustors based on the lean burn concept has caused a strong reduction (approximately 50%) in air availability for liner cooling which is instead employed for controlling the combustion process. In fact, large research efforts have been devoted to the development of such combustion systems which are considered as the most effective technology to meet the future increasingly emission standards imposed by ICAO-CAEP. However, further improvements are permitted only by the design of very effective cooling schemes. According to several manufactures, effusion cooling represents one of the most promising solution to ensure an efficient thermal protection of combustor walls with a reduced consumption of coolant air by means of multi-perforated liners.

From a numerical perspective, performing conjugate heat transfer analyses of aeroengine combustors means to deal with several complex phenomena as combustion, convection, radiation and conduction which are characterized by complex multiphysics/multiscale interactions that must be accurately modelled. This is especially evident in a scale-resolving framework which is required for a reliable prediction of reactive flows behaviour and flame-wall interactions, but where the different thermal inertia of fluid and solid domains must be correctly take into account. A standard direct coupling of fluid and solid solutions involves computational efforts which are not suitable in an industrial context and the computational cost is even more higher when the investigated combustor is equipped with an effusion cooling system where thousands of holes should be finely discretized. Therefore, proper CFD methodologies must be developed to make such multiphysics analyses feasible for industrial applications.

For these reasons, a desynchronized loosely coupling methodology, called U-THERM3D and developed in ANSYS Fluent, has been firstly assessed as a detailed investigation tool to achieve a deep comprehension of heat transfer modes within aeroengine combustors with high-fidelity prediction of combustion and near-wall processes in an unsteady CHT simulation framework with affordable computational costs. The numerical investigation has been performed on a laboratory-scale combustor representative of a RQL technology for which several measurements are available from gas temperature and species to the quartz window temperature. The attention has been focused on the impact of wall and radiative heat losses on the aero-thermal fields and soot production by means of different type of simulations. Comparing CHT simulation with adiabatic and no-radiation modelling cases, a strong coupling between radiation, aero-thermal fields, soot formation and wall temperature is observed, highlighting the need to properly compute radiative heat transfer and solid conduction. In fact, U-THERM3D procedure is able to provide a reliable prediction of the flow field and of the flame structure with an overall agreement against experimental data, showing, at the same time, a significant improvement with respect to previous RANS calculations thanks to the resolution of the largest scales of the turbulence spectrum with an affordable computational cost. Moreover, the correct prediction of the flame lateral spreading and of the turbulence levels in the near-wall region allows to achieve a better estimation of wall temperature profile, especially in the first part of the combustor where the flame-wall interaction is stronger. Further investigations are required to improve the under-predicted soot production by means of more complex modelling strategies.

The main objective of the work is, however, the development of a novel approach for effusion modelling in order to improve and speed up the design of effusion cooled combustors. With the aim of providing a suitable solution for CFD simulations of this kind of devices with reduced computational resources, a 2D boundary sources-based model has been proposed and implemented within U-THERM3D framework, replacing the effusion hole with an inlet (hot side) and an outlet (cold side) patches to consider the related coolant injection. The innovative effusion model is based on the application of a Reduced-Order technique in combination with a Regression method to derive a low-order Surrogate Model, starting from the numerical results of a DoE carried out on a single effusion hole. Coupled with the CFD solver, such model permits an accurate run-time prediction of injection velocity and turbulence profiles at hole outlets for a proper computation of main-coolant interactions and film coverage along the wall. The proposed procedure has been successfully tested and validated against full-mesh reference simulations on simple single-hole and multi-hole geometries in presence of uniform main flow with different operating conditions of the included effusion cooling system in the context of steady and unsteady simulations. A more relevant assessment has been performed on a non-reactive combustor simulator rig equipped with an effusion cooled plate where a representative swirling main flow interacts with the effusion jets. In this context, the modelled simulation has been compared to a full-discretized calculation and to available experimental data. Very interesting results have been achieved for RANS calculations whereas some discrepancies have been observed with scale-resolving approaches and in terms of film coverage due to the RANS-based formulation of the developed effusion model. However, significant improvements have been demonstrated with respect to the use of flat velocity and turbulent quantities profiles, generally employed in the state-of-the-art approaches available in technical literature. From a numerical perspective, the novel modelling strategy shows good capabilities in improving and speeding up the design process of effusion cooled aeroengine combustors since it allows to explore different effusion cooling schemes and operating conditions with a reduced computational cost and with a reliable prediction of the related flow field.

The next step of this research activity is to prove the feasibility of the present film cooling model and of the related coupling strategy within U-THERM3D framework in a conjugate calculation in order to evaluate its impact in terms of thermal field and metal temperature. The extension of the model to the promising shaped holes configuration is already under investigation together with a methodology to improve the predictive capabilities of the model when boundary values of the input parameter space are explored.

Appendix A

RANS SH - Validation set

As said in Chapter 6, analogous quantitative comparisons are reported in the following for the other operating conditions of the validation set (see Table A.1). The comparisons regard both the stream-wise and span-wise velocity profiles along the normal to the wall on the mid-plane for $X/D = 0, 1, 2, 4, 8$ downstream the trailing edge of the hole imprint and the laterally averaged adiabatic effectiveness distribution on the wall.

Table A.1: Input parameters values for the validation set.

Design Point	α	L/D	BR	DR
1	30°	5	5	1.25
2	40°	5	5	1.25
3	20°	5	5	1.25
4	30°	2	5	1.25
5	30°	8	5	1.25
6	30°	5	5	1
7	30°	5	5	2.5
8	30°	5	9	1.25
9	30°	5	1	1.25

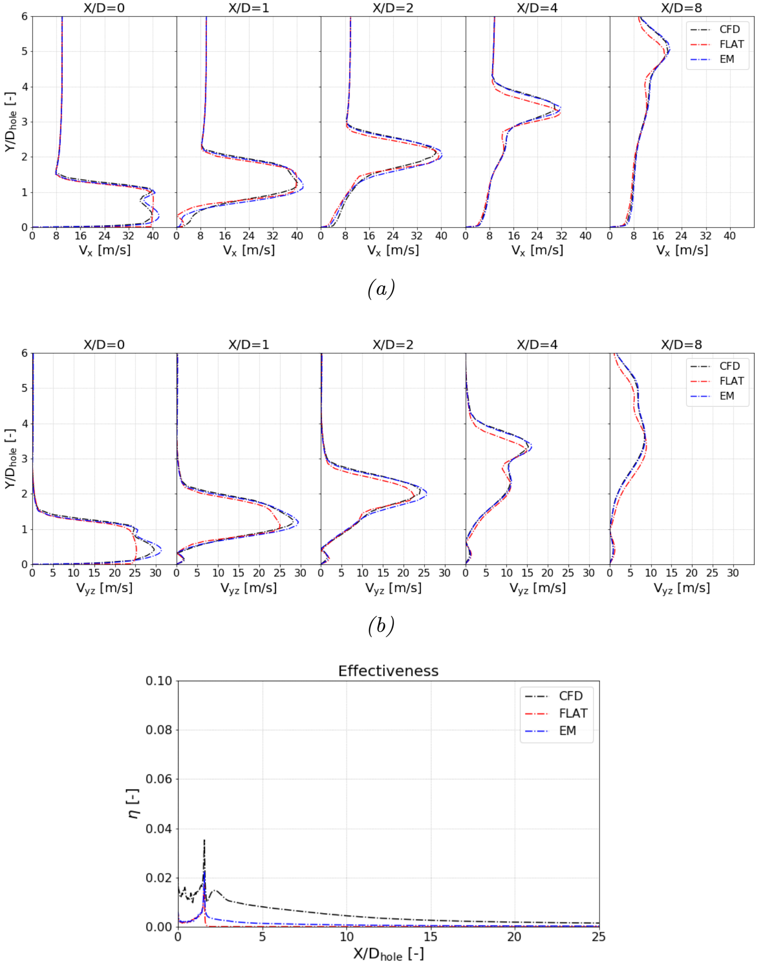

(a)

(b)

(c)

Figure A.1: (a) Stream-wise and (b) span-wise velocity profiles along the normal to the wall on the mid-plane for $X/D = 0, 1, 2, 4, 8$, and (c) laterally averaged adiabatic effectiveness distributions along the wall for DP2 case.

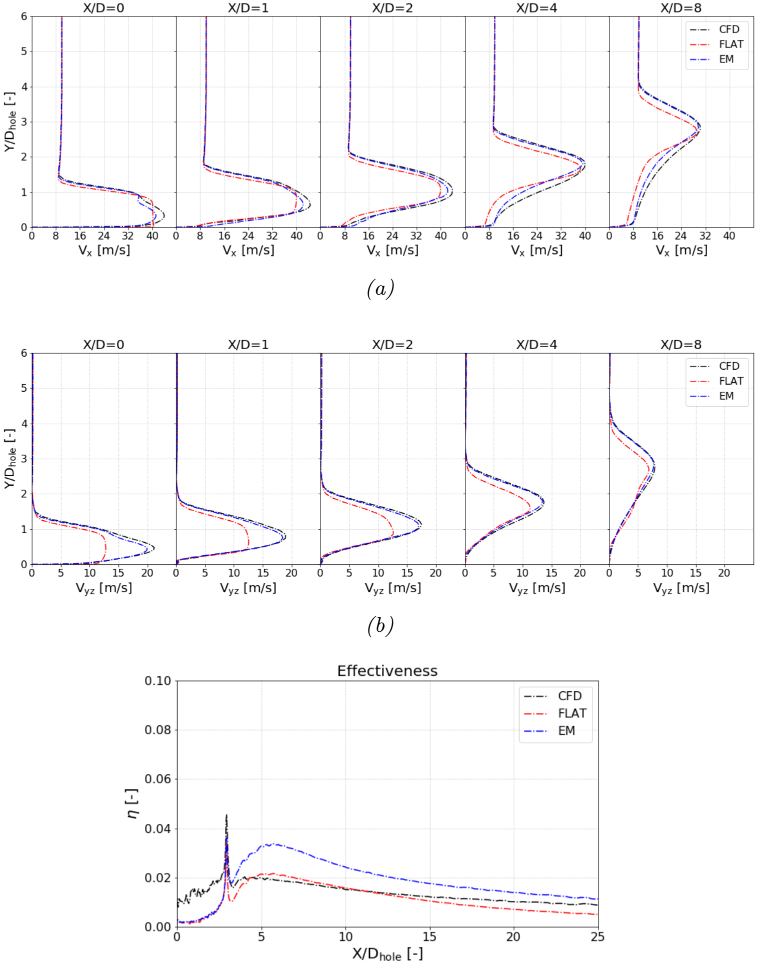

(a)

(b)

(c)

Figure A.2: (a) Stream-wise and (b) span-wise velocity profiles along the normal to the wall on the mid-plane for $X/D = 0, 1, 2, 4, 8$, and (c) laterally averaged adiabatic effectiveness distributions along the wall for DP3 case.

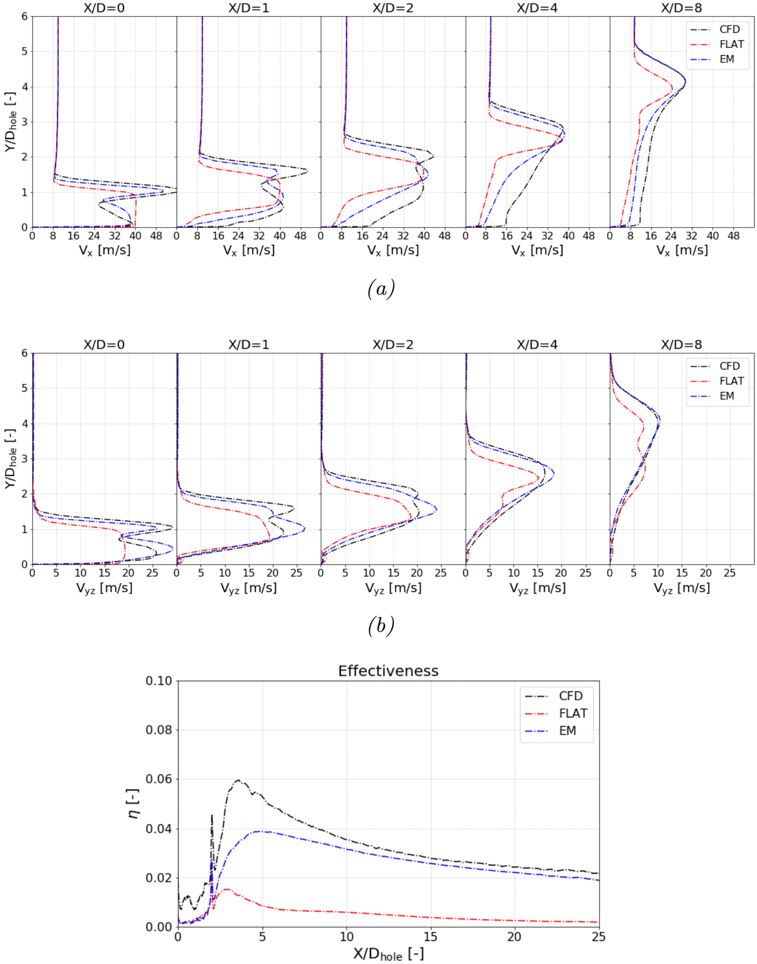

(a)

(b)

(c)

Figure A.3: (a) Stream-wise and (b) span-wise velocity profiles along the normal to the wall on the mid-plane for $X/D = 0, 1, 2, 4, 8$, and (c) laterally averaged adiabatic effectiveness distributions along the wall for DP4 case.

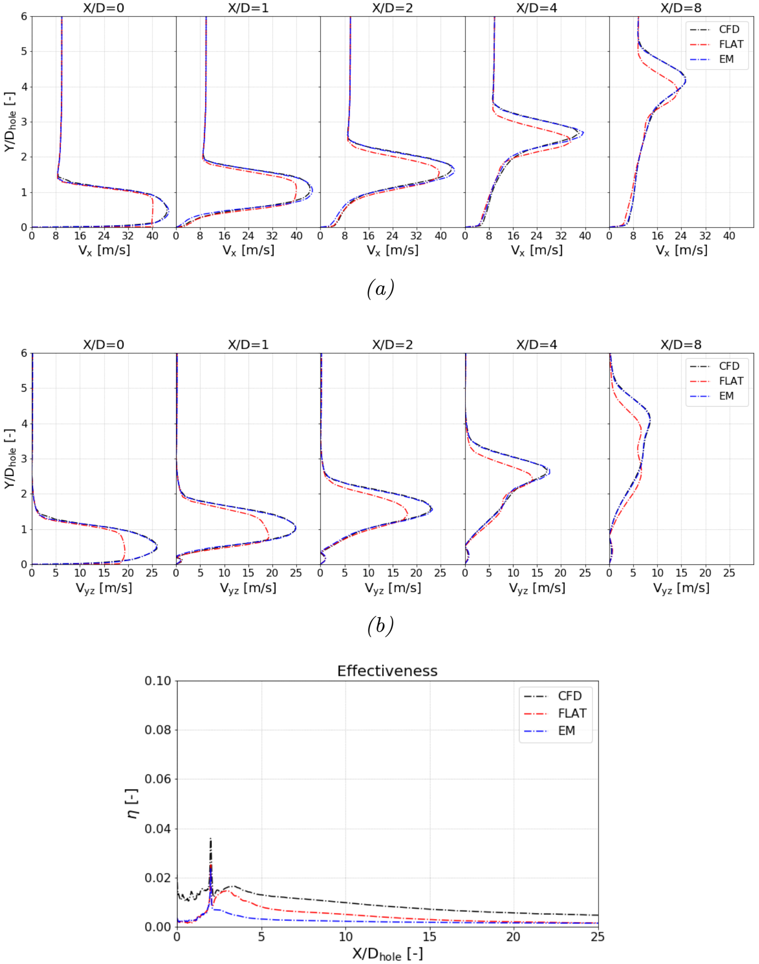

(a)

(b)

(c)

Figure A.4: (a) Stream-wise and (b) span-wise velocity profiles along the normal to the wall on the mid-plane for $X/D = 0, 1, 2, 4, 8$, and (c) laterally averaged adiabatic effectiveness distributions along the wall for DP5 case.

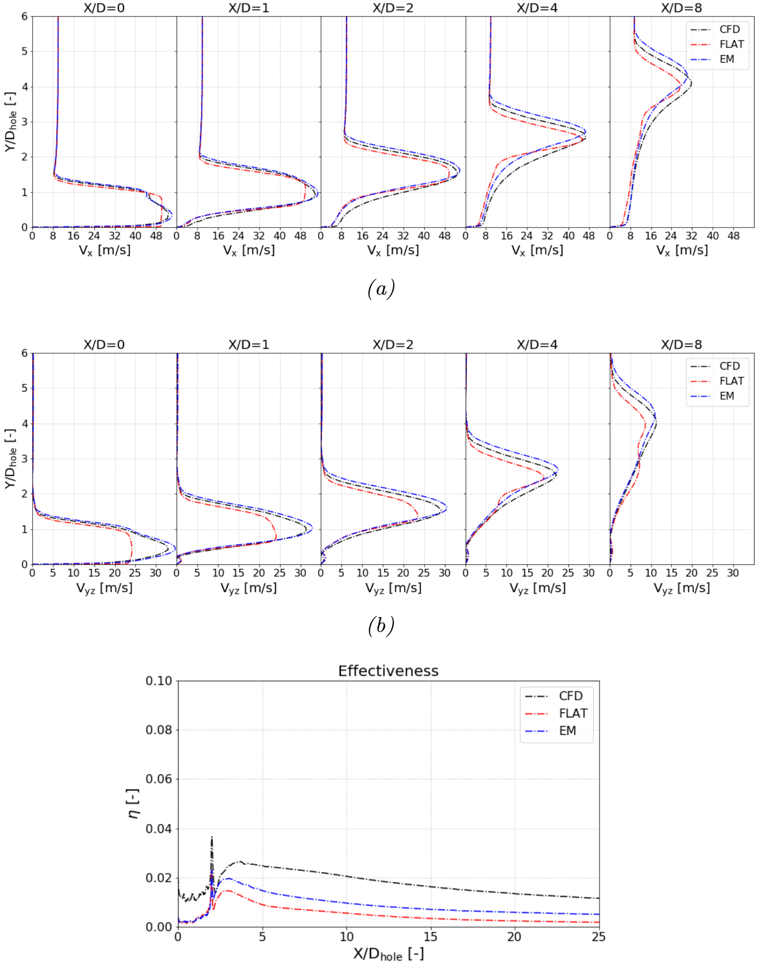

(a)

(b)

(c)

Figure A.5: (a) Stream-wise and (b) span-wise velocity profiles along the normal to the wall on the mid-plane for $X/D = 0, 1, 2, 4, 8$, and (c) laterally averaged adiabatic effectiveness distributions along the wall for DP6 case.

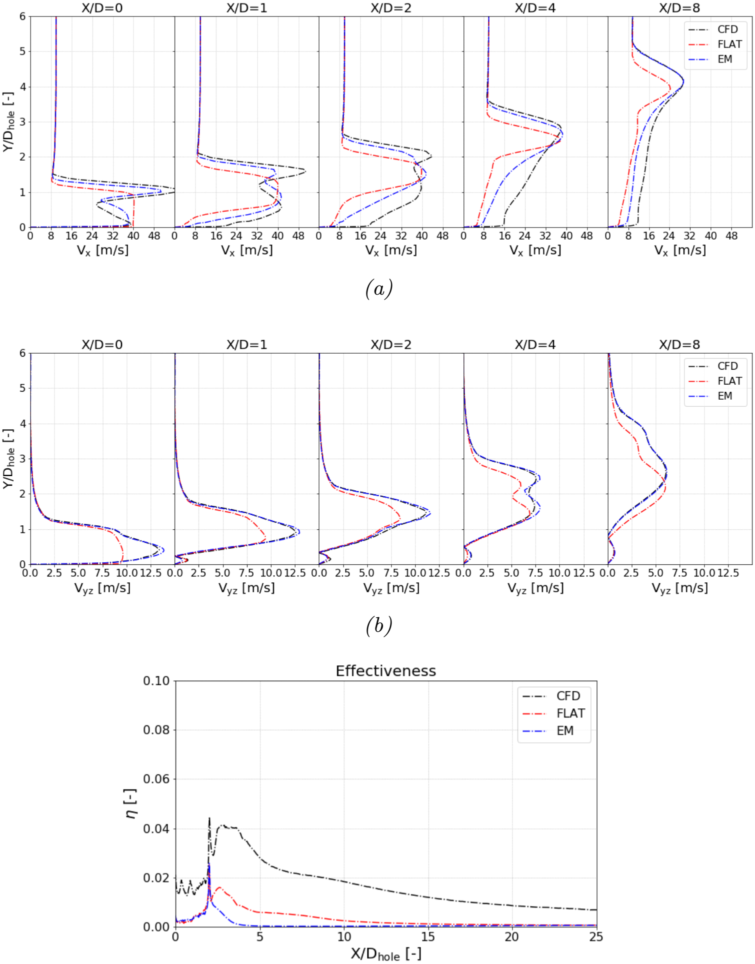

(a)

(b)

(c)

Figure A.6: (a) Stream-wise and (b) span-wise velocity profiles along the normal to the wall on the mid-plane for $X/D = 0, 1, 2, 4, 8$, and (c) laterally averaged adiabatic effectiveness distributions along the wall for DP7 case.

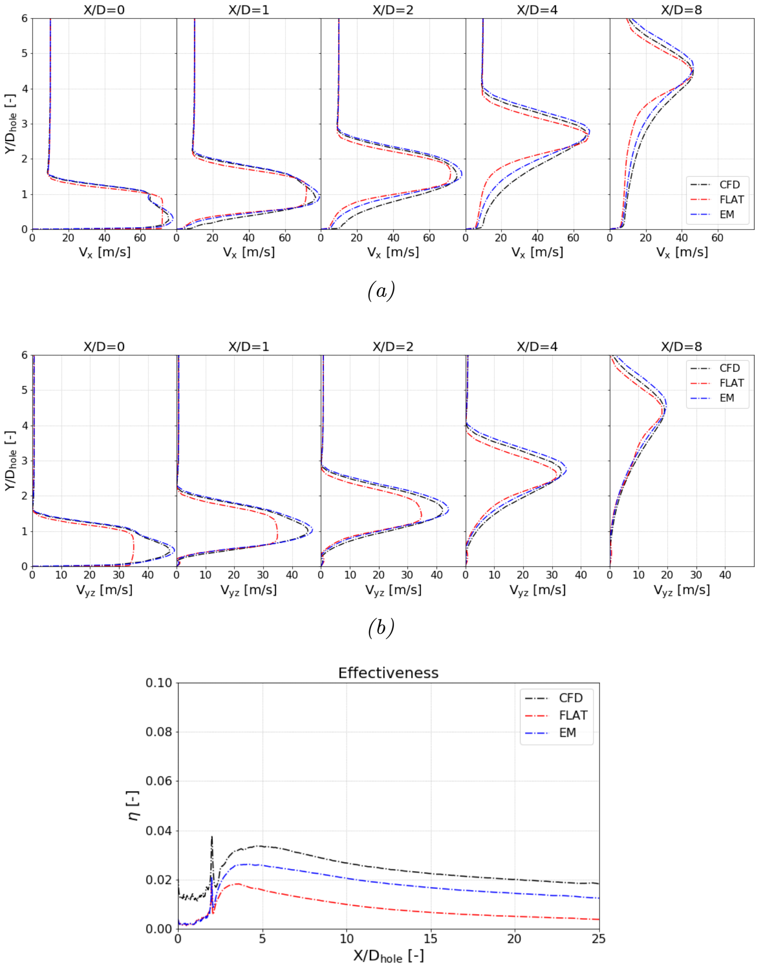

(a)

(b)

(c)

Figure A.7: (a) Stream-wise and (b) span-wise velocity profiles along the normal to the wall on the mid-plane for $X/D = 0, 1, 2, 4, 8$, and (c) laterally averaged adiabatic effectiveness distributions along the wall for DP8 case.

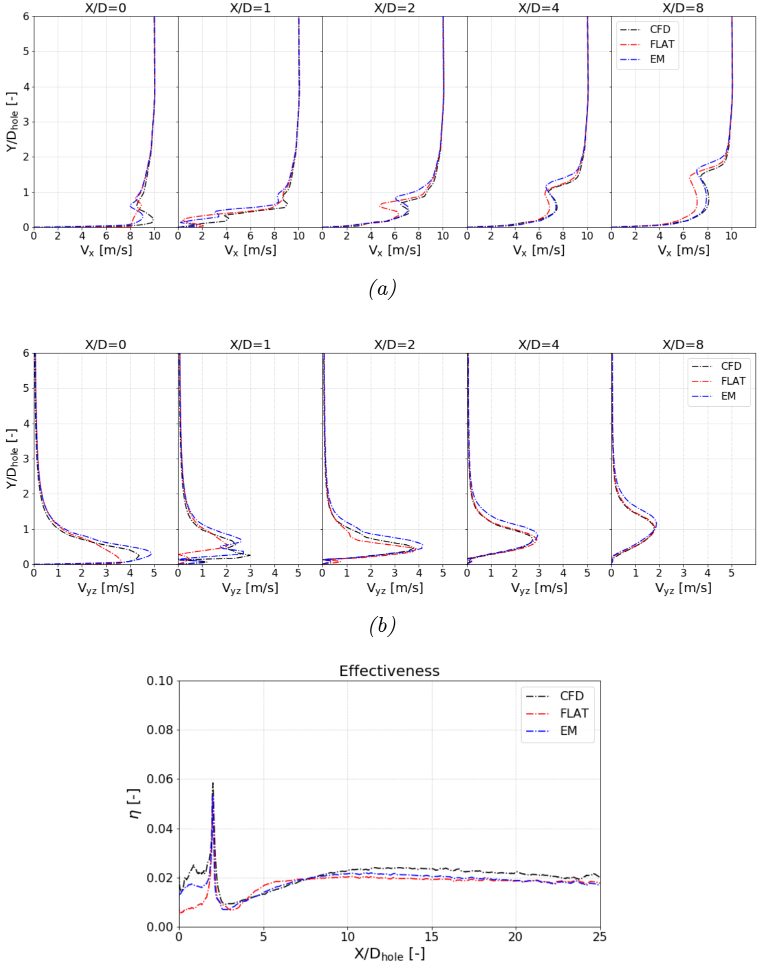

(a)

(b)

(c)

Figure A.8: (a) Stream-wise and (b) span-wise velocity profiles along the normal to the wall on the mid-plane for $X/D = 0, 1, 2, 4, 8$, and (c) laterally averaged adiabatic effectiveness distributions along the wall for DP9 case.

List of Figures

List of Tables

Bibliography

[1] ICAO. Future of aviation.

[2] Liu, Yize, Sun, Xiaoxiao, Sethi, Vishal, Nalianda, Devaiah, Li, Yi-Guang, and Wang, Lu. “Review of modern low emissions combustion technologies for aero gas turbine engines.” *Progress in Aerospace Sciences*, 94:12–45, 2017.

[3] ACARE. Flightpath 2050 europe’s vision for aviation, 2011. URL `http://ec.europa.eu/transport/sites/transport/files/modes/air/doc/flightpath2050.pdf`.

[4] Kyprianidis, Konstantinos G. *Future aero engine designs: an evolving vision.* INTECH Open Access Publisher, 2011.

[5] McGuirk, JJ. “The aerodynamic challenges of aeroengine gas-turbine combustion systems.” *The Aeronautical Journal*, 118(1204): 557–599, 2014.

[6] Andrews, GE, Bazdidi-Tehrani, F, Hussain, CI, and Pearson, JP. Small diameter film cooling hole heat transfer: The influence of the hole length. In *Turbo Expo: Power for Land, Sea, and Air*, volume 79016, page V004T09A021. American Society of Mechanical Engineers, 1991.

[7] Andrews, GE, Khalifa, IM, Asere, AA, and Bazdidi-Tehrani, F. Full coverage effusion film cooling with inclined holes. In *Turbo Expo:*

Power for Land, Sea, and Air, volume 78811, page V004T09A045. American Society of Mechanical Engineers, 1995.

[8] Gustafsson, KM Bernhard and Johansson, T Gunnar. “An experimental study of surface temperature distribution on effusion-cooled plates.” *J. Eng. Gas Turbines Power*, 123(2):308–316, 2001.

[9] Andreini, Antonio, Caciolli, Gianluca, Facchini, Bruno, and Tarchi, Lorenzo. “Experimental evaluation of the density ratio effects on the cooling performance of a combined slot/effusion combustor cooling system.” *ISRN Aerospace Engineering*, 2013, 2013.

[10] Andreini, Antonio, Bertini, D, Facchini, B, and Puggelli, S. “Large-eddy simulation of a turbulent spray flame using the flamelet generated manifold approach.” *Energy Procedia*, 82:395–401, 2015.

[11] Puggelli, S, Bertini, D, Mazzei, L, and Andreini, A. “Assessment of scale resolved cfd methods for the investigation of lean burn spray flames.” *ASME J. Eng. Gas Turbines Power*, 2016.

[12] Puggelli, S, Bertini, D, Mazzei, L, and Andreini, A. “Modeling strategies for large eddy simulation of lean burn spray flames.” *Journal of Engineering for Gas Turbines and Power*, 140(5), 2018.

[13] Paccati, Simone, Bertini, Davide, Mazzei, Lorenzo, Puggelli, Stefano, and Andreini, Antonio. “Large-eddy simulation of a model aero-engine sooting flame with a multiphysics approach.” *Flow, Turbulence and Combustion*, pages 1–26, 2020.

[14] Bertini, Davide. *High-fidelity prediction of metal temperature in gas turbine combustors using a loosely coupled multiphysics approach.* PhD thesis, University of Florence, 2019.

[15] Giusti, Andrea. *Development of numerical tools for the analysis of advanced airblast injection systems for lean burn aero-engine combustors.* PhD thesis, University of Florence, 2013.

[16] Madden, Paul. “Caep combustion technology review process and caep nox goals.” *CAEP Publication July*, 2014.

[17] Flightpath, ACARE. “2050-europe’s vision for aviation.” *Advisory Council for Aeronautics Research in Europe*, 2011.

[18] Khosravy el_Hossaini, M. *Review of the new combustion technologies in modern gas turbines.* ISBN, 2013.

[19] Zeldovich, YA, Frank-Kamenetskii, D, and Sadovnikov, P. *Oxidation of nitrogen in combustion.* Publishing House of the Acad of Sciences of USSR, 1947.

[20] Mosier, SA and Pierce, RM. “Advanced combustor systems for stationary gas turbine engines, phase i. review and preliminary evaluation, vol i.” *contract*, pages 68–02, 1980.

[21] Lefebvre, Arthur H and Ballal, Dilip R. *Gas turbine combustion: alternative fuels and emissions.* CRC press, 2010.

[22] Li, Jianzhong, Chen, Jian, Yuan, Li, Hu, Ge, and Feng, Jianhan. “Flow characteristics of a rich-quench-lean combustor-combined low-emission and high-temperature rise combustion.” *International Journal of Aerospace Engineering*, 2019, 2019.

[23] Hatch, M, Sowa, W, SAMUELSON, G, and Holdeman, J. Jet mixing into a heated cross flow in a cylindrical duct-influence of geometry and flow variations. In *30th Aerospace Sciences Meeting and Exhibit*, page 773, 1992.

[24] Holdeman, James D and Chang, Clarence T. “The effects of air preheat and number of orifices on flow and emissions in an rql mixing section.” 2007.

[25] Levy, Yeshayahou, Sherbaum, Valery, and Arfi, Patric. “Basic thermodynamics of floxcom, the low-nox gas turbines adiabatic combustor.” *Applied thermal engineering*, 24(11-12):1593–1605, 2004.

[26] Mongia, Hukam. On continuous nox reduction of aero-propulsion engines. In *48th AIAA Aerospace Sciences Meeting Including the New Horizons Forum and Aerospace Exposition*, page 1329, 2010.

[27] Darwish, M, Abdulrahim, H, Mabrouk, A, and Hassan, A. "Cogeneration power-desalting plants using gas turbine combined cycle." *Desalination updates*, page 127, 2015.

[28] Koff, BL. "Aircraft gas turbine emissions challenge." 1994.

[29] Bahr, DW. "Technology for the design of high temperature rise combustors." *Journal of propulsion and power*, 3(2):179–186, 1987.

[30] Leonard, Gary and Stegmaier, James. "Development of an aeroderivative gas turbine dry low emissions combustion system." 1994.

[31] Plee, SL and Mellor, AM. "Review of flashback reported in prevaporizing/premixing combustors." *Combustion and Flame*, 32: 193–203, 1978.

[32] Stickles, Rick and Barrett, Jack. Taps ii technology final report–technology assessment open report. Technical report, DTFAWA-1C-00046, FAA Continuous Lower Energy, Emissions and Noise (CLEEN . . . , 2013.

[33] Giusti, Andrea, Andreini, Antonio, Facchini, Bruno, Vitale, Ignazio, and Turrini, Fabio. Thermoacoustic analysis of a full annular aero-engine lean combustor with multi-perforated liners. In *19th AIAA/CEAS Aeroacoustics Conference*, page 2099, 2013.

[34] Lieuwen, Timothy C and Yang, Vigor. *Combustion instabilities in gas turbine engines: operational experience, fundamental mechanisms, and modeling.* American Institute of Aeronautics and Astronautics, 2005.

[35] of Virginia, University. High temperature coatings. URL `https://www2.virginia.edu/ms/research/wadley/high-temp.html`.

[36] Arrhenius, Svante. “Über die dissociationswärme und den einfluss der temperatur auf den dissociationsgrad der elektrolyte.” *Zeitschrift für physikalische Chemie*, 4(1):96–116, 1889.

[37] Upadhyay, Santosh K. *Chemical kinetics and reaction dynamics*. Springer Science & Business Media, 2007.

[38] Friedman, Raymond and Burke, Edward. “Measurement of temperature distribution in a low-pressure flat flame.” *The Journal of Chemical Physics*, 22(5):824–830, 1954.

[39] Glassman, Irvin, Yetter, Richard A, and Glumac, Nick G. *Combustion*. Academic press, 2014.

[40] Veynante, Denis and Vervisch, Luc. “Turbulent combustion modeling.” *Progress in energy and combustion science*, 28(3):193–266, 2002.

[41] Liu, Kexin, Burluka, AA, and Sheppard, CGW. “Turbulent flame and mass burning rate in a spark ignition engine.” *Fuel*, 107:202–208, 2013.

[42] Andreini, Antonio and Facchini, Bruno. *SVILUPPO DI MODELLI NUMERICI PER L’ANALISI DELLA COMBUSTIONE TURBOLENTA PREMISCELATA NELLE TURBINE A GAS*. Ph. D. thesis, Università degli Studi di Firenze, Dipartimento di Energetica, 2004.

[43] Peters, Norbert. “The turbulent burning velocity for large-scale and small-scale turbulence.” *Journal of Fluid mechanics*, 384:107–132, 1999.

[44] Rohsenow, Warren M, Hartnett, James P, Cho, Young I, et al. *Handbook of heat transfer*, volume 3. McGraw-Hill New York, 1998.

[45] Cengel, YA. Termodinamica e trasmissione del calore. 1998.

[46] Kreith, Frank, Manglik, Raj M, and Bohn, Mark S. *Principles of heat transfer*. Cengage learning, 2012.

[47] Cintolesi, Carlo. *Large-eddy simulations of conjugate heat transfer with evaporation-condensation and thermal radiation*. PhD thesis, 04 2016.

[48] Lienhard, IV and John, H. *A heat transfer textbook*. phlogiston press, 2005.

[49] Modest, Michael F. *Radiative heat transfer*. Academic press, 2013.

[50] Boyce, M.P. 2 - advanced industrial gas turbines for power generation. In Rao, Ashok D., editor, *Combined Cycle Systems for Near-Zero Emission Power Generation*, Woodhead Publishing Series in Energy, pages 44 – 102. Woodhead Publishing, 2012. ISBN 978-0-85709-013-3. doi: https://doi.org/10.1533/9780857096180.44. URL `http://www.sciencedirect.com/science/article/pii/B978085709013350002X`.

[51] Han, Je-Chin, Dutta, Sandip, and Ekkad, Srinath. *Gas turbine heat transfer and cooling technology*. CRC press, 2012.

[52] Goldstein, Richard J. Film cooling. In *Advances in heat transfer*, volume 7, pages 321–379. Elsevier, 1971.

[53] Liming, HE, Yi, CHEN, Jun, DENG, Jianping, LEI, Li, FEI, and Pengfei, LIU. “Experimental study of rotating gliding arc discharge plasma-assisted combustion in an aero-engine combustion chamber.” *Chinese Journal of Aeronautics*, 32(2):337–346, 2019.

[54] Acharya, Sumanta and Kanani, Yousef. Advances in film cooling heat transfer. In *Advances in Heat Transfer*, volume 49, pages 91–156. Elsevier, 2017.

[55] Huang, Gan, Zhu, Yinhai, Liao, Zhiyuan, Ouyang, Xiao-Long, and Jiang, Pei-Xue. “Experimental investigation of transpiration cooling

with phase change for sintered porous plates." *International Journal of Heat and Mass Transfer*, 114:1201–1213, 2017.

[56] Arai, Masayuki and Suidzu, T. "Porous ceramic coating for transpiration cooling of gas turbine blade." *Journal of Thermal Spray Technology*, 22(5):690–698, 2013.

[57] Hayashi, Toshimitsu and Wakayama, Shuichi. "Thermal fatigue behavior of 3d-woven sic/sic composite with porous matrix for transpiration cooling passages." *Advanced Composite Materials*, 18 (1):61–75, 2009.

[58] Rong, Yisheng, Wei, Yuechuan, and Zhan, Renjun. "Research on thermal protection by opposing jet and transpiration for high speed vehicle." *Aerospace Science and Technology*, 48:322–327, 2016.

[59] Xu, Guoqiang, Liu, Yangpeng, Luo, Xiang, Ma, Jiandong, and Li, Haiwang. "Experimental investigation of transpiration cooling for sintered woven wire mesh structures." *International journal of heat and mass transfer*, 91:898–907, 2015.

[60] Wassell, AB and Bhangu, JK. The development and application of improved combustor wall cooling techniques. In *Turbo Expo: Power for Land, Sea, and Air*, volume 79658, page V01AT01A066. American Society of Mechanical Engineers, 1980.

[61] Nealy, DA and Reider, SB. "Evaluation of laminated porous wall materials for combustor liner cooling." *gatu*, 1979.

[62] Huang, Gan, Min, Zheng, Yang, Li, Jiang, Pei-Xue, and Chyu, Minking. "Transpiration cooling for additive manufactured porous plates with partition walls." *International Journal of Heat and Mass Transfer*, 124:1076–1087, 2018.

[63] Kretschmer, D and Odgers, J. A simple method for the prediction of wall temperatures in gas turbines. In *Turbo Expo: Power for*

Land, Sea, and Air, volume 79719, page V01AT01A090. American Society of Mechanical Engineers, 1978.

[64] Gerendas, Miklos, Hoeschler, K., and Schilling, Th. “Development and modeling of angled effusion cooling for the br715 low emission staged combustor core demonstrator.” page 13, 03 2003.

[65] Mendez, Simon and Nicoud, Franck. Numerical investigation of an anisothermal turbulent flow with effusion. In *Fifth International Symposium on Turbulence and Shear Flow Phenomena*. Begel House Inc., 2007.

[66] Facchini, Bruno, Tarchi, Lorenzo, Toni, Lorenzo, and Ceccherini, Alberto. “Adiabatic and Overall Effectiveness Measurements of an Effusion Cooling Array for Turbine Endwall Application.” *Journal of Turbomachinery*, 132(4), 04 2010. ISSN 0889-504X. doi: 10.1115/1.3213555. URL `https://doi.org/10.1115/1.3213555`. 041008.

[67] Andreini, Antonio, Facchini, Bruno, Picchi, Alessio, Tarchi, Lorenzo, and Turrini, Fabio. “Experimental and theoretical investigation of thermal effectiveness in multiperforated plates for combustor liner effusion cooling.” *Journal of Turbomachinery*, 136(9), 2014.

[68] Harrington, Mark K, McWaters, Marcus A, Bogard, David G, Lemmon, Christopher A, and Thole, Karen A. “Full-coverage film cooling with short normal injection holes.” *J. Turbomach.*, 123(4): 798–805, 2001.

[69] Qu, Li-hong, Zhang, Jing-zhou, and Tan, Xiao-ming. “Improvement on film cooling effectiveness by a combined slot-effusion scheme.” *Applied Thermal Engineering*, 126:379–392, 2017.

[70] Andrei, Luca, Andreini, Antonio, Bianchini, Cosimo, Caciolli, Gianluca, Facchini, Bruno, Mazzei, Lorenzo, Picchi, Alessio, and

Turrini, Fabio. “Effusion cooling plates for combustor liners: experimental and numerical investigations on the effect of density ratio.” *Energy Procedia*, 45(0):1402–1411, 2014.

[71] Facchini, Bruno, Maiuolo, Francesco, Tarchi, Lorenzo, and Coutandin, Daniele. Combined effect of slot injection, effusion array and dilution hole on the heat transfer coefficient of a real combustor liner: Part 1—experimental analysis. In *Turbo Expo: Power for Land, Sea, and Air*, volume 43994, pages 753–762, 2010.

[72] *Combined Effect of Slot Injection, Effusion Array and Dilution Hole on the Heat Transfer Coefficient of a Real Combustor Liner: Part 2—Numerical Analysis*, volume Volume 4: Heat Transfer, Parts A and B of *Turbo Expo: Power for Land, Sea, and Air*, 06 2010. doi: 10.1115/GT2010-22937. URL `https://doi.org/10.1115/GT2010-22937`.

[73] Tarchi, Lorenzo, Facchini, Bruno, Maiuolo, Francesco, and Coutandin, Daniele. “Experimental investigation on the effects of a large recirculating area on the performance of an effusion cooled combustor liner.” *Journal of engineering for gas turbines and power*, 134(4), 2012.

[74] Andreini, A, Caciolli, G, Facchini, B, Tarchi, L, Coutandin, D, Peschiulli, A, and Taddei, S. Density ratio effects on the cooling performances of a combustor liner cooled by a combined slot/effusion system. In *Turbo Expo: Power for Land, Sea, and Air*, volume 44700, pages 903–914. American Society of Mechanical Engineers, 2012.

[75] Andrei, Luca, Andreini, Antonio, Bianchini, Cosimo, Facchini, Bruno, Mazzei, Lorenzo, and Turrini, Fabio. “Investigation on the effect of a realistic flow field on the adiabatic effectiveness of an effusion-cooled combustor.” *Journal of Engineering for Gas Turbines and Power*, 137(5), 2015.

[76] Bogard, David G and Thole, Karen A. “Gas turbine film cooling.” *Journal of propulsion and power*, 22(2):249–270, 2006.

[77] New, TH, Lim, TT, and Luo, SC. “Elliptic jets in cross-flow.” *Journal of fluid mechanics*, 494(10):119–140, 2003.

[78] Moussa, ZM, Trischka, John W, and Eskinazi, S. “The near field in the mixing of a round jet with a cross-stream.” *Journal of Fluid Mechanics*, 80(1):49–80, 1977.

[79] Andreopoulos, J. “On the structure of jets in a crossflow.” *Journal of Fluid Mechanics*, 157:163–197, 1985.

[80] Kelso, Richard Malcolm, Lim, TT, and Perry, AE. “An experimental study of round jets in cross-flow.” *Journal of fluid mechanics*, 306: 111–144, 1996.

[81] Cortelezzi, Luca, Karagozian, Ann R, et al. “On the formation of the counter-rotating vortex pair in transverse jets.” *Journal of Fluid Mechanics*, 446:347–374, 2001.

[82] Muppidi, Suman and Mahesh, Krishnan. Direct numerical simulation of turbulent jets in crossflow. In *43rd AIAA Aerospace Sciences Meeting and Exhibit*, page 1115, 2005.

[83] Mahesh, Krishnan. “The interaction of jets with crossflow.” *Annual review of fluid mechanics*, 45:379–407, 2013.

[84] Kelso, RM and Smits, AJ. “Horseshoe vortex systems resulting from the interaction between a laminar boundary layer and a transverse jet.” *Physics of Fluids*, 7(1):153–158, 1995.

[85] Fric, TF and Roshko, A. “Vortical structure in the wake of a transverse jet.” *Journal of Fluid Mechanics*, 1994:1–47, 1994.

[86] Margason, Richard J. “Fifty years of jet in cross flow research.” *ceaj*, 1993.

[87] Sen, Basav, Schmidt, Donald L, and Bogard, David G. "Film cooling with compound angle holes: heat transfer." 1996.

[88] Foster, NW and Lampard, D. "The flow and film cooling effectiveness following injection through a row of holes." 1980.

[89] Baldauf, S, Schulz, A, and Wittig, S. "High-resolution measurements of local effectiveness from discrete hole film cooling." *J. Turbomach.*, 123(4):758–765, 2001.

[90] Yuen, CHN and Martinez-Botas, RF. "Film cooling characteristics of rows of round holes at various streamwise angles in a crossflow: Part i. effectiveness." *International Journal of Heat and Mass Transfer*, 48(23-24):4995–5016, 2005.

[91] Behrendt, Thomas and Hassa, Ch. "A test rig for investigations of gas turbine combustor cooling concepts under realistic operating conditions." *Proceedings of the Institution of Mechanical Engineers, Part G: Journal of Aerospace Engineering*, 222(2):169–177, 2008.

[92] Andreini, Antonio, Becchi, Riccardo, Facchini, Bruno, Picchi, Alessio, and Peschiulli, Antonio. "The effect of effusion holes inclination angle on the adiabatic film cooling effectiveness in a three-sector gas turbine combustor rig with a realistic swirling flow." *International Journal of Thermal Sciences*, 121:75–88, 2017.

[93] Ligrani, PM, Ciriello, S, and Bishop, DT. "Heat transfer, adiabatic effectiveness, and injectant distributions downstream of a single row and two staggered rows of compound angle film-cooling holes." 1992.

[94] Ligrani, PM, Wigle, JM, and Jackson, SW. "Film-cooling from holes with compound angle orientations: Part 2—results downstream of a single row of holes with 6d spanwise spacing." 1994.

[95] Ekkad, Srinath V, Zapata, Dyrk, and Han, Je-Chin. "Film effectiveness over a flat surface with air and co2 injection through compound angle holes using a transient liquid crystal image method." 1997.

[96] Schmidt, Donald L, Sen, Basav, and Bogard, David G. “Film cooling with compound angle holes: adiabatic effectiveness.” 1996.

[97] Al-Hamadi, AK, Jubran, BA, and Theodoridis, G. “Turbulence intensity effects on film cooling and heat transfer from compound angle holes with particular application to gas turbine blades.” *Energy conversion and management*, 39(14):1449–1457, 1998.

[98] Liu, YQ, Wang, YP, et al. Flow and heat transfer characteristics of two effused cooling models: transpiration cooling and full coverage film cooling. pages 622–629, 2008.

[99] Goodro, Matt, Ligrani, Phil, Fox, Mike, and Moon, Hee-Koo. Full-coverage film cooling: film effectiveness and heat transfer coefficients for dense hole arrays at different hole angles, contraction ratios, and blowing ratios. In *Turbo Expo: Power for Land, Sea, and Air*, volume 44700, pages 1707–1723. American Society of Mechanical Engineers, 2012.

[100] Burd, Steven W, Kaszeta, Richard W, and Simon, Terrence W. “Measurements in film cooling flows: hole l/d and turbulence intensity effects.” 1998.

[101] Burd, Steven W and Simon, Terrence W. “Turbulence spectra and length scales measured in film coolant flows emerging from discrete holes.” 1999.

[102] Lutum, Ewald and Johnson, Bruce V. “Influence of the hole length-to-diameter ratio on film cooling with cylindrical holes.” 1999.

[103] Sinha, AK, Bogard, DG, and Crawford, ME. “Film-cooling effectiveness downstream of a single row of holes with variable density ratio.” 1991.

[104] Pedersen, DR, Eckert, Ernest RG, and Goldstein, Richard J. “Film cooling with large density differences between the mainstream and

the secondary fluid measured by the heat-mass transfer analogy." 1977.

[105] Johnson, Blake, Tian, Wei, Zhang, Kai, and Hu, Hui. "An experimental study of density ratio effects on the film cooling injection from discrete holes by using piv and psp techniques." *International Journal of Heat and Mass Transfer*, 76:337–349, 2014.

[106] Goldstein, RJ, Eckert, ERG, and Burggraf, F. "Effects of hole geometry and density on three-dimensional film cooling." *International Journal of heat and mass transfer*, 17(5):595–607, 1974.

[107] Baldauf, Set al, Scheurlen, M, Schulz, A, and Wittig, S. Correlation of film cooling effectiveness from thermographic measurements at engine like conditions. In *Turbo Expo: Power for Land, Sea, and Air*, volume 36088, pages 149–162, 2002.

[108] Bernsdorf, Stefan, Rose, Martin G, and Abhari, Reza S. "Modeling of film cooling—part i: experimental study of flow structure." 2006.

[109] Duchaine, F., Corpron, A., Pons, L., Moureau, V., Nicoud, F., and Poinsot, T. "Development and assessment of a coupled strategy for conjugate heat transfer with large eddy simulation: application to a cooled turbine blade." *International Journal of Heat and Fluid Flow*, 30(6):1129–1141, 2009.

[110] Bohn, Dieter, Ren, Jing, and Kusterer, Karsten. "Systematic investigation on conjugate heat transfer rates of film cooling configurations." *International Journal of Rotating Machinery*, 2005, 2005.

[111] Garg, Vijay K. "Heat transfer research on gas turbine airfoils at nasa grc." *International Journal of Heat and Fluid Flow*, 23(2): 109–136, 2002.

[112] Heselhaus, A and Vogel, D. Numerical simulation of turbine blade cooling with respect to blade heat conduction and inlet temperature

profiles. In *31st Joint Propulsion Conference and Exhibit*, page 3041, 1995.

[113] Papanicolaou, E, Giebert, D, Koch, R, and Schulz, A. "A conservation-based discretization approach for conjugate heat transfer calculations in hot-gas ducting turbomachinery components." *International Journal of Heat and Mass Transfer*, 44(18):3413–3429, 2001.

[114] Roe, B, Jaiman, R, Haselbacher, A, and Geubelle, Philippe H. "Combined interface boundary condition method for coupled thermal simulations." *International journal for numerical methods in fluids*, 57(3):329–354, 2008.

[115] Sondak, Douglas L and Dorney, Daniel J. "Simulation of coupled unsteady flow and heat conduction in turbine stage." *Journal of Propulsion and Power*, 16(6):1141–1148, 2000.

[116] John, Bibin, Senthilkumar, P, and Sadasivan, Sreeja. "Applied and theoretical aspects of conjugate heat transfer analysis: a review." *Archives of Computational Methods in Engineering*, 26(2):475–489, 2019.

[117] Alonso, Juan, Hahn, Seonghyeon, Ham, Frank, Herrmann, Marcus, Iaccarino, Gianluca, Kalitzin, Georgi, LeGresley, Patrick, Mattsson, Ken, Medic, Gorazd, Moin, Parviz, et al. Chimps: A high-performance scalable module for multi-physics simulations. In *42nd AIAA/ASME/SAE/ASEE Joint Propulsion Conference & Exhibit*, page 5274, 2006.

[118] Gourdain, N, Gicquel, L, Montagnac, M, Vermorel, O, Gazaix, M, Staffelbach, G, Garcia, M, Boussuge, JF, and Poinsot, T. "High performance parallel computing of flows in complex geometries: I. methods." *Computational Science & Discovery*, 2(1):015003, 2009.

[119] Buis, Samuel, Piacentini, Andrea, and Déclat, Damien. "Palm: a computational framework for assembling high-performance com-

puting applications." *Concurrency and computation: practice and experience*, 18(2):231–245, 2006.

[120] Zhang, Shengtao, Chen, Fang, and Liu, Hong. "Time-adaptive, loosely coupled strategy for conjugate heat transfer problems in hypersonic flows." *Journal of Thermophysics and Heat Transfer*, 28 (4):635–646, 2014.

[121] Zhao, Xiaoli, Sun, Zhenxu, Tang, Longsheng, and Zheng, Gangtie. "Coupled flow-thermal-structural analysis of hypersonic aerodynamically heated cylindrical leading edge." *Engineering Applications of Computational Fluid Mechanics*, 5(2):170–179, 2011.

[122] He, L and Oldfield, MLG. "Unsteady conjugate heat transfer modeling." *Journal of turbomachinery*, 133(3), 2011.

[123] Fadl, M and He, L. On les based conjugate heat transfer procedure for transient natural convection. In *Turbo Expo: Power for Land, Sea, and Air*, volume 50879, page V05AT10A002. American Society of Mechanical Engineers, 2017.

[124] Fadl, M, He, L, Stein, P, and Marinescu, G. "Assessment of unsteadiness modeling for transient natural convection." *Journal of Engineering for Gas Turbines and Power*, 140(1), 2018.

[125] Koren, Chai, Vicquelin, Ronan, and Gicquel, Olivier. "Self-adaptive coupling frequency for unsteady coupled conjugate heat transfer simulations." *International Journal of Thermal Sciences*, 118:340–354, 2017.

[126] Koren, Chai, Vicquelin, Ronan, and Gicquel, Olivier. "Multiphysics simulation combining large-eddy simulation, wall heat conduction and radiative energy transfer to predict wall temperature induced by a confined premixed swirling flame." *Flow, Turbulence and Combustion*, 101(1):77–102, 2018.

[127] Mazzei, Lorenzo. *A 3d coupled approach for the thermal design of aeroengine combustor liners.* PhD thesis, University of Florence, 2014.

[128] Rida, Samir, Reynolds, Robert, Chakravorty, Saugata, and Gupta, Kapil. Imprinted effusion modeling and dynamic cd calculation in gas turbine combustors. In *Turbo Expo: Power for Land, Sea, and Air*, volume 44687, pages 589–599. American Society of Mechanical Engineers, 2012.

[129] Nguyen, Phu Hung and Dorignac, Eva. "Experimental study of convective exchange in a low aspect ratio perforation: Application to cooling of multiperforated wall." *Experimental thermal and fluid science*, 33(1):114–122, 2008.

[130] Fanning, John Thomas. *A practical treatise on hydraulic and water-supply engineering.* 1882.

[131] Crawford, ME, Kays, WM, and Moffat, RJ. "Full-coverage film cooling—part ii: heat transfer data and numerical simulation." 1980.

[132] Heidmann, James D and Hunter, Scott D. *Coarse grid modeling of turbine film cooling flows using volumetric source terms*, volume 78521. American Society of Mechanical Engineers, 2001.

[133] Hunter, Scott David. *Source term modeling of endwall cavity flow effects on gaspath aerodynamics in an axial flow turbine.* PhD thesis, University of Cincinnati, December 1998.

[134] Burdet, André, Abhari, Reza S, and Rose, Martin G. "Modeling of film cooling—part ii: Model for use in three-dimensional computational fluid dynamics." 2007.

[135] Völker, Stefan et al. "A model for cylindrical hole film cooling—part ii: model formulation, implementation and results." *Journal of turbomachinery*, 134(6), 2012.

[136] Voigt, Stefan, Noll, Berthold, and Aigner, Manfred. Development of a macroscopic cfd model for effusion cooling applications. In *Turbo Expo: Power for Land, Sea, and Air*, volume 44700, pages 1235–1243. American Society of Mechanical Engineers, 2012.

[137] Andreini, Antonio, Da Soghe, Riccardo, Facchini, Bruno, Mazzei, Lorenzo, Colantuoni, Salvatore, and Turrini, Fabio. "Local source based cfd modeling of effusion cooling holes: Validation and application to an actual combustor test case." *Journal of engineering for gas turbines and power*, 136(1), 2014.

[138] Mazzei, Lorenzo, Andreini, Antonio, and Facchini, Bruno. "Assessment of modelling strategies for film cooling." *International Journal of Numerical Methods for Heat & Fluid Flow*, 27(5):1118–1127, 2017.

[139] Andrei, Luca, Innocenti, Luca, Andreini, Antonio, Facchini, Bruno, and Winchler, Lorenzo. "Film cooling modeling for gas turbine nozzles and blades: Validation and application." *Journal of Turbomachinery*, 139(1), 2017.

[140] Mendez, Simon and Nicoud, Franck. "Adiabatic homogeneous model for flow around a multiperforated plate." *AIAA journal*, 46(10): 2623–2633, 2008.

[141] Lahbib, Dorian. "Modélisation aérodynamique et thermique des multiperforations en les." 2015.

[142] Bizzari, R, Dauptain, A, Gicquel, L, and Nicoud, F. A thickened-hole model for les over multiperforated liners. In *4e Colloque du réseau d'INitiative en Combustion Avancée (INCA)*, page 46, 2017.

[143] Thomas, Martin, Dauptain, Antoine, Duchaine, Florent, Gicquel, Laurent, Koupper, Charlie, and Nicoud, Franck. Comparison of heterogeneous and homogeneous coolant injection models for large eddy simulation of multiperforated liners present in a combustion simulator. In *Turbo Expo: Power for Land, Sea, and Air*,

volume 50794, page V02BT41A038. American Society of Mechanical Engineers, 2017.

[144] Jolliffe, Ian T and Cadima, Jorge. “Principal component analysis: a review and recent developments.” *Philosophical Transactions of the Royal Society A: Mathematical, Physical and Engineering Sciences*, 374(2065):20150202, 2016.

[145] Aversano, Gianmarco, Bellemans, Aurelie, Li, Zhiyi, Coussement, Axel, Gicquel, Olivier, and Parente, Alessandro. “Application of reduced-order models based on pca & kriging for the development of digital twins of reacting flow applications.” *Computers & Chemical Engineering*, 121:422–441, 2019.

[146] Haag, Sebastian and Anderl, Reiner. “Digital twin–proof of concept.” *Manufacturing Letters*, 15:64–66, 2018.

[147] Aversano, Gianmarco, Ferrarotti, Marco, and Parente, Alessandro. “Digital twin of a combustion furnace operating in flameless conditions: reduced-order model development from cfd simulations.” *Proceedings of the Combustion Institute*, 2020.

[148] Abdi, Hervé and Williams, Lynne J. “Principal component analysis.” *Wiley interdisciplinary reviews: computational statistics*, 2(4):433–459, 2010.

[149] Parente, Alessandro and Sutherland, James C. “Principal component analysis of turbulent combustion data: Data pre-processing and manifold sensitivity.” *Combustion and flame*, 160(2):340–350, 2013.

[150] Peerenboom, Kim, Parente, Alessandro, Kozák, Tomáš, Bogaerts, Annemie, and Degrez, Gérard. “Dimension reduction of non-equilibrium plasma kinetic models using principal component analysis.” *Plasma Sources Science and Technology*, 24(2):025004, 2015.

[151] Smola, Alex J and Schölkopf, Bernhard. "A tutorial on support vector regression." *Statistics and computing*, 14(3):199–222, 2004.

[152] Rasmussen, Carl Edward and Nickisch, Hannes. "Gaussian processes for machine learning (gpml) toolbox." *The Journal of Machine Learning Research*, 11:3011–3015, 2010.

[153] Leclercq, Florent. "Bayesian optimization for likelihood-free cosmological inference." *Physical Review D*, 98(6):063511, 2018.

[154] Freier, Lars, Wiechert, Wolfgang, and von Lieres, Eric. "Kriging with trend functions nonlinear in their parameters: Theory and application in enzyme kinetics." *Engineering in Life Sciences*, 17 (8):916–922, 2017.

[155] Constantine, Paul G, Dow, Eric, and Wang, Qiqi. "Active subspace methods in theory and practice: applications to kriging surfaces." *SIAM Journal on Scientific Computing*, 36(4):A1500–A1524, 2014.

[156] Simpson, Timothy, Mistree, Farrokh, Korte, John, and Mauery, Timothy. Comparison of response surface and kriging models for multidisciplinary design optimization. In *7th AIAA/USAF/NASA/ISSMO Symposium on Multidisciplinary Analysis and Optimization*, page 4755, 1998.

[157] Duchaine, Florent, Morel, Thierry, and Gicquel, LYM. "Computational-fluid-dynamics-based kriging optimization tool for aeronautical combustion chambers." *AIAA journal*, 47(3): 631–645, 2009.

[158] Geigle, K. P., Hadef, R., and Meier, W. "Soot formation and flame characterization of an aero-engine model combustor burning ethylene at elevated pressure." *ASME J Eng Gas Turb Pwr*, 136 (2):021505, 2014.

[159] Geigle, K. P., O'Loughlin, W., Hadef, R., and Meier, W. "Visualization of soot inception in turbulent pressurized flames by

simultaneous measurement of laser-induced fluorescence of polycyclic aromatic hydrocarbons and laser-induced incandescence, and correlation to oh distributions.” *Applied Physics B*, 119(4):717–730, 2015.

[160] Franzelli, B., Riber, E., Cuenot, B., and Ihme, M. Numerical modeling of soot production in aero-engine combustors using large eddy simulations. In *ASME Turbo Expo 2015: Turbine Technical Conference and Exposition*, number GT2015-43630, page V04BT04A049. American Society of Mechanical Engineers, 2015.

[161] Eberle, Christian, Gerlinger, Peter, Geigle, Klaus Peter, and Aigner, Manfred. “Toward finite-rate chemistry large-eddy simulations of sooting swirl flames.” *Combustion Science and Technology*, 190(7):1194–1217, 2018.

[162] Grader, Martin, Eberle, Christian, Gerlinger, Peter, and Aigner, Manfred. Les of a pressurized, sooting aero-engine model combustor at different equivalence ratios with a sectional approach for pahs and soot. In *ASME Turbo Expo 2018: Turbomachinery Technical Conference and Exposition*, pages V04AT04A012–V04AT04A012. American Society of Mechanical Engineers, 2018.

[163] Koo, Heeseok, Raman, Venkatramanan, Mueller, Michael E, and Geigle, Klaus-Peter. Les of a sooting flame in a pressurized swirl combustor. In *54th AIAA Aerospace Sciences Meeting*, page 2123, 2016.

[164] Chong, Shao Teng, Hassanaly, Malik, Koo, Heeseok, Mueller, Michael E, Raman, Venkat, and Geigle, Klaus-Peter. “Large eddy simulation of pressure and dilution-jet effects on soot formation in a model aircraft swirl combustor.” *Combustion and Flame*, 192:452–472, 2018.

[165] Wick, Achim, Priesack, Frederic, and Pitsch, Heinz. Large-eddy simulation and detailed modeling of soot evolution in a model

aero engine combustor. In *ASME Turbo Expo 2017: Turbomachinery Technical Conference and Exposition*, pages V04AT04A020–V04AT04A020. American Society of Mechanical Engineers, 2017.

[166] Rodrigues, Pedro. *Modélisation multiphysique de flammes turbulentes suitées avec la prise en compte des transferts radiatifs et des transferts de chaleur pariétaux.* PhD thesis, 06 2018.

[167] Eberle, C., Gerlinger, P., Geigle, K. P., and Aigner, M. "Numerical investigation of transient soot evolution processes in an aero-engine model combustor." *Combustion Science and Technology*, 187(12): 1841–1866, 2015.

[168] Paccati, S, Bertini, D, Puggelli, S, Mazzei, L, and Andreini, A. "Soot prediction in a model aero engine combustor with multiphysics approach."

[169] Paccati, Simone, Bertini, Davide, Puggelli, Stefano, Mazzei, Lorenzo, Andreini, Antonio, and Facchini, Bruno. "Numerical analyses of a high pressure sooting flame with multiphysics approach." *Energy Procedia*, 148:591–598, 2018.

[170] Ansys, Inc. *Ansys Fluent Theory Guide*, release 19.3 edition, 2019.

[171] Nicoud, Franck and Ducros, Frédéric. "Subgrid-scale stress modelling based on the square of the velocity gradient tensor." *Flow, turbulence and Combustion*, 62(3):183–200, 1999.

[172] van Oijen, Jeroen. *Flamelet-generated manifolds: development and application to premixed laminar flames.* Technische Universiteit Eindhoven, 2002.

[173] Donini, A., Bastiaans, R., van Oijen, J., and de Goey, L. The implementation of five-dimensional fgm combustion model for the simulation of a gas turbine model combustor. In *ASME turbo expo 2015: turbine technical conference and exposition*, page V04AT04A007. American Society of Mechanical Engineers, 2015.

[174] ANSYS. *ANSYS Fluent, 19.3 Theory Guide.*

[175] *The Implementation of Five-Dimensional FGM Combustion Model for the Simulation of a Gas Turbine Model Combustor*, volume Volume 4A: Combustion, Fuels and Emissions of *Turbo Expo: Power for Land, Sea, and Air*, 06 2015. doi: 10.1115/GT2015-42037. URL `https://doi.org/10.1115/GT2015-42037`. V04AT04A007.

[176] Puggelli, Stefano, Bertini, Davide, Mazzei, Lorenzo, and Andreini, Antonio. "Assessment of Scale-Resolved Computational Fluid Dynamics Methods for the Investigation of Lean Burn Spray Flames." *Journal of Engineering for Gas Turbines and Power*, 139(2), 09 2016. ISSN 0742-4795. doi: 10.1115/1.4034194. URL `https://doi.org/10.1115/1.4034194`. 021501.

[177] Puggelli, S., Bertini, D., Mazzei, L., and Andreini, A. "Modeling Strategies for Large Eddy Simulation of Lean Burn Spray Flames." *Journal of Engineering for Gas Turbines and Power*, 140(5), 11 2017. ISSN 0742-4795. doi: 10.1115/1.4038127. URL `https://doi.org/10.1115/1.4038127`. 051501.

[178] Brookes, SJ and Moss, JB. "Predictions of soot and thermal radiation properties in confined turbulent jet diffusion flames." *Combustion and Flame*, 116(4):486–503, 1999.

[179] Wang, H. and Laskin, A. "A comprehensive kinetic model of ethylene and acetylene oxidation at high temperatures." *Progress Report for an AFOSR New World Vista Program*, 1998.

[180] Murthy, JY and Mathur, SR. "Finite volume method for radiative heat transfer using unstructured meshes." *Journal of thermophysics and heat transfer*, 12(3):313–321, 1998.

[181] Paccati, S., Bertini, D., S.Puggelli, Mazzei, L., Andreini, A., and Facchini, B. "Numerical analyses of a high pressure sooting flame with multiphysics approach." *Energy Procedia*, 148:591 – 598, 2018.

doi: https://doi.org/10.1016/j.egypro.2018.08.146. ATI 2018 - 73rd Conference of the Italian Thermal Machines Engineering Association.

[182] Rodrigues, P, Gicquel, O, Darabiha, N, Geigle, KP, and Vicquelin, R. Assessment of external heat transfer modeling of a laboratory-scale combustor inside a pressure-housing environment. In *ASME Turbo Expo 2018: Turbomachinery Technical Conference and Exposition*, pages V05CT17A008–V05CT17A008. American Society of Mechanical Engineers, 2018.

[183] Pope, Stephen B. "Ten questions concerning the large-eddy simulation of turbulent flows." *New journal of Physics*, 6(1):35, 2004.

[184] Shih, Tsan-Hsing, Liou, William W, Shabbir, Aamir, Yang, Zhigang, and Zhu, Jiang. "A new $k-\epsilon$ eddy viscosity model for high reynolds number turbulent flows." *Computers & fluids*, 24(3):227–238, 1995.

[185] Nau, Patrick, Yin, Zhiyao, Geigle, Klaus Peter, and Meier, Wolfgang. "Wall temperature measurements at elevated pressures and high temperatures in sooting flames in a gas turbine model combustor." *Applied Physics B*, 123(12):279, 2017.

[186] Menter, Florian R. "Two-equation eddy-viscosity turbulence models for engineering applications." *AIAA journal*, 32(8):1598–1605, 1994.

[187] Frank, Thomas and Menter, Florian. "Validation of urans sst and sbes in ansys cfd for the turbulent mixing of two parallel planar water jets impinging on a stationary pool." *jets*, pages 1–9, 2015.

[188] Kampe, T. and Völker, S. "Numerical investigation of flat plate film cooling and analysis of variance of relevant flow parameters." pages 569–578, 01 2009.

[189] Géron, Aurélien. *Hands-on machine learning with Scikit-Learn, Keras, and TensorFlow: Concepts, tools, and techniques to build intelligent systems*. O'Reilly Media, 2019.

[190] Scrittore, Joseph J, Thole, Karen Ann, and Burd, Steven W. "Investigation of velocity profiles for effusion cooling of a combustor liner." 2007.

[191] McGovern, Kevin T and Leylek, James H. "A detailed analysis of film cooling physics: Part ii—compound-angle injection with cylindrical holes." *J. Turbomach.*, 122(1):113–121, 2000.

[192] Kohli, A and Thole, Karen Ann. Entrance effects on diffused film-cooling holes. In *Turbo Expo: Power for Land, Sea, and Air*, volume 78651, page V004T09A070. American Society of Mechanical Engineers, 1998.

[193] Welch, Peter. "The use of fast fourier transform for the estimation of power spectra: a method based on time averaging over short, modified periodograms." *IEEE Transactions on audio and electroacoustics*, 15(2):70–73, 1967.

[194] Mazzei, Lorenzo, Andreini, Antonio, Facchini, Bruno, and Turrini, Fabio. "Impact of swirl flow on combustor liner heat transfer and cooling: a numerical investigation with hybrid reynolds-averaged navier–stokes large eddy simulation models." *Journal of Engineering for Gas Turbines and Power*, 138(5), 2016.

[195] Bertini, D, Mazzei, L, Andreini, A, and Facchini, B. Multiphysics numerical investigation of an aeronautical lean burn combustor. In *Turbo Expo: Power for Land, Sea, and Air*, volume 58653, page V05BT17A004. American Society of Mechanical Engineers, 2019.

[196] Lenzi, Tommaso, Palanti, Lorenzo, Picchi, Alessio, Bacci, Tommaso, Mazzei, Lorenzo, Andreini, Antonio, and Facchini, Bruno. "Time-resolved flow field analysis of effusion cooling system with representative swirling main flow." *Journal of Turbomachinery*, 142 (6), 2020.

[197] Lenzi, Tommaso, Picchi, Alessio, Bacci, Tommaso, Andreini, Antonio, and Facchini, Bruno. "Unsteady flow field characterization

of effusion cooling systems with swirling main flow: Comparison between cylindrical and shaped holes.” *Energies*, 13(19):4993, 2020.